UC San Diego
UC San Diego Electronic Theses and Dissertations

Title

Composition, sources, and formation of secondary organic aerosols from urban emissions

Permalink

https://escholarship.org/uc/item/5cm9h9xp

Authors

Liu, Shang
Liu, Shang

Publication Date

2012

Peer reviewed|Thesis/dissertation

UNIVERSITY OF CALIFORNIA, SAN DIEGO

**Composition, Sources, and Formation of Secondary Organic Aerosols
from Urban Emissions**

A dissertation submitted in partial satisfaction of the
requirements for the degree
Doctor of Philosophy

in

Earth Sciences

by

Shang Liu

Committee in charge:

Professor Lynn Russell, Chair
Professor Andrew Dickson
Professor Joel Norris
Professor Kimberly Prather
Professor Michael Tauber

2012

The dissertation of Shang Liu is approved, and it is acceptable in quality and form for publication on microfilm and electronically:

_____

_____

_____

_____

_____

Chair

University of California, San Diego

2012

This thesis is dedicated to my parents and grandparents for their endless support, encouragement, care, and love.

TABLE OF CONTENTS

LIST OF FIGURES

ACKNOWLEDGEMENTS

First and foremost, I would like to acknowledge my advisor Professor Lynn Russell, who has provided me with continuous support and invaluable opportunities to learn new knowledge. I am most grateful for the time she spent on insightful discussions and on my paper drafts. Her guidance and advice will benefit me the rest of my academic life. I am also grateful to past and current members in the Russell laboratory for their collaboration and teamwork, without which this thesis cannot be finished. Special thanks are given to my girlfriend, Xiaochen Tang, for her care, accompany, and understandings of my busy schedule and many working weekends. Besides, I would like to thank the Chinese community and all the international friends who have helped enormously along the way and made my life colorful.

Chapter 1, in full, is a reprint of the material as it appears in Atmospheric Chemistry and Physics 2009 with slight modifications. Liu, S., Takahama, S., Russell, L. M., Gilardoni, S., and Baumgardner, D. (2009), Oxygenated organic functional groups and their sources in single and submicron organic particles in MILAGRO 2006 campaign, Atmospheric Chemistry and Physics, 9, 6849-6863. The dissertation author was the primary investigator and author of this paper.

Chapter 2, in full, is a reprint of the material as it appears in Atmospheric Chemistry and Physics 2011 with slight modifications. Liu, S., Day, D. A., Shields, J. E., and Russell, L. M. (2011), Ozone-driven daytime formation of secondary organic aerosol containing carboxylic acid groups and alkane groups, Atmospheric Chemistry and Physics, 11, 8321-8341. The dissertation author was the primary investigator and author of this paper.

Chapter 3, in full, has been submitted for publication to Journal of Geophysical Research-Atmospheres 2012. Liu, S., Ahlm, L., Day, D. A., Russell, L. M., Zhao, Y., Gentner, D. R., Weber, R. J., Goldstein, A. H., Jaoui, M., Offenberg, J. H., Kleindienst, T. E., Rubitschun, C., Surratt, J. D, Sheesley, R. J., and Scheller, S. (2012), Secondary organic aerosol formation from fossil fuel sources contribute majority of summertime organic mass at Bakersfield. The dissertation author was the primary investigator and author of this paper.

Chapter 4, in full, is a reprint of the material as it appears in Atmospheric Measurement Techniques Discussion 2012 with slight modifications. Liu, S., Russell, L. M., Sueper, D. T., and Onasch, T. B. (2012), Organic particle types by single-particle measurements using a time-of-flight aerosol mass spectrometer coupled with a light scattering module, Atmospheric Measurement Techniques Discussion, 5, 3047-3077. The dissertation author was the primary investigator and author of this paper.

Chapter 5, in full, is a reprint of the material as it appears in Aerosol Science and Technology 2012. Liu, S., Shilling, J.E., Song, C., Hiranuma, N., Zaveri, A.Z., and Russell, L.M. (2012), Hydrolysis of organonitrate functional groups in aerosol particles, 46, 1359-1369. The dissertation author was the primary investigator and author of this paper.

VITA

2003	B. S. in Environmental Sciences, Jilin University, China
2006	M. S. in Environmental Sciences, Peking University, China
2012	Ph. D. in Earth Sciences, University of California, San Diego, USA

PUBLICATIONS

Liu, **S**., Takahama, S., Russell, L. M., Gilardoni, S. and Baumgardner, D.:Oxygenated organic functional groups and their sources in single and submicron organic particles in MILAGRO 2006 campaign, Atmos. Chem. Phys., 9 (18), 6849-6863, 2009.

Liu, **S**., Day, D.A., Shields, J. E., and Russell, L. M.: Ozone-driven daytime formation of secondary organic aerosol containing carboxylic acid groups and alkane groups, Atmos. Chem. Phys., 11, 8321-8341, 2011.

Liu, **S**., Russell, L. M., Day, D. A., and Onasch, T. B.: Organic particle types by single-particle measurements using a time-of-flight aerosol mass spectrometer coupled with a light scattering module, Atmos. Meas. Tech. Discuss., 5, 3047-3077, 2012 (under review).

Liu, **S**., Ahlm, L., Day, D. A., Russell, L. M., Zhao, Y., Gentner, D. R., Weber, R. J., Goldstein, A. H., Jaoui, M., Offenberg, J. H., Kleindienst, T. E., Rubitschun, C., Surratt, J. D, Sheesley, R. J., and Scheller, S.: Secondary organic aerosol formation from fossil fuel sources contribute majority of summertime organic mass at Bakersfield, *submitted*.

Liu, **S**., Shilling, J.E., Song, C., Hiranuma, N., Zaveri, A.Z., and Russell, L.M.: Hydrolysis of organonitrate functional groups in aerosol particles, Aerosol Science and Technology, 46, 1359-1369, 2012.

Gilardoni, S., **Liu**, **S**., Takahama, S., Russell, L. M., Allan, J. D., Steinbrecher, R., Jimenez, J. L., De Carlo, P. F., Dunlea, E. J. and Baumgardner, D.: Characterization of organic ambient aerosol during MIRAGE 2006 on three platforms, Atmos. Chem. Phys., 9 (15), 5417-5432, 2009.

Takahama, S., **Liu**, **S**. and Russell, L. M.: Coatings and clusters of carboxylic acids in carbon-containing atmospheric particles from spectromicroscopy and their implications for cloud-nucleating and optical properties, J. Geophys. Res.-Atmos., 115, 2010.

Day, D. A., **Liu**, **S.**, Russell, L. M. and Ziemann, P. J.: Organonitrate group concentrations in submicron particles with high nitrate and organic fractions in coastal southern California, Atmos. Environ., 44 (16), 1970-1979, 2010.

Ahlm, L., **Liu**, **S.**, Day, D. A., Russell, L. M., Weber, R., Gentner, D. R., Goldsteid, A. H., DiGangi, J. P., Henry, S. B., Keutsch, F. N., VandenBoer, T. C., Markovic, M. Z., Murphy, J. G., Ren X., and Scheller, S.: Formation and growth of ultrafine particles from secondary sources in Bakersfield, California, J. Geophys. Res.-Atmos., 117, D00V08, doi:10.1029/2011JD017144, 2012.

Shakya, K. M., **Liu**, **S.**, Russell1, L. M., Takahama1, S., Keutsch, F. N., Shilling, J. E., Hiranuma, N., Song, C., Pfaffenberger, L., Slowik, J., Prvt, A., Dommen, J., Baltensperger, U., Leaitch, R., Craven, J. S., Loza, C. L., Seinfeld, J. H.: Similarities in STXM-NEXAFS Spectra of Atmospheric Particles and SOA from the uptake of glyoxal, and photooxidation of alpha-pinene, isoprene, and 1,2,4-trimethylbenzene, *in preparation*.

Kim, H., **Liu**, **S.**, Russell, L. M., Paulson, S. E.: Real refractive indices and elemental composition of secondary organic aerosol generated from ozonolysis and photooxidation of limonene and alpha-pinene, *in preparation*.

Russell, L. M., Takahama, S., **Liu**, **S.**, Hawkins, L. N., Covert, D. S., Quinn, P.K. and Bates, T. S.: Oxygenated fraction and mass of organic aerosol from direct emission and atmospheric processing measured on the R/V Ronald Brown during TEXAQS/GoMACCS 2006, J. Geophys. Res.-Atmos., 114, 2009.

Riedel, T. P., Bertram, T. H., Ryder, O. S., **Liu**, **S.**, Day, D. A., Russell, L. M., Gaston, C. J., Prather, K. A., Thornton, J. A.: Direct N2O5 reactivity measurements at a polluted coastal site, Atmos. Chem. Phys., 12, 2959-2968, 2012.

O′Brien, R. E., Laskin, A., Laskin, J., **Liu**, **S.**, Weber, R., Russell, L. M., Goldstein, A. H.: Molecular Characterization of Organic Aerosol Using Nanospray Desorption/Electrospray Ionization Mass Spectrometry: CalNex 2010 field study, *submitted*.

O′Brien, R. E., Nguyen, T. B., Laskin, A., Laskin, J., Hayes, P., **Liu**, **S.**, Jimenez, J., Sergey A. Nizkorodov, Russell, L. M., Goldstein, A. H.: Probing Molecular Associations of Field-Collected and Laboratory-Generated SOA with Nano-DESI High-Resolution Mass Spectrometry, *submitted*.

Gentner, D. R., Isaacman, G., Worton, D. R., Chan, A. W. H., Dallmann, T. R., Davis, L., **Liu**, **S.**, Day, D. A., Russell, L. M., Wilson, K. R., Weber, R., Guha, A., Harley, R. A. and Goldstein, A. H.: Secondary organic aerosol and the burning question of gasoline vs. diesel, *submitted*.

Rollins, A. W., Browne, E. C., Min, K. E., Pusede, S., Wooldrideg, P. J., Gentner, D., Goldstein, A. H., **Liu**, **S**., Day, D. A., Russell, L. M. and Cohen, R. C.: Nighttime growth of particulate organic nitrates: a significant source of atmospheric secondary organic aerosols, *in press in Science.*

Zhao, Y., Kreisberg, N. M., Worton, D. R., Isaacman, G., Weber, R. J., Markovic, M. Z., Vandenboer, T. C., **Liu**, **S**., Day, D. A., Murphy, J. G., Russell, L. M., Hering, S. V., Goldstein, A. H.: Insights for SOA formation mechanisms from measured gas/particle partitioning of specific organic tracer compounds, *in preparation.*

Leaitch, W. R., Macdonald, A. M., Anlauf, K. G., Liu, P. S. K., Toom-Sauntry, D., Li, S. M., Liggio, J., Hayden, K., Wasey, M. A., Russell, L. M., Takahama, S., **Liu**, **S**., van Donkelaar, A., Duck, T., Martin, R. V., Zhang, Q., Sun, Y., McKendry, I., Shantz, N. C. and Cubison, M.: Evidence for Asian dust effects from aerosol plume measurements during INTEX-B 2006 near Whistler, BC, Atmos. Chem. Phys., 9 (11), 3523-3546, 2009.

ABSTRACT OF THE DISSERTATION

Composition, Sources, and Formation of Secondary Organic Aerosols from Urban Emissions

by

Shang Liu

Doctor of Philosophy in Earth Sciences

University of California, San Diego, 2012

Professor Lynn Russell, Chair

Secondary organic aerosols (SOA), known to form in the atmosphere, are a poorly understood but important component of atmospheric fine particles. This study aims to improve the understanding of the composition, source, and formation mechanism of SOA. Ambient particles were measured at urban centers (Mexico City, Mexico; Bakersfield, US), urban pollution-influenced coastal area (San Diego, US), high-elevation (4010 m) site (Altzomoni; 60 km southeast of Mexico City), and onboard the NCAR C130 flight (over Mexico and the coast of the Gulf of Mexico). Ensemble- and single-particle functional group and mass spectral compositions were analyzed using complementary techniques, mainly including Fourier transform infrared spectroscopy (FTIR), high-resolution time-of-flight aerosol mass spectrometer (HR-ToF-AMS) coupled with a light scattering module, and scanning transmission X-ray microscopy combined with near-edge X-ray absorption fine structure (STXM-NEXAFS). The organic mass was found to be dominated by alkane, carboxylic acid, hydroxyl, and nonacid carbonyl groups. By applying factor analysis independently to the FTIR- and AMS-measured organic mass, a

variety of sources was consistently identified in the urban plumes, with fossil fuel combustion emission accounting for 60– 90% of the organic mass. Volatile organic compounds emitted by the sources underwent fast oxidation. As a result, SOA contributed to 60– 90% of the organic mass, even in regions close to the sources. The SOA components formed from different precursor hydrocarbons were distinguished, with their mass fraction, diurnal cycle, size, and likely formation pathway discussed. The field studies were facilitated by laboratory reaction chamber studies focusing on organonitrate (ON) groups, which are potentially important photochemical products. It was found that ON groups hydrolyze in aerosol water at a rate of 4 day^{-1} (corresponds to a lifetime of 6 hours) when relative humidity exceeds 20%, which could explain the lower concentration of ON groups in aerosol particles than model prediction. Overall, the combined field and laboratory studies demonstrate that SOA formation is a dynamic and multivariate process; more work is needed to characterize SOA for quantitative and predictive understanding of the impacts of aerosols.

Introduction

Although it is well established that atmospheric aerosols can alter the radiative balance of the Earth, deteriorate air quality, and affect human health, the extent of these impacts is largely uncertain. It is therefore crucial to accrue knowledge on the composition, source, and formation mechanism of aerosols, which are a complex mixture of inorganic and organic compounds. While the inorganic fraction is mainly composed of sulfate, nitrate, ammonium, and dust components, the organic fraction, which often dominates the particle mass (11), remains elusive. To date, less than 20% of the total organic mass (OM) has been measured at the molecular level using gas chromatography- mass spectrometry (GC-MS) (6, 8, 10). The difficulty of quantifying organic compounds arises from the large number of sources (including anthropogenic and biogenic) as well as complicated formation and transformation pathways. OM is either formed at the source (primary organic aerosol or POA) or in the atmosphere (secondary organic aerosol or SOA) by oxidation of precursor hydrocarbons. Major gas-phase atmospheric oxidants include hydroxyl radicals (OH), ozone (O_3), and nitrate radicals (NO_3), with the former two prevailing during daytime and the third mainly existing at night. Reactions of precursor hydrocarbons and oxidants occur continuously in the gas and particle phase (typically aqueous phase), forming multigeneration products with a variety of vapor pressures. These products are transformed physically (e.g., evaporation and deposition) and chemically (e.g., oxidation) during atmospheric processes (e.g., air mixing), making it extremely difficult to identify their compositions, sources, and mass concentrations.

Recently developed aerosol mass spectrometer (AMS) and Fourier transform infrared spectroscopy (FTIR) allow for measuring bonds and fragments of

organic molecules, respectively, the sum of which makes up 80– 90% of the total OM (1). Measurements with these techniques have provided new insights into the sources and formation of organic aerosols (OA). Since each of the fragment-based mass spectra or functional group-based infrared spectra of OA is a linear combination of the mass-weighted spectra of individual components, multivariate factor analysis, such as positive matrix factorization (PMF) developed by Paatero and Tapper (5), is capable of decomposing the AMS- and FTIR-measured OA into linearly-independent factors. The factors are then linked to different sources or processes by correlating their time series to source markers or comparing their spectra to the spectra retrieved from sources or processes. Application of PMF to the AMS-measured OA typically results in one type of reduced, one or two types of oxidized, and sometimes biomass-burning factors, with the reduced and oxidized factors characterized by hydrocarbon-like (e.g., $C_4H_9^+$) and oxygenated fragments ($C_2H_3O^+$ or CO_2^+), respectively (3). Correlation of the oxidized factors with photochemical activities and other secondary components (e.g. sulfate) suggests that the oxidized factors are likely secondary (4, 2). The separation of oxidized components from OA makes it possible to study the composition and formation of SOA, which evolves dynamically by atmospheric processing (3). Application of PMF to the FTIR measurements has augmented the ability of identifying source and formation mechanisms of SOA, since the functional group compositions of the FTIR-PMF factors have proven to be precursor-specific (7). For example, by comparing functional group compositions of the PMF-derived components with those products derived from laboratory experiments, Russell et al. (2011) proposed a multigeneration oxidation pathway of SOA formation involving both gas- and particle-phase reactions. Despite these improvements, complete source inventories and detailed SOA formation mechanisms are still not available. As a result, the current models significantly underestimate the atmospheric SOA (9).

To help address these uncertainties, the present work integrates field and laboratory studies to explore the chemical and physical properties of aerosol particles. The field studies are based on ground and aircraft measurements, spanning a range of locations, including two polluted urban centers, a high-elevation site, and

a coastal region; the laboratory study was conducted in chemical reaction chamber to test hypotheses and facilitate field measurements.

Chapter 1 presents ambient measurements during the Megacity Initiative: Local and Global Research Observation (MILAGRO) in March 2006. Submicron particles were collected at three platforms: Mexico City urban area (2240 m), Altzomoni (4010 m; 60 km southeast of the Mexico City metropolitan area), and onboard the NCAR C130 aircraft. Statistical approaches, including correlation, cluster, and factor analyses were applied separately to the three datasets to identify common sources and significant differences among the three platforms. When compared with the Mexico City, enhanced correlation of cross-source elemental markers was observed at Altzomoni along with a distinct cluster composed of high oxygen-to-carbon ratio (O/C). Altzomoni FTIR spectra suggest that the high-elevation site is influenced by mixed sources or atmospheric (photochemical) processing, whereas the urban area is dominated by fresh emissions. In contrast to the ground sites, the C130 sampled particles at different altitudes of a wide region, resulting in similar FTIR spectra (to the ground sites) when the flight approached the Mexico City basin, suggesting that the air pollution not only affects local areas but also expands horizontally and vertically to the surrounding areas to create regional effects. The major sources, identified from the PMF analysis, were fossil fuel combustion (93% OM) and biomass burning (7% OM). While alkane, carboxylic acid, hydroxyl, and amine groups were associated with fossil fuel combustion, the nonacid carbonyl groups formed a major fraction of particles originated from the biomass burning processes.

Further examination of source and atmospheric processing of urban pollution was conducted at the Scripps pier (San Diego) during 15 August to 1 October of 2009, and the results are presented in Chapter 2. During the measurement, the sampling site consistently experienced air masses transported from the Los Angeles basin, which is 200 km to the north and known for its high air pollution in the United States. As a result, SOA formed from fossil fuel combustion, transported from the Los Angeles basin and identified by the PMF analysis, accounted for 60% of the OM. The other OM components included organic aerosols (OA) from

biomass burning (20%) and marine (20%) sources. Because of the consistency of the air masses that arrived at the sampling site, a pseudo-Lagrangian framework was used to interpret the evolution of the organic mass. Using this method, today's SOA (defined as the increase in SOA relative to the morning minimum during the 12-h daytime period of one day) and background SOA (defined as the low concentration in the early morning) accounted for 20– 50% and 50– 75% of the total SOA, respectively. In addition, the decrease in OM-to-PM (total particle mass) ratio with increasing particle size suggests that the OM (and likely the SOA) in submicron particles is formed by surface-limited condensation processes.

The SOA components identified from the MILAGRO and Scripps Pier studies were not assigned to specific gas-phase precursors, largely due to the lack of compound-specific molecular makers. In Chapter 3, this link was made using the measurements at Bakersfield, a supersite of the CalNex (California Research at the Nexus of Air Quality and Climate Change) campaign during 15 May to 29 June of 2010. In this study, factors that contributed to the OM were consistently identified from the FTIR and AMS measurements using PMF analysis. The OM was largely (80– 90%) explained by the SOA factors. The alkane and aromatic SOA (formed from alkane and aromatic hydrocarbon precursors, respectively), identified by their correlation with the molecular source markers measured by thermal desorption aerosol GC/MS-FID (TAG), accounted for 65% of the OM. In particular, the alkane SOA were mainly composed of alkane and carboxylic acid groups and correlated to O_3, providing evidence of the alkane SOA formation mechanism proposed by Russell et al. (2011). In contrast, the aromatic SOA (dominated by nonacid carbonyl groups) were more likely to have formed in OH radical-driven oxidation processes. Nighttime SOA production by NO_3 radical oxidation was observed when nighttime easterly winds transported monoterpenes emitted from surrounding forests to the sampling site. As a result of the NO_3 radical oxidation, 50– 80% of organonitrate (ON) groups were produced at night. The SOA components not only differed in composition, diurnal cycle, and formation pathway, but also had different size distributions. The alkane and aromatic SOA components were associated with 200–500-nm-sized particles, suggesting that they were

formed by condensation of gas-phase oxidation products. On the other hand, the biogenic SOA components were largely distributed in 400–700-nm-sized particles, most likely due to condensation of biogenic organic aerosols on larger, primary particles. This study demonstrated that the SOA components are distinguishable and that their distinct functional group compositions likely reflect the carbon "backbones" of their volatile organic compound (VOC) precursors.

In addition to the ensemble measurements, single-particle mass spectra were acquired using HR-ToF-AMS coupled with a light scattering module (LS-ToF-AMS) during the CalNex campaign, as described in Chapter 4. The LS-ToF-AMS does not influence the performance of the standard HR-ToF-AMS, but rather optically detects all the particles that reach the vaporizer. By comparing the timing of the optical (detected by the light scattering module) and chemical ion (detected by the mass spectrometer) signals, the number-based collection efficiency (CE) of the AMS instrument was measured, with CE of approximate 50% for particles larger than 180 nm vacuum aerodynamic diameter. Cluster analysis of the single-particle mass spectra exhibited three major particle types, representing highly oxidized particles (characterized by m/z 44), less oxidized particles (characterized by m/z 43), and freshly emitted particles of mixed sources. The mass spectra and diurnal cycles of the three single-particle types were found to be in good agreement with the ensemble-derived factors (from PMF analysis), confirming that the PMF factors represented the organic components of different sources and atmospheric processes.

Chapter 5 presents the laboratory study carried out to test whether ON groups hydrolyze in aerosol water. In this study, formation of ON group-containing SOA was simulated using 1,2,4- trimethylbenzene (TMB) as the hydrocarbon precursor. Oxidation by OH radicals occurred in the presence of NO_x under a wide range of relative humidity (0– 90%). The decrease in ON group mass fraction with increasing relative humidity suggests that ON groups hydrolyze at relative humidity greater than 20%. The hydrolysis rate constant was determined at 4 day^{-1}, corresponding to a lifetime of 6 hours. The hydrolysis of ON groups at short time scales potentially explains the gap between modeled and measured ON group con-

centrations. In addition, the light absorption efficiency of SOA correlated with ON group mass fraction, indicating that ON groups are potentially important for aerosols effects on solar radiation.

Together, the field measurements show that urban OA originates from a variety of sources, with fossil fuel combustion being the largest source at each of the three sampling sites. Emissions from this source are oxidized by O_3, OH, and NO_3 radicals, producing SOA components that changed diurnally. The composition of the SOA components is likely affected by ambient conditions, such as RH that could reduce organonitrate group mass by hydrolysis reaction in aerosol particles. The composition, source, and formation of OA are summarized in the Conclusion section, where future studies that could help improve understanding of OA are also discussed.

References

[1] Hallquist, M., Wenger, J. C., Baltensperger, U., Rudich, Y., Simpson, D., Claeys, M., Dommen, J., Donahue, N. M., George, C., Goldstein, A. H., Hamilton, J. F., Herrmann, H., Hoffmann, T., Iinuma, Y., Jang, M., Jenkin, M. E., Jimenez, J. L., Kiendler-Scharr, A., Maenhaut, W., McFiggans, G., Mentel, T. F., Monod, A., Prevot, A. S. H., Seinfeld, J. H., Surratt, J. D., Szmigielski, R., Wildt, J., 2009. The formation, properties and impact of secondary organic aerosol: current and emerging issues. Atmospheric Chemistry and Physics 9 (14), 5155–5236.

[2] Herndon, S., Onasch, T., Wood, E., Kroll, J., Canagaratna, M., Jayne, J., Zavala, M., Knighton, W., Mazzoleni, C., Dubey, M., et al., 2008. Correlation of secondary organic aerosol with odd oxygen in mexico city. Geophys. Res. Lett 35 (15), L15804.

[3] Jimenez, J. L., Canagaratna, M. R., Donahue, N. M., Prevot, A. S. H., Zhang, Q., Kroll, J. H., DeCarlo, P. F., Allan, J. D., Coe, H., Ng, N. L., Aiken, A. C., Docherty, K. S., Ulbrich, I. M., Grieshop, A. P., Robinson, A. L., Duplissy, J., Smith, J. D., Wilson, K. R., Lanz, V. A., Hueglin, C., Sun, Y. L., Tian, J., Laaksonen, A., Raatikainen, T., Rautiainen, J., Vaattovaara, P., Ehn, M., Kulmala, M., Tomlinson, J. M., Collins, D. R., Cubison, M. J., Dunlea, E. J., Huffman, J. A., Onasch, T. B., Alfarra, M. R., Williams, P. I., Bower, K., Kondo, Y., Schneider, J., Drewnick, F., Borrmann, S., Weimer, S., Demerjian, K., Salcedo, D., Cottrell, L., Griffin, R., Takami, A., Miyoshi, T., Hatakeyama, S., Shimono, A., Sun, J. Y., Zhang, Y. M., Dzepina, K., Kimmel, J. R., Sueper, D., Jayne, J. T., Herndon, S. C., Trimborn, A. M., Williams, L. R., Wood, E. C., Middlebrook, A. M., Kolb, C. E., Baltensperger, U., Worsnop, D. R., 2009. Evolution of organic aerosols in the atmosphere. Science 326 (5959), 1525–1529.

[4] Lanz, V., Alfarra, M., Baltensperger, U., Buchmann, B., Hueglin, C., Prévôt, A., et al., 2007. Source apportionment of submicron organic aerosols at an urban site by factor analytical modelling of aerosol mass spectra. Atmospheric Chemistry and Physics 7 (6), 1503–1522.

[5] Paatero, P., Tapper, U., 1994. Positive matrix factorization: A non-negative

factor model with optimal utilization of error estimates of data values. Environmetrics 5 (2), 111–126.

[6] Rogge, W., Mazurek, M., Hildemann, L. M., Cass, G. R., Simoneit, B. R. T., 1993. Quantification of urban organic aerosols at a molecular level: identification, abundance and seasonal variation. Atmospheric Environment. Part A. General Topics 27 (8), 1309–1330.

[7] Russell, L. M., Bahadur, R., Ziemann, P. J., 2011. Identifying organic aerosol sources by comparing functional group composition in chamber and atmospheric particles. Proceedings of the National Academy of Sciences 108 (9), 3516–3521.

[8] Schauer, J. J., Kleeman, M. J., Cass, G. R., Simoneit, B. R. T., 2002. Measurement of emissions from air pollution sources. 5. c1-c32 organic compounds from gasoline-powered motor vehicles. Environmental science & technology 36 (6), 1169–1180.

[9] Volkamer, R., Jimenez, J., San Martini, F., Dzepina, K., Zhang, Q., Salcedo, D., Molina, L., Worsnop, D., Molina, M., 2006. Secondary organic aerosol formation from anthropogenic air pollution: Rapid and higher than expected. Geophys. Res. Lett 33 (17), L17811.

[10] Yu, J., Flagan, R. C., Seinfeld, J. H., 1998. Identification of products containing-cooh,-oh, and-co in atmospheric oxidation of hydrocarbons. Environmental Science & Technology 32 (16), 2357–2370.

[11] Zhang, Q., Jimenez, J. L., Canagaratna, M. R., Allan, J. D., Coe, H., Ulbrich, I., Alfarra, M. R., Takami, A., Middlebrook, A. M., Sun, Y. L., Dzepina, K., Dunlea, E., Docherty, K., DeCarlo, P. F., Salcedo, D., Onasch, T., Jayne, J. T., Miyoshi, T., Shimono, A., Hatakeyama, S., Takegawa, N., Kondo, Y., Schneider, J., Drewnick, F., Borrmann, S., Weimer, S., Demerjian, K., Williams, P., Bower, K., Bahreini, R., Cottrell, L., Griffin, R. J., Rautiainen, J., Sun, J. Y., Zhang, Y. M., Worsnop, D. R., 2007. Ubiquity and dominance of oxygenated species in organic aerosols in anthropogenically-influenced northern hemisphere midlatitudes. Geophys. Res. Lett 34 (13), L13801.

Chapter 1

Oxygenated organic functional groups and their sources in single and submicron organic particles in MILAGRO 2006 campaign

Abstract. Fourier Transform Infrared (FTIR) and X-ray Fluorescence (XRF) were used to measure organic functional groups and elements of submicron particles collected during MILAGRO in March 2006 on three platforms: the Mexico City urban area (SIMAT), the high altitude site at 4010 m (Altzomoni), and the NCAR C130 aircraft. Scanning Transmission X-ray Microscopy (STXM) and Near-Edge X-ray Absorption Fine Structure (NEXAFS) were applied to single particle organic functional group abundance analysis of particles simultaneously collected at SIMAT and C130. Correlations of elemental concentrations showed different groups of source-related elements at SIMAT, Altzomoni, and C130, suggesting different processes affecting the air masses sampled at the three platforms. Cluster analysis resulted in seven distinct clusters of FTIR spectra, with the last

9

three clusters consisting of spectra collected almost exclusively on the C130 platform, reflecting the variety of sources contributing to C130 samples. Positive Matrix Factorization (PMF) of STXM-NEXAFS spectra identified three main factors representing soot, secondary, and biomass burning type spectra. PMF of FTIR spectra resulted in two fossil fuel combustion factors and one biomass burning factor, the former representative of source regions to the northeast and southwest of SIMAT. Alkane, carboxylic acid, amine, and alcohol functional groups were mainly associated with combustion related sources, while non-acid carbonyl groups were likely from biomass burning events. The majority of OM and O/C was attributed to combustion sources, although no distinction between direct emissions and atmospherically processed OM could be identified.

1.1   Introduction

Atmospheric aerosols have been causing increased concerns during the last few decades since they reduce air quality (Eidels-Dubovoi, 2002), threaten human health (Dockery et al., 1993), and affect climate (Liepert et al., 2004). The effects of organic aerosols remain largely unknown because of their complex composition, especially in urban areas. The Mexico City Metropolitan Area (MCMA) is the second largest megacity in the world. Although its pollution problem has been studied for more than 40 years (Raga et al., 2001), there are only a limited number of organic aerosol measurements (Salcedo et al., 2006; DeCarlo et al., 2008; Aiken et al., 2008). The main sources of MCMA aerosols include biomass burning (Johnson et al., 2006; Salcedo et al., 2006; Molina et al., 2007), motor vehicle emissions, oil burning, and crustal components (Querol et al., 2008; Stone et al., 2008).

The MILAGRO (Megacity Initiative: Local and Global Research Observations) campaign is the largest intensive measurement to date in the MCMA to quantify properties of atmospheric aerosols. This study builds on the measurements presented by Gilardoni et al. (2009) to identify overall statistical trends that span the organic aerosol properties across the MCMA basin. Site-by-site correlations, clusters of organic types, and underlying source-related factors are combined in this work to identify the contributions to organic mass from the major source types in the MCMA. In this work we also establish that the same organic functional group signatures and source types found in bulk submicron samples are evident in external mixtures of internally mixed single particles.

Gilardoni et al. (2009) have shown that the organic mass (OM) measurements from FTIR were well correlated with simultaneous Aerosol Mass Spectrometry (AMS) measurements during this campaign. Alkane functional groups dominated the OM. The average OM/OC and carboxylic acid COOH to aliphatic saturated C-C-H ratios were higher at Altzomoni than at SIMAT, as a consequence of a larger contribution of oxidized functional groups. The OM was found to correlate with non-soil K, indicating biomass burning being a source of OM in the MCMA.

In this paper, we will extend their work using chemometric techniques and specific statistical tests to identify additional and significant trends in the measure-

ments, in particular for normalized organic functional group composition and fraction of oxidized organic carbon. Correlations of each pair of elements and organic functional groups were investigated. The co-varying of organic functional groups with elemental markers provides an indication of the fraction of organic compound associated with specific metal source signatures. Ward clustering (Ward, 1963) was applied to FTIR spectra to identify the similarities and differences across the three platforms. In addition, PMF was applied to STXM-NEXAFS and FTIR spectra independently to identify the contributions of some general classes of sources to the organic particles. PMF factor time series were correlated to time series of source-specific elements to link factors to the sources that emitted them, in either the gas or particle phase. This work illustrates important differences in the characteristics of the organic mixtures from biomass burning and combustion sources for SIMAT, Altzomoni, and C130 flight measurements, and the analysis quantifies the approximate contribution of each source type to OM in the MCMA and surrounding areas.

1.2 Methods

Submicron particles were collected on Teflon filters in March 2006, during the MIRAGE (Megacity Impacts on Regional and Global Environments)/MILAGRO field campaign. The SIMAT site is located at the Mexico City Atmospheric Monitoring System building (19°24′12″ N, 99°10′34″ W), and the Altzomoni site is located about 60 km southeast of Mexico City, in the Pass of Cortez between the volcanoes of Popocatépetl and Iztaccíhuatl (19°7′ N, 98°38′ W; Baumgardner et al., 2009). At SIMAT and Altzomoni, two 12-h samples or three 8-h samples were collected along with one 24-h sample. Samples were collected for 20 min to 1 h on board NCAR C130 at constant altitudes. A field blank (backup filter) was simultaneously collected with each sample. Samples were stored below 0°C after collection before FTIR analysis. The FTIR spectra were quantified as mass concentrations of organic functional groups using an automated algorithm (Russell et al., 2009), including additional calibrations of primary amine functional

groups (Appendix A) in addition to standard compound calibrations presented in previous work (Maria et al., 2002, 2003, 2004; Maria and Russell, 2005; Gilardoni et al., 2007). The field blank spectra were baselined using the same algorithm.

Elements heavier than Na (including Na) were analyzed by Chester Laboratories on the same filters used for the FTIR analysis (Maria et al., 2003). Elemental concentrations reported were above detection limit for more than 70% of the ambient samples collected. The elements Mg, P, Co, Ga, Ge, As, Rb, Sr, Y, Zr, Mo, Pd, Ag, Cd, In, Sb, La, and Hg were always below detection limits. A data matrix was constructed including organic functional group concentrations and elemental concentrations for each sample filter. Correlations of each pair of components were calculated to provide the covariance of these aerosol components and to investigate possible sources.

Normalized FTIR spectra of three platforms were grouped into clusters using the Agglomerative Hierarchical Clustering technique with the Ward algorithm. In this algorithm, each spectrum is initially considered as a separate category, a dendrogram is built from the spectra by progressively merging them and minimizing the sum-of-square errors for the spectra being merged (ultimately resulting in all spectra collapsing into one single category). The dendrogram can be grouped into clusters by choosing a level of branching (similarity) that results in a meaningful number of categories (Kaufman et al., 1990). In this work, seven clusters were selected.

Positive matrix factorization (PMF) was applied to all 263 mass-weighted baselined FTIR spectra of three platforms (Paatero et al., 1994; Russell et al., 2009). PMF can be used to infer unknown source profiles and source contributions from ambient measurements (Lee et al., 1999; Ramadan et al., 2000). Baselining error (which was calculated from the variability of the baselined field blank spectra) was used to estimate the scaling factor as a function of wavelength (Appendices in Russell et al., 2009). The robust mode of PMF was used, and the outliers were down-weighted during the fitting procedure. Fixed Size Moving Window - Evolving Factor Analysis (FSMW-EFA) was applied to the spectra from all three sites for the determination of the number of factors. FSMW-EFA performs Singular Value

Table 1.1: Mean and standard deviation of OM, organic functional group concentrations, O/C and OM/OC ratios, and elemental concentrations for SIMAT (N = 109), Altzomoni (N = 52), and C130 (N = 102) platforms measured by FTIR and XRF. Mass fraction of organic functional groups are shown in the parentheses.

		SIMAT	Altzomoni	C130
	FTIR OM $\mu\mathrm{g\,m^{-3}}$	9.9±4.4	6.6±3.9	5.3±4.2
	FTIR OM/OC	1.8±0.1	2.0±0.3	1.5±0.2
	FTIR O/C	0.4±0.1	0.5±0.1	0.2±0.2
FTIR Organic Functional Groups ($\mu\mathrm{g\,m^{-3}}$)	Alcohol	1.5±1.0 (14%)	1.1±1.2 (19%)	1.1±1.3 (19%)
	Alkane	4.6±2.0 (47%)	2.7±1.5 (41%)	3.4±2.0 (73%)
	Non-Acid Carbonyl	0.0±0.3 (0%)	0.1±0.3 (1%)	0.1±0.6 (0%)
	Amine	0.8±0.3 (9%)	0.7±0.5 (11%)	0.1±0.3 (2%)
	Carboxylic Acid	3.0±1.4 (30%)	2.0±1.1 (28%)	0.5±1.4 (5%)
XRF Elements ($\mathrm{ng\,m^{-3}}$)	Na	91.3±93.2		
	Al	51.2±63.5	50.8±86.3	125±112
	Si	133±126	134±249	135±108
	S	955±517	706±462	476±476
	Cl	40.9±40.1		
	K	168±86.5	160±105	96.7±60.3
	Ca	107±115	83.6±212	25.4±18.5
	Ti	4.5±4.3	3.2±4.6	
	V	7.8±14.0	2.3±2.6	9.5±9.8
	Cr	0.9±1.2		
	Mn	4.3±4.4	0.9±1.7	
	Fe	92.9±73.4		25.9±23.4
	Ni	1.6±2.7		
	C	9.6±10.9		
	Zn	36.4±29.3		15.1±11.6
	Se	3.3±4.6		
	Br	6.3±7.6	2.9±1.6	
	Sn	6.6±7.3		68.5±69.4

Decomposition (SVD) analysis on a subset of spectra contained in a "window" of a fixed size, which is moved along the spectra (Keller et al., 1992). The results of the analysis on all "windows" were plotted together to show the percentage of data recovery at each wavenumber using different numbers of factors. The rotation parameter FPEAK was set to −0.2, 0, 0.2, and 0.4 since FPEAK $\leq$−0.4 and FPEAK $\geq$0.6 resulted in physically unrealistic spectra (e.g. non-Gaussian spectra). The effects of rotation were small, likely because the non-negativity constraint was set for more than 1500 wavenumbers. FPEAK=0 was used to represent the solutions. The output sample contribution factor was normalized by volume and correlated to metal concentrations to identify sources most likely

associated with each factor.

Potential Source Contribution Function (PSCF; Pekney et al., 2006) analysis was used to determine the most probable potential source regions to each PMF factor. PSCF calculates the probability that a source is located at a particular geographical region. Eight-hour long back trajectories ending at the SIMAT and Altzomoni coordinates were computed each hour at 200 m above ground level for the entire campaign using the Hybrid Single-Particle Lagrangian Integrated Trajectory (HYSPLIT) model (Escudero et al., 2006). These trajectories were grouped into periods in which PMF source contributions were either high or low. Periods in which the source contribution for each factor was higher than its 75th percentile value were classified as high periods, and the rest of the periods were classified as low. The trajectories were interpolated into 15-min intervals and superposed on a 4 (latitude)×4 (longitude) degree domain centered around the city and gridded into a total of 250 000 cells. Frequencies for high and low periods were normalized by total counts for each grid cell for the PSCF analysis (Pekney et al., 2006). To reduce the uncertainties of large ratios in cells with low trajectory endpoints, a cumulative distribution function of trajectory endpoints in grid cells was used to set a threshold of 40% so that the cells with less than 10 trajectory endpoints were not considered in the PSCF calculation.

Particles were also collected on silicon nitride windows, and single particle K-edge X-ray absorption spectra were acquired using a combination of Scanning Transmission X-ray Microscopy (STXM) and Near-Edge X-ray Absorption Fine Structure (NEXAFS) spectroscopy at the Lawrence Berkeley National Laboratory Advanced Light Source on beam line 5.3.2 (Russell et al., 2002; Maria et al., 2004). PMF was applied to the total 270 STXM-NEXAFS spectra of SIMAT and C130 measurements. The rotation parameter and the number of factors were explored similarly to PMF of FTIR spectra. FPEAK was set to −0.2, 0, 0.2, and 0.4 for 2 to 8 factors. Two to eight factors were found to reproduce 85–99% of the measured abundances. The 4-factor solution with FPEAK set to 0 produced the most representative results by comparing factor spectra with standard reference spectra.

1.3 Results

The average OM concentrations at STP were $9.9\,\mu g\,m^{-3}$ at SIMAT, $6.6\,\mu g\,m^{-3}$ at Altzomoni, and $5.3\,\mu g\,m^{-3}$ on the C130 (Gilardoni et al., 2009). Alkane functional groups dominated the total OM, with the mass fractions 47%, 41%, and 73% for SIMAT, Altzomoni, and C130 measurements, respectively. Carboxylic acid functional groups contributed 30% and 28% to OM at SIMAT and Altzomoni, with a lower fraction of 5% on average for the C130 flights. Alcohol functional groups accounted for 14% of OM at SIMAT, with larger fractions of 19% both at Altzomoni and on the C130. The mass fractions of primary amine functional groups were 9% at SIMAT, 11% at Altzomoni, and 2% on the C130 (Table 1.1). Of the C130 samples, 87% of amine functional group masses and 73% of carboxylic acid functional group masses were below detection limit, and typically could have accounted for up to 1% and 15% of OM, respectively. FTIR spectra were analyzed for evidence consistent with organosulfate functional groups, but no samples had detectable absorbance at $876\,cm^{-1}$. Alkene and aromatic functional group masses were below detection limit in all samples of the three platforms, accounting for less than 1% of the average OM. All of the normalized and fractional quantities in the following discussion omit these two functional groups.

The Oxygen-to-Carbon ratio (O/C) can be estimated from FTIR measurements (Russell et al., 2009). The average FTIR O/C was 0.4 for SIMAT, and this value is comparable to the AMS O/C=0.41 at the nearby T0 sampling site ($9\,km$ north of SIMAT sampling site) from AMS-based estimates (Aiken et al., 2008). The FTIR O/C was compared with the O/C calculated from quadrupole AMS measurements using the reported ambient relationship for m/z 44 (Aiken et al., 2008; Shilling et al., 2009) for Altzomoni and C130 platforms. At Altzomoni, the FTIR O/C was consistently lower than the AMS O/C, but the differences were within the uncertainties of both FTIR and AMS. On the C130, the FTIR and AMS-based O/C compared well for the samples with carboxylic acid functional groups above detection limit. These comparisons are consistent with the previous study (Russell et al., 2009), showing that the O/C estimates from FTIR and AMS are within the uncertainties associated with inlet transmission. The standard deviations of FTIR

O/C were 0.07, 0.12, and 0.18 for SIMAT, Altzomoni, and C130 measurements, respectively. The larger O/C variation during the NCAR C130 flights indicates that the larger altitude and geographic range of these measurements showed greater variability in organic composition than either of the two ground sites.

1.3.1   Correlations in concentrations

The SIMAT measurements showed correlations of elemental markers from three groups: dust elemental markers (Al, Si, Ca, Ti, Fe) correlated with each other, with correlation coefficients (r) ranging from 0.5 to 0.9; S and Se were correlated with r of 0.55, indicating coal combustion source types (Qureshi et al., 2006); V and Ni are indicators of oil combustion (Qureshi et al., 2006), they were correlated with r of 0.87. Concentrations of alcohol, alkane, amine, and carboxylic acid functional groups correlated with each other as well as S, suggesting their common combustion sources. Alkane and carboxylic acid group mass fractions correlated with each other, but they anti-correlated with alcohol group mass fraction, indicating that the alcohol group was dominated by different source types or processes from alkane and carboxylic acid groups.

At Altzomoni, dust elemental markers (Al, Si, Ca, Ti, and Fe) were correlated with each other with r ranging from 0.6 to 1.0, and combustion elemental markers (V, S, K, Br, Pb, and Se) were correlated with each other with r ranging from 0.5 to 0.7 (Fig. 1.1). The high correlations of the dust elemental concentrations may be caused by the single-lane local road, which is located 5 km southeast from Altzomoni site (Baumgardner et al., 2009). Compared to SIMAT and other urban sites (Russell et al., 2009), the combustion-generated components did not fall into clear fuel-specific combustion categories, consistent with higher contributions of more processed or mixed-source organic mass at Altzomoni. This result is also consistent with a higher O/C and OM/OC at Altzomoni than at SIMAT. Similar to SIMAT, concentrations of alkane, amine, and carboxylic acid functional groups at Altzomoni correlated with each other as well as S, likely from industrial or diesel vehicular emissions. Alkane and carboxylic acid group mass fractions were correlated with each other but were anti-correlated with alcohol group mass
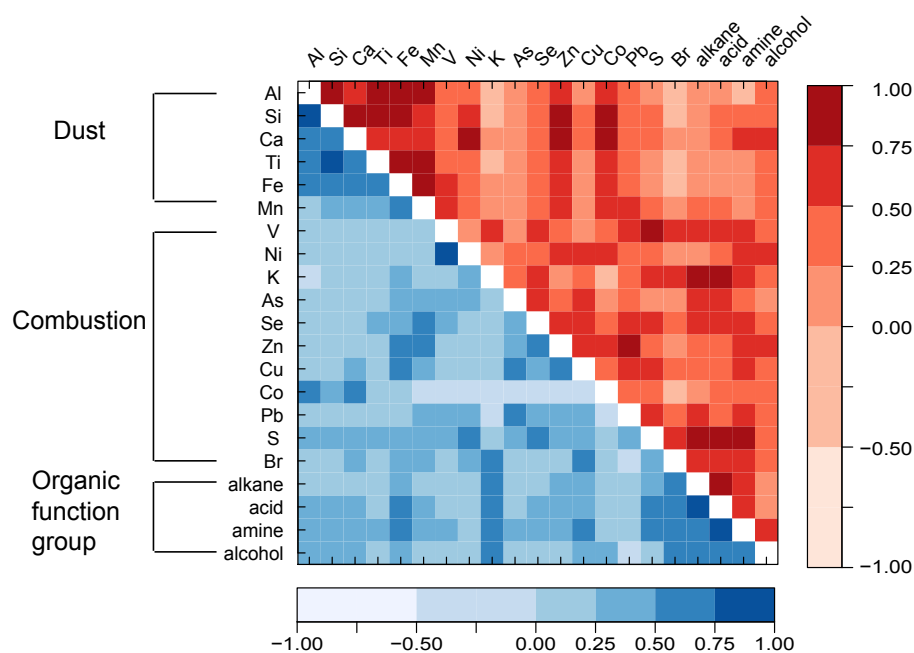
Figure 1.1: Correlations of organic functional group and elemental concentrations for SIMAT (blue) and Altzomoni (red) samples. Color bars indicate correlation coefficients.

fractions.

Dust elemental markers (Si, Ca, and Fe) were correlated with each other, with r ranging from 0.5 to 0.6 for the C130 measurements; Ca also correlated with combustion and industrial markers (S, K, and V) with r of 0.4, 0.5 and 0.6, respectively, indicating particles from mixed source types. The correlations between organic functional groups and elements were weak, indicating that the particles were mixed or processed during atmospheric transport, leaving no clear source signature. Concentrations of alcohol and alkane functional groups correlate with each other, but the mass fractions of alcohol and alkane functional groups were anti-correlated.

1.3.2   Cluster analysis of FTIR spectra

Cluster analysis was used to identify similarities among the measured normalized FTIR spectra. The Ward-type cluster analysis method was used and two to ten branches were tested. Spectra from the C130 measurements were separated
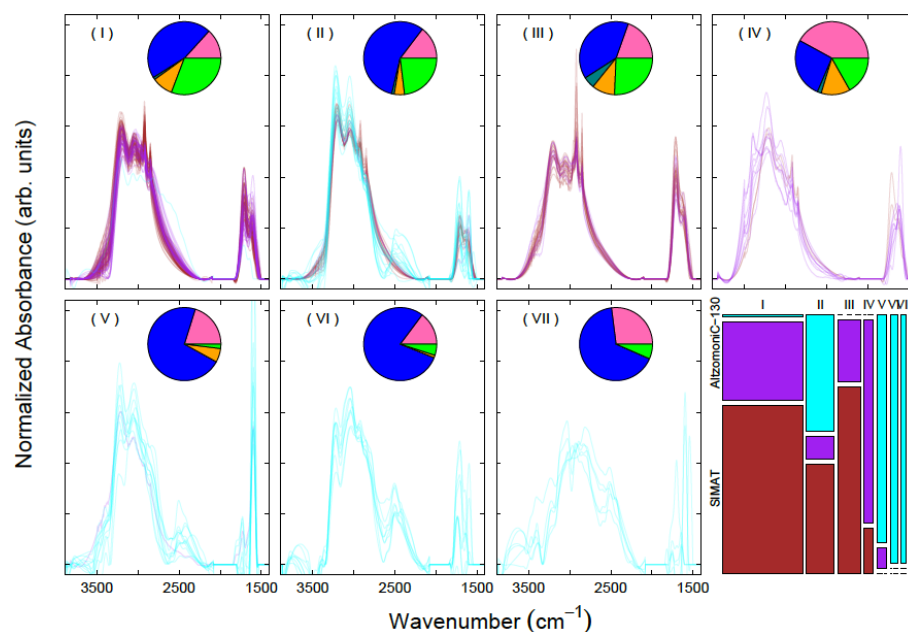
Figure 1.2: FTIR spectra from cluster categories I–VII (Panels I-VII). The last panel shows the cluster-platform comparison: the width of the bar is proportional to the number of spectra in each cluster and the height of the bar represents the fraction of spectra from each platform. Colors indicate SIMAT (brown), Altzomoni (green), and C130 (blue). The pie chart in each cluster panel shows the average organic functional group fractions of the cluster.

from the Altzomoni and SIMAT spectra at the first branch; Altzomoni spectra started to be separated when five or more branches were used. Seven clusters were used to best represent different types of FTIR spectra associated with different organic functional group compositions (Fig. 1.2). Using more than seven clusters resulted in small clusters consisting of only two C130 spectra, which were not statistically significant.

Clusters I, II, and III were the dominant clusters, as they contained 65% of the spectra. Seventy-percent of the spectra from clusters I and III were from SIMAT and the other 30% were from Altzomoni, with the difference between these two clusters being the presence of sharper peaks in the alkane functional group region of cluster III spectra. Samples from cluster III also had the lowest O/C among clusters I–IV. Forty-percent of the spectra in cluster II were from SIMAT and 45% from C130 measurements. The C130 samples in this cluster were col-

Table 1.2: Correlations of PMF factors to elements with $r>0.5$ (bold) and $0.25<r<0.5$, average organic mass concentrations $\mu\mathrm{g\,m^{-3}}$, and pie charts of organic functional group mass contributions by sampling platforms. Colors indicate alkane (blue), alcohol (pink), carboxylic acid (green), amine (orange), and non-acid carbonyl (teal) functional groups.

	Combined PMF			Combined PMF			PMF of SIMAT	PMF of Altzomoni
	SIMAT	Altzomoni	C130	SIMAT	Altzomoni	C130		
Biomass burning		Fe, Br			Fe, Br		S, Fe, Cu	**Cl, Br, Pb**, S, K, V, Cu, Zn, Se
	0.2	0.7	0.7	0.8	0.5	0.1	0.7	0.8
							S, K, Br, Ca, Ti, Fe, Zn, Mn, Se			**S, K**, Ca, Ti, Fe, Zn, Br			S, K, Mn, Fe, Cu, Zn, Se, Br	**Si, S, Al, Ca, Ti, Mn, Fe, Ni, Zn, Se**, K, V, Cu
	6.8	4.3	4.3	4.2	3.7	2.1	4.3	3.2
							Northeast combustion	
Combustion								
				S, Cl, K, Ti, Mn, Fe, Cu, Zn, Se, Br			S, Cl, K, Mn, Fe, Zn, Cu, Se, Br	**S**, Cl, K, Se, Br Cu, Pb
				3.6	2.9	3.3	4.2	2.9
							Southwest combustion	

lected at lower altitudes and closer to the Mexico City basin than the samples in the other clusters, indicating these samples were influenced by the city outflow. Samples from this cluster had the largest alkane functional group fraction among clusters I-IV. The similarities among spectra from different platforms suggest that many of the sources were associated with region-wide pollution that was transported in air masses sampled by all three platforms, which is consistent with the findings of Baumgardner et al. (2009). 85% of the spectra in cluster IV were from Altzomoni and 15% from SIMAT. The average O/C of the samples in cluster IV was significantly higher (at a 95% confidence level) than O/C of the samples in the other clusters, and samples from this cluster had the largest alcohol functional group fraction among all clusters. Clusters V, VI, and VII consisted almost exclusively of C130 spectra, with only 5% of the spectra from Altzomoni in cluster V. The three distinct branches of clusters of C130 measurements separated from the ground site measurements indicates the wide variety of different sources and air

masses sampled by the C130.

1.3.3 Positive matrix factorization of FTIR spectra

PMF was applied to the FTIR spectra of the three platforms ("combined PMF") and spectra from each site separately ("separate PMF") using three to six factors. By investigating factor chemical compositions, time series, and their possible source regions, similar factors were identified from both "combined PMF" and "separate PMF", indicating similar sources and regional pollution in the MCMA. The five- and six-factor solutions resulted in correlated factors with similar compositions and source regions, indicating some factors split into smaller but indistinguishable components because too many factors were used given the size of the data set. A distinct factor with significant mass was missing when three factors were used, causing the OM reconstructed from the factors to under-represent the measured OM. The four-factor solution was selected because four factors were found to reproduce 98% of the measured mass and to generate factors that represented sufficient organic mass for interpretation. Both the "combined PMF" and the "separate PMF" (calculated separately for the SIMAT and Altzomoni measurements) solutions are discussed below to show the consistency and quantitative variability of the PMF solutions, with the time series of OM concentrations for PMF factors shown in Fig. 1.3. The apportionment of OM concentrations and OC-weighted O/C to the factors are shown in Fig. 1.4. The functional group concentrations of these factors are summarized in Table 1.2 for SIMAT and Altzmoni measurements. The OM concentration of each factor was correlated with the corresponding elemental concentrations to show the contributions of different source types to organic functional groups. For each factor, correlations to elements with $r>0.5$ and $0.25<r<0.5$ are listed in Table 1.2.

The first factor was persistent in all PMF runs and was identified as a biomass burning factor, since the OM of this factor increased significantly during the fire period (12–14 March 2006) at 99% confidence level, while the other factors did not show strong correspondence with the fire period. The fire period was identified by Aiken et al. (2009) by measuring biomass burning tracers including
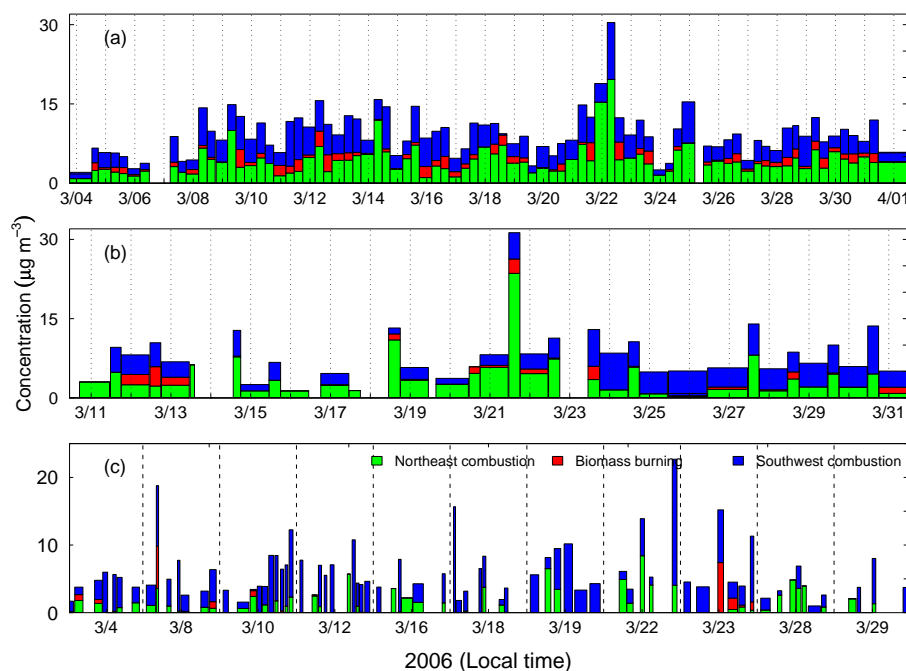
Figure 1.3: OM concentrations of northeast combustion (green), biomass burning (red), and southwest combustion (blue) factors for SIMAT **(a)**, Altzomoni **(b)**, and C130 **(c)** samples.

potassium, levoglucosan, and acetonitrile at the T0 site. This result is consistent with the effects of biomass burning events on the organic mass concentrations of Mexico City described elsewhere (Moffet et al., 2008b; Gilardoni et al., 2009). PSCF of this factor showed that the potential source of this factor was located south of the SIMAT and Altzomoni sites (Fig. 1.5a, d) in the mixed forest region (Yokelson et al., 2007). This source region also matches well with the possible source region of aged biomass burning particles described by Moffet et al. (2008b) from single particle analysis. Non-acid carbonyl functional groups dominated this factor, accounting for 26–47% of the OM. The OM contribution of this factor at SIMAT was comparable to the OM contribution of this factor at Altzomoni, indicating that biomass burning had a regional influence during the MILAGRO campaign.

The three remaining factors were identified as fossil fuel combustion type factors because they were associated with more than one elemental marker of fossil
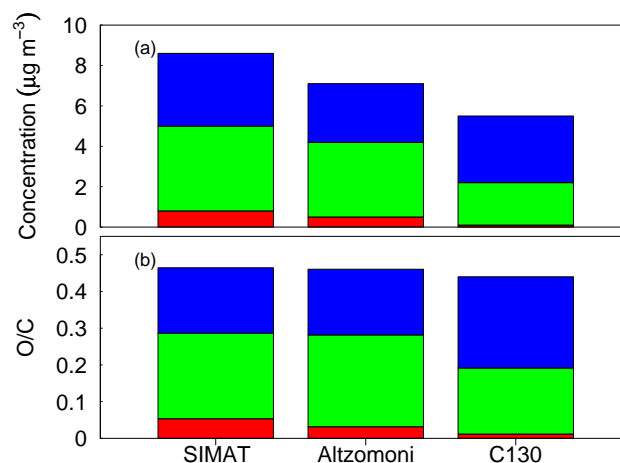
Figure 1.4: Average contributions of **(a)** OM concentrations and **(b)** O/C of northeast combustion (green), biomass burning (red), and southwest combustion (blue) factors for SIMAT, Altzomoni, and C130 platforms.

fuel combustion. Similar metal combustion tracers were associated with these factors. All three remaining factors had weak correlations with K and Br; and two also had weak or mild correlations with S, Se, Cu, Zn, Fe, and Mn. These elements can be attributed to various combustion processes, for example, S could be emitted from industrial or motor vehicular combustions using fossil fuels (Flore et al., 1999). The other sources of these elements could also include oil burning, coal burning, and solid waste incineration (Sharma et al., 2005; Li et al., 2004; Balasubramanian et al., 2004; Finlayson-Pitts et al., 2000). The combustion sources around Mexico City include incineration (Moffet et al., 2008a), oil combustion (Flore et al., 1999; Moffet et al., 2008b), motor vehicle emissions (Vega et al., 1997; Chow et al., 2002; Querol et al., 2008; Stone et al., 2008), and local charcoal burning (CICA, 1999), which can produce the elements associated with these three factors. While some studies show diurnal trends and weekday or weekend variations of OC (Stone et al., 2008), none of these factors were found to have these patterns. As a result, there were insufficient constraints to separate these factors by specific source types. The similarities of the trace metal signatures and the variety of fuels used in Mexico City did not allow us to identify a single, specific fuel type associated with these combustion sources.
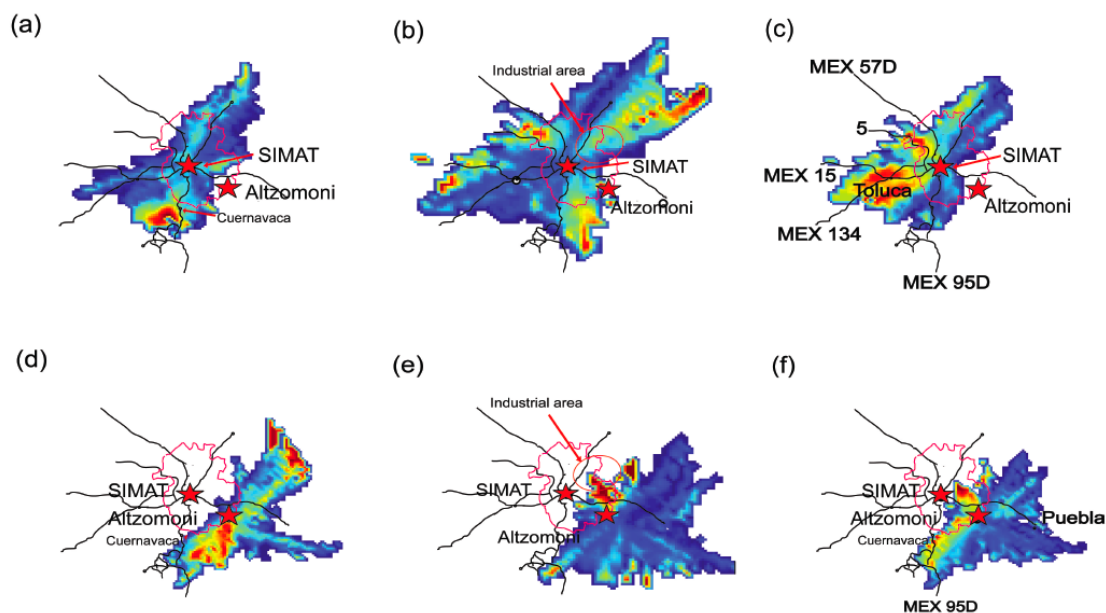
Figure 1.5: PSCF of biomass burning, northeast combustion, and southwest combustion factors at SIMAT **(a)**, **(b)**, and **(c)** and at Altzomoni **(d)**, **(e)**, and **(f)**. The color shows the probability of possible source regions of each factor with colder colors indicate lower possibilities.

The air mass back trajectories and OM concentrations provide some information about the differences among the combustion type factors. PSCF showed high OM concentrations of two of the combustion factors originated from similar source regions, and both of these factors correlated with dust markers (Al, Si, Ca, and Ti) at the Altzomoni site in addition to the combustion markers noted above. These common features provided evidence that both of these factors came from very similar and collocated sources. For these reasons, these two factors were combined to represent a "northeast combustion" factor, since they were associated most strongly with northeastern sources, likely from the industrial areas located at the northeastern MCMA (Fig. 1.5b, e; Johnson et al., 2006; Moffet et al., 2008b). The combined factor had stronger correlation with S than the individual uncombined factors. Alkane functional group dominated this factor, accounting for 30–40% of the OM. At SIMAT, alcohol and carboxylic acid group fractions of this factor were comparable, accounting for 19% and 21% of the OM, respectively. At

Altzomoni, alcohol group was a larger contributor to OM (37%) than carboxylic group (19%). This factor had the largest OM among all factors.

The factor associated with a strong source region located to the southwest of SIMAT (Fig. 1.5c) close to the city of Toluca was denoted as the southwest combustion factor. Toluca is the capital city of Mexico State. Toluca has reduced air quality due to recent, rapid industrial growth (Aldape et al., 2008). The source region also tracked the freeways connecting Toluca and Mexico City, including freeways MEX 15 and MEX 134. Freeway 5 was also identified as a potential source. PSCF at Altzomoni showed the source region was near freeway MEX 95D (Fig. 1.5f). This factor represented industrial and motor vehicular emissions. Similar to the "northeast combustion" factor, alkane group dominated this factor but had a larger fraction of 44–51%. Carboxylic acid group was the second largest component in this factor, accounting for 29–34% of the OM.

1.3.4   PMF and clusters of STXM-NEXAFS spectra

Three factors were consistently observed in 80% of all PMF runs. These factors were interpreted by comparing them with reference STXM-NEXAFS spectra of pure compounds and typical types of STXM-NEXAFS spectra identified in atmospheric particle measurements described by Takahama et al. (2007).

The first factor spectrum showed ketone and alkene group absorption peaks at 285 eV and 287.7 eV. This factor was identified as a soot factor, as the shape of this factor spectrum was comparable to the soot type spectra (Fig. 1.6a) described by Braun et al. (2005) and Hopkins et al. (2007). The second factor spectrum was dominated by a strong carboxylic acid absorption peak at 288.7 eV and shared similarities with the spectra of category (a) described by Takahama et al. (2007; Fig. 1.6b). Particles in category (a) are likely from secondary organic aerosol formation, so this factor was identified as a secondary factor. Factor 3 compared well with the STXM-NEXAFS spectrum for fulvic acid (Fig. 1.6c; Ade et al., 2002). Fulvic acid in atmospheric particles are likely to originate from biomass burning events (Tivanski et al., 2007), thus this factor was identified as a biomass burning factor. The 4-factor solution with a rotation of 0 resulted in the most

representative results. This solution contained the three main factors identified above and an additional factor, which was present in only a few particles. The three main factors accounted for 80% of the particles analyzed by STXM-NEXAFS for the SIMAT and C130 during MILAGRO.
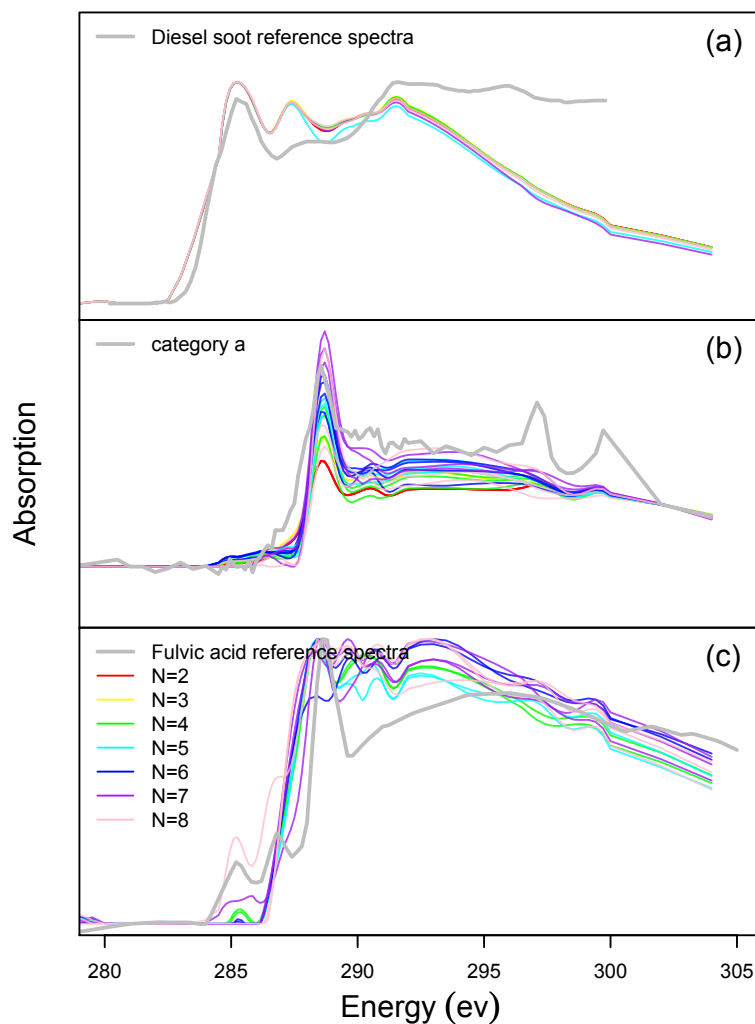
Figure 1.6: Comparisons of major factor spectra from PMF of STXM-NEXAFS spectra with reference spectra: diesel soot (Braun, 2005), category a (Takahama et al., 2007), and fulvic acid (Ade and Urquhart, 2002). Colors indicate 2 (red), 3 (yellow), 4 (green), 5 (cyan), 6 (blue), 7 (purple), and 8-factor (pink) PMF run.

STXM-NEXAFS spectra were grouped into "secondary" type, "biomass burning" type, and "soot" type spectra described by Takahama et al. (2007). Figure 1.7 summarizes the size distributions of analyzed particles and the average

fractions of the three major factors within each size range. The "secondary" type particles were in the size range of 0.2–5 μm, while the "biomass burning" and "soot" type particles were in the size range of 0.1–10 μm. The "soot" type particles were the most abundant, and 70% of these particles have diameters falling between 0.2 and 1 μm. The soot factor was the largest factor for particles smaller than 1 μm, and its fractions were lower in large size ranges. The biomass burning factor showed an increased fraction from submicron to supermicron size ranges.

1.4   Discussion

In this section, we consider how the organic mass and oxygenated fraction of organic mass are affected by diurnal trends at three platforms. We also use the FTIR spectral clusters to highlight the differences observed among the three platforms. Our PMF analysis provides a way to link some of these differences in measurements from the three platforms to the types of sources that affect each. In addition, we compare and contrast our results from STXM-NEXAFS spectra from single particle measurements and FTIR spectra from submicron bulk particle samples.

1.4.1   Diurnal trend of functional groups and elements

Samples were divided into "morning", "afternoon", and "night" categories according to the sampling time to investigate the differences of organic functional groups and elements as a function of time of day. Tukey's Honest Significant Difference method was applied to calculate the differences of the mean concentrations among the categories at a 90% confidence level.

At SIMAT, concentrations of OM, alkane, and carboxylic acid functional groups were found to be significantly higher in the morning than in the afternoon or at night. The high OM and organic functional group concentrations could be explained by either the emission of compounds containing alkane and carboxylic acid functional groups by traffic in the morning or by the low boundary layer in the early morning (Shaw et al., 2007). OM/OC and O/C was significantly higher in

the afternoon, indicating that photochemical processes may contribute to the oxidation of organic compounds in the afternoon. Fractions of alcohol and carboxylic acid functional groups had higher values at night than in the afternoon, likely indicating the relative reduction of alkane functional groups and the concomitant accumulation of oxygenated compounds emitted and produced during the day.

At Altzomoni, concentrations of alkane groups, carboxylic acid groups, amine groups, Se, V, K, and S were found to be higher during the day than at night. Back trajectories at Altzomoni showed that the air masses mainly came from the east and southeast during daytime. The city of Puebla, which is located approximately 50 km east of Altzomoni, is the fourth most populous city in the country and has intense vehicular traffic as well as an important industrial zone in its metropolitan area (Juarez et al., 2005). The boundary layer can reach as high as 6 km during the day (Shaw et al., 2007), which is higher than the 4010 m location of the Altzomoni site. The elevated concentrations of those species during the day may be caused by the transport of pollutants from Puebla. During the night, the boundary layer decreased, and the site was influenced by air masses in the free troposphere, resulting in low concentrations.

No significant differences were found between the morning and afternoon for the C130 measurements, which is not surprising as the measurements were sparse and the sampling location for each observation varied on this mobile platform. While other studies have found that there were coarse particle concentration differences between weekdays and weekends (Stephens et al., 2008), differences in submicron organic functional group and elemental concentrations between days of the week were not found in this study for any platform.

1.4.2 FTIR spectral clusters and O/C

The shapes of spectra in cluster II are comparable to the spectral shapes in cluster S1 identified in shipboard measurements during TexAQS/GoMACCS 2006 near Houston (Russell et al., 2009). Sample spectra in cluster S1 were mainly from the relatively clean southerly flow from the Gulf or polluted by some nearby land-based sources. The similarities of the spectra from different geographical
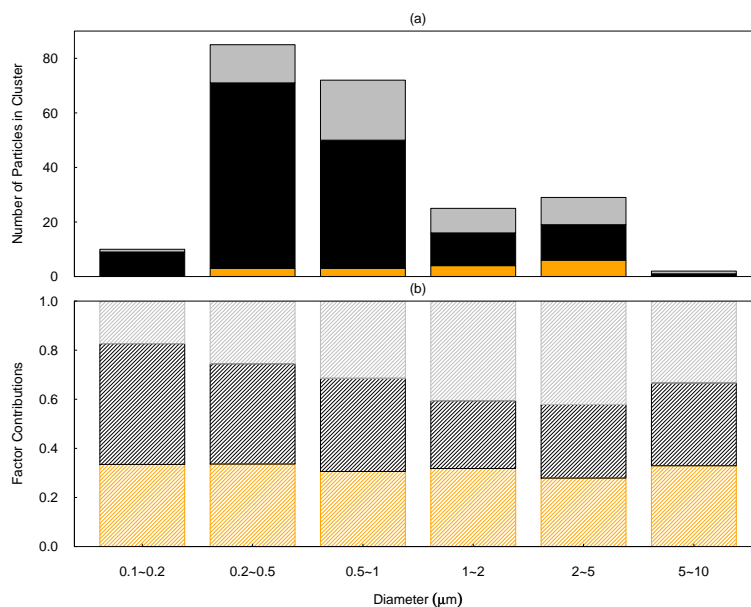
Figure 1.7: (a) Size distributions of single particles for processed type (corresponding to category a), soot type (corresponding to categories b, c, d, e, g, h, and m), and biomass burning type (corresponding to categories i and j) particles described by Takahama et al. (2007) from cluster analysis of STXM-NEXAFS spectra. Colors indicate STXM-NEXAFS cluster categories for "processed" (orange), "soot" (black), and "biomass burning" (grey). (b) Average fractions of processed (orange), soot (black), and biomass burning (grey) factors in 0.1–0.2 μm, 0.2–0.5 μm, 0.5–1 μm, 1–2 μm, 2–5 μm, and 5–10 μm size ranges for 4-factor PMF run of STXM-NEXAFS spectra.

locations indicate that there are some common sources or processes occurring in the atmosphere.

Cluster I and cluster III mainly consist of spectra from SIMAT and Altzomoni, reflecting the similarities of submicron organic composition at these two platforms during certain time periods. Back trajectories at Altzomoni showed that air masses mainly came from northeast, east, and southeast of the site for samples in cluster I and cluster III, indicating the influence of urban pollution from Puebla, including vehicular and industrial emissions (Juarez et al., 2005). It is possible that the transport of Puebla plumes to Altzomoni resulted in organic particles with similar composition at Altzomoni and SIMAT.

Alkane, carboxylic acid, and alcohol groups were the main functional groups
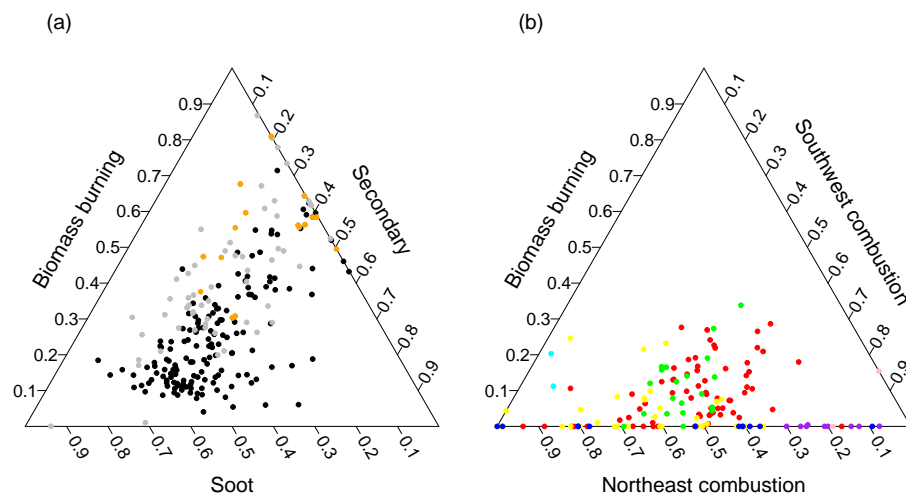
Figure 1.8: **(a)**: Ternary plot of soot, processed, and biomass burning factor fractions from PMF of STXM-NEXAFS spectra. Colors indicate clusters associated with soot type (b–e, g, h, m) particles (black), processed type (a) particles (orange), and biomass burning type (i, j) particles (grey). **(b)**: Ternary plot of northeast combustion, biomass burning, and southwest combustion factor fractions resulted from PMF of FTIR spectra. Colors indicate cluster I (red), cluster II (yellow), cluster III (green), cluster IV (cyan), cluster V (blue), cluster VI (purple), and cluster VII (pink).

in particles and they accounted for more than 80% of OM for three platforms. Figure 1.9 shows the distributions of clustered spectra as a function of alkane, carboxylic acid, and alcohol group mass fractions. At SIMAT, the clustered spectra were relatively centered on the triangle plot, showing comparable mass fractions of the three main functional groups. At Altzomoni, cluster IV was separated from other clusters. Samples from cluster IV showed high alcohol group concentrations, and the highest O/C. This cluster mainly consisted of Altzomoni samples (Fig. 1.2), which were collected during times when the wind direction was from the north or northwest (Gilardoni et al., 2009), suggesting that cluster IV spectra may be associated with processed particles that originated in Mexico City.

1.4.3   PMF factors and associated sources

PMF factors attributed alkane, carboxylic acid, amine, and alcohol groups largely to combustion type sources. Industrial combustion and motor vehicular
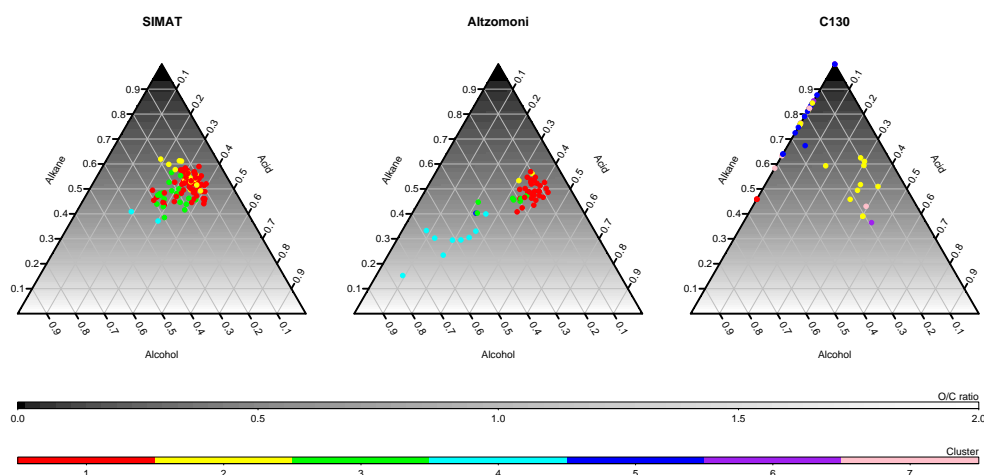
Figure 1.9: Ternary plot of alcohol, alkane, and carboxylic acid functional group mass fractions of SIMAT, Altzomoni, and C130 FTIR measurements. Surface shading indicates O/C. Colors of cluster groups for FTIR spectra indicate cluster I (red), cluster II (yellow), cluster III (green), cluster IV (cyan), cluster V (blue), cluster VI (purple), and cluster VII (pink).

emissions are the most possible combustion sources in the MCMA (Stone et al., 2008; Johnson et al., 2006). This result supports the findings that direct emission processes, such as gasoline combustion and oil burning are sources of alkane and carboxylic acid groups in atmospheric particles (Rogge et al., 1993; Oros et al., 2000). Amines have also been suggested to originate from motor vehicle exhaust and industrial processes (Murphy et al., 2007). PMF attributed the main source of amine to combustion sources, which is consistent with the possible industrial sources discussed by Moffet et al. (2008b). Volatile organic compounds emitted from motor vehicles can form alcohol groups during photochemical processes (Sax et al., 2005). Alcohol species are efficient additives added to lubricant oil to reduce friction (Lenard et al., 1998), thus the alcohol group could be from evaporation of oils used in gasoline and diesel motor vehicles. Sugar industries (Chollett, 2009) in the MCMA could be another source of the observed alcohol functional group. Biomass burning was the major source of the the non-acid carbonyl group, which could be from ketone- and aldehyde- containing species emitted as breakdown products during lignin burning processes (Oros et al., 1999; Simoneit et al., 1999).

Combustion was the major source of both OM and O/C. The OM and O/C

were dominated by the northeast combustion factor at the ground sites and by the southwest combustion factor during the flight measurement (Fig. 1.4). Biomass burning accounted for 0-8% of submicron organic mass (Fig. 1.4), which was close to the biomass burning contribution of 5–15% to $PM_{2.5}$ at the T0 site suggested by Querol et al. (2008). We did not distinguish source types by direct emission and atmospherically-processed as all three combustion sources had weak correlations to combustion marker elements. The southwest combustion factor had the greatest fraction of carboxylic acid group among all factors and had relatively weaker correlations to elements compared to the northeast combustion factor. This factor probably had a larger atmospherically-processed component, which could be affected by meteorology or transport that weakened the correlation to tracers of a single source (Russell et al., 2009).

1.4.4 Comparison of STXM-NEXAFS and FTIR factors from PMF

While the single-particle STXM-NEXAFS spectra were sparse in terms of particle number and sampling times, the submicron particle types that were frequently identified were expected to have some organic components that were similar to the composition of submicron particle mass collected on bulk filters.

PMF of both single and bulk particle spectra resulted in biomass burning and combustion type factors. Figure 1.8b shows the fractions of the northeast combustion factor, the southwest combustion factor, and the biomass burning factor of FTIR samples from SIMAT and C130 platforms. Clusters V, VI, and VII (exclusively consisted of C130 samples) were separated from the other clusters. Clusters II and III were separated: cluster II was associated with larger southwest combustion factor fractions, while cluster III was associated with greater northeast combustion factor fractions. Results from single particle spectra showed that the soot type particles were separated from biomass burning type particles (Fig. 1.8a). This indicates some clusters of both single particle spectra and bulk particle spectra were source-related.

Figure 1.8a shows that the contributions of soot and biomass burning fac-

tors to each ambient particle spectrum varied, but most particles showed consistent contributions from processing. The secondary factor accounted for 10–60% of the carbon absorbance, while the fractions of the other two factors showed a larger variation ranging from about 0–80% and 0–90%, suggesting the biomass burning and soot factors were more source-related, while the secondary factor had a consistent contribution to most particles. Figure 1.8b shows that 85% of the samples had southwest factor fraction of OM between 30 and 65%, while the northeast factor fraction of OM varied from 20 to 70%. Both results show that the factors associated with processed component was more consistent during the sampling period than the combustion factors, since they had a smaller range of contribution for most particles.

1.5 Conclusions

Organic mass concentrations were $9.9\,\mu\mathrm{g\,m^{-3}}$, $6.6\,\mu\mathrm{g\,m^{-3}}$, and $5.3\,\mu\mathrm{g\,m^{-3}}$ for SIMAT, Altzomoni, and C130 flight measurements. Alkane functional group concentrations dominated the OM, with the fractions ranging from 41% to 73%. Dust markers (Ca, Fe, and Si) correlated with each other for all three platforms, while combustion type elements showed different correlations among the three platforms. At SIMAT, two source-related groups of elements were identified: coal combustion type elements (S and Se) and V and Ni from oil combustions; while at Altzomoni, elements from several types of fossil fuel combustion (V, S, K, Br, Pb, Se) correlated with each other. For the C130 measurements, Ca was found to correlate with S, K, and V. The differences in correlations of elements among the three platforms suggest that the urban area was more influenced by fresh emissions, while the high altitude site was more influenced by mixed sources or atmospheric (photochemical) processing.

The cluster analysis of FTIR spectra showed both similarities and differences among the three platforms. Seven distinct clusters of FTIR spectra were identified, from which the last three clusters consisted almost exclusively of samples collected aboard the C130 research flights based in Veracruz, indicating the

wide variety of different sources and air masses sampled by the C130. More than 80% of SIMAT spectra and more than 70% of Altzomoni spectra are identified as clusters I and III, while cluster IV consists almost exclusively of Altzomoni spectra with high alcohol group fractions. The easterly and southeasterly transport of Puebla pollutants to Altzomoni may result in the similarities of organic particles from Altzomoni and SIMAT, while the distinct cluster IV of Altzomoni samples with high O/C suggests more processed particles at the Altzomoni site than at the SIMAT site.

PMF analysis was applied to STXM-NEXAFS spectra and FTIR spectra. PMF of STXM-NEXAFS spectra resulted in three main factors, which represented biomass burning, secondary, and fossil fuel combustion type spectra. PMF of FTIR spectra resulted in one biomass burning factor and two combustion factors, which were not attributed to specific source types as a consequence of the complexity of emission sources in the MCMA. The two combustion type factors were separated by potential source regions: one of them (the northeast combustion factor) was strongly associated with industrial sources to the northeast of SIMAT in the MCMA, and the other (the southwest combustion factor) could represent industrial and motor vehicular emissions mainly from the vicinity of City of Toluca. The southwest combustion factor has significant OM contributions from processed components, but a separate "processed" component was not identified. Several trends in composition were consistent for the factors and rotations selected. Combustion was the largest source of both OM and O/C. PMF attributed alkane, carboxylic acid, amine, and alcohol functional groups largely to combustion sources, among which industrial and motor vehicular emissions were the most probable contributors. Biomass burning contributed to a small fraction (0-8%) of submicron particle mass. Non-acid carbonyl groups, which could be emitted as breakdown products during lignin or other biomass burning (Simoneit et al., 1999), dominated this factor. Both PMF of single particle STXM-NEXAFS spectra and PMF of submicron FTIR spectra showed that the clusters were associated with different fractions of the factor contributions. Narrower ranges of the fraction of the processed factor contributions to single particles and submicron OM (10 to 60% from PMF of single

particle spectra and 35 to 60% from PMF of submicron OM spectra) than combustion type factors suggests that the combustion factors (0–90%) varied more with local sources, while the factors related to atmospheric processing were more constant during the campaign.

1.6 Appendix

Calibrations of organic functional groups of FTIR spectra were conducted using the measured absorption per mole of each component from laboratory-generated standards (Maria et al., 2002). Three primary amine standards (n-Tridecylamine, n-Tetradecylamine, alanine) and three secondary amine standards (N-Methyl-n-octadecylamine, Di-n-decylamine, Di-n-dodecylamine) were used to quantify amine functional group absorption at $1625\,cm^{-1}$ observed in our ambient particle spectra. Results showed that secondary amines do not have detectable absorption peaks at $1625\,cm^{-1}$. Alanine was used as the standard for quantification of primary amine groups as it best represents the absorption peak at $1625\,cm^{-1}$. The revised guided algorithm (Russell et al., 2009) was applied to do peak fitting and integration of alanine standard spectra. The absorptivity of amine functional group is $0.12\,\mu mol$/unit of peak area, with a linear fit (R^2=0.97) of absorption and moles per functional group. Deviations from this absorptivity were not observed for mixtures of alanine and ammonium sulfate. Possibilities of absorption at $1625\,cm^{-1}$ by organonitrate compounds were ruled out by the absence of absorption at $1280\,cm^{-1}$ in the ambient FTIR spectra (Mylonas et al., 1991; Allen et al., 1994; Garnes et al., 2002; Laurent et al., 2004). Water absorption at $1625\,cm^{-1}$ is removed by purging the sample chamber of FTIR instrument for $3\,min$ before scanning each sample.

1.7 Acknowledgments

0511772).

Chapter 1, in full, is a reprint of the material as it appears in Atmospheric Chemistry and Physics 2009 with slight modifications. Liu, S., Takahama, S., Russell, L. M., Gilardoni, S., and Baumgardner, D. (2009), Oxygenated organic functional groups and their sources in single and submicron organic particles in MILAGRO 2006 campaign, Atmospheric Chemistry and Physics, 9, 6849-6863. The dissertation author was the primary investigator and author of this paper.

References

[1] Ade, H. and Urquhart, S. G.: NEXAFS spectroscopy and microscopy of natural and synthetic polymers, in: Chemical Applications of Synchrotron Radiation, World Scientific Publishing, Singapore, 285–355, 2002.

[2] Aldape, F., Flores, J. M. and Martínez-pontón, A. A.: Evaluation of fine airborne particulate matter at toluca, Estado de Mexico, using pixe, International Journal of PIXE, 18 (Nos. 3 and 4), 187–197, 2008.

[3] Aiken, A. C., Decarlo, P. F., Kroll, J. H., Worsnop, D. R., Huffman, J. A., Docherty, K. S., Ulbrich, I. M., Mohr, C., Kimmel, J. R., Sueper, D., Sun, Y., Zhang, Q., Trimborn, A., Northway, M., Ziemann, P. J., Canagaratna, M. R., Onasch, T. B., Alfarra, M. R., Prevot, A. S. H., Dommen, J., Duplissy, J., Metzger, A., Baltensperger, U., and Jimenez, J. L.: O/C and OM/OC ratios of primary, secondary, and ambient organic aerosols with high-resolution time-of-flight aerosol mass spectrometry, Environ. Sci. Technol., 42(12), 4478–4485, 2008.

[4] Aiken, A. C., de Foy, B., Wiedinmyer, C., et al.: Mexico City aerosol analysis during MILAGRO using high resolution aerosol mass spectrometry at the urban supersite (T0) - Part 2: Analysis of the biomass burning contribution and the modern carbon fraction, Atmos. Chem. Phys., in preparation, 2009.

[5] Allen, D. T., Palen, E. J., Haimov, M. I., Hering, S. V., and Young, J. R.: Fourier-Transform Infrared-Spectroscopy Of Aerosol Collected In A Low-Pressure Impactor (Lpi/Ftir) - Method Development And Field Calibration, Aerosol Sci. Tech., 21(4), 325–342, 1994.

[6] Balasubramanian, R. and Qian, W. B.: Characterization and source identification of airborne trace metals in Singapore, J. Environ. Monitor., 6(10), 813–818, 2004.

[7] Baumgardner, D., Grutter, M., Allan, J., Ochoa, C., Rappenglueck, B., Russell, L. M., and Arnott, P.: Physical and chemical properties of the regional mixed layer of Mexico's Megapolis, Atmos. Chem. Phys., 9, 5711–5727, 2009.

[8] Braun, A., Shah, N., Huggins, F. E., Kelly, K. E., Sarofim, A., Jacobsen, C., Wirick, S., Francis, H., Ilavsky, J., Thomas, G. E., and Huffman, G. P.: X-ray scattering and spectroscopy studies on diesel soot from oxygenated fuel under various engine load conditions, Carbon, 43(12), 2588–2599, 2005.

[9] Chollett, D. L.: From Sugar to Blackberries Restructuring Agro-export Production in Michoacan, Mexico, Latin American Perspectives, 36(3), 79–92, 2009.

[10] Chow, J. C., Watson, J. G., Edgerton, S. A., and Vega, E.: Chemical composition of $PM_{2.5}$ and PM_{10} in Mexico City during winter 1997, Sci. Total Environ., 287(3), 177–201, 2002.

[11] CICA: Emissions from Street Vendor Cooking Devices (Charcoal Grilling), EPA-600/R-99-048, available at: http://www.epa.gov/ttn/catc/dir1/mexfr.pdf(last access: 29 January 2009), 1999.

[12] DeCarlo, P. F., Dunlea, E. J., Kimmel, J. R., Aiken, A. C., Sueper, D., Crounse, J., Wennberg, P. O., Emmons, L., Shinozuka, Y., Clarke, A., Zhou, J., Tomlinson, J., Collins, D. R., Knapp, D., Weinheimer, A. J., Montzka, D. D., Campos, T., and Jimenez, J. L.: Fast airborne aerosol size and chemistry measurements above Mexico City and Central Mexico during the MILAGRO campaign, Atmos. Chem. Phys., 8, 4027–4048, 2008.

[13] Dockery, D. W., Pope, C. A., Xu, X. P., Spengler, J. D., Ware, J. H., Fay, M. E., Ferris, B. G., and Speizer, F. E.: An Association Between Air-Pollution And Mortality In 6 United-States Cities, New Engl. J. Med., 329(24), 1753–1759, 1993.

[14] Eidels-Dubovoi, S.: Aerosol impacts on visible light extinction in the atmosphere of Mexico City, Sci. Total Environ., 287(3), 213–220, 2002.

[15] Finlayson-Pitts, B. J. and Pitts, J. N.: Chemistry of the Upper and Lower Atmosphere, Academic Press, San Diego, USA, 386–388, 2000.

[16] Escudero, M., Stein, A., Draxler, R. R., Querol, X., Alastuey, A., Castillo, S. and Avila, A.: Determination of the contribution of northern Africa dust source areas to PM10 concentrations over the central Iberian Peninsula using the Hybrid Single-Particle Lagrangian Integrated Trajectory model (HYSPLIT) model, J. Geophys. Res.-Atmos., 111(D6), D06210, doi:10.1029/2005JD006395, 2006.

[17] Flores, J., Aldape, F., Diaz, R. V., Hernandez-Mendez, B., and Garcia, R.: PIXE analysis of airborne particulate matter from Xalostoc, Mexico: winter to summer comparison, Nuclear Instruments and Methods In Physics Research Section B-Beam Interactions With Materials And Atoms, 150(1–4), 445–449, 1999.

[18] Garnes, L. A. and Allen, D. T.: Size distributions of organonitrates in ambient aerosol collected in Houston, Texas, Aerosol Sci. Technol., 36(10), 983–992, 2002.

[19] Gilardoni, S., Russell, L. M., Sorooshian, A., Flagan, R. C., Seinfeld, J. H., Bates, T. S., Quinn, P. K., Allan, J. D., Williams, B., Goldstein, A. H., Onasch, T. B., and Worsnop, D. R.: Regional variation of organic functional groups in aerosol particles on four US east coast platforms during the International Consortium for Atmospheric Research on Transport and Transformation 2004 campaign, J. Geophys. Res.-Atmos., 112, D10S27, doi:10.1029/2006JD007737, 2007.

[20] Gilardoni, S., Liu, S., Takahama, S., Russell, L. M., Allan, J. D., Steinbrecher, R., Jimenez, J. L., Decarlo, P. F., Dunlea, E. J. and Baumgardner, D.: Characterization of organic ambient aerosol during MIRAGE 2006 on three platforms, Atmos. Chem. Phys., 9, 5417–5432, 2009.

[21] Hopkins, R. J., Tivanski, A. V., Marten, B. D., and Gilles, M. K.: Chemical bonding and structure of black carbon reference materials and individual carbonaceous atmospheric aerosols, J, Aerosol Sci,, 38(6), 573–591, 2007.

[22] Johnson, K. S., de Foy, B., Zuberi, B., Molina, L. T., Molina, M. J., Xie, Y., Laskin, A., and Shutthanandan, V.: Aerosol composition and source apportionment in the Mexico City Metropolitan Area with PIXE/PESA/STIM and multivariate analysis, Atmos. Chem. Phys., 6, 4591–4600, 2006.

[23] Juarez, A., Gay, C., and Flores, Y.: Impact of the Popocatepetl's volcanic activity on the air quality of Puebla City, Mexico, Atmosfera, 18(1), 57–69, 2005.

[24] Kaufman, L. and Rousseeuw, P. J.: Finding Groups in Data: An Introduction to cluster Analysis, Wiley, New York, USA, 45–48, 1990.

[25] Keller, H. R., Massart, D. L., Liang, Y. Z., and Kvalheim, O. M.: Evolving Factor-Analysis In The Presence Of Heteroscedastic Noise, Analytica Chimica Acta, 263(1–2), 29–36, 1992.

[26] Laurent, J. P. and Allen, D. T.: Size distributions of organic functional groups in ambient aerosol collected in Houston, Texas, Aerosol Sci. Technol., 38, 82–91, 2004.

[27] Lee, E., Chan, C. K., and Paatero, P.: Application of positive matrix factorization in source apportionment of particulate pollutants in Hong Kong, Atmos. Environ., 33(19), 3201–3212, 1999.

[28] Lenard, J. G.: The effect of lubricant additives on the coefficient of friction in cold rolling, J. Mat. Proc. Technol., 80(1), 232–238, 1998.

[29] Li, Z., Hopke, P. K., Husain, L., Qureshi, S., Dutkiewicz, V. A., Schwab, J. J., Drewnick, F., and Demerjian, K. L.: Sources of fine particle composition in New York city, Atmos. Environ., 38(38), 6521–6529, 2004.

[30] Liepert, B. G., Feichter, J., Lohmann, U., and Roeckner, E.: Can aerosols spin down the water cycle in a warmer and moister world?, Geophys. Res. Lett., 31, L06207, doi:10.1029/2003GL019060, 2004.

[31] Maria, S. F., Russell, L. M., Turpin, B. J., and Porcja, R. J.: FTIR measurements of functional groups and organic mass in aerosol samples over the Caribbean, Atmos. Environ., 36(33), 5185–5196, 2002.

[32] Maria, S. F., Russell, L. M., Turpin, B. J., Porcja, R. J., Campos, T. L., Weber, R. J., and Huebert, B. J.: Source signatures of carbon monoxide and organic functional groups in Asian Pacific Regional Aerosol Characterization Experiment (ACE-Asia) submicron aerosol types, J. Geophys. Res.-Atmos., 108(D23), 8637, doi:10.1029/2003JD003703, 2003.

[33] Maria, S. F., Russell, L. M., Gilles, M. K., and Myneni, S. C. B.: Organic aerosol growth mechanisms and their climate-forcing implications, Science, 306(5703), 1921–1924, 2004.

[34] Maria, S. F. and Russell, L. M.: Organic and inorganic aerosol below-cloud scavenging by suburban New Jersey precipitation, Environ. Sci. Technol., 39, 13, 4793–4800, 2005.

[35] Moffet, R. C., Desyaterik, Y., Hopkins, R. J., Tivanski, A. V., Gilles, M. K., Wang, Y., Shutthanandan, V., Molina, L. T., Abraham, R. G., Johnson, K. S., Mugica, V., Molina, M. J., Laskin, A., and Prather, K. A.: Characterization of aerosols containing Zn, Pb, and Cl from an industrial region of Mexico City, Environ. Sci. Technol., 42(19), 7091–7097, 2008a.

[36] Moffet, R. C., de Foy, B., Molina, L. T., Molina, M. J., and Prather, K. A.: Measurement of ambient aerosols in northern Mexico City by single particle mass spectrometry, Atmos. Chem. Phys., 8, 4499–4516, 2008b.

[37] Molina, L. T., Kolb, C. E., de Foy, B., Lamb, B. K., Brune, W. H., Jimenez, J. L., Ramos-Villegas, R., Sarmiento, J., Paramo-Figueroa, V. H., Cardenas, B., Gutierrez-Avedoy, V., and Molina, M. J.: Air quality in North America's most populous city - overview of the MCMA-2003 campaign, Atmos. Chem. Phys., 7, 2447–2473, 2007.

[38] Murphy, S. M., Sorooshian, A., Kroll, J. H., Ng, N. L., Chhabra, P., Tong, C., Surratt, J. D., Knipping, E., Flagan, R. C., and Seinfeld, J. H.: Secondary aerosol formation from atmospheric reactions of aliphatic amines, Atmos. Chem. Phys., 7, 2313–2337, 2007.

[39] Mylonas, D. T., Allen, D. T., Ehrman, S. H., and Pratsinis, S. E.: The Sources And Size Distributions Of Organonitrates In Los-Angeles Aerosol, Atmos. Environ. A-Gen., 25, 12, 2855–2861, 1991.

[40] Oros, D. R. and Simoneit, B. R. T.: Identification of molecular tracers in organic aerosols from temperate climate vegetation subjected to biomass burning, Aerosol Sci. Technol., 31(6), 433–445, 1999.

[41] Oros, D. R. and Simoneit, B. R. T.: Identification and emission rates of molecular tracers in coal smoke particulate matter, Fuel, 79(5), 515–536, 2000.

[42] Paatero, P. and Tapper, U.: Positive Matrix Factorization – A Nonnegative Factor Model With Optimal Utilization Of Error-Estimates Of Data Values, Environmetrics, 5(2), 111–126, 1994.

[43] Pekney, N. J., Davidson, C. I., Zhou, L. M., and Hopke, P. K.: Application of PSCF and CPF to PMF-modeled sources of $PM_{2.5}$ in Pittsburgh, Aerosol Sci. Technol., 40(10), 952–961, 2006.

[44] Querol, X., Pey, J., Minguillón, M. C., Pérez, N., Alastuey, A., Viana, M., Moreno, T., Bernabé, R. M., Blanco, S., Cárdenas, B., Vega, E., Sosa, G., Escalona, S., Ruiz, H., and Artíñano, B.: PM speciation and sources in Mexico during the MILAGRO-2006 Campaign, Atmos. Chem. Phys., 8, 111–128, 2008.

[45] Qureshi, S., Dutkiewicz, V. A., Khan, A. R., Swami, K., Yang, K. X., Husain, L., Schwab, J. J., and Demerjian, K. L.: Elemental composition of $PM_{2.5}$ aerosols in Queens, New York: Solubility and temporal trends, Atmos. Environ., 40, S238–S251, 2006.

[46] Raga, G. B., Baumgardner, D., Castro, T., Martinez-Arroyo, A., and Navarro-Gonzalez, R.: Mexico City air quality: a qualitative review of gas and aerosol measurements (1960–2000), Atmos. Environ., 35(23), 4041–4058, 2001.

[47] Ramadan, Z., Song, X. H., and Hopke, P. K.: Identification of sources of Phoenix aerosol by positive matrix factorization, J. Air Waste Manage., 50(8), 1308–1320, 2000.

[48] Rogge, W. F., Hildemann, L. M., Mazurek, M. A., Cass, G. R., and Simoneit, B. R. T.: Sources Of Fine Organic Aerosol. 2. Noncatalyst And Catalyst-Equipped Automobiles And Heavy-Duty Diesel Trucks, Environ. Sci. Technol., 27(4), 636–651, 1993.

[49] Russell, L. M., Maria, S. F., and Myneni, S. C. B.: Mapping organic coatings on atmospheric particles, Geophys. Res. Lett., 29(16), 1779, doi:10.1029/2002GL014874, 2002.

[50] Russell, L. M., Takahama, S., Liu, S., Hawkins, L. N., Covert, D. S., Quinn, P. K., and Bates, T. S.: Oxygenated fraction and mass of organic aerosol from direct emission and atmospheric processing measured on the R/V Ronald Brown during TEXAQS/GoMACCS 2006, Journal Of Geophysical Research-Atmospheres, 114, D00F05, doi:10.1029/2008JD011275, 2009.

[51] Salcedo, D., Onasch, T. B., Dzepina, K., Canagaratna, M. R., Zhang, Q., Huffman, J. A., DeCarlo, P. F., Jayne, J. T., Mortimer, P., Worsnop, D. R., Kolb, C. E., Johnson, K. S., Zuberi, B., Marr, L. C., Volkamer, R., Molina, L. T., Molina, M. J., Cardenas, B., Bernabé, R. M., Márquez, C., Gaffney, J. S., Marley, N. A., Laskin, A., Shutthanandan, V., Xie, Y., Brune, W., Lesher, R., Shirley, T., and Jimenez, J. L.: Characterization of ambient aerosols in Mexico City during the MCMA-2003 campaign with Aerosol Mass Spectrometry: results from the CENICA Supersite, Atmos. Chem. Phys., 6, 925–946, 2006.

[52] Sax, M., Zenobi, R., Baltensperger, U., and Kalberer, M.: Time resolved infrared spectroscopic analysis of aerosol formed by photo-oxidation of 1,3,5-trimethylbenzene and alpha-pinene, Aerosol Sci. Technol., 39(9), 822–830, 2005.

[53] Shilling, J. E., Chen, Q., King, S. M., Rosenoern, T., Kroll, J. H., Worsnop, D. R., DeCarlo, P. F., Aiken, A. C., Sueper, D., Jimenez, J. L., and Martin, S. T.: Loading-dependent elemental composition of α-pinene SOA particles, Atmos. Chem. Phys., 9, 771–782, 2009.

[54] Sharma, M. and Maloo, S.: Assessment of ambient air PM_{10} and $PM_{2.5}$ and characterization of PM_{10} in the city of Kanpur, India, Atmos. Environ., 39(33), 6015–6026, 2005.

[55] Shaw, W. J., Pekour, M. S., Coulter, R. L., Martin, T. J., and Walters, J. T.: The daytime mixing layer observed by radiosonde, profiler, and lidar during MILAGRO, Atmos. Chem. Phys. Discuss., 7, 15025–15065, 2007.

[56] Simoneit, B. R. T., Schauer, J. J., Nolte, C. G., Oros, D. R., Elias, V. O., Fraser, M. P., Rogge, W. F., and Cass, G. R.: Levoglucosan, a tracer for cellulose in biomass burning and atmospheric particles, Atmos. Environ., 33 (2), 173–182, 1999.

[57] Stephens, S., Madronich, S., Wu, F., Olson, J. B., Ramos, R., Retama, A., and Muñoz, R.: Weekly patterns of México City's surface concentrations of CO, NO_x, PM_10 and O_3 during 1986-2007, Atmos. Chem. Phys., 8, 5313–5325, 2008.

[58] Stone, E. A., Snyder, D. C., Sheesley, R. J., Sullivan, A. P., Weber, R. J., and Schauer, J. J.: Source apportionment of fine organic aerosol in Mexico City during the MILAGRO experiment 2006, Atmos. Chem. Phys., 8, 1249–1259, 2008.

[59] Takahama, S., Gilardoni, S., Russell, L. M., and Kilcoyne, A. L. D.: Classification of multiple types of organic carbon composition in atmospheric particles by scanning transmission X-ray microscopy analysis, Atmos. Environ., 41(40), 9435–9451, 2007.

[60] Tivanski, A. V., Hopkins, R. J., Tyliszczak, T., and Gilles, M. K.: Oxygenated interface on biomass burn tar balls determined by single particle scanning transmission X-ray microscopy, J. Phys. Chem. A, 111(25), 5448–5458, 2007.

[61] Vega, E., Garcia, I., Apam, D., Ruiz, M. E., and Barbiaux, M.: Application of a chemical mass balance receptor model to respirable particulate matter in Mexico city, J. Air Waste Manage., 47(4), 524–529, 1997.

[62] Ward, J. H.: Hierarchical Grouping To Optimize An Objective Function, J. Am. Stat. Assoc., 58(301), 236–244, 1963.

[63] Yokelson, R. J. and Urbanski, S. P.: Emissions from forest fires near Mexico City, Atmos. Chem. Phys., 7, 5569–5584, 2007.

Chapter 2

Ozone-driven daytime formation of secondary organic aerosol containing carboxylic acid groups and alkane groups

Abstract. Carboxylic acids are present in substantial quantities in atmospheric particles, and they play an important role in the physical and chemical properties of aerosol particles. During measurements in coastal California in the summer of 2009, carboxylic acid functional groups were exclusively associated with a fossil fuel combustion factor derived from factor analysis of Fourier transform infrared spectroscopic measurements and closely correlated with oxygenated organic factors from aerosol mass spectrometry measurements. The high fraction of acid groups and the high ratio of oxygen to carbon in this factor suggest that this factor is composed of secondary organic aerosol (SOA) products of combustion emissions from the upwind industrial region (the ports of Los Angeles and Long Beach). Another indication of the photochemically-driven secondary formation

of this combustion-emitted organic mass (OM) was the daytime increase in the concentrations of acid groups and the combustion factors. This daytime increase closely tracked the O_3 mixing ratio with a correlation coefficient of 0.7, indicating O_3 was closely associated with the SOA maximum and thus likely the oxidant that resulted in acid group formation. Using a pseudo-Lagrangian framework to interpret this daytime increase of carboxylic acid groups and the combustion factors, we estimate that the carboxylic acid groups formed in a 12-h daytime period of one day ("Today's SOA") accounted for 25–33 % of the measured carboxylic acid group mass, while the remaining 67–75 % (of the carboxylic acid group mass) was likely formed 1–3 days previously (the "Background SOA"). A similar estimate of the daytime increase in the combustion factors suggests that "Today's SOA" and the "Background SOA" respectively contributed 25–50 % and 50–75 % of the combustion factor (the "Total SOA"), for a "Total SOA" contribution to the OM of 60 % for the project average. Further, size-resolved spectrometric and spectroscopic characterization of the particle OM indicate that the majority of the OM formed by condensation of gas-phase oxidation products. This unique set of measurements and methods to quantify and characterize photochemically and ozone-linked carboxylic acid group formation provide independent and consistent assessments of the secondary fraction of OM, which could result from second generation products of the oxidation of gas-phase alkane (molecules).

2.1 Introduction

Organic compounds typically account for 10–70 % of dry particle mass (82). Understanding the chemistry of particle-phase organic compounds is important for assessing the effects of aerosol particles on air quality, human health, and climate change (20). The major organic components identified in ambient particles include alkane (saturated C-C-H), carboxylic acid (C(O)OH), hydroxyl (C-OH), amine (C-NH), and non-acid carbonyl (C=O) functional groups (51, 49, 66, 21, 34, 59), among which alkane and carboxylic acid functional groups, taken together, often account for more than 70 % of the OM (69). Alkane groups, a large component of ambient organic compounds (51), are typically associated with primary gas and particle-phase emissions that originate from fossil fuel combustion emissions, including vehicular exhaust (63) and coal burning (86). In addition to being prevalent in primary emissions, alkane groups are found in many oxygenated secondary organic products, e.g. β-pinene oxidation products might include norpinic acid (88), which has two oxygenated groups and five hydrogenated carbons, each with one to three C-H bonds. Carboxylic acid groups are observed in urban, rural, and remote atmospheric particles and sometimes account for more than 30 % of OM (25, 37, 36, 18, 85, 74, 5, 66, 86, 93). Because many carboxylic acids are highly soluble and tend to absorb water under high relative humidity (RH), they could affect radiative (e.g. light scattering) and chemical (e.g. aqueous-phase reaction) properties of ambient particles.

Carboxylic acids have been frequently observed in atmospheric particles since 1970s (Schuetzle et al., 1975; Cronn et al., 1977; Satsumabayashi et al., 1989; Satsumabayashi et al., 1990; Kawamura and Ikushima, 1993; Rogge et al., 1993). In these measurements, carboxylic acid concentration either correlated to solar radiation or correlated to oxidant concentration (mostly ozone), suggesting they are formed in the atmosphere during photochemical processes. For example, enhanced abundance of ambient carboxylic acids in summer and in the afternoon suggests that carboxylic acids are secondary (Kawamura and Ikushima, 1993; Kawamura and Yasui, 2005). Although primary emission of carboxylic acids from engine exhaust and meat cooking were identified in a few studies (Kawamura and Kaplan,

1987; Rogge et al., 1991), the lack of correlation of carboxylic acids to traffic emission and meat cooking tracers suggest that these primary acid sources may not reflect a majority of carboxylic acid mass. Recent laboratory studies have shown condensed-phase carboxylic acid groups formed as SOA from anthropogenic and biogenic precursors (88, 17, 5). Aqueous-phase or in-cloud formation of carboxylic acids has been suggested by several field studies and modeling simulations (4, 87, 16, 89, 75, 1), indicating carboxylic acid groups can be formed through various processes under different ambient conditions. Recently, reactions of gas-phase alkanes (molecules) have been studied by several research groups (28, 47, 54, 60), which suggest gas-phase alkane (molecules) could be a precursor of carboxylic acid group formation (Russell et al., 2011).

Despite an increasing number of studies on carboxylic acids in recent years, the formation mechanism of carboxylic acids and other SOA components are still poorly understood, making identification of ambient SOA controversial. The organic carbon (OC) to elemental carbon (EC) ratio has been used to estimate SOA by assuming an average OC/EC from emission source measurements. OC/EC exceeding the average OC/EC is assumed to be SOA (81). The SOA mass estimated from this method is highly uncertain, since OC/EC is highly variable from source to source (24) and the average OC/EC is dependent on meteorological conditions. Another approach is to identify SOA products from individual precursors (88). This method requires detection of SOA by molecular level speciation and known SOA formation mechanisms, which are often not available.

In this work, we compare the contributions of carboxylic acid group and other oxygenated organic groups that can be attributed to photochemical SOA formation in the atmosphere. We use factors identified from the Positive Matrix Factorization (PMF) analyses on the complementary Fourier Transform Infrared (FTIR) spectroscopy and Aerosol Mass Spectrometry (AMS) measurements to separate organic components based on their sources, so that the SOA formation for each source can be considered separately. The oxygenated nature of the fossil fuel combustion factors is used to provide an initial estimate of the total contribution of acid groups to SOA. A second estimate of SOA formation is provided by using

a pseudo-Lagrangian framework to identify the fraction of SOA formed in a single day ("Today's SOA"). In addition, we use the size distribution of acid groups to provide evidence of the mechanism by which the SOA forms. By comparing the extent to which these three methods are consistent, this study provides both an evaluation of the contribution of acid groups to SOA and evidence for the timescale, precursors, and oxidants involved in SOA formation.

2.2   Sample collection and instrumentation

Submicron particles were continuously collected at the Scripps Pier (8 m above sea level (a.s.l.)) in La Jolla (32.87° N, 117.25° W), California, from 15 August to 1 October 2009. Instruments were deployed in a temperature-controlled container at the end of the pier (300 m west of the shoreline) and shared a common $3/8''$ o.d. stainless steel inlet. Submicron particles were separated by a PM_1 cyclone and were collected on four filters daily for the time periods: 06:00–10:00 PST, 10:00–14:00 PST, 14:00–18:00 PST, and 18:00–06:00 PST (the next day) Pacific Standard Time (PST, one hour earlier than local daylight time), representing morning, midday, afternoon, and nighttime samples, respectively. A 24-h sample was simultaneously collected in parallel with shorter samples for each day. 37 mm Teflon filters (Teflo, Pall Inc., Ann Arbor, MI) were used for the FTIR analysis performed using a Bruker Tensor 27 FTIR Spectrometer with a DTGS detector (Bruker, Waltham, MA). Samples were frozen during storage to reduce desorption. Each Teflon filter was scanned before and after sampling using the FTIR and the pre-scanned spectrum was subtracted from the post-scanned spectrum to correct for variability in the polytetrafluoroethylene absorption of the Teflon filters. An automated algorithm was used to conduct spectrum subtraction, baselining, peak-fitting, and error estimation (66). Mass concentrations of alkane, carboxylic acid, hydroxyl, amine, non-acid carbonyl, organonitrate, alkene, and aromatic functional groups were quantified using previously reported algorithms and standards (66, 7).

Concentrations of non-refractory organics, sulfate, ammonium, nitrate, and chloride were measured using a quadrupole AMS (Aerodyne, Billerica, MA). In

this instrument, particles passed through a 100 μm orifice were focused by an aerodynamic lens followed by vaporization (600 °C) and ionization at the entrance of a quadropole mass spectrometer. Particle size is measured by time-of-flight between a rotating chopper, which modulates the particle beam (35). The "mass spectrum" (MS) mode and the "time-of-flight" (TOF) mode alternated during the measurements. Complete mass spectra (1–300 amu) and size distributions for selected mass fragments were stored at 5-min resolution. Transmission efficiency was approximately 100 % for 60 to 600 nm particles (35). Dry ammonium nitrate particles (350 nm) were used to calibrate the ionization efficiency weekly. Collection efficiency (CE) of the AMS was assigned to each 5-min organic and inorganic measurement to correct for particle loss due to bouncing off of the vaporizer. The CE was determined as a linear function of the ammonium to sulfate molar ratio, with 0.45 and 1 corresponding to ratios ≥ 1 and 0, respectively (61). Another commonly used method for CE correction is to use CE = 0.5, when no other simultaneous measurements are available. In this study, the sulfate-based correction resulted in a greater correlation of the FTIR and the AMS OM than using a constant CE of 0.5. Therefore, the sulfate-based method is used in this study. The campaign average ammonium to sulfate molar ratio was 1.9±1.2, and the CE was 0.45 for approximately 85 % of the measurements.

Single particles were impacted on Si_3N_4 windows on 27 August and 4, 14, 20, and 22 September, 2009. Four samples were collected (15–30 min) on these days for periods overlapping the four FTIR filter sampling periods. Samples were stored at temperatures below 0 °C before analysis at the Advanced Light Source (Lawrence Berkeley National Laboratory, CA) on beamline 5.3.2 (41, 49). Single particle image and K-edge X-ray absorption spectrum were acquired using a combination of Scanning Transmission X-ray Microscopy (STXM) and Near-Edge X-ray Absorption Fine Structure (NEXAFS) spectroscopy. Organic functional groups (including alkane, hydroxyl, ketone, alkene, and carboxylic acid groups) and inorganic potassium and carbonate of carbon-containing single particles were measured (65, 52). Particle size, image, and organic functional group abundance were analyzed using an automated algorithm described by Takahama et al. (78).

Carbon monoxide (CO) dry air mole fractions were measured by a newly installed Horiba APMA-370 NDIR analyzer. Air was continuously pumped through a sampling line (400 m; 1/2″ Dekabon) with an inlet 20 m a.s.l. Measurements were reported as 5-min averages, initially using the factory calibration. The instrument was subsequently calibrated against standards on the NOAA/ESRL 2004 CO calibration scale, and the field campaign results were recalculated based on the measurement of a whole air reference cylinder that was measured during the field campaign and also during the NOAA standard calibrations. In the absence of a more thorough real-time calibration, we estimate that the precision of the 5-min averaged CO measurements is 5–10 ppb. Ozone (O_3) mixing ratio was monitored using a Thermo Environmental Instruments (TEI) 49C analyzer and measurements were recorded as 1-min averages. The O_3 measurements were not calibrated during the campaign, so only the concentrations relative to the campaign average are reported.

2.3   Results

This section describes the meteorological conditions under which carboxylic acid groups are formed, the composition of organic mass quantified by FTIR, AMS, and STXM-NEXAFS, and the components contributing to organic mass identified from factor analysis. The daily variations in organic functional groups, AMS measured components, and O_3 mixing ratio are then compared.

2.3.1   Meteorological conditions during the sampling period

The sampling period was characterized by consistent temperature and RH with the averages and standard deviations being 20.2±2.5 °C and 79.3±8.6 %, respectively. Temperature peaked in the afternoon and showed a minimum in the early morning, anti-correlating with RH. Photosynthetically active radiation peaked at noon. Land-sea breeze circulation was observed during the measurement period and was consistent with previous studies (33). In general, surface
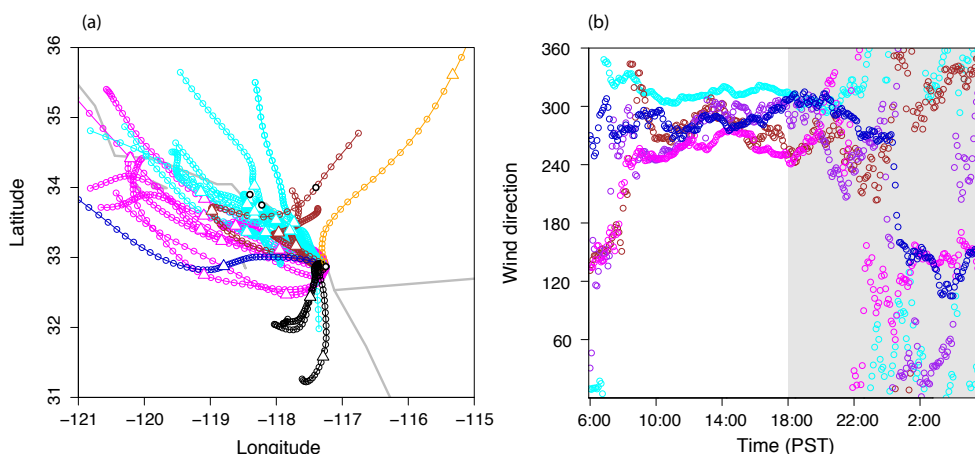
Figure 2.1: **(a)**: Averaged 48-h back trajectories for each day (daytime only) representing Los Angeles-Long Beach (cyan; air mass coming from Los Angeles and Long Beach regions), Riverside (brown; air mass originating from Riverside vicinity), Inland (orange; easterly/northeasterly air mass), Tijuana-Ensenada (black; southerly air mass), Mixed coastal (magenta; northerly air mass coming along the coast of California), and Ocean (dark blue; westerly air mass) air mass sectors during the campaign. The triangle in each trajectory indicates 24-h before the air mass arrived at the sampling site. The black circles (from top to bottom) indicate Riverside, Los Angeles, Los Angeles – Long Beach port, and the sampling site; **(b)** vector-averaged diurnal profile of wind direction (0 degree represents wind coming from north) for the air mass sectors specified in **(a)**. Shaded areas indicate nighttime periods.

wind shifted at about 07:00 PST from offshore to onshore wind and at 22:00 PST from onshore to offshore wind (Fig. 2.1b).

Back trajectories were calculated hourly using the Hybrid Single-Particle Lagrangian Integrated Trajectory (HYSPLIT) model (14, 64) at 200 m and were used to determine the origin of air masses. The FTIR filter samples were grouped into sectors representing the origin of air masses (Fig. 2.1a) as indicated by the top bars in Fig. 2.2a. Each air mass sector (along with consistent daytime onshore flow) allows analysis of particles originating from the same source region (most frequently the ports of Los Angeles and Long Beach region) for 1–3 consecutive days. To further investigate likely sources of OM, potential source contribution function (PSCF) was applied to the factors resulted from factor analysis. PSCF classifies the back trajectories as "high" and "low" by concentration of the target

component and calculates the probability that a source is located at a particular region (58). Examples of PSCF results are shown in Fig. 2.11.

2.3.2 Organic and inorganic composition of submicron particles

Table 2.1 summarizes the campaign average concentrations of the FTIR and AMS-measured components. Figure 2.2a shows the time series and the average fraction of organic functional groups measured by FTIR. The OM concentration varied from 0.39 to 11 μg m^{-3} with an average concentration of 3.3±1.9 μg m^{-3}, which was comparable to the OM concentration in the summer of 2008 (29) and about twice the OM concentration measured in the winter of 2009 (7) at the same site. Alkane functional group concentration was 1.5±1.1 μg m^{-3} and contributed 47 % of the OM. Carboxylic acid functional groups accounted for 34 % of the OM with an average concentration of 1.1±0.8 μg m^{-3}. The concentration of hydroxyl functional groups was 0.40±0.24 μg m^{-3}, accounting for 12 % of the OM. Amine, non-acid carbonyl, and organonitrate functional groups contributed small fractions to the OM (3 %, 2 %, and 2 %, respectively). Alkene and aromatic functional groups were below detection limit for all samples and each was estimated to account for no more than 4 % of the OM. These two functional groups were excluded from the analyses in this study. Samples associated with different air mass sectors had similar organic functional group compositions but differed in mass concentration. The Los Angeles-Long Beach port and the Riverside sectors contain significantly higher OM, indicating transport of pollutants from these heavily polluted regions to the sampling site, which is consistent with the findings of Ault et al. (2). Each "day" was defined as "06:00 to 06:00 PST". 32 out of 47 days were associated with a single air mass sector during the daytime. These days (as indicated by the top green bars in Fig. 2.2a) are included in an analysis of their diurnal cycles.

The OM fraction of carboxylic acid groups in single particles, calculated as carboxylic acid group absorption normalized by the sum of absorption of all functional groups from the X-ray spectra, are 42±14 % for the morning particles and 38±17 % for the afternoon particles. These values are comparable to the car-
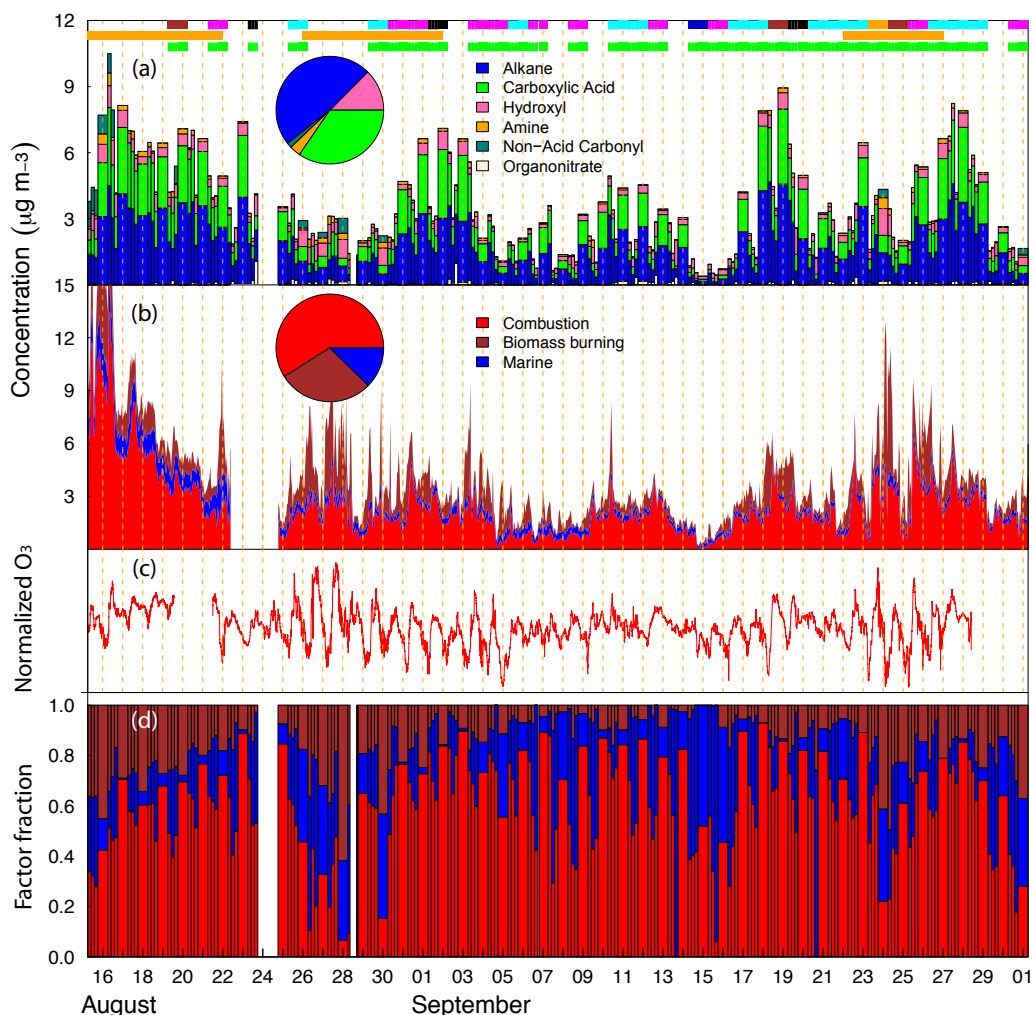
Figure 2.2: **(a)** Time series of organic functional group concentrations measured by the FTIR; sectors are indicated by the top color bars (same colors as in Fig. 1), for which the sector associated with each FTIR sample was determined as the air mass origin shown by the majority (>80 %) of the back trajectories during the sampling time; top brown bars indicate fire periods corresponding to the La Brea fire (in Santa Barbara County), the Station fire (in Los Angeles County), and the Guiberson fire (in Ventura County), respectively (from left to right); top green bars indicate samples that were used for diurnal profile analysis. **(b)** Time series of AMS factors identified by PMF analysis. The inner pie charts in **(a)** and **(b)** respectively show campaign average compositions of FTIR components and AMS factors. **(c)** Time series of normalized O_3 (normalized by campaign average) mixing ratio. **(d)** Mass fractions of the FTIR combustion factor (red), the biomass burning factor (brown), and the marine factor (blue) during the measurement.

Table 2.1: Campaign average and standard deviation of FTIR-measured OM, FTIR organic functional group concentrations, and AMS-measured OM, sulfate, ammonium, nitrate, and chloride concentrations in μg m^{-3}. Functional group OM mass fractions (for FTIR) and component mass fractions of PM$_{AMS}$ (for AMS) are shown in the parentheses.

FTIR	OM	3.3 ± 1.9
	Alkane	1.5 ± 1.1 (47 %)
	Carboxylic Acid	1.1 ± 0.77 (34 %)
	Hydroxyl	0.40 ± 0.24 (12 %)
	Amine	0.11 ± 0.09 (3 %)
	Non-Acid Carbonyl	0.06 ± 0.21 (2 %)
	Organonitrate	0.07 ± 0.12 (2 %)
AMS	OM	3.9 ± 3.0 (43 %)
	Sulfate	3.1 ± 1.7 (39 %)
	Ammonium	1.0 ± 0.53 (12 %)
	Nitrate	0.43 ± 0.49 (5 %)
	Chloride	0.03 ± 0.05 (0.3 %)

boxylic acid group fraction of 34 % from the submicron FTIR measurement, given the uncertainties and approximations in both methods. There was no measurable difference in the number or mass fraction of carboxylic acid groups in the afternoon particles compared to the morning particles (likely due to the small number of particles (37 in total) that could be analyzed with the limited beamtime available), but the results support the presence of carboxylic acid groups in submicron particles, as expected for SOA formation (Claeys et al., 2007). Further, it is worth noting that acid groups are prevalent throughout the particles, rather than being limited to surface coatings.

The non-refractory particle mass concentration measured by the AMS (which is an estimate of submicron PM and denoted as "PM$_{AMS}$") showed similar variation to the FTIR OM concentration (Fig. 2b), indicating common sources or formation pathways of organic and inorganic compounds. Non-refractory OM (nrOM) was the largest component of PM$_{AMS}$ (43 %). Sulfate concentration was 3.1±1.7 μg m^{-3} and accounted for 39 % of PM$_{AMS}$. Ammonium and nitrate contributed 12 % and 5 % of PM$_{AMS}$, respectively. Only non-refractory species of chloride were measured by the AMS, and these accounted for a negligible amount

Table 2.2: Concentration and composition of PMF factors identified from the FTIR and the AMS measurements. Colors in the pie charts indicate alkane (blue), carboxylic acid (green), hydroxyl (hot pink), amine (orange), and non-acid carbonyl (teal) functional groups. Mass fractions of the factors are shown in the parentheses.

		combustion	biomass burning	marine Origin
FTIR	Concentration (μg m^{-3})	3.0 (62%)	0.88 (18%)	0.97 (20%)
	O/C	0.46	0.48	1.04
	Composition			
AMS	Concentration (μg m^{-3})	2.5 (61%)	1.1 (26%)	0.51 (13%)
	(m/z 44)/OM	26%	5%	2.6%
	(m/z 60)/OM	0.1%	0.1%	0.6%
	(m/z 44)/(m/z 43)	7.5	0.6	1.5
	(m/z 44)/(m/z 57)	146	2.7	3.6

of PM$_{\mathrm{AMS}}$ with a mass fraction of 0.3% (Table 2.1).

The FTIR and AMS-measured OM compared reasonably well as shown in Fig. 2.3. The slope (1.1) and correlation coefficient ($r = 0.7$) of the OM correlation in this study fall into the typical ranges of the FTIR and AMS-measured OM comparison as summarized by Russell et al. (67) from eight previous field campaigns. These values are comparable to the average slope (1.1) and r (0.67) derived from the Scripps Summer 2008 and the Scripps Winter 2009 projects (67). Pearson's correlation coefficient for a reduced major axis regression is used in this study. For samples associated with low sulfate fractions, the trend becomes more scattered from the 1:1 line and the sulfate-based CE has better agreement when sulfate accounts for more than 20% of PM$_{\mathrm{AMS}}$. This is consistent with the fact that the sulfate-based CE used here was developed for ambient samples associated with relatively high sulfate fractions that were about 40% on average (61).

2.3.3 Identification of sources contributing to the organic mass

PMF (57) can be used to separate the contributions of different sources, each with characteristic compositions, to the multi-component mixtures in ambient organic and inorganic particles (58). We applied PMF to the FTIR spectra and
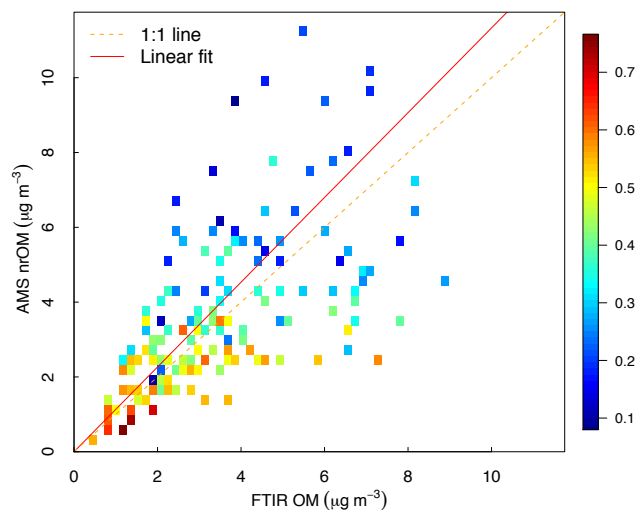
Figure 2.3: Comparison of OM measured by the FTIR and the AMS. Colors indicate sulfate mass fraction of PM_{AMS}. Correlation coefficients for high sulfate mass samples (mass fraction $>20\,\%$) and low sulfate mass samples (sulfate fraction $<20\,\%$) are 0.8 and 0.6, respectively.

the AMS-measured organic fragment concentrations separately to identify robust, linearly-independent components that compose the OM (45, 66).

Identification of the factors is described in detail in Appendix A. The factor composition and concentration are summarized in Table 2.2. In brief, a combustion factor, a biomass burning factor, and a marine-derived factor were identified from both the FTIR and the AMS PMF analyses, representing fossil fuel combustion, biomass burning, and marine sources, respectively. The reconstructed OM (the sum of the three factors) from the FTIR and the AMS PMF analyses correlated with $r = 0.7$ and a slope of 1.1 (with the FTIR OM $10\,\%$ higher). The combustion factors dominated the OM (approximately $60\,\%$) from both analyses (Tables 2.2 and 2.3) and the time series correlated to each other with $r = 0.5$ and a slope of 1.2 (FTIR factor OM was $20\,\%$ higher). The large fraction of carboxylic acid groups in the FTIR combustion factor ($42\,\%$) and the dominance of m/z 44 ($26\,\%$ of OM) in the AMS combustion factor suggest that the combustion factors represent photochemically processed products of vapor emissions, most likely from the Los Angeles and Long Beach regions. The biomass burning factors resulting from the FTIR and the AMS measurements correspond to the three largest

fires occurred in Southern California during the sampling period: the Station fire (in Los Angeles County), the La Brea fire (in Santa Barbara County), and the Guiberson fire (in Ventura County). The FTIR and AMS biomass burning factors correlated with $r = 0.7$ and slope $= 0.9$ (FTIR factor OM was 10% lower). The OM fractions of the two biomass burning factors agreed with less than 10% difference, well within the expected accuracies of both FTIR and AMS OM. The two marine factors correlated to each other with $r = 0.5$, with the FTIR factor OM higher by a factor of 2.1. The weaker correlation and the lower mass of the AMS marine factor may be caused by a low transmission efficiency for organic compounds on NaCl particles as well as a lack of marine-aerosol specific fragments in the AMS measurements. Alternatively it could result from lower absorptivity of carbohydrate hydroxyl groups relative to the hydroxyl standards employed in the quantification algorithm (66). In summary, the factors identified by PMF analyses of the FTIR and the AMS measurements agreed well and the mass differences were within 30% for the total OM, the combustion factors, and the biomass burning factors. The good agreement shows the consistency of the measurements and the robustness of the identified factors.

2.3.4   Diurnal cycles of organic and inorganic components

Diurnal variations of organic functional groups, organic and inorganic mass fragments, and the PMF factors are discussed in this section. For the diurnal cycle analyses, the concentrations were normalized by the enhancement of carbon monoxide (ΔCO) mixing ratio (with respect to the background or unpolluted CO mixing ratio measured at the site during the study) for the FTIR and the AMS measurements. This background CO mixing ratio was determined as the y-intercept of the linear regression of CO versus OM (11), which differed slightly for the FTIR OM and the AMS nrOM at 89 ppb and 80 ppb, respectively. The difference of the two intercepts results from the larger AMS nrOM (10% higher than the FTIR OM). Since the difference of the two intercepts is small relative to the ambient variations (which had a standard deviation of 71 ppb), an average value of 85 ppb was used as the background CO mixing ratio for both the FTIR and
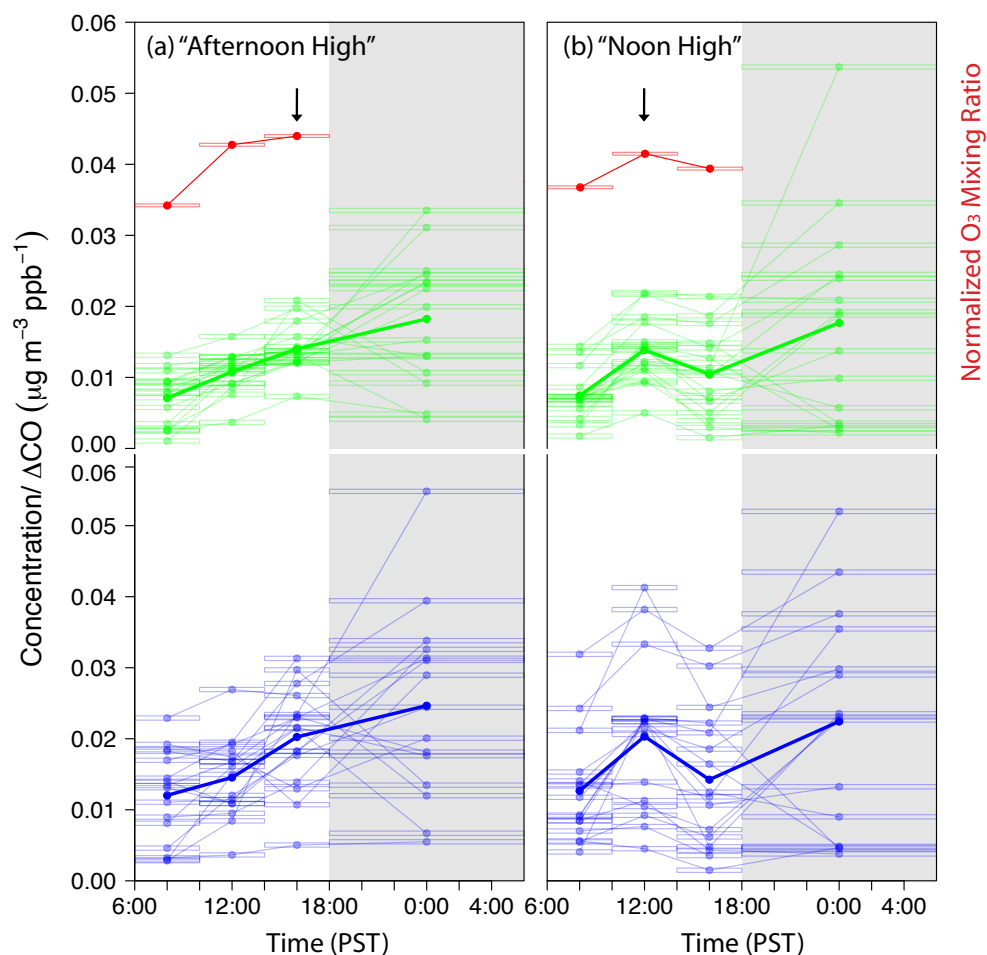
Figure 2.4: Diurnal cycles of normalized carboxylic acid group concentrations (green; top part in each panel) and alkane group concentrations (blue; bottom part in each panel) divided into **(a)** "Afternoon High" and **(b)** "Noon High" types. Each rectangle represents one FTIR sample with the length of the rectangle indicating the sampling duration. The lines connecting the rectangles show samples collected in the same day. The thinner rectangles and lines represent daily diurnal profiles, while the thicker lines show the averages for the days in the corresponding panel. The red dashed lines represent average diurnal profiles of normalized O_3 mixing ratio for the days in each panel. The arrows indicate daytime peak concentration in each panel. Shaded areas indicate nighttime periods corresponding to the FTIR nighttime samples, which were excluded from the diurnal cycle analyses.

the AMS measurements. Normalizing the concentration by ΔCO, which does not react significantly on timescales of a few days, is used to separate the variations caused by the change of combustion source strength and effective dilution rates with variable meteorological conditions (which vary with ΔCO) from changes associated with aerosol processing in the atmosphere (which do not vary with ΔCO) (9, 10, 23, 12).

2.3.4.1 Diurnal cycles of carboxylic acid and alkane group concentrations

Diurnal profiles of normalized carboxylic acid group concentrations are classified into the "Afternoon High" and the "Noon High" types (Fig. 2.4). Both types show higher concentrations at local noon (solar maximum) relative to the early morning period, but they differ in whether the concentration peaked at noon or after noon: the "Afternoon High" type days (type A) have peak concentrations in the afternoon and "Noon High" type days (type B) have peak concentrations at noon. For days within each type, nighttime carboxylic acid group concentrations were variable, with concentrations that were sometimes higher and other times lower than the noon and afternoon values. The variability in concentration at night is likely the result of variations in the land-sea breeze circulations, as illustrated in Fig. 2.13. Winds coming from the northwest dominate during daytime, and easterlies dominate at night. The variability in nighttime concentrations within each type likely resulted from different air masses brought by the nighttime easterlies. In contrast, there was no evidence for impacts on daytime concentrations from variable sea breezes during the day, consistent with the nearly constant northerly winds shown in Fig. 2.13 for all days selected for this study. For this reason, our analysis has focused only on the daytime measurements, when the constant wind direction provided a consistent source and nearly constant transport times for emissions from the ports of Los Angeles and Long Beach. This consistency of back trajectories also made the time series measurements effectively pseudo-Lagrangian. The resulting daytime alkane group profiles (for the same samples as in Fig. 2.4) resemble and correlate in time with carboxylic acid group

concentrations (Fig. 2.4), indicating alkane and carboxylic acid groups were likely part of the same molecules, forming and condensing at the same time.

The daytime variations of carboxylic acid group concentrations track the O_3 mixing ratios (Fig. 2.4), suggesting that the maximum in acid formation results from O_3-driven oxidation (rather than OH-driven). A correlation of carboxylic acid groups with odd oxygen $(O_3 + NO_2)$ may be stronger than O_3 alone (31), but the NO_2 measurements were not available in this study. The atmospheric O_3 mixing ratio is affected by a number of parameters, including meteorological variables such as solar intensity, temperature, and RH and gas-phase chemical compositions such as NO_x, VOCs, and other factors (44, 48, 79). There was no consistent difference in the variations and magnitudes of meteorological conditions, including temperature, ambient RH, wind direction and speed, and photosynthetically active radiation between the "Afternoon High" and "Noon High" days, suggesting that the peak time of O_3 mixing ratio was likely affected by other parameters, such as NO_x and VOC mixing ratios (which were not measured at the pier site).

2.3.4.2 Diurnal cycles of AMS measured components

Figure 2.5 shows diurnal profiles of the AMS-measured fragment m/z 44 and the AMS combustion factor divided into the "Afternoon High" and the "Noon High" days. Fragment m/z 44, which is CO_2^+ and representative of highly oxygenated organic components, tracked well with the AMS combustion factor. These two components followed similar patterns to the acid and alkane groups, peaking in the afternoon (14:00–18:00 PST) in the "Afternoon High" days and between noon and afternoon (10:00–14:00 PST) in the "Noon High" days. The daytime peaks of m/z 44 and the combustion factor indicate enhanced SOA formation during the day (8). Carboxylic acid group concentration correlated well with m/z 44 and the AMS combustion factor concentrations for both "Afternoon High" and "Noon High" type days (Fig. 2.6), with the latter having better correlation coefficients of both carboxylic acid groups to m/z 44 and to the combustion factor $(r = 0.8)$ but similar slopes. The correlation of carboxylic acid groups and m/z 44 indicates that for these organic compositions, carboxylic acid groups and m/z 44 were likely

associated with the same molecules and same formation mechanisms.
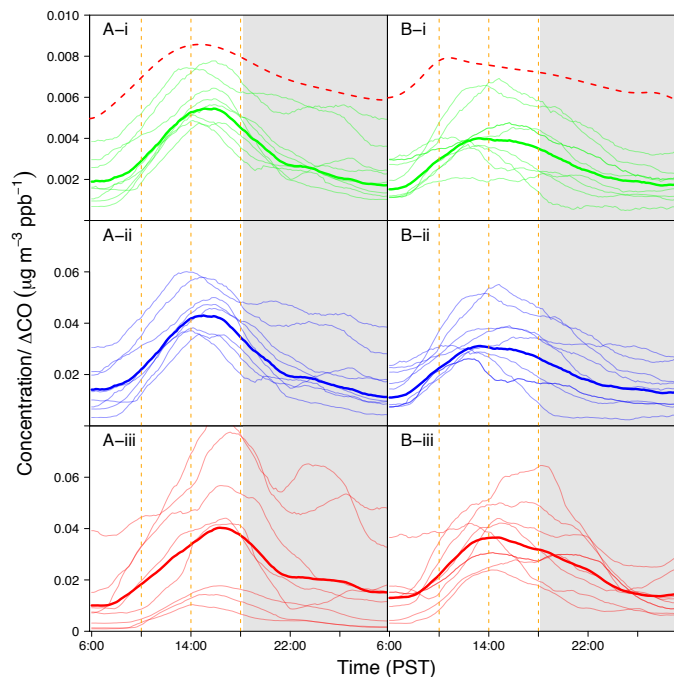
Figure 2.5: Diurnal cycles of (i) m/z 44, (ii) the AMS combustion factor, and (iii) sulfate for **A** ("Afternoon High") and **B** ("Noon High") days. The thinner lines represent daily diurnal cycles and the thicker lines represent the averages. The red dashed lines are average diurnal profiles of normalized O_3 mixing ratios for **A** ("Afternoon High") and **B** ("Noon High") days. The curves (except for O_3) are smoothed using the "Boxcar Smoothing" method with 30-point averaging to reduce high-frequency noise in the measurements. Shaded areas indicate nighttime periods.

The average diurnal pattern of sulfate is nearly the same as that of m/z 44, the AMS combustion factor (Fig. 2.5), and the carboxylic acid groups. However, there is no correlation of sulfate and carboxylic acid group concentrations ($r = 0.1$) both for all time-resolved samples and for daily averages. The similarity of the diurnal patterns and the poor correlation of sulfate and carboxylic acid groups suggest that OH radicals contribute to the formation of both components but that the magnitude of the sulfur and combustion emissions that produce the particles are emitted by different sources. The magnitude of the average daily sulfate concentration shows more variability than the OM concentrations. Dominguez et al. (2008) found that 44 % of the non-sea-salt sulfate in fine particles during a

previous study at the same Scripps pier site could be attributed to sulfate from SO_2 emitted by ships. However, ship traffic is likely more variable than the OM emissions associated with the urban and port (trucking) activities.
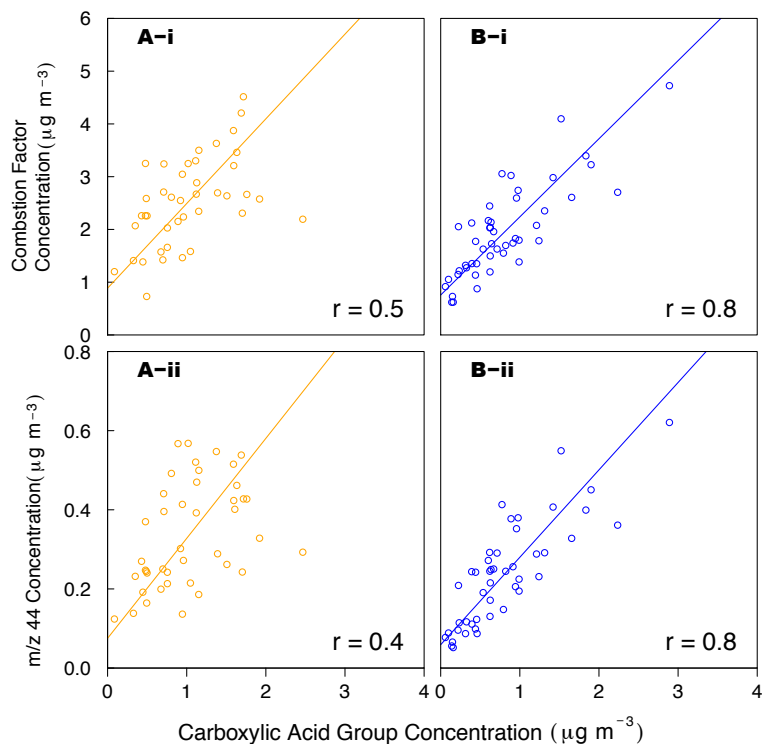
Figure 2.6: Mass concentration correlation of carboxylic acid groups with (i) the AMS combustion factor and (ii) m/z 44 for **A** ("Afternoon High") and **B** ("Noon High") days. The correlation coefficients are shown in the legends.

2.3.4.3 Diurnal cycles of components in single particles

To evaluate evidence for photochemical processing in single particles, the average X-ray absorption spectra of single particles are shown in Fig. 2.7. Twenty-one morning particles and sixteen afternoon particles (collected on the same days as the morning particles) were analyzed. The afternoon-particle spectrum was characterized by a flat and broad black carbon peak at 285 eV, a broad peak ranging from 287 to 289 eV (peaks at 288.7 eV) indicative of alkane (the shoulder at 287.7 eV) and carboxylic acid (288.7 eV) functional group absorption, a carbon-

ate peak at 290.4 eV, and two potassium peaks at 297.4 and 299.9 eV (Russell et al., 2002). These spectra are comparable to the spectrum of $CaCO_3$ (30) except for the carboxylic acid group absorption, suggesting that some carboxylic acid groups may condense on marine particles originating from marine calcareous phytoplankton (30) when air masses passed over the ocean. Compared to the afternoon spectrum, the morning spectrum had a narrower and sharper black carbon peak with more variations at all energies. The graphite content of particles is represented by calculating the $\%sp^2$ hybridization for each particle (77). Morning particles were associated with greater $\% sp^2$ hybridization than afternoon particles at a 84 % confidence level, indicating morning particles were more influenced by primary emissions that likely included black carbon cores.
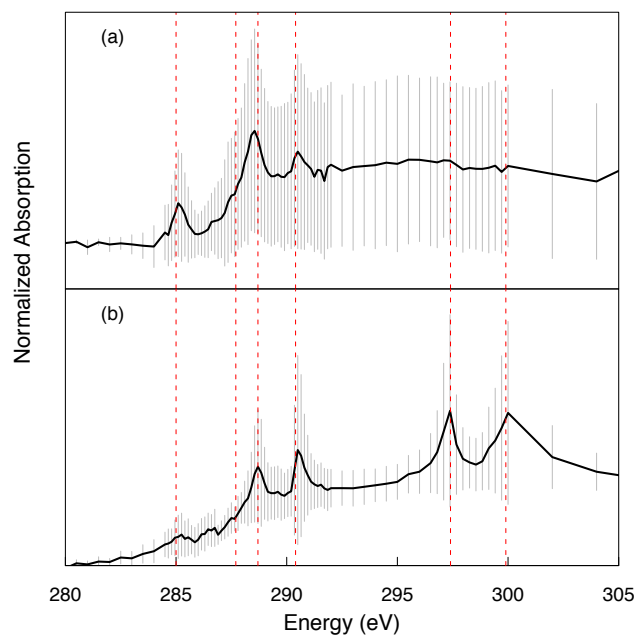
Figure 2.7: Average X-ray spectra of **(a)** twenty-one morning and **(b)** sixteen afternoon particles. Grey vertical bars indicate the standard deviations of absorption at corresponding energies. Red vertical lines indicate alkene group (285 eV), alkane group (287.7 eV), carboxylic acid group (288.7 eV), carbonate (290.4 eV), and K (297.4 and 299.9 eV) absorptions.

2.4 Discussion

In this section, we identify the fraction of the measured organic mass that is secondary. We start with the approach that is implicit in a number of recent studies (summarized in Table 2.4), namely that oxygen-containing organic components that are from fossil fuel combustion emissions, and the other (non-oxygen-containing) organic components that co-occur with them, are secondary. Special attention is given to carboxylic acid functional groups, as they are the canonical low-volatility products of photochemical oxidation of hydrocarbons (Haagen-Smit, 1952). Next, we use the assumption of a Lagrangian evolution of the air mass and the availability of daytime sunlight to separate the OM that is produced in a single day of photochemical reactions. Accounting for the expected multi-day lifetime of SOA, we then compare the two different approaches to quantifying SOA. Finally, we note that marine and terrestrial primary biogenic oxygen-containing organic components need to be excluded from both of these estimates, which is possible using PMF separation and tracers for marine production.

2.4.1 SOA identification by chemical composition: contributions of acid groups and oxygenated organic fragments

Several studies of tropospheric carboxylic acids (Table 2.4) proposed that carboxylic acids are formed in the atmosphere, based on observed correlations of carboxylic acids to solar radiation or ozone mixing ratio. These methods of SOA identification are supported by model predictions and smog chamber studies that predicted or measured the formation of carboxylic acids (Madronich et al., 1990; Grosjean et al., 1992; Yu et al., 1999). Although direct emission of carboxylic acids (molecules) was also associated with vehicular exhaust (Kawamura and Kaplan, 1987) and meat cooking (Rogge et al., 1991), the lack of correlation of carboxylic acids with tracers from these emissions suggests that the contributions from these primary sources are minor. In addition to carboxylic acid groups, other oxygenated groups (e.g. hydroxyl groups and non-acid carbonyl groups) were identified in smog

Table 2.3: Mass concentration and OM fraction of "Total SOA" (estimated from the "chemical-composition" based method) and "Today's SOA" (estimated from the "pseudo-Lagrangian" based method) calculated from carboxylic acid groups, the FTIR combustion factor, and the AMS combustion factor for the "Afternoon High" and the "Noon High" days.

"Afternoon High" Days	Concentration (μg m^{-3})		Fraction of total OM	
	Total SOA	Today's SOA	Total SOA	Today's SOA
Carboxylic Acid Group	1.2	0.3	36 %	9 %
FTIR Combustion Factor	2.9	1.0	60 %	20 %
AMS Combustion Factor	2.5	1.1	61 %	27 %
"Noon High" Days	Concentration (μg m^{-3})		Fraction of total OM	
	Total SOA	Today's SOA	Total SOA	Today's SOA
Carboxylic Acid Group	1.0	0.3	30 %	10 %
FTIR Combustion Factor	3.0	0.7	62 %	14 %
AMS Combustion Factor	2.1	0.8	51 %	19 %

chamber studies (Kleindienst et al., 2004; Sax et al., 2005; Lim and Ziemann, 2005). The common conclusion in these studies is that for most urban sources, the oxygenated fraction of OM is secondary. Using this assumption (that highly oxygenated OM is SOA), these recent studies in a variety of urban and rural regions have found that 50–100 % of the OM measured was SOA (Table 2.4).

Similarly, if we take this approach to identifying SOA in the Scripps Pier measurements (which were dominated by urban emissions from Los Angeles), we find that the fossil fuel combustion factor is likely secondary, given its high fraction of carboxylic acid groups and associated high O/C. This result gives an average "Total SOA" for this study of 60 % of the OM, well within the range of these other measurements. Since we have specifically separated out the 40 % of OM from non-urban sources (biomass burning and marine OM), it is not surprising that we are at the low end of the 50 to 100 % range given in Table 2.4 (since the studies that reported higher SOA fractions had low non-urban contributions to OM). Furthermore, we can look specifically at what fraction of the SOA is actually acid groups: the "Total SOA" estimated from carboxylic acid groups was 34 % of OM, namely half of the SOA (by mass) is carboxylic acid groups.

Table 2.4: Comparison of SOA mass fractions in this study with previous studies. Quantities include (1) OM fraction (PM fraction if specified) of "Total SOA", (2) OM fraction of "Recent SOA" (SOA formed within 1 day or 2 days), (3) OM fraction of "Background SOA", (4) OM fraction (PM fraction if specified) of carboxylic acid (groups), and (5) fraction of "Recent SOA" in "Total SOA".

Reference	Total SOA	Recent SOA	Background SOA	Carboxylic Acid (Groups)	Fraction of Recent SOA in Total SOA	Method of Identification of SOA
Schuetzle et al. (1975)[1,2]	4 %	–	–	3 %	–	correlation of acids with solar radiation
Cronn et al. (1977)[1,2]	9 %	–	–	6 %	–	correlation of acids with solar radiation
Satsumabayashi et al. (1989)	–	–	–	–	–	correlation of acids with ozone
Satsumabayashi et al. (1990)[1,3]	30–50 %	22–42 %	58–78 %	30–50 %	72–84 %	correlation of acids with ozone
Kawamura and Ikushima (1993)[1,2]	–	–	–	0–1 %	–	correlation of acids with ozone
Rogge et al. (1993)[1]	–	–	–	15–19 %	–	correlation of acids with solar radiation
Kawamura and Yasui (2005)[1,2]	–	–	–	0–1 %	–	correlation of acids with solar radiation
Gilardoni et al. (2007)	50 %	–	–	31 %	–	high O/C component
Lanz et al. (2007)	60–69 %	–	–	–	–	high O/C component
Zhang et al. (2007b)	64–95 %	–	–	–	–	high O/C component
Russell et al. (2009a)	70 %	–	–	31 %	–	high O/C component
Hildebrandt et al. (2010)	nearly 100 %	–	–	–	–	high O/C component
Liggio et al. (2010)	75–95 %	40–50 %	35–45 %	–	42–71 %	high O/C component and phothchemcial age
This study	60 %	15–30 %	30–45 %	34 %	25–50 %	high O/C component and correlation of acid groups with ozone

[1] The mass fractions are calculated using a limited number of measured species.

[2] The numbers indicate PM fractions.

[3] The SOA in this study is assumed to be composed of carboxylic acids only.

2.4.2 SOA identification by pseudo-Lagrangian observations: daytime formation of carboxylic acid groups and oxygenated organic fragments

An alternative way to estimate SOA mass fraction is to assess the amount of additional OM formed during the sunny part of a single day. This approach requires measurements in a pseudo-Lagrangian framework, where we can infer that the photochemical exposure (aging) of the emissions tracks with the time of day. In this case, the majority of the volatile organic compounds (VOCs), in particular those from fossil fuel combustion, was emitted in the Los Angeles – Long Beach region. Further, the transit from that emission point to the Scripps Pier was largely over clean marine regions with small OM sources (as in Hawkins and Russell, 2010a). The other aspect of this study region is that northwesterly flow predominated in daytime, thus also providing sufficient regional homogeneity on the selected days, as illustrated by the day-to-day similarities in Figs. 2.4 and 2.5.

With this pseudo-Lagrangian approach, we can identify SOA more specifically using the dependence on sunlight and oxidants during a single day, separating SOA into "Background SOA" (formed on prior days) and "Today's SOA" (formed during a 12-h daytime period of one particular day). In this calculation, "Today's SOA" contributions from carboxylic acid groups and the combustion factors are both estimated by assuming that the minimum concentration that occurs in the early morning is representative of a background value (the "Background SOA" from formation on previous days) and that the increase that occurs (relative to ΔCO) is from photochemical processing during one specific 12-h daytime (Fig. 2.8). Since only the combustion factor is accounted for in this calculation, this method estimates only the portion of "Today's SOA" from fossil fuel combustion.

To evaluate the time scale of carboxylic acid group formation, we evaluate the lag time between the peak concentrations in O_3 and either m/z 44 or the AMS combustion factor. The peak concentrations of m/z 44 and the AMS combustion factor occurred approximately 1–2 h later than the O_3 peak for both the "Afternoon High" and the "Noon High" type days (Fig. 2.5), suggesting that the time scale
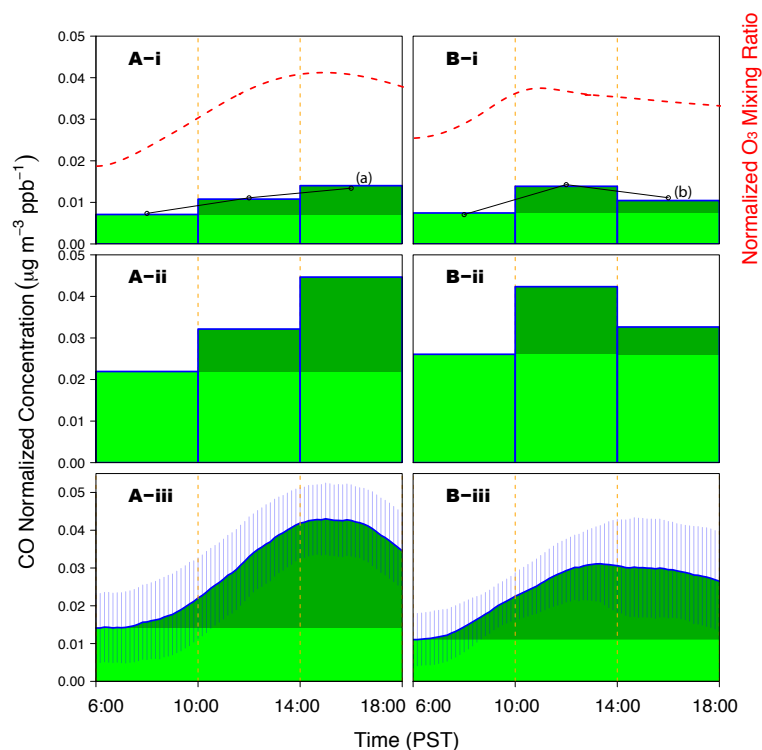
Figure 2.8: Daytime profiles of **A** ("Afternoon High" days) and **B** ("Noon High" days) for (i) carboxylic acid groups, (ii) the FTIR combustion factor, and (iii) the AMS combustion factor concentration. Colors indicate "Background SOA" (light green) and "Today's SOA" (dark green), respectively. Red dashed lines in panels **A**-i and **B**-i represent average daytime profiles of normalized O_3. Black lines in panels **A**-i and **B**-i are the average diurnal carboxylic acid group profiles corresponding to the two panels shown in Fig. 2.4 as indicated by the labels beside the lines. Vertical blue bars in panels **A**-iii and **B**-iii show standard deviations of the averaged diurnal cycles.

for the formation of m/z 44 and the AMS combustion factor is 1–2 h. The good correlations of carboxylic acid groups to m/z 44 and the AMS combustion factor throughout this study allow us to infer that carboxylic acid group formation also had a time scale of 1–2 h (although a direct observation of the lag is not possible, given the 4-h duration of the FTIR daytime samples, as shown in Fig. 2.4).

2.4.3 SOA identification by size dependence: surface -limited condensation of oxygenated organic fragments

The size dependence of the organic components provides additional evidence of how the SOA formed. Representative size distributions of m/z 44 and the AMS nrOM are shown in Fig. 2.9 for the "Afternoon High" days (for time period of 14:00–18:00 PST) and the "Noon High" days (for time period of 10:00–14:00 PST). For both cases, m/z 44 and nrOM showed similar size distributions with peaks at 300–500 nm, indicating the two components were internally mixed in the particle phase, consistent with the results of the FTIR PMF which associated acid and alkane groups in the combustion factor. The m/z 44 fraction of OM was nearly independent of particle size, while $nrOM/PM_{AMS}$ decreased with increasing particle diameter, consistent with theoretical models in which acid and alkane groups are added proportionally so give a constant ratio with size (Fig. 2.9iii), and the total amount of OM increases relative to the particle mass giving a dependence on the reciprocal of the diameter (Fig. 2.9iv). This result differs slightly from the model presented by Maria et al. (2004), in which the proportionality of added acid and alkane groups is masked by pre-existing distributions of POA carbon. In this study, the degree and consistency of oxygenation of the fossil fuel combustion fraction (noted in Sect. 4.1) indicates that there was likely no significant mass fraction of preexisting POA.

Single particle analysis using STXM-NEXAFS provides additional information on the size dependence of SOA formation, including specific identification of carboxylic acid groups. The resulting size dependence of OM/PM decreases with increasing size, similar to Fig. 2.9iv, but the small number of particles analyzed (37) is insufficient to justify more than a linear fit (with $r = -0.6$). Interestingly, the size dependence of the acid group fraction of OM increased with increasing size, indicating a possible difference from the $(m/z$ 44)/OM results (such as non-acid contributions to m/z 44). However, the variability in the acid fraction for the five different sampling days that were included in these 37 analyzed particles
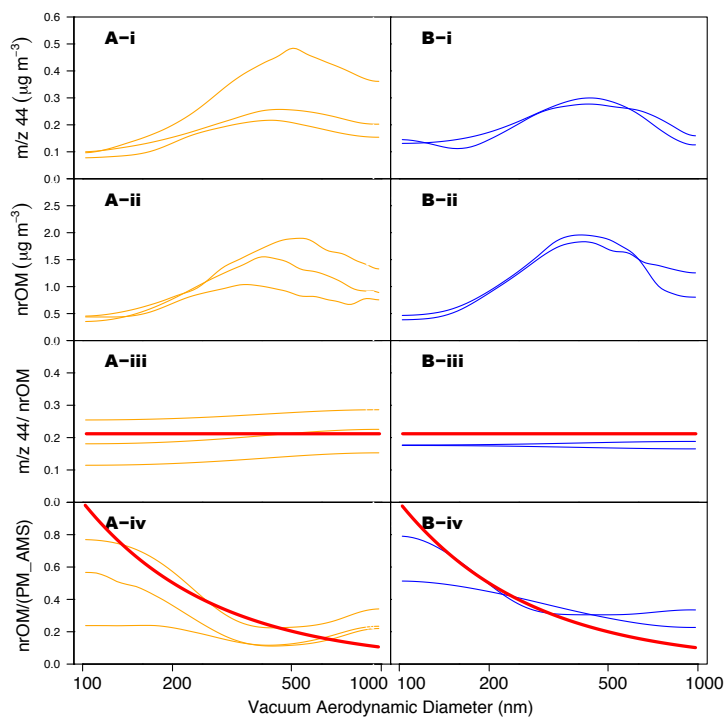
Figure 2.9: Representative size distributions for **A** ("Afternoon High" days) on 12, 16, and 21 September, in time period 14:00–18:00 PST and **B** ("Noon High" days) on 17 and 20 September in time period 10:00–14:00 PST for (i) m/z 44, (ii) nrOM, (iii) $(m/z$ 44)/nrOM, and (iv) nrOM/PM$_{AMS}$. The ratios $((m/z$ 44)/nrOM and nrOM/PM$_{AMS}$) were calculated for each size bin then plotted versus particle size. The curves are smoothed with the "Boxcar Smoothing" method with 20-point averaging and wavelet de-noising method to reduce high-frequency noise in the measurements. Red lines are theoretical models representing (iii) constant with respect to particle diameter and (iv) inversely proportional to the particle diameter (1/Dp), for comparison to results of Maria et al. (52).

was greater than the dependence on size, suggesting that the aggregation of five samples (each 15–30 min duration) may not be appropriate. Since we also did not have sufficient AMS signal to obtain a size distribution in 30 min of sampling, it is not possible to rule out other factors.

2.4.4   Comparing SOA identification methods

The three SOA identification methods were employed independently using three independent types of OM measurements (FTIR, AMS, STXM-NEXAFS)

to characterize SOA, so it is worth assessing the extent to which the resulting characterizations are consistent. The "chemical composition" method was used to quantify the SOA mass and fraction based on the oxygenated nature of the organic associated with fossil fuel combustion tracers (summarized in Table 2.4). The pseudo-Lagrangian method was used to identify the daytime formation of "Today's SOA" (Table 2.3 and 2.4). The "size-dependence" method was used to identify how SOA was formed in the particle phase.

Comparing the two quantitative approaches to SOA, we find from the "chemical composition" method that 60 % of OM is SOA. From the "pseudo-Lagrangian" method, we find that 15–30 % of OM is "Today's SOA." Combining these two results, we find that 25–50 % of SOA is formed each day (on average). This finding is consistent with the expected boundary layer lifetime of particles of 4–5 days, suggesting that the submicron SOA remains on average 4 days (less for the upper bound value of 50 %, more after accounting for losses).

There are two previous studies that have separated recent SOA from background SOA (Table 2.4). The "Background SOA" fraction used here is analogous to the "Background OA" estimated by Liggio et al. (2010) from measurements at Egbert, Ontario (Table 2.4), except that rather than looking only at "Today's SOA" Liggio et al. (2010) evaluated the SOA formed within 24–48 h. Their estimate for that central Canadian region was 42–71 % of the "Total SOA" (40–50 % of the total OM), which overlaps the range of the "Today's SOA" fraction of 25–50 % of the "Total SOA" (15–30 % of the total OM) estimated from the combustion factors found for the coastal region in this study. The median value of the Liggio et al. (2010) range of 56 % is about 50 % larger than the median value of the "Today's SOA" range of 38 % found here, which is consistent with the fact that their time period for "recent" formation was twice as long (and that different sites have different mixtures of sources), the estimates are well within the expected consistency.

We can also look specifically at the acid fraction formed today, which here was found to be 25–33 % of the total acid group concentration. Satsumabayashi et al. (1990) found that in central Japan "Today's acid (molecule)" fraction was 72–
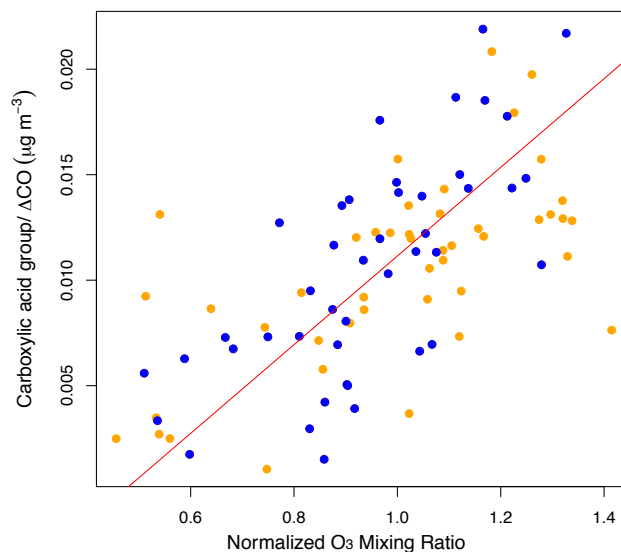
Figure 2.10: Correlation of normalized carboxylic acid group concentration and normalized O_3 mixing ratio (by campaign average) for the "Afternoon High" (orange) and "Noon High" (blue) days. The correlation coefficient is 0.7.

84 % of the "Total acids (molecules)." However, the pseudo-Lagrangian approach used in Satsumabayashi et al. (1990) was limited to measurements of only two commonly-observed acids, i.e. succinic acid and phthalic acid, and their emissions in central Japan are quite high.

Taking the results of all three approaches together, the co-variation of daytime concentrations and the correlation of overall concentrations ($r = 0.7$) of carboxylic acid groups and O_3 (Figs. 2.4 and 2.10) provide substantial evidence for an O_3-driven oxidation that forms carboxylic acid groups. The carboxylic acid, hydroxyl, non-acid carbonyl, and alkane group mole fractions of the combustion factor were 0.11, 0.04, 0.00, and 0.85, comparable to the C_{12} alkane (molecule) oxidation products with mole fractions of 0.12, 0.13, 0.02, and 0.73 estimated by Russell et al. (2011). In the mechanism proposed by Russell et al. (2011), gas-phase alkanes (molecules) are oxidized by OH radicals to form dihydrofuran in the particle phase by H-atom subtraction, isomerization, cyclization, and dehydration processes. Dihydrofuran then evaporates into the gas phase and reacts primarily with O_3 to form acid groups – since there is little evidence for carboxylic acid formation from OH oxidation (Russell et al., 2011; Martin et al., 2002), produc-

ing products that are expected to be similar to cyclic alkene oxidation products, namely multi-functional products with carboxylic acid functional groups (which would be expected to partition into the particle phase due to their low vapor pressures). This mechanism is consistent with the observed SOA composition (for the combustion factor) in this study and the co-variation of carboxylic acid and alkane groups. Combining this information with the size dependence of oxygenated mass fragments (m/z 44) supports the hypothesis that these two functional groups were likely formed in the same molecules in the gas phase and condensed simultaneously on particles as second-generation products of gas-phase alkane (molecule) oxidation.

2.4.5 Sources and characteristics of hydroxyl functional groups

Hydroxyl functional groups were mainly from marine sources, since their variation was uncorrelated with the AMS and FTIR combustion factors. Larger contributions from the hydroxyl groups and hence the marine factor were associated with onshore winds from 07:00 to 22:00 PST (compared to the offshore-wind concentrations at night), which could bring concentrated marine aerosols to the sampling site, indicating the hydroxyl functional group concentration was modulated by the land-sea breeze circulation at the coastal site. This land-sea breeze effect was not observed for the fossil fuel combustion factors, which dominated the OM. The marine factor concentration weakly correlated with local wind speed ($r = 0.3$ during onshore winds), consistent with the expected increase in particle production from wind-related bubble bursting on the ocean surface (68) but sufficiently influenced by other variables to mask a one-to-one link. This marine-derived origin of hydroxyl groups indicates that hydroxyl groups are likely dominated by primary emission, especially at coastal regions. This primary contribution was excluded in the SOA mass estimation.

2.5   Conclusions

Measurements at the Scripps Pier show that OM accounted for nearly 50 % of ambient submicron particle mass. The OM was dominated by a fossil fuel combustion factor with a high oxygen-to-carbon ratio. This factor likely represented SOA products formed from fossil fuel emissions from Los Angeles and Long Beach regions, suggesting the "Total SOA" accounted for 60 % of the total OM, with 42 % from acid groups and 51 % from alkane groups. Based on the recurrence of diurnal cycles of the combustion factor and carboxylic acid groups, the "Total SOA" was further separated into "Today's SOA" (formed in the 12-h daytime of a single day) and "Background SOA" (formed on prior days) using a pseudo-Lagrangian approach. In this calculation, the fraction of the combustion factor OM that formed as "Today's SOA" accounted for 25–50 % of the "Total SOA" and 15–30 % of the total OM, while the "Background SOA" contributed to 30–45 % of the total OM, which likely represented the SOA formed in the previous 1–3 days. Similarly, carboxylic acid groups formed as "Today's SOA" accounted for 25–33 % of the total carboxylic acid groups and 10 % of the OM. The SOA was likely formed through surface-limited condensation processes, as suggested by the size dependence of $nrOM/PM_{AMS}$ (decrease with an increase in particle size). In addition, the independence of $(m/z\ 44)/nrOM$ on particle size suggests that particle-phase $m/z\ 44$ (and likely carboxylic acid groups) and other organic components (largely alkane groups) were formed and condensed simultaneously.

The daytime increase of carboxylic acid groups and the combustion factor mass concentration closely correlated with the O_3 mixing ratio, indicating the SOA formation was likely driven by O_3. Moreover, the composition of the SOA (the combustion factor) was consistent with the O_3-driven gas-phase alkane (molecule) oxidation mechanism proposed by Russell et al. (2011), suggesting carboxylic acid and alkane groups are second-generation products (of gas-phase alkane (molecule) oxidation) formed in the same molecules, consistent with the observed co-variation of these two functional groups in the particle phase size distribution. This large contribution of gas-phase alkane (molecule)-derived SOA is not surprising given their large contributions to VOC emissions in the Los Angeles-Long Beach source

region and the relative absence of significant additional organic precursors during transit in the coastal marine boundary layer. This study indicates the importance of gas-phase alkane (molecule) photochemistry for the air quality of regions downwind of large emission sources.

2.6   Appendix

2.6.1   PMF analysis of the FTIR and the AMS measurements

2.6.1.1   PMF of the FTIR spectra

PMF was applied to the 234 mass-weighted and baselined FTIR spectra. The scaling factors were estimated by baselining errors calculated using the automated algorithm described by Russell et al. (66). The robust mode was used and the outliers were downweighted during the fitting procedure. Two to six factors with an FPEAK range of (0, ±0.2, ±0.4, ±0.6, ±0.8, ±1) were tested. Plotting Q (the sum of squared scaled residuals) versus FPEAK showed that the lowest Q values corresponded to FPEAK of -0.2, 0, and 0.2, which resulted in the same factors. The edge-FPEAK values (±0.6, ±0.4, ±0.8, and ±1) resulted in increased Q values, indicating increased residuals associated with the PMF model (45). Because the sensitivity to rotation was negligible for FPEAK $= -0.2$, 0, and 0.2, FPEAK $= 0$ was selected to represent the solution.

Q can also be used as a mathematical diagnostic of the PMF solutions. Q/Q_{exp} (normalized Q), in which Q_{exp} approximately represents the degree of freedom of the fitted data, is greater than 4 for the two- and three-factor solutions and smaller than 3 for the $n > 3$ solutions (Fig. 2.12). This decrease of normalized Q indicates that the additional factors in the $n > 3$ solutions explain significantly more variation of the data. Therefore, two- and three-factor solutions were excluded.

Factors that correlated ($r > 0.5$) with similar compositions were identified in the four-, five-, and six- factor solutions, indicating some factors that split into

indistinguishable and non-independent components (84). The correlated factors in each solution were combined to one factor, resulting in three factors for each of the four-, five-, and six-factor solutions. The combined factors explain the same degree of the OM variability as the individual factors used from the four-, five-, and six-factor solutions, and the combined factor mass is equal to the sum of individual factor masses. The three recombined factors resulting from the six-factor solution were selected because these factors captured events that were associated with trajectories from either known wildfires or from Los Angeles-Long Beach ports. In addition, the factor profiles had similar peak structure ($r > 0.8$) with the known factors derived from the TEXAQS/GoMACCS 2006 and the Scripps Pier 2008 measurements (29, 66).

The factors were identified by comparing factor spectrum and composition with previously identified factors. The first factor spectrum correlated to the fossil fuel combustion factor profiles of the TEXAQS/GoMACCS (66) and the Scripps Pier 2008 measurements (29) projects with r of 0.97 and 0.99, respectively, indicating similar organic compositions from similar sources or processes. This factor was characterized by large fractions and co-existence of alkane and carboxylic acid functional groups (51 % and 42 % of the factor OM, respectively) and was identified as a fossil fuel combustion factor. The concentration of this factor was 3.0 μg m^{-3}, accounting for 62 % of the OM on average (Fig. 2.2c). Hydroxyl and amine functional groups contributed 7 % and 1 % of the factor OM, respectively. The PSCF image (Fig. 2.11a) shows the origin of this factor was mainly located at the vicinity of the Los Angeles region, which are dominated by fossil fuel combustion emissions. The second factor spectrum correlated to the biomass burning factor profiles identified from the TEXAQS/GoMACCS (66) and the Scripps Pier 2008 measurements (29) with r of 0.87 and 0.93, respectively. The factor fraction time series (Fig. 2.12c) showed three high concentration periods: 26 August–2 September, 8–22 August, and 22–27 September, corresponding to the three largest fires (by acreage) that occurred in the Southern California region that summer: the Station fire (in Los Angeles County), the La Brea fire (in Santa Barbara County), and the Guiberson fire (in Ven-

tura County), respectively (`http://www.fire.ca.gov/fire_protection/fire_protection_fire_info_redbooks_2009.php`). The PSCF image (Fig. 2.11b) indicates that this factor is likely from north of Los Angeles - Santa Barbara County, as well as Baja California regions, consistent with fire events that occurred during the sampling period and fire maps from satellite measurements (Fig. 2.11c). Based on the similarity of this factor spectrum to previously identified biomass burning factors and the increase in concentration during fire-influenced time periods, this factor was identified as a biomass burning factor. The factor concentration was 0.88 μg m^{-3} on average and accounted for 18% of the OM. Non-acid carbonyl and alkane functional groups dominated this factor, accounting for 44% and 34% of the factor OM, respectively. The factor spectrum of the third factor was comparable ($r = 0.82$) to the spectrum of the polluted marine factor described in the Scripps Pier 2008 measurements (29). This factor was identified as a marine factor that accounted for 20% of the OM on average and was dominated by hydroxyl functional groups (72%). Alkane, carboxylic acid, and amine functional groups contributed 20%, 4%, and 3% of the OM, respectively. The concentration and composition of the factors are summarized in Table 2.4.

2.6.1.2 PMF of organic fragment concentrations

PMF was applied to the time series of concentrations of 271 AMS-measured organic mass fragments. The input matrix and the error files for PMF of the AMS measurements were prepared using the Igor Pro 5 (Wavemetrics Inc.) codes based on the work of Zhang et al. (90). Two to six factors with FPEAK-range of [0, ± 0.2, ± 0.4, ± 0.6, ± 0.8, ± 1] were investigated. The Q versus FPEAK plot shows the lowest Q values corresponding to FPEAK values of -0.2, 0, and 0.2. The factors generated for each rotation were nearly indistinguishable. FPEAK $= 0$ was selected to represent the solutions. A distinct factor with significant mass was missing when two factors were used. For each of the four-, five-, and six-factor solutions, highly correlated factors ($r > 0.7$) were combined, resulting in three recombined factors, which resembled the three factors generated from the three-factor solution. The normalized Q values for the three-six factor solutions are comparable (differences
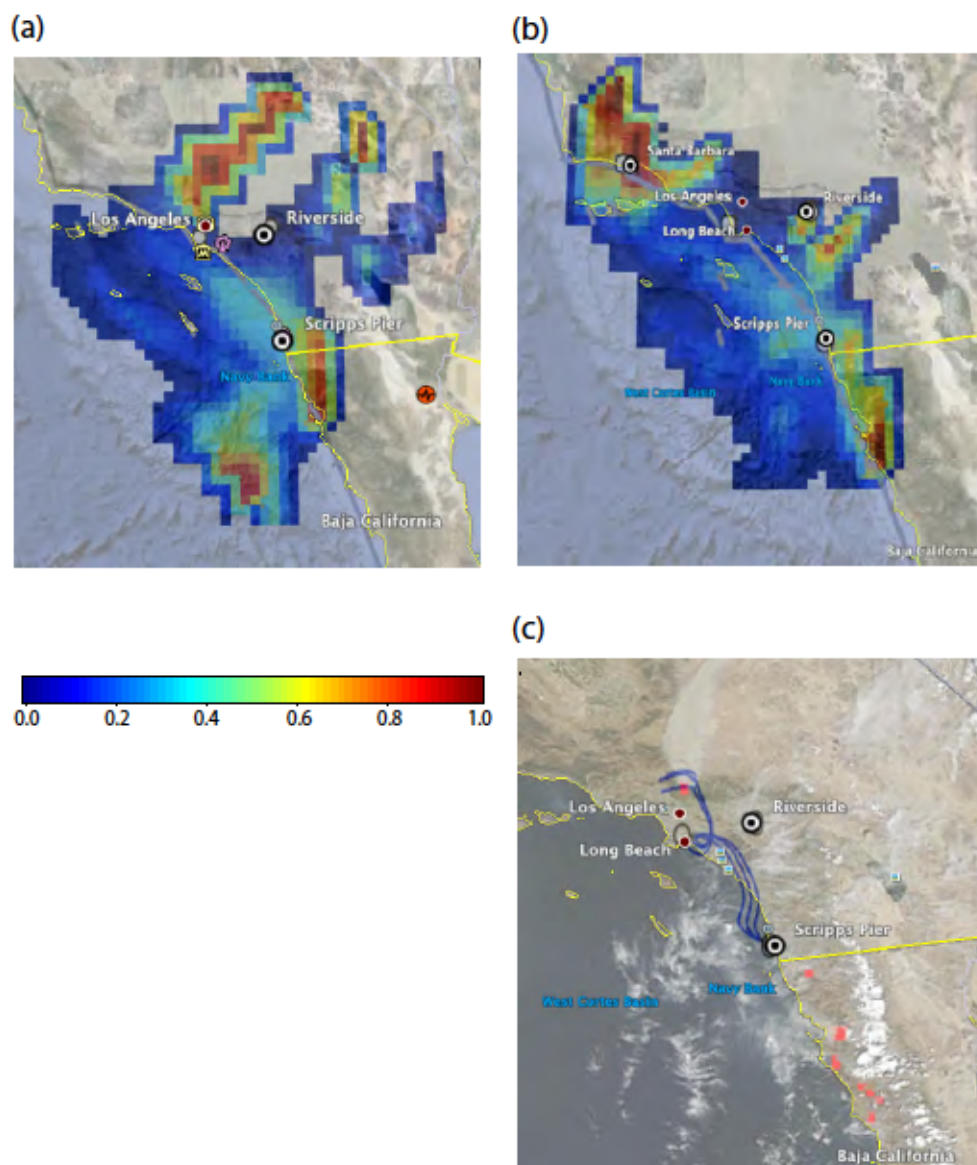
Figure 2.11: Potential Source Contribution Function (PSCF) images of **(a)** the FTIR combustion factor and **(b)** the FTIR biomass burning factor with warmer colors indicate higher probability. **(c)** Fire map on 29 August 2009 with red points showing fire spots and blue lines indicating back trajectories ending at the Scripps Pier. The fire image was obtained from NOAA's Aqua satellite.
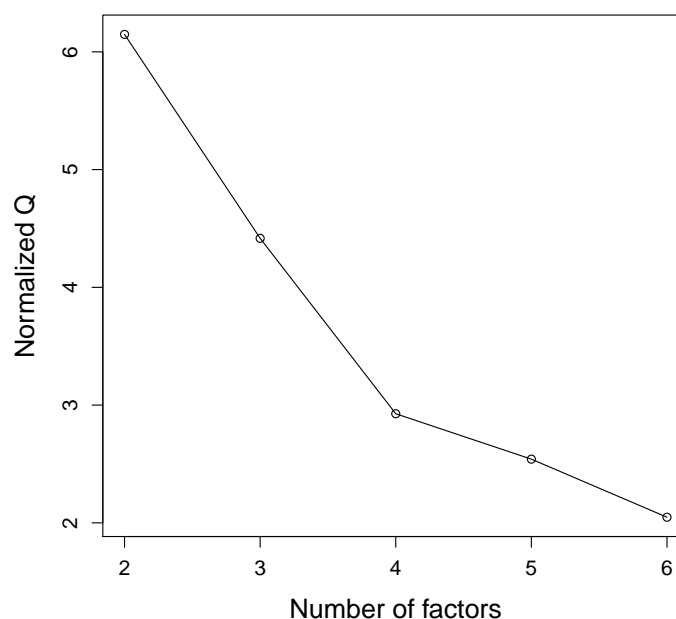
Figure 2.12: Normalized Q values versus number of factors for the FTIR PMF analysis.

are within 10 %), indicating three factors were enough for explaining the variability of the input data matrix. Therefore, the three-factor solution was selected, which reproduced 98 % of the OM variability.

The factors were identified by comparing normalized factor spectra with the online AMS reference spectra (83, 84). The first factor m/z spectrum correlated to several LV-OOA (low-volatility oxygenated organic aerosol) and SOA spectra. For example, the factor spectrum correlated to the Pittsburgh OOA factor spectrum (Zhang et al., 2005; $r = 0.93$ for $m/z{>}44$ and $r = 0.95$ for all m/z) and the spectrum from the photooxidation of m-xylene with seed aerosols under RH $= 55$ % (Bahreini et al., 2005; $r = 0.94$ for $m/z > 44$ and $r = 0.90$ for all m/z). The factor could not be further split into LV-OOA and SV-OOA (semi-volatile OOA) factors as shown in many previous studies (56), likely because of the relatively low particle concentration at the sampling site as well as the lower resolution of the quadropole MS. The diurnal cycle of this factor showed a significant increase in concentration during the day and lower values in the morning and at night (Fig. 2.5), indicating photochemical origins of this factor. This factor likely represented an aged com-

ponent formed from processed primary emissions. The factor was identified as an aged combustion factor, which accounted for 61 % of the nrOM and was associated with the largest m/z 44 fraction (of nrOM) and the largest m/z 44 to m/z 43 ratio of all of the factors (Table 2.4). The second factor profile strongly correlated with the wood burning spectrum ($r = 0.90$ for both $m/z > 44$ for all m/z) identified by Lanz et al. (45) and the brush fire spectrum ($r = 0.94$ for $m/z > 44$ and $r = 0.92$ for all m/z) described by Bahreini et al. (3). This factor was identified as a biomass burning factor, accounting for 26 % of the nrOM. No correlation was found between the third factor spectrum and the spectra from the AMS database. The factor concentration correlated to none of the concentrations of the AMS-measured inorganic compounds. The factor profile correlated moderately ($r = 0.5$) with the third factor (which was likely influenced by the ocean) from the ICEALOT study (19) and the time series correlated to that of the FTIR marine factor with $r = 0.5$. This factor may be a shipping or marine factor, which accounted for 13 % of the nrOM.

2.6.2   Wind direction effects on chemical concentration

The daytime wind direction was consistent during the study, with winds coming from northwest dominating during the 32 days selected for sample analysis. At night, easterly winds dominated but were more variable (Fig. 2.1b). The average diurnal profiles of wind direction for the "Afternoon High" and the "Noon High" days are shown in Fig. 2.13. Sea breeze effects on the daytime particle concentrations were not identified. Variability in the concentrations of carboxylic acid groups and alkane groups at night likely result from different sources brought by easterly winds at night. For this reason, the nighttime samples were excluded from the diurnal cycle analysis.
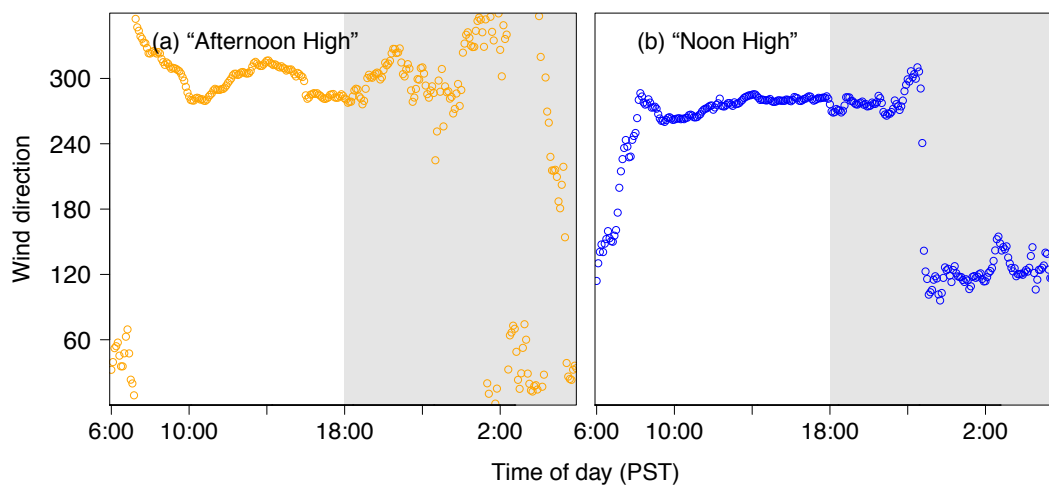
Figure 2.13: Vector-averaged diurnal cycles of wind direction (0 degree indicates wind coming from north) divided into (a) "Afternoon High" and (b) "Noon High" types. Shaded areas indicate nighttime periods.

2.7   Acknowledgments

We acknowledge Ray Weiss for providing CO measurements, with funding from the California Air Resources Board. We also are grateful for support from the University of California, San Diego – Pacific Northwest National Laboratory Aerosol Chemistry Climate Institute and NSF grant ATM-0744636. We also thank Kimberly Prather and Cassandra Gaston for providing O_3 measurements during this project.

Chapter 2, in full, is a reprint of the material as it appears in Atmospheric Chemistry and Physics 2011 with slight modifications. Liu, S., Day, D. A., Shields, J. E., and Russell, L. M. (2011), Ozone-driven daytime formation of secondary organic aerosol containing carboxylic acid groups and alkane groups, Atmospheric Chemistry and Physics, 11, 8321-8341. The dissertation author was the primary investigator and author of this paper.

References

[1] Altieri, K., Carlton, A., Lim, H., Turpin, B., and Seitzinger, S.: Evidence for oligomer formation in clouds: Reactions of isoprene oxidation products, Environ. Sci. Technol., 40, 4956–4960, 2006.

[2] Ault, A., Moore, M., Furutani, H., and Prather, K.: Impact of emissions from the Los Angeles port region on san diego air quality during regional transport events, Environ. Sci. Technol., 43, 3500–3506, 2009.

[3] Bahreini, R., Keywood, M., Ng, N., Varutbangkul, V., Gao, S., Flagan, R., Seinfeld, J., Worsnop, D., and Jimenez, J.: Measurements of secondary organic aerosol from oxidation of cycloalkenes, terpenes, and m-xylene using an Aerodyne aerosol mass spectrometer, Environ. Sci. Technol., 39, 5674–5688, 2005.

[4] Blando, J. and Turpin, B.: Secondary organic aerosol formation in cloud and fog droplets: a literature evaluation of plausibility, Atmos. Environ., 34, 1623–1632, 2000.

[5] Claeys, M., Szmigielski, R., Kourtchev, I., Van der Veken, P., Vermeylen, R., Maenhaut, W., Jaoui, M., Kleindienst, T., Lewandowski, M., Offenberg, J., and Edney, E. O.: Hydroxydicarboxylic acids: Markers for secondary organic aerosol from the photooxidation of α-pinene, Environ. Sci. Technol., 41, 1628–1634, 2007.

[6] Cronn, D. R., Charlson, R. J., Knights, R. L., Crittenden, A. L., and Appel, B. R.: A survey of the molecular nature of primary and secondary components of particles in urban air by high-resolution mass spectrometry, Atmos. Environ., 11, 929–937, 1977.

[7] Day, D., Liu, S., Russell, L., and Ziemann, P.: Organonitrate group concentrations in submicron particles with high nitrate and organic fractions in coastal southern California, Atmos. Environ., 44, 1970–1979, 2010.

[8] De Gouw, J. and Jimenez, J.: Organic aerosols in the Earth's atmosphere, Environ. Sci. Technol., 43, 7614–7618, 2009.

[9] De Gouw, J., Middlebrook, A., Warneke, C., Goldan, P., Kuster, W., Roberts, J., Fehsenfeld, F., Worsnop, D., Canagaratna, M., Pszenny, A., Keene, W. C., Marchewka, M., Bertman, S. B., and Bates, T. S.: Budget of organic carbon in a polluted atmosphere: Results from the New England Air Quality Study in 2002, J. Geophys. Res.-Atmos., 110, D16305, doi:10.1029/2004JD005623, 2005.

[10] De Gouw, J., Brock, C., Atlas, E., Bates, T., Fehsenfeld, F., Goldan, P., Holloway, J., Kuster, W., Lerner, B., Matthew, B., Middlebrook, A. M., Onasch, T. B., Peltier, R. E., Quinn, P. K., Senff, C. J., Stohl, A, Sullivan, A. P., Trainer, M., Warneke, C., Weber, R. J., and Williams, E. J.: Sources of particulate matter in the northeastern United States in summer: 1. Direct emissions and secondary formation of organic matter in urban plumes, J. Geophys. Res.-Atmos., 113, D08301, doi:10.1029/2007JD009243, 2008.

[11] DeCarlo, P. F., Dunlea, E. J., Kimmel, J. R., Aiken, A. C., Sueper, D., Crounse, J., Wennberg, P. O., Emmons, L., Shinozuka, Y., Clarke, A., Zhou, J., Tomlinson, J., Collins, D. R., Knapp, D., Weinheimer, A. J., Montzka, D. D., Campos, T., and Jimenez, J. L.: Fast airborne aerosol size and chemistry measurements above Mexico City and Central Mexico during the MILAGRO campaign, Atmos. Chem. Phys., 8, 4027–4048, doi:10.5194/acp-8-4027-2008, 2008.

[12] DeCarlo, P. F., Ulbrich, I. M., Crounse, J., de Foy, B., Dunlea, E. J., Aiken, A. C., Knapp, D., Weinheimer, A. J., Campos, T., Wennberg, P. O., and Jimenez, J. L.: Investigation of the sources and processing of organic aerosol over the Central Mexican Plateau from aircraft measurements during MILAGRO, Atmos. Chem. Phys., 10, 5257–5280, doi:10.5194/acp-10-5257-2010, 2010.

[13] Dominguez, G., Jackson, T., Brothers, L., Barnett, B., Nguyen, B., and Thiemens, M. H.: Discovery and measurement of an isotopically distinct source of sulfate in Earth's atmosphere, Proc. Natl. Acad. Sci., doi:10.1073/pnas.0805255105, 2008.

[14] Draxler, R. and Rolph, G.: HYSPLIT (HYbrid Single-Particle Lagrangian Integrated Trajectory) Model access via NOAA ARL READY Website: http://www.arl.noaa.gov/ready/hysplit4.html, NOAA Air Resources Laboratory, Silver Spring, 2003.

[15] Edney, E., Kleindienst, T., Jaoui, M., Lewandowski, M., Offenberg, J., Wang, W., and Claeys, M.: Formation of 2-methyl tetrols and 2-methylglyceric acid in secondary organic aerosol from laboratory irradiated isoprene/NO_x/SO_2/air mixtures and their detection in ambient $PM_{2.5}$ samples collected in the eastern United States, Atmos. Environ., 39, 5281–5289, 2005.

[16] Ervens, B., Feingold, G., Frost, G., and Kreidenweis, S.: A modeling study of aqueous production of dicarboxylic acids: 1. Chemical pathways and

speciated organic mass production, J. Geophys. Res.-Atmos., 109, D15205, doi:10.1029/2003JD004387, 2004.

[17] Fisseha, R., Dommen, J., Sax, M., Paulsen, D., Kalberer, M., Maurer, R., H "ofler, F., Weingartner, E., and Baltensperger, U.: Identification of organic acids in secondary organic aerosol and the corresponding gas phase from chamber experiments, Anal. Chem., 76, 6535–6540, 2004.

[18] Fraser, M., Yue, Z., Tropp, R., Kohl, S., and Chow, J.: Molecular composition of organic fine particulate matter in Houston, TX, Atmos. Environ., 36, 5751–5758, 2002.

[19] Frossard, A. A., Shaw, P. M., Russell1, L. M., Kroll, J. H., Canagartna, M., Worsnop, D., Quinn, P. K., and Bates, T. S.: Springtime Arctic Haze Contributions of Submicron Organic Particles from European and Asian combustion Sources, J. Geophys. Res.-Atmos., 116, D05205, doi:10.1029/2010JD015178, 2011.

[20] Fuzzi, S., Andreae, M. O., Huebert, B. J., Kulmala, M., Bond, T. C., Boy, M., Doherty, S. J., Guenther, A., Kanakidou, M., Kawamura, K., Kerminen, V.-M., Lohmann, U., Russell, L. M., and Pöschl, U.: Critical assessment of the current state of scientific knowledge, terminology, and research needs concerning the role of organic aerosols in the atmosphere, climate, and global change, Atmos. Chem. Phys., 6, 2017–2038, 2006.

[21] Ge, X., Wexler, A. S., and Clegg, S. L.: Atmospheric Amines-Part I. A review, Atmos. Environ., 524–546, 2011.

[22] Gilardoni, S., Russell, L. M., Sorooshian, A., Flagan, R. C., Seinfeld, J. H., Bates, T. S., Quinn, P. K., Allan, J. D., Williams, B., Goldstein, A. H., Onasch, T. B., Worsnop, D. R.: Regional variation of organic functional groups in aerosol particles on four US east coast platforms during the International Consortium for Atmospheric Research on Transport and Transformation 2004 campaign, J. Geophys. Res.-Atmos., 112, D10S27, doi:10.1029/2006JD007737, 2007.

[23] Gilardoni, S., Liu, S., Takahama, S., Russell, L. M., Allan, J. D., Steinbrecher, R., Jimenez, J. L., De Carlo, P. F., Dunlea, E. J., and Baumgardner, D.: Characterization of organic ambient aerosol during MIRAGE 2006 on three platforms, Atmos. Chem. Phys., 9, 5417–5432, 2009.

[24] Gray, H., Cass, G., Huntzicker, J., Heyerdahl, E., and Rau, J.: Characteristics of atmospheric organic and elemental carbon particle concentrations in Los Angeles, Environ. Sci. Technol., 20, 580–589, 1986.

[25] Grosjean, D., Van Cauwenberghe, K., Schmid, J., Kelley, P., and Pitts Jr., J.: Identification of C3-C10 aliphatic dicarboxylic acids in airborne particulate matter, Environ. Sci. Technol., 12, 313–317, 1978.

[26] Grosjean, D.: In situ organic aerosol formation during a smog episode: estimated production and chemical functionality, Atmospheric Environment. Part A. General Topics, 26, 953–963, 1992.

[27] Haagen-Smit, A. J.: Chemistry and physiology of Los Angeles smog, Ind. Eng. Chem., 17, 1342–1346, 1952.

[28] Hallquist, M., Wenger, J. C., Baltensperger, U., Rudich, Y., Simpson, D., Claeys, M., Dommen, J., Donahue, N. M., George, C., Goldstein, A. H., Hamilton, J. F., Herrmann, H., Hoffmann, T., Iinuma, Y., Jang, M., Jenkin, M. E., Jimenez, J. L., Kiendler-Scharr, A., Maenhaut, W., McFiggans, G., Mentel, Th. F., Monod, A., Prvt, A. S. H., Seinfeld, J. H., Surratt, J. D., Szmigielski, R., and Wildt, J.: The formation, properties and impact of secondary organic aerosol: current and emerging issues, Atmos. Chem. Phys., 9, 5155–5236, 2009.

[29] Hawkins, L. N. and Russell, L. M.: Oxidation Of Ketone Groups In Transported biomass burning Aerosol From The 2008 Northern California Lightning Series Fires, Atmos. Environ., 44, 4142–4154, 2010.

[30] Hawkins, L. N. and Russell, L. M.: Polysaccharides, Proteins, and Phytoplankton Fragments: Four Chemically Distinct Types of marine Primary Organic Aerosol Classified by Single Particle Spectromicroscopy, Adv. Meteorol., 2010, 612132, doi:10.1155/2010/612132, 2010.

[31] Herndon, S., Onasch, T., Wood, E., Kroll, J., Canagaratna, M., Jayne, J., Zavala, M., Knighton, W., Mazzoleni, C., Dubey, M., Ulbrich, I. M., Jimenez, J. L., Seila, R., de Gouw J. A., de Foy, B., Fast, J., Molina, L. T., Kolb, C. E., and Worsnop, D. R.: Correlation of secondary organic aerosol with odd oxygen in Mexico City, Geophys. Res. Lett., 35, L15804, doi:10.1029/2008GL034058, 2008.

[32] Hildebrandt, L.,Engelhart, G. J., Mohr, C., Kostenidou, E., Lanz, V. A., Bougiatioti, A., DeCarlo, P. F., Prevot, A. S. H., Baltensperger, U., Mihalopoulos, N., Donahue, N. M., and Pandis, S. N.: Aged organic aerosol in the Eastern Mediterranean: the Finokalia aerosol measurement experiment-2008, Atmos. Chem. Phys, 10, 4167–4186, doi:10.5194/acp-10-4167-2010, 2010.

[33] Hughes, M., Hall, A., and Fovell, R.: Dynamical controls on the diurnal cycle of temperature in complex topography, Clim. Dynam., 29, 277–292, 2007.

[34] Jaoui, M., Kleindienst, T. E., Lewandowski, M., and Edney, E. O.: Identification and quantification of aerosol polar oxygenated compounds bearing carboxylic or hydroxyl groups. 1. Method development, Anal. Chem., 76, 4765–4778, 2004.

[35] Jayne, J., Leard, D., Zhang, X., Davidovits, P., Smith, K., Kolb, C., and Worsnop, D.: Development of an aerosol mass spectrometer for size and composition analysis of submicron particles, Aerosol. Sci. Tech., 33, 49–70, 2000.

[36] Kawamura, K.: Identification of C2-C10. omega.-oxocarboxylic acids, pyruvic acid, and C2-C3. alpha.-dicarbonyls in wet precipitation and aerosol samples by capillary GC and GC/MS, Anal. Chem., 65, 3505–3511, 1993.

[37] Kawamura, K. and Gagosian, R.: Implications of ω-oxocarboxylic acids in the remote marine atmosphere for photo-oxidation of unsaturated fatty acids, Nature, 325, 330–332, 1987.

[38] Kawamura, K. and Ikushima, K.: Seasonal changes in the distribution of dicarboxylic acids in the urban atmosphere, Environ. Sci. Technol., 27, 2227–2235, 1993.

[39] Kawamura, K. and Yasui, O.: Diurnal changes in the distribution of dicarboxylic acids, ketocarboxylic acids and dicarbonyls in the urban Tokyo atmosphere, Atmos. Environ., 39, 1945–1960, 2005.

[40] Kawamura, K. and Kaplan, I. R.: Motor exhaust emissions as a primary source for dicarboxylic acids in Los Angeles ambient air, Environ. Sci. Technol, 21, 105–110, 1987.

[41] Kilcoyne, A. L. D., Tyliszczak, T., Steele, W. F., Fakra, S., Hitchcock, P., Franck, K., Anderson, E., Harteneck, B., Rightor, E. G., Mitchell, G. E., Hitchcock, A. P., Yang, L., Warwickc, T., and Ade, H.: Interferometer-controlled scanning transmission X-ray microscopes at the Advanced Light Source, J. Synch. Radiat., 10 (2), 125–136, 2003.

[42] Kleindienst, T., Smith, D., Li, W., Edney, E., Driscoll, D., Speer, R., and Weathers, W.: Secondary organic aerosol formation from the oxidation of aromatic hydrocarbons in the presence of dry submicron ammonium sulfate aerosol, Atmos. Environ., 33, 3669–3681, 1999.

[kleindienst2004] Kleindienst, T. E., Conver, T. S., McIver, C. D., and Edney, E. O.: Determination of secondary organic aerosol products from the photooxidation of toluene and their implications in ambient $PM_{2.5}$, Environ. Sci. Technol., 47, 79–100, 2004.

[43] Kleindienst, T., Edney, E., Lewandowski, M., Offenberg, J., and Jaoui, M.: Secondary organic carbon and aerosol yields from the irradiations of isoprene and α-pinene in the presence of NO_x and SO_2, Environ. Sci. Technol., 40, 3807–3812, 2006.

[44] Kleinman, L., Lee, Y., Springston, S., Nunnermacker, L., Zhou, X., Brown, R., Hallock, K., Klotz, P., Leahy, D., Lee, J., and Newman, L.: Ozone formation at a rural site in the southeastern United States, J. Geophys. Res.-Atmos., 99, 3469–3482, doi:10.1029/93JD02991, 1994.

[45] Lanz, V. A., Alfarra, M. R., Baltensperger, U., Buchmann, B., Hueglin, C., and Prvt, A. S. H.: Source apportionment of submicron organic aerosols at an urban site by factor analytical modelling of aerosol mass spectra, Atmos. Chem. Phys., 7, 1503–1522, 2007.

[46] Liggio, J., Li, S. M., Vlasenko, A., Sjostedt, S., Chang, R., Shantz, N., Abbatt, J., Slowik, J. G., Bottenheim, J. W., Brickell, P. C., Stroud, C., and Leaitch, W. R.: Primary and secondary organic aerosols in urban air masses intercepted at a rural site, J. Geophys. Res.-Atmos., 115, D21305, doi:10.1029/2010JD014426, 2010.

[47] Lim, Y. and Ziemann, P.: Chemistry of secondary organic aerosol formation from OH radical-initiated reactions of linear, branched, and cyclic alkanes in the presence of NO_x, Aerosol. Sci. Tech., 43, 604–619, 2009.

[48] Liu, C., Huang, C., Shieh, S., and Wu, C.: Important meteorological parameters for ozone episodes experienced in the Taipei basin, Atmos. Environ., 28, 159–173, 1994.

[49] Liu, S., Takahama, S., Russell, L. M., Gilardoni, S., and Baumgardner, D.: Oxygenated organic functional groups and their sources in single and submicron organic particles in MILAGRO 2006 campaign, Atmos. Chem. Phys., 9, 6849–6863, 2009.

[50] Madronich, S., Chatfield, R. B., Calvert, J. G., Moortgat, G. K., Veyret, B., and Lesclaux, R.: A photochemical origin of acetic acid in the troposphere, Geophys. Res. Lett., 17, 2361–2364, 1990.

[51] Maria, S., Russell, L., Turpin, B., and Porcja, R.: FTIR measurements of functional groups and organic mass in aerosol samples over the Caribbean, Atmos. Environ., 36, 5185–5196, 2002.

[52] Maria, S., Russell, L., Gilles, M., and Myneni, S.: Organic aerosol growth mechanisms and their climate-forcing implications, Science, 306, 1921–1924, 2004.

[53] Martin, P., Tuazon, E. C., Aschmann, S. M., Arey, J., and Atkinson, R.: Formation and atmospheric reactions of 4, 5-dihydro-2-methylfuran, J. Phys. Chem. A, 106, 11492–11501, 2002.

[54] Miracolo, M., Presto, A., Lambe, A., Hennigan, C., Donahue, N., Kroll, J., Worsnop, D., and Robinson, A.: Secondary organic aerosol formation from low-volatility organic vapors in motor vehicle emissions, Environ. Sci. Technol., 44, 1638–1643, 2010.

[55] Morgan, W., Allan, J., Bower, K.,Highwood, E.J., Liu, D., McMeeking, G., Northway, M.,Williams, P., Krejci, R., and Coe, H.: Airborne measurements of the spatial distribution of aerosol chemical composition across Europe and evolution of the organic fraction, Atmos. Chem. Phys., 10, 4065–4083, 2010.

[56] Ng, N. L., Canagaratna, M. R., Zhang, Q., Jimenez, J. L., Tian, J., Ulbrich, I. M., Kroll, J. H., Docherty, K. S., Chhabra, P. S., Bahreini, R., Murphy, S. M., Seinfeld, J. H., Hildebrandt, L., Donahue, N. M., DeCarlo, P. F., Lanz, V. A., Prévôt, A. S. H., Dinar, E., Rudich, Y., and Worsnop, D. R.: Organic aerosol components observed in Northern Hemispheric datasets from Aerosol Mass Spectrometry, Atmos. Chem. Phys., 10, 4625–4641, 2010.

[57] Paatero, P. and Tapper, U.: Positive matrix factorization: A non-negative factor model with optimal utilization of error estimates of data values, Environmetrics, 5, 111–126, 1994.

[58] Pekney, N., Davidson, C., Robinson, A., Zhou, L., Hopke, P., Eatough, D., and Rogge, W.: Major Source Categories for $PM_{2.5}$ in Pittsburgh using PMF and UNMIX, Aerosol. Sci. Tech., 40, 910–924, 2006.

[59] Pietrogrande, M. C., Mercuriali, M., Perrone, M. G., Ferrero, L., Sangiorgi, G., and Bolzacchini, E.: Distribution of n-Alkanes in the Northern Italy Aerosols: Data Handling of GC-MS Signals for Homologous Series Characterization, Environ. Sci. Technol, 44, 4232–4240, 2010.

[60] Presto, A., Miracolo, M., Donahue, N., and Robinson, A.: Secondary organic aerosol formation from high-NO_x photo-oxidation of low volatility precursors: n-alkanes, Environ. Sci. Technol, 44, 2029–2034, 2010.

[61] Quinn, P., Bates, T., Coffman, D., Onasch, T., Worsnop, D., Baynard, T., De Gouw, J., Goldan, P., Kuster, W., Williams, E., Roberts, J. M., Lerner, B., Stohl, A., Pettersson, A., and Lovejoy, R. E.: Impacts of sources and aging on submicrometer aerosol properties in the marine boundary layer across the Gulf of Maine, J. Geophys. Res.-Atmos., 111, D23S36, doi:10.1029/2006JD007582, 2006.

[62] Rogge, W. F., Hildemann, L. M., Mazurek, M. A., Cass, G. R., Simoneit, and B. R. T.: Sources of fine organic aerosol. 1. Charbroilers and meat cooking operations, Environ. Sci. Technol., 25, 1112–1125, 1991.

[63] Rogge, W., Mazurek, M., Hildemann, L., Cass, G., and Simoneit, B.: Quantification of urban organic aerosols at a molecular level: identification, abundance and seasonal variation, Atmos. Environ., 27, 1309–1330, 1993.

[64] Rolph, G.: Real-time Environmental Applications and Display sYstem (READY) Website (http://www.arl.noaa.gov/ready/hysplit4.html), NOAA Air Resources Laboratory, Silver Spring, Silver Spring, MD, USA, 2003.

[65] Russell, L. M., Maria, S., and Myneni, S.: Mapping organic coatings on atmospheric particles, Geophys. Res. Lett., 29, 1779, doi:10.1029/2002GL014874, 2002.

[66] Russell, L. M., Takahama, S., Liu, S., Hawkins, L., Covert, D., Quinn, P., and Bates, T.: Oxygenated fraction and mass of organic aerosol from direct emission and atmospheric processing measured on the R/VRonald Brown during TEXAQS/GoMACCS 2006, J. Geophys. Res.-Atmos., 114, D00F05, doi:10.1029/2008JD011275, 2009a.

[67] Russell, L. M., Bahadur, R., Hawkins, L., Allan, J., Baumgardner, D., Quinn, P., and Bates, T.: Organic aerosol characterization by complementary measurements of chemical bonds and molecular fragments, Atmos. Environ., 43, 6100–6105, 2009b.

[68] Russell, L. M., Hawkins, L. N., Frossard, A., Quinn, P., and Bates, T.: Carbohydrate-like composition of submicron atmospheric particles and their production from ocean bubble bursting, Proc. Natl. Acad. Sci., 107, 6652, doi:10.1073/pnas.0908905107, 2010.

[69] Russell, L. M., Bahadur, R., and Ziemann, P. J.: Identifying organic aerosol sources by comparing functional group composition in chamber and atmospheric particles, Proc. Natl. Acad. Sci., doi:10.1073/pnas.1006461108, 2011.

[70] Satsumabayashi, H., Kurita, H., Yokouchi, Y., and Ueda, H.: Mono-and dicarboxylic acids under long-range transport of air pollution in central Japan, Tellus B, 41, 219–229, 1989.

[71] Satsumabayashi, H., Kurita, H., Yokouchi, Y., and Ueda, H.: Photochemical formation of particulate dicarboxylic acids under long-range transport in central Japan, Atmospheric Environment. Part A. General Topics, 24, 1443–1450, 1990.

[72] Sax, M., Zenobi, R., Baltensperger, U., and Kalberer, M.: Time resolved infrared spectroscopic analysis of aerosol formed by photo-oxidation of 1, 3, 5-trimethylbenzene and α-pinene, Aerosol. Sci. Tech., 39, 822–830, 2005.

[73] Schuetzle, D., Cronn, D., Crittenden, A. L., and Charlson, R. J.: Molecular composition of secondary aerosol and its possible origin, Environ. Sci. Technol., 9, 838–845, 1975.

[74] Sullivan, A. and Weber, R.: Chemical characterization of the ambient organic aerosol soluble in water: 1. Isolation of hydrophobic and hydrophilic fractions with a XAD-8 resin, J. Geophys. Res.-Atmos., 111, D05314, doi:10.1029/2005JD006485, 2006.

[75] Sullivan, R. and Prather, K.: Investigations of the diurnal cycle and mixing state of oxalic acid in individual particles in Asian aerosol outflow, Environ. Sci. Technol., 41, 8062–8069, 2007.

[76] Surratt, J., Lewandowski, M., Offenberg, J., Jaoui, M., Kleindienst, T., Edney, E., and Seinfeld, J.: Effect of acidity on secondary organic aerosol formation from isoprene, Environ. Sci. Technol., 41, 5363–5369, 2007.

[77] Takahama, S., Gilardoni, S., Russell, L., and Kilcoyne, A.: Classification of multiple types of organic carbon composition in atmospheric particles by scanning transmission X-ray microscopy analysis, Atmos. Environ., 41, 9435–9451, 2007.

[78] Takahama, S., Liu, S., and Russell, L.: Coatings and clusters of carboxylic acids in carbon-containing atmospheric particles from spectromicroscopy and their implications for cloud-nucleating and optical properties, J. Geophys. Res.-Atmos., 115, D01202, doi:10.1029/2009JD012622, 2010.

[79] Talbot, R., Mao, H., and Sive, B.: Diurnal characteristics of surface level O3 and other important trace gases in New England, J. Geophys. Res.-Atmos., 110, D09307, doi:10.1029/2004JD005449, 2005.

[80] Tan, Y., Perri, M., Seitzinger, S., and Turpin, B.: Effects of Precursor Concentration and Acidic Sulfate in Aqueous Glyoxal- OH Radical Oxidation and Implications for Secondary Organic Aerosol, Environ. Sci. Technol., 43, 8105–8112, 2009.

[81] Turpin, B., Huntzicker, J., Larson, S., and Cass, G.: Los Angeles summer midday particulate carbon: primary and secondary aerosol, Environ. Sci. Technol., 25, 1788–1793, 1991.

[82] Turpin, B., Saxena, P., and Andrews, E.: Measuring and simulating particulate organics in the atmosphere: problems and prospects, Atmos. Environ., 34, 2983–3013, 2000.

[83] Ulbrich, I. M., Lechner, M., and Jimenez, J. L.: AMS Spectral Database, http://cires.colorado.edu/jimenez-group/AMSsd, access: 10 Feb 2010, 2007.

[84] Ulbrich, I. M., Canagaratna, M. R., Zhang, Q., Worsnop, D. R., and Jimenez, J. L.: Interpretation of organic components from Positive Matrix Factorization of aerosol mass spectrometric data, Atmos. Chem. Phys., 9, 2891–2918, 2009.

[85] Wang, G., Niu, S., Liu, C., and Wang, L.: Identification of dicarboxylic acids and aldehydes of PM_{10} and $PM_{2.5}$ aerosols in Nanjing, China, Atmos. Environ., 36, 1941–1950, 2002.

[86] Wang, G., Kawamura, K., Xie, M., Hu, S., Gao, S., Cao, J., An, Z., and Wang, Z.: Size-distributions of n-alkanes, PAHs and hopanes and their sources in the urban, mountain and marine atmospheres over East Asia, Atmos. Chem. Phys., 9, 8869–8882, 2009.

[87] Warneck, P.: In-cloud chemistry opens pathway to the formation of oxalic acid in the marine atmosphere, Atmos. Environ., 37, 2423–2427, 2003.

[88] Yu, J., Griffin, R., Cocker, D., Flagan, R., Seinfeld, J., and Blanchard, P.: Observation of gaseous and particulate products of monoterpene oxidation in forest atmospheres, Geophys. Res. Lett., 26, 1145–1148, doi:10.1029/1999GL900169, 1999.

[89] Yu, J., Huang, X., Xu, J., and Hu, M.: When aerosol sulfate goes up, so does oxalate: implication for the formation mechanisms of oxalate, Environ. Sci. Technol., 39, 128–133, 2005.

[90] Zhang, Q., Alfarra, M., Worsnop, D., Allan, J., Coe, H., Canagaratna, M., and Jimenez, J.: Deconvolution and quantification of hydrocarbon-like and oxygenated organic aerosols based on aerosol mass spectrometry, Environ. Sci. Technol., 39, 4938–4952, 2005.

[91] Zhang, Q., Jimenez, J., Worsnop, D., and Canagaratna, M.: A case study of urban particle acidity and its influence on secondary organic aerosol, Environ. Sci. Technol., 41, 3213–3219, 2007a.

[92] Zhang, Q., Jimenez, J. L., Canagaratna, M. R., Allan, J. D.,Coe, H., Ulbrich, I.,Alfarra, M. R.,Takami, A., Middlebrook, A. M., Sun, Y. L., Dzepina, K., Dunlea, E., Docherty, K., DeCarlo, P. F., Salcedo, D., Onasch, T., Jayne, J. T., Miyoshi, T., Shimono, A., Hatakeyama, S., Takegawa, N., Kondo, Y., Schneider, J., Drewnick, F., Borrmann, S., Weimer, S., Demerjian, K., Williams, P., Bower, K., Bahreini, R., Cottrell, L., Griffin, R. J., Rautiainen, J., Sun, J. Y., Zhang, Y. M., and Worsnop, D. R.: Ubiquity and dominance of oxygenated species in organic aerosols in anthropogenically-influenced Northern Hemisphere midlatitudes, Geophys. Res. Lett., 34, L13801, doi:10.1029/2007GL029979, 2007b.

[93] Zhang, Y. Y., Müller, L., Winterhalter, R., Moortgat, G. K., Hoffmann, T., and Pöschl, U.: Seasonal cycle and temperature dependence of pinene oxidation products, dicarboxylic acids and nitrophenols in fine and coarse air particulate matter, Atmos. Chem. Phys., 10, 7859–7873, 2010.

Chapter 3

Secondary organic aerosol formation from fossil fuel sources contribute majority of summertime organic mass at Bakersfield

Abstract. Secondary organic aerosols (SOA), known to form in the atmosphere from oxidation of volatile organic compounds (VOCs) emitted by anthropogenic and biogenic sources, are a poorly understood but substantial component of atmospheric particles. In this study, we examined the chemical and physical properties of SOA at Bakersfield, California, a site influenced by anthropogenic and terrestrial biogenic emissions. Factor analysis was applied to the infrared and mass spectra of fine particles to identify sources and processing that contributed to the organic mass (OM). We found that OM accounted for 56%

of submicron particle mass, with SOA components contributing 80% to 90% of OM from 15 May to 29 June 2010. SOA formed from alkane and aromatic compounds, the two major classes of vehicle-emitted hydrocarbons, accounted for 65% OM (72% SOA). The alkane and aromatic SOA components were associated with 200- to 500-nm-accumulation-mode particles, likely from condensation of daytime photochemical products of VOCs. In contrast, biogenic SOA likely formed from condensation of secondary organic vapors, produced from NO_3 radical oxidation reactions during nighttime hours, on 400- to 700-nm-sized primary particles, and accounted for less than 10% OM. Local petroleum operation emissions contributed 13% to the OM, and the moderate O/C (0.2) of this factor suggested it was largely secondary. Approximately 10% of organic aerosols in submicron particles was identified as either vegetative detritus (10%) or cooking activities (7%), from Fourier transform infrared spectroscopic and aerosol mass spectrometry measurements, respectively. While the mass spectra of several linearly-independent SOA components were nearly identical and external source markers were needed to separate them, each component had distinct infrared spectrum, likely associated with the source-specific VOCs from which they formed.

3.1   Introduction

The organic fraction of atmospheric particles is comprised of a complex mixture of thousands of individual compounds [Hamilton et al., 2004], which originate from a variety of sources and processes. In urban areas, the major source is fossil fuel combustion from gasoline- and diesel-powered vehicles and other industrial activities (e.g., oil burning). Emissions from these sources are largely composed of alkane and aromatic hydrocarbons, with a minor fraction of alkene compounds [Kirchstetter et al., 1999; Schauer et al., 1999]. Another important source, biogenic emissions, accounts for 90% of total volatile organic compounds (VOCs) globally [Goldstein and Galbally, 2007] and is key to particle formation in some regions (e.g., the southeastern US) [Goldstein et al., 2009]. After emission, VOCs are transported from their sources during which time they are oxidized in the atmosphere, forming low-volatility products that can condense into the particle phase. The organic aerosols formed in the atmosphere are categorized as "SOA" (secondary organic aerosol) as opposed to "POA," organic aerosols directly emitted at their sources.

Formation of SOA is a dynamic process that involves complex chemical reactions and physical transformations. Despite significant progress in the past years, quantitative measurement of SOA mass and its mass fraction in organic aerosols remains challenging. The elemental carbon (EC)-tracer analysis has been used to identify non-SOA components since the 1980s [Grosjean, 1984]: The organic carbon (OC)-to-EC ratio that exceeds the average OC/EC from source measurements is assumed to be SOA [Turpin et al., 1991]. Using this method, field measurements conducted at Los Angeles suggested that production of SOA could be 3 to 4 times more than that of POA during smog events [Grosjean, 1984; Turpin et al., 1991]. Supporting the argument that SOA could be the major OM component were reaction chamber studies carried out during this time, which showed high mass yields of precursor compounds [Hatakeyama et al., 1985, 1987]. However, the EC-tracer approach suffers from large uncertainties, since OC/EC of emission sources is highly variable and is substantially affected by meteorological conditions (e.g., air mixing) [Gray et al., 1986]. Another approach, the organic tracer-based chemistry

mass balance (CMB) model [Schauer et al., 1996; Cass, 1998], has been applied to identify sources of atmospheric fine particles since the 1990s. In this method, the mass that cannot be predicted by the model is assigned to SOA [Schauer et al., 2002a; Zheng et al., 2002]. Therefore, the CMB model does not directly predict SOA but provides an upper limit of SOA mass based on limited source markers (source types) [Cass, 1998]. Over the last 10 years, the development of aerosol mass spectrometer (AMS) and Fourier transform infrared (FTIR) spectroscopy has provided new insights for SOA quantification [Jayne et al., 2000; Maria et al., 2002]. Positive matrix factor (PMF) analysis applied to the AMS and FTIR measurements during field experiments carried out worldwide consistently showed that 65% to 95% of OM is oxygenated organic aerosols (OOA), having higher OM/OC and oxygen-to-carbon molar ratio (O/C) composition than expected for primary organic components [Jimenez et al., 2009; Lanz et al., 2007; Liu et al., 2011; Russell et al., 2011; Russell 2003; Turpin et al., 2000; Zhang et al., 2007].

However, there is a lack of direct evidence that oxidized OA equates to SOA, because some primary aerosols are oxidized (e.g., marine polysaccharides and vegetative detritus). Consequently, there is a need to directly compare OOA to laboratory-produced SOA. Russell et al. [2011] compared OOA to SOA generated in smog chamber. In this case, OOA was derived by factor analysis of FTIR measurements, a technique that provides more molecular functional group specificity than mass spectra methods that employ electron ionization. Results of this comparison suggested that functional group compositions of OOA and SOA are comparable and precursor (and sometimes oxidant) dependent, making it possible to separate out SOA and, so, help address the controversy of POA and SOA mass fractions. In addition, Russell et al. [2011] proposed that atmospheric alkanes are important SOA precursors–oxidation of alkanes produces multigeneration SOA products, which is supported by a recent model simulation study [Yee et al., 2012] that suggests more than two-thirds of alkane SOA are fourth or higher generation products after reaction for 10 hrs. Despite the improvements in laboratory and model studies, more field measurements are needed to separate SOA formed from different precursors and identify which mechanisms best explain chemical

properties of SOA formed in the complex atmosphere.

Size distributions of SOA components can provide additional insights for identifying source and formation mechanisms of ambient particles. Primary combustion-related particles, such as those emitted from gasoline- and diesel-powered vehicles, are typically smaller than 100 nm [Kittelson, 1998], whereas dust particles are usually larger than 500 nm [Tegen and Lacis, 1996]. Primary particles from cooking activities, including charbroiling and frying, are found to be smaller than 200 nm [Wallace et al., 2004]. Particles in 200- to 500-nm size range typically contain SOA formed by condensation of secondary organic vapors, because particles in this size range have the highest relative surface area that make mass transfer most efficient for growth [Maria et al., 2004; Seinfeld and Pandis, 2006]. Size distributions of organic components are also important for evaluating climate impacts of aerosols, since radiative parameters of aerosol particles are strongly dependent on particle size [Tegen and Lacis, 1996]. Further, lifetime of particles, which determines the distance that particles can travel and hence particles regional impacts, is affected by particle size. For these reasons, particle size distributions have been studied extensively [Heintzenberg et al., 2000; Hoppel et al., 1990; Whitby et al., 1972]. Although some specific SOA molecules (e.g., oxalic acid) or mass fragments (e.g., m/z 44) have been measured as functions of size [Kawamura et al., 2007; Alfarra et al., 2004], predicting size distributions of different types of ambient SOA (formed from different sources or processes) is challenging. A few studies have applied factor analysis to each size fraction of size-resolved filter measurements (2-6 size ranges) with limited organic mass quantification [Han et al., 2006; Karanasiou et al., 2009; Richard et al., 2011; Srivastava et al., 2008]. In these studies, estimates of factor size distribution were made by comparing masses of the common factors (typically representing primary sources) derived from each size fraction. However, this approach is not practical for highly size-resolved data sets (e.g., AMS measurements with more than 100 size bins). Another approach, 3-D factorization method, has been valuable for providing time-resolved size distribution of factors and have been recently applied to AMS measurements with success [Ulbrich et al., 2012]. However, to generate

physically meaningful factors, this analysis often requires prior information derived from 2-D factorization plus comparisons of results derived from different 3-D factorization methods, which is complicated and, so, the 3-D factorization methods have not been widely used. Thus, despite these improvements, size distributions of ambient SOA components have not been widely investigated.

In this context, we used collaborative measurements at Bakersfield in the San Joaquin Valley (SJV), one of the most polluted regions in the United States [Chow et al., 1996], to study the oxidized fraction of OM. We began by quantifying oxygenated organic functional group and mass fragment abundances of bulk and single particles. Next, we identified sources and processes that contributed to OM using factor analysis and source-specific organic and inorganic marker compounds. After distinguishing secondary components from primary emissions, we evaluated the SOA fraction of OM. In addition, primary and secondary single-particle types were identified using cluster analysis. Finally, we compared different secondary organic components—their precursors, oxidants that lead to formation, and time of production. Size distributions of the SOA components were used to help identify their potential formation mechanisms. These analyses were built on a set of particle- and gas-phase measurements presented as follows.

3.2   Experimental

3.2.1   Sampling site and meteorological conditions during the CalNex campaign

The CalNex (California Research at the Nexus of Air Quality and Climate Change) campaign is a collaborative effort aimed at characterizing chemical and physical properties of aerosols in California. One supersite was located at Bakersfield in Kern County in the San Joaquin Valley (SJV). SJV is surrounded by coastal mountain ranges to the west, the Sierra Nevada range to the east, and the Tehachapi Mountains to the south [Chow et al., 2006b], topography that regularly precludes air ventilation. The basin's air pollution levels are especially high during

wintertime [Chow et al., 2006a, 2006b]. Bakersfield, located in SJV's southern region and one of its biggest cities, has a wintertime $PM_{2.5}$ concentration often exceeding 50 μg m^{-3}, with OM typically accounting for more than 50% of the $PM_{2.5}$ mass [Chow et al., 2006b]. Previous studies conducted at other sites in Bakersfield showed that gasoline- and diesel-powered vehicles, wood combustion, and meat cooking comprise the site's major air pollution sources [Kleeman et al., 2009; Schauer and Cass, 2000]; wood combustion may prevail only in winter [Chow et al., 2006b]. In addition, biogenic hydrocarbons emitted from trees in the foothills are likely significant contributors to summertime VOCs [Tanner and Zielinska, 1994], providing potential biogenic precursors to form biogenic SOA. Thus, the high concentration of air pollution and the variety of its sources make Bakersfield an ideal site for studying ambient particles.

Measurements were conducted from 15 May to 29 June 2010 at Bakersfield (35.35°N, 118.97°W). The sampling site, located in an open urban area at the southeast edge of the city center close to freeway 99 (7 km to the west) and highway 58 (0.8 km to the north), had no nearby obstructions (e.g., tall trees or buildings). Instruments were deployed in temperature-controlled (20°C) containers with sampling heights of 3 to 5 m and 18 to 20 m above ground level, respectively, for particle-phase and gas-phase measurements. The sampling period was characterized by a series of clear, dry days with consistent diurnal cycles of temperature and relative humidity (RH), except for 15 to 17 May when intermittent rainfall occurred. The average temperature for the campaign, 24°C, included a 7°C standard deviation, with minimums typically occurring at ~0500 hr and maximums often observed at ~1500 hr (lagged by 3 hr of solar radiation). RH was anticorrelated with temperature, with an average of 38% and a standard deviation of 17%. The observed diurnal cycle of wind direction was consistent with the pattern described by Zhong et al. [2004]: Northwesterly winds prevailed during daytime (0800 to 2100 hr); between midnight and early morning, easterly and southeasterly winds prevailed for 34 (of 45) days. Easterly and southeasterly winds represented downslope flows [Zhong et al., 2004] that were likely associated with biogenic VOCs emitted from the mountains' coniferous trees (e.g., Sequoia National Forest), the

chemistry of which being distinct from anthropogenic pollutants (e.g., aromatic and alkane hydrocarbons).

3.2.2 Spectroscopic measurements

3.2.2.1 Bulk particle organic functional groups

PM_1 and $PM_{2.5}$ filter (Teflon filters with pore size of 1 μm) samples were collected for FTIR analysis. Five PM_1 samples were collected daily, representing morning (0600–1200 hr), early afternoon (1200–1500 hr), late afternoon (1500–1800 hr), evening (1800–2300 hr), and nighttime (0000–0600 hr) periods (local time is used throughout the text). Improved time resolution of FTIR PM_1 samples (compared to previously reported 12- or 24-hr samples in Russell et al., [2011]) allows analysis of diurnal variations of organic functional groups. Shorter sampling times also greatly enhanced statistical significance of data analysis (e.g., correlation analysis) and reduced uncertainties caused by loss of semivolatile compounds. The one $PM_{2.5}$ sample collected each day (0000–2300 hr) that overlapped the multiple PM_1 sample collection times represented daily average $PM_{2.5}$ concentrations. Sample preparation and postprocessing have been detailed previously [Gilardoni et al., 2009; Liu et al., 2009]. Briefly, the filters were scanned using a Bruker Tensor 27 FTIR spectrometer with a deuterated triglycine sulfate (DTGS) detector (Bruker, Waltham, MA) before and after sample collection. Collected samples were immediately stored in a freezer ($<$ 0°C). An automated algorithm was used to conduct background subtraction, spectrum baselining, peak fitting, and peak integration procedures [Day et al., 2010; Russell et al., 2009]. Mass concentrations of organic functional groups, including alkane, hydroxyl, carboxylic acid, amine, carbonyl, organonitrate, alkene, aromatic, and organosulfate groups, were quantified. We excluded alkene and aromatic groups from this study because they were below the detection limit of the FTIR measurements for all samples.

3.2.2.2   Single-particle microscopy of organic functional groups

Single particles were impacted on Si_3N_4 windows on 18, 20, 22 May and 13 June. One morning and one afternoon sample were collected on each collection day. Stored samples were frozen below 0°C. Sample analysis was performed at the Advanced Light Source (Lawrence Berkeley National Laboratory, CA) on beamline 5.3.2. Single-particle X-ray absorption spectra were acquired using a combination of scanning transmission X-ray microscopy (STXM) and near-edge X-ray absorption fine structure (NEXAFS) spectroscopy [Russell, 2002], which provided relative quantification of single-particle organic functional groups, including alkane, hydroxyl, ketone, alkene, and carboxylic acid groups. Functional group abundance was quantified using an automated algorithm developed by Takahama et al. [2010].

3.2.2.3   Elemental concentrations

A total of 150 PM_1 and 46 $PM_{2.5}$ filter samples used for FTIR analysis (65% and 100% of PM_1 and $PM_{2.5}$ samples, respectively) were selectively analyzed using X-ray fluorescence (XRF) at Chester Laboratories (Chester LabNet, Tigard, Oregon). Concentrations of 38 elements (heavier than Ne) were quantified. Elements Al, Si, S, K, Ca, Fe, Co, Zn, and Br were above detection limit in 80% of the samples.

3.2.3   Size-resolved organic and inorganic mass fragments for bulk and single particles

A high resolution time-of-flight aerosol mass spectrometer (HR-ToF-AMS; Aerodyne, Billerica, MA) was deployed to provide high time-resolution measurements of nonrefractory components, including OM, sulfate, nitrate, ammonium, and chloride. Particles passing through a 100-μm pinhole are focused and accelerated by an aerodynamic lens. The accelerated particles impact a heated surface (600°C), and the nonrefractory components flash vaporized and ionized. The ionized vapor fragments are subsequently analyzed by a time-of-flight mass spectrometer [Canagaratna et al., 2007]. The resulting high mass resolution allows the HR-

ToF-AMS to separate ions that would otherwise overlap in a relatively low-mass resolution quadrupole detector (in a Quadrupole-AMS). As a result, the detector provides detailed quantitative elemental compositions from which the O/C, an indicator of the oxidation state of ambient aerosols [Jimenez et al., 2009], can be calculated. The ionization efficiency (IE) of nitrate, which is used to calculate the mass of the fragments, was calibrated using 350 nm NH_4NO_3 particles (selected by a scanning differential mobility analyzer) every 3-5 days during the campaign. The relative IE (RIE) of ammonium, derived from the NH_4NO_3 calibration, was 4.1 during this study (the default RIE is 4.0 in the standard AMS data analysis software). Particle sizes, measured by the time-of-flight between a rotating chopper and the vaporizer [Jayne et al., 2000], provide size-resolved chemical composition measurements of submicron particles. A light-scattering (LS) module, coupled with the HR-ToF-AMS, optically detects single particles from a 405-nm laser before particles reach the vaporizer. Light pulses scattered by the particles trigger acquisition of single-particle mass spectra [Cross et al., 2007], enabling real-time measurements of single-particle chemical compositions. The "mass spectrum" (MS) mode (including high S/N "V" mode and high mass resolution "W" mode), the "time-of-flight" (TOF) mode, and the "LS" mode alternated during operation, with a $\sim$5-min time resolution for each measurement cycle.

The collection efficiency (CE) of the AMS measurements was evaluated by comparing AMS-measured particle mass to the mass derived from a scanning differential mobility analyzer (DMA; described in Section 2.3). Comparisons were made for particles of vacuum aerodynamic diameters (d_{va}) smaller than 700 nm and d_{va} smaller than 1 μm (Figure 3.1). The 700-nm size cut was selected (in addition to 1 μm) because smaller particle sizes (60 to 700 nm d_{va}) have nearly 100% transmission efficiency [Jayne et al., 2000] and likely compare better with the DMA measurements in the same size range. AMS-measured PM_{700nm} and PM_1 were calculated by summing the concentrations of the individual components, each of which was derived by integrating their mass size distributions measured in TOF mode. A factor of 2 was applied to the integrated concentrations (i.e., multiply by 2) to scale the integrated concentration (from the TOF-mode measurements)
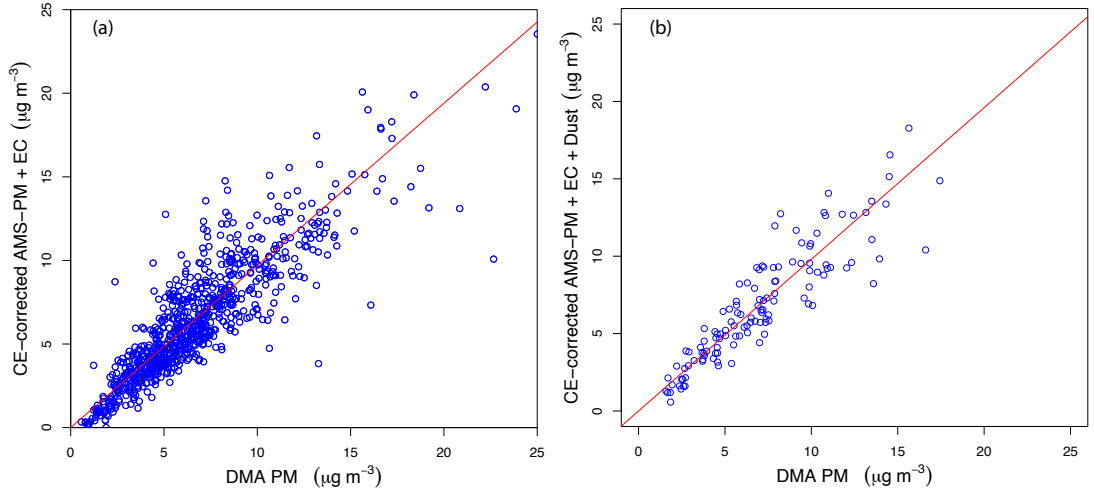
Figure 3.1: (a) Comparison of DMA-measured PM_{500nm} (d_m) with the sum of concentrations for AMS-measured PM_{700nm} (d_m) and EC. Correlation coefficient and slope are 0.88 and 0.97, respectively. Hourly-averaged concentrations were used to match the 1-hr time resolution of EC measurements; (b) comparison of DMA-measured PM_{700nm} (d_m) with the sum of concentrations for AMS-measured PM_1 (d_m), EC, and dusts. Correlation coefficient and slope are 0.90 and 0.98, respectively. Averaged concentrations of 3 or 6 hr (time resolution for FTIR measurements) were used for comparison. Dust was assumed to be a mixture of metal oxides and salts, including SiO_2, Al_2O_3, Fe_2O_3, Na_2O, K_2O, TiO_2, BaO, MnO, $CaCO_3$, and $MgCO_3$ [Usher et al., 2003]; their concentrations were calculated from corresponding elemental concentrations quantified by XRF. In both figures, a CE of 0.8 was used for AMS measurements. The red line in each panel shows the best linear fit for the data points.

to the concentration measured from the MS-V mode. To account for the missing refractory components, elemental carbon (EC) and the sum of EC and dust were added to PM_{700nm} and PM_1, respectively, assuming that dust mainly existed in the larger particles (700 nm–1 μm d_{va}). A density (ρ) of 1.4 g cm^{-3} was applied to convert the DMA-measured number concentration to mass concentration, assuming spherical particles [Ahlm et al., 2012]. The density was calculated by converting the vacuum aerodynamic diameter (d_{va}) measured by the AMS to the mobility diameter measured by the SMPS (d_m), using the equation $d_m = (d_{va}/\rho)\rho_0$ [DeCarlo et al., 2004], where ρ is the effective density and $\rho_0 = 1.0$ g cm^{-3}. Ahlm

et al. [2012] found that $\rho = 1.4$ g cm^{-3} resulted in the best agreement between the SMPS-derived and AMS-measured mass size distributions. Concentrations were calculated by integrating the DMA-derived mass size distributions for particles smaller than 500 nm and 700 nm in mobility diameter (d_{m}), which corresponded to 700 nm and 1 μm in d_{va} $(d_{\mathrm{m}} = d_{\mathrm{va}}/\rho)$, respectively. A set of CE (0.5–1) values was tested, and a CE of 0.80 resulted in the best comparison of the AMS- and DMA-derived masses (slopes are close to 1) for both PM$_{700nm}$ and PM$_1$ (Figure 3.1). Therefore, a CE of 0.8 was assigned to each of the 5-min AMS-measured organic and inorganic components and the PMF-factors throughout the campaign.

3.2.4 Molecular organic markers

Speciated organic marker compounds were measured with 1- or 2-hr resolution using thermal desorption aerosol gas chromatograph-mass spectrometer (TAG) [Williams et al., 2006; Worton et al., 2010]. The sampling strategy and configuration of TAG in this study are detailed in Zhao et al. [2012] (manuscript in preparation, 2012). Briefly, aerosols (gases and particles) passed through a PM2.5 cyclone (SCC BGI Inc., Waltham, MA; $\sim$5 m above ground level) are collected by a collection-thermal desorption cell. Collected particles are thermally desorbed and transferred into gas chromatograph-mass spectrometer for quantification. Gas- and particle-phase organic marker compounds are measured by periodically alternating an active carbon denuder situated downstream of the sampling inlet. The molecular source markers used in this study are from the TAG measurements (particle-phase marker compounds are used) unless otherwise specified.

In addition to in situ measurements using TAG, organic marker compounds were measured from daily filter (prebaked quartz fiber filters) samples that were collected (synchronizing the FTIR PM$_{2.5}$ sampling time) by high-volume filter samplers (Tisch Environmental Village of Cleves, OH) from 15 May to 30 June 2010. Multiple samplers were operated simultaneously so that multiple sets of samples were collected. One set of the samples was extracted using 125 mL 1:1 (v/v) dichloromethane and methanol mixture for 24 hr in a Soxhlet extractor. Filter extracts were evaporated to dryness, followed by derivatization using 250 μL

N,O-bis (trimethylsilyl) trifluoroacetamide (BSTFA) with 1% trimethylchlorosilane (TMCS) and 100 μL pyridine [Jaoui et al., 2004]. The derivatized sample was analyzed by GC-ion trap mass spectrometer (GC-MS; Thermoquest Model GCQ+, Austin, TX), with analysis procedures described previously [Kleindienst et al., 2007, 2012; Offenberg et al., 2011]. Another set of samples was spiked with deuterated internal standards (alkanes, polycyclic aromatic hydrocarbons, and cholestane) and extracted using accelerated solvent extraction (Dionex ASE 300) with dichloromethane and methanol (1:1). Extracts were then concentrated to 250 μL and analyzed using an Agilent 7890 GC coupled to an Agilent 5975 MS in electron impact (EI) ionization scan mode [Sheesley et al., 2004]. A third set of the samples was extracted in 15 mL high-purity methanol (LC-MS Chromasolv grade, Sigma-Aldrich) by ultrasonication for 45 min. The extracts were dried under a gentle stream of N_2 gas. Dried extracts were reconstituted using 250 μL 1:1 (v/v) solvent mixture of 0.1% acetic acid in water (LC-MS Chromasolv grade, Sigma-Aldrich) and 0.1% acetic acid in methanol (LC-MS Chromasolv grade, Sigma-Aldrich). Reconstituted samples were shaken and sonicated for 5 min before being analyzed by an Agilent ultra performance liquid chromatography (UPLC) system coupled to a Agilent 6520 Series Accurate-Mass high resolution quadrupole time-of-flight mass spectrometer (Q-TOFMS) equipped with an electrospray ionization (ESI) source operated in the negative ion mode (UPLC/ESI-HR-Q-TOFMS). Detailed operating conditions and spectral analyses are presented in [Zhang et al., 2011].

3.2.5 Additional measurements

Other supporting particle-phase and gas-phase measurements included submicron particle number size distributions measured by a custom-built DMA with a time resolution of 11 min [Ahlm et al., 2012], elemental carbon measured using a Sunset real-time EC/OC analyzer (Oregon, USA), ozone monitored by a Dasibi 1008 PC ozone monitor, and OH radicals measured by a ground-based tropospheric hydrogen oxides sensor (GTHOS).

Meteorological measurements included temperature and relative humidity
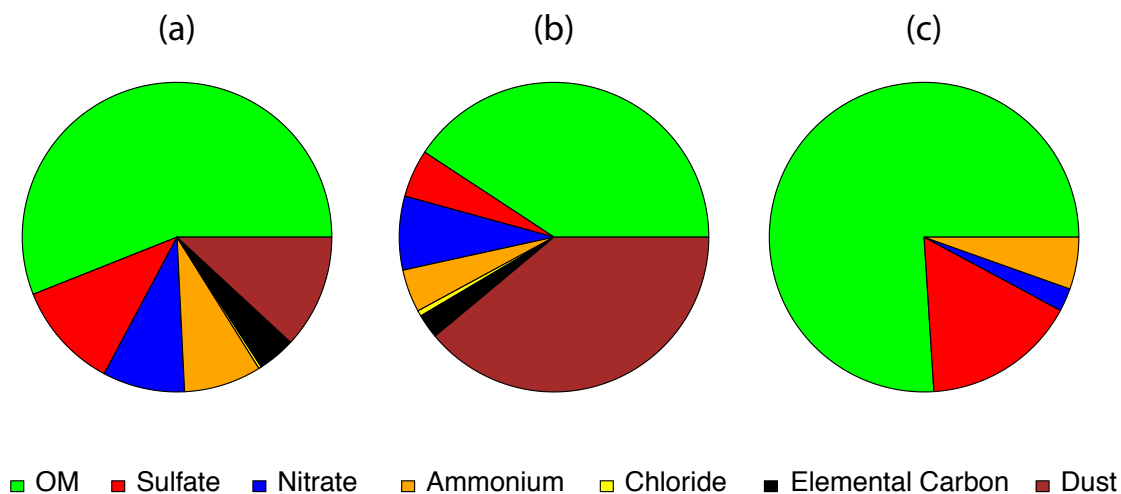
Figure 3.2: Campaign average composition of (a) PM_1, (b) $PM_{2.5}$, and (c) PM_{150nm} [Ahlm et al., 2012]. The OM concentration in PM_1 and PM_{150nm} was measured by the AMS. The OM in $PM_{2.5}$ was calculated by scaling the AMS-measured OM_1 by the FTIR-measured $OM_{2.5}$-to-OM_1 ratio. The concentration of dust in (a) and (b) was calculated using the XRF-measured dust elements in PM_1 and $PM_{2.5}$ as described in Figure 3.1. EC was not shown in PM_{150nm} because ultrafine EC measurements were not available.

(RH) monitored by a Vaisala HMP45C RH/T sensor, and wind direction and wind speed recorded using an R. M. Young 5103 Wind Monitor.

3.3 Results

OM was the major component in submicron particle mass (56%), followed by dust (12%), sulfate (11%), nitrate (9%), ammonium (8%), and EC (4%) (Figure 3.2a). In comparison, for particles smaller than 150 nm (PM_{150nm}), OM accounted for 76% of the particle mass [Ahlm et al., 2012] (Figure 3.2c).The submicron OM (OM_1) concentration measured by FTIR varied from 0.4 to 11.5 μg m^{-3}, averaging 2.4 μg m^{-3} for the entire campaign (Table 3.1). This OM was substantially lower than the OM measured in Mexico City (9.9 μg m^{-3}) and in the vicinity of Houston (4.9 μg m^{-3}), using the same technique [Liu et al., 2009; Russell et al., 2009]; this suggested a lower PM pollution level at Bakersfield during CalNex than that in
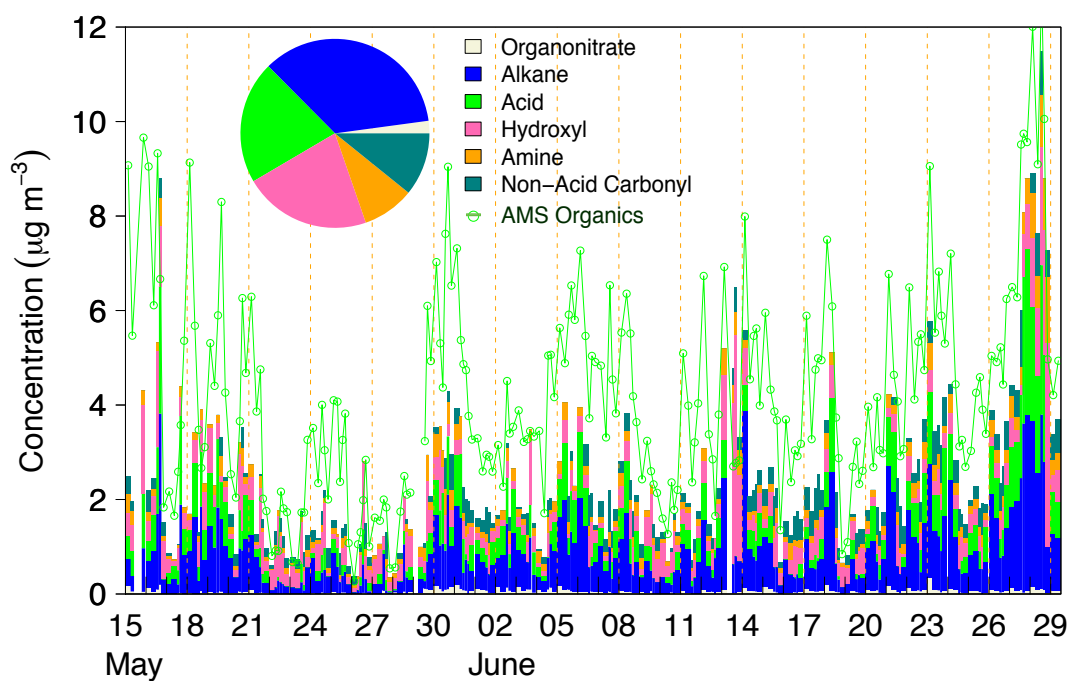
Figure 3.3: Time series of FTIR-measured organic functional group concentrations (stacked bars) in PM_1 and AMS-measured OM (green line). The pie chart shows campaign average functional group composition in PM_1.

Mexico City and Houston. AMS- and FTIR-measured OM closely tracked each other (Figure 3.3) with a correlation coefficient (r) of 0.77. Linear regression of the two quantities (intercept forced to zero) suggested that the FTIR-measured OM was on average nearly 70% of the CE-corrected AMS-measured OM. Given the measurement uncertainties (25%–30% for the FTIR and AMS measurements), the differences lie within the expected range for the two independent measurements. However, the possibility of desorption of semivolatile components from the 3- or 6-hr filter samples could not be ruled out, although the comparability of the AMS-FTIR mass differences for both the 3-hr and 6-hr samples suggests that volatile losses did not increase with sampling time as is usually expected [Mader et al., 2001].

Major functional groups contributing to OM_1 included alkane (35%), hydroxyl (22%), and carboxylic acid (21%) groups, among which carboxylic acid and

Table 3.1: Campaign average OM (measured by FTIR and AMS) and organic functional group (measured by FTIR) concentrations (μg m^{-3}) in PM$_1$ and PM$_{2.5}$. Functional group mass fractions are shown in parentheses.

	FTIR$_{PM1}$	FTIR$_{PM2.5}$	AMS
OM	2.42±1.68	3.24±1.42	3.38±2.20
Alkane	0.85±0.73 (35%)	1.09±0.45 (34%)	-
Hydroxyl	0.53±0.58 (22%)	0.98±1.00 (30%)	-
Carboxylic acid	0.51±0.58 (21%)	0.61±0.29 (19%)	-
Nonacid carbonyl	0.26±0.24 (11%)	0.14±0.20 (4%)	-
Amine	0.22±0.18 (9%)	0.33±0.15 (10%)	-
Organonitrate	0.05±0.05 (2%)	0.07±0.06 (2%)	-
Organosulfate	BDL	0.02±0.04 (1%)	-

alkane groups correlated with an r of 0.90. Similar correlation between these two groups was observed previously [Liu et al., 2011], suggesting that carboxylic acid and alkane groups formed from the same source and likely via the same mechanism, likely by photooxidation of gas-phase alkane molecules [Russell et al., 2011]. Nonacid carbonyl groups, typically associated with oxidation products of aromatic compounds [Lee and Lane, 2010], accounted for 11% of the OM. Amine groups (9% OM) were likely associated with bovine emissions in the region, as animal husbandry operations are major sources of atmospheric ammonia and amines [Schade and Crutzen, 1995]. Organosulfate groups were below detection limit for all submicron particles and identified as 1% of OM$_{2.5}$ (Table 3.1), which is consistent with the low mass of organosulfate molecules ($\sim$0.2% OM) measured by UPLC/ESI-HR-Q-TOFMS at the same site.
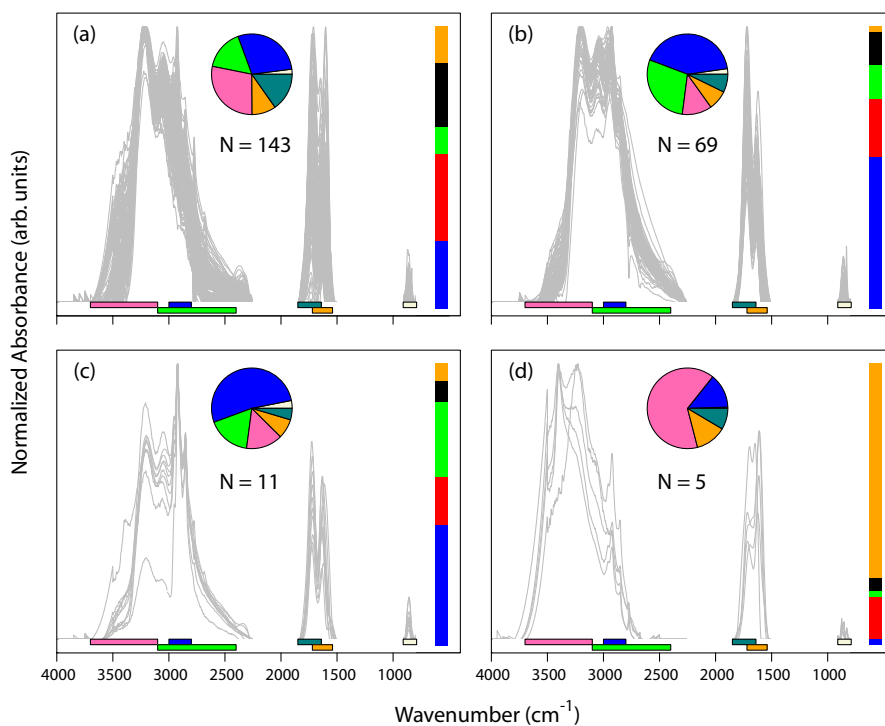
Figure 3.4: FTIR spectra during CalNex for (a) cluster 1 (143 spectra), (b) cluster 2 (69 spectra), (c) cluster 3 (11 spectra), and (d) cluster 4 (5 spectra). Horizontal bars represent functional group absorbance ranges: hydroxyl (pink), carboxylic acid (green), alkane (blue), nonacid carbonyl (teal), amine (orange), organonitrate (beige). Pie chart shows the average functional group composition in each cluster. Vertical bar represents the average relative contributions of the FTIR factors in each clusters, with colors indicating alkane SOA (blue), aromatic SOA (red), nighttime OA (green), PO SOA (black), and vegetative detritus (orange).

To identify particle types, normalized FTIR (PM_1) spectra were grouped using the hierarchical clustering technique with the Ward algorithm [Liu et al., 2009; Russell et al., 2009; Ward, 1963]. In the Ward algorithm, each IR spectrum is initially considered as one category. The spectra are progressively merged by minimizing the sum-of-square errors. By selecting a level of branching (k), the spectra can be grouped into k clusters. Using $k \geq 5$ resulted in at least two clusters that had similar functional group compositions, indicating splitting of certain clusters into smaller clusters that are not distinguishable. Hence k = 4 was selected as the largest number of clusters without splitting, resulting in four chemically distinct clusters (Figure 3.4). Particles in Cluster 1 had the largest

fraction of nonacid carbonyl groups (15%) among the four clusters, with alkane, hydroxyl, and carboxylic acid groups contributing 29%, 28%, and 16% to the OM, respectively. Cluster 2 particles were mainly composed of alkane (42%) and carboxylic acid (29%) groups. Together, Cluster 1 and Cluster 2 accounted for 93% of the submicron FTIR spectra. Spectra in Cluster 3 were characterized by sharp alkane group peaks and had the largest fraction of alkane groups (52%) among the four clusters. Cluster 4 represented particles that were mainly composed of hydroxyl groups (65%). The distinct chemical composition of the four clusters indicated differing contributions from various sources and processes throughout the study.
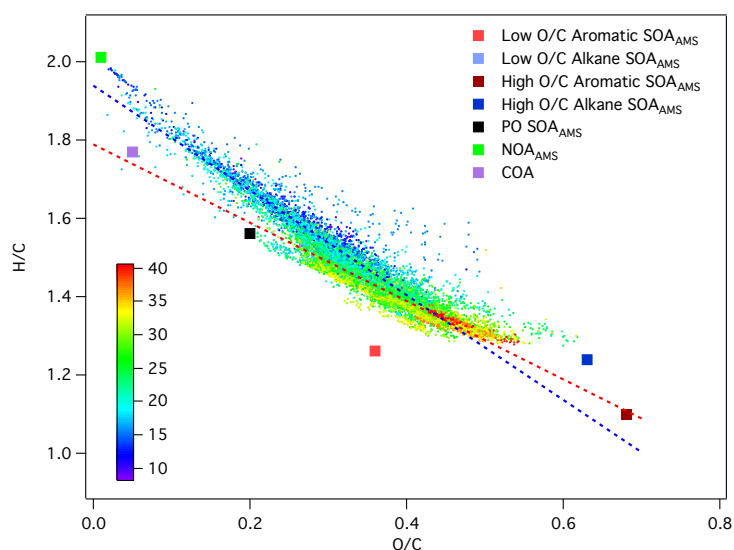
Figure 3.5: Van Krevelen diagram (H/C versus O/C) from the AMS measurements. The points are colored by temperature (°C), with the scale shown by the vertical bar. The points with temperature greater and less than 25 °C are fitted by the red and blue dashed lines, respectively. The slopes of the red and blue lines are -0.93 and -1.3, respectively. The intercepts of the red and blue lines are 1.76 and 1.91, respectively.

We found m/z 44 (CO_2^+) accounted for 10% of AMS-measured OM. AMS-measured sulfate, nitrate, and ammonium contributed almost equally to PM_1, the mass fraction ranging from 8% to 11% on average. Using these three components in an ion balance calculation revealed that the PM_1 positive ions (ammonium)

were 20% higher than that of the negative ions (2x sulfate + nitrate). The time series of the positive and negative ions correlated with an r of 0.99, indicating that these ions likely formed and condensed simultaneously, i.e., sulfuric acid and nitric acid interact with ammonia to form ammonium sulfate and ammonium nitrate salts, respectively, followed by condensation of the salts into preexisting particles. High ammonium levels in Bakersfield aerosols are consistent with large ammonia emissions in the SJV [Sorooshian et al., 2008]. The excess ammonium (relative to inorganic sulfate and nitrate) was likely formed by reaction of ammonia with secondary organic acids, such as phthalic acid [Na et al., 2007; Zhao et al., in preparation]. Because the excess ammonium (relative to inorganic sulfate and nitrate) was ~50% less (in molar concentration) than the FTIR-measured carboxylic acid groups, the aerosol might be slightly acidic.

Elemental ratios (H/C and O/C) measured by the HR-ToF-AMS are illustrated in the Van Krevelen diagram space (Figure 3.5). The Van Krevelen diagram, displayed as H/C versus O/C, has proven to be useful for describing evolution of atmospheric organic aerosols [Heald et al., 2010; Ng et al., 2011]. For example, conversion of alkane groups ($-CH_2-$) to carbonyl groups ($-C(=O)-$) results in a slope of -2 (addition of 1 oxygen and loss of 2 hydrogen atoms), whereas processes that convert alkane groups to hydroxyl groups (–OH) have a slope of 0. Consequently, formation of hydroxycarbonyl or carboxylic acid groups yields a slope of -1. The O/C and H/C in this study ranged from 0.02 to 0.62 and from 1.28 to 1.99, respectively. The points in the Van Krevelen diagram can be grouped into two categories that have different slopes. The relatively high-temperature points have a slope of -0.93, while the slope of the low-temperature points is -1.3 (Figure 3.5). The distinct slope and temperature for the two categories suggest different chemical and physical processes, including oxidation, condensation, volatilization, and mixing, between daytime and nighttime hours. The measured O/C and H/C in both categories strongly anticorrelated (r = -0.94 to -0.92), suggesting these atmospheric processes changed the O/C and H/C along straight lines. The slopes of -0.93 and -1.3 of the linear fit from this study was similar to the slope of -1.1 observed during the SOAR-1 (Study of Organic Aerosol at Riverside) measurements

at Riverside [Heald et al., 2010], but organic aerosol composition at Bakersfield had larger ranges of O/C and H/C than at Riverside (O/C and H/C varied in 0.2-0.5 and 1.4-1.7, respectively, during SOAR-1), which reflects a larger variety of emission sources at Bakersfield.

Compared to PM_1, $PM_{2.5}$ was comprised of a larger fraction of dust components (39%) and a lower fraction of OM (41%) (Figure 3.2b). Dust components were mainly composed of elements Ca, Si, Al, and Fe (more likely by their oxides and salts). OM in $PM_{2.5}$ ($OM_{2.5}$) was largely (75%) in submicron particles. The mass difference between OM_1 and $OM_{2.5}$ (55% of OM_1) can be explained by the hydroxyl groups, suggesting that they were associated with larger particles such as dust components (details in following section). Scaling the AMS-measured OM_1 by the $OM_{2.5}$-to-OM_1 ratio measured by FTIR, the calculated AMS $OM_{2.5}$ was 5.6 μg m^{-3}, which is comparable to the $OM_{2.5}$ ($\sim$6–7 μg m^{-3}) measured during May-June 1999-2001 at Bakersfield [Chow et al., 2006a].

3.3.1 Identification of organic mass sources

The main factors contributing to the OM were identified separately from FTIR (PM_1 and $PM_{2.5}$) and AMS measurements using positive matrix factorization (PMF) method (PMF2) [Paatero and Tapper, 1994]. PMF procedures are described in the appendices. The factors were identified primarily by their correlations with particle-phase source markers, facilitated by comparisons of factor composition and spectra to factors identified from past studies. The correlations were done at the highest time resolution possible with the tracer measurements. The time resolution of the AMS, TAG, and XRF measurements was $\sim$5 min, 1-2 hours, and 3-4 hours, respectively. Subscripts "FTIR," "FTIR2.5," and "AMS" denote the factors commonly identified from FTIR PM_1, FTIR $PM_{2.5}$, and AMS measurements. Detailed factor identification procedures are presented below.

3.3.1.1 Factors identified from FTIR PM_1 and $PM_{2.5}$ measurements

Five factors were identified from FTIR PM_1 and $PM_{2.5}$ measurements (Appendix A), respectively. The PM_1 and $PM_{2.5}$ factors were similar in factor spectra
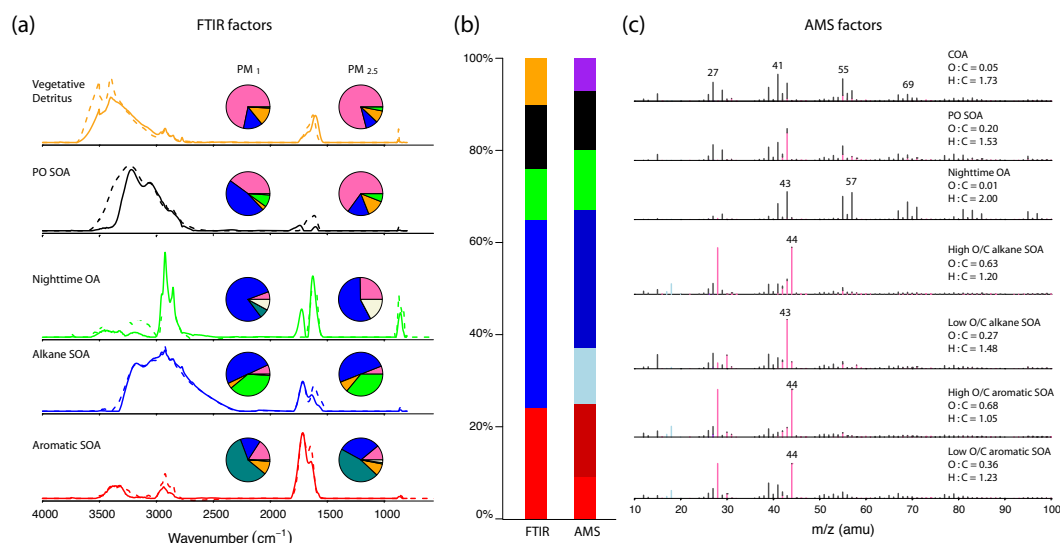
Figure 3.6: (a) FTIR factor spectra derived from PM_1 (solid line) and $PM_{2.5}$ (dashed line) measurements. The pie charts show factor compositions, with functional groups as follows: alkane (blue), hydroxyl (hot pink), carboxylic acid (green), nonacid carbonyl (teal), and organonitrate (beige) functional groups. (b) Campaign average mass fractions of FTIR PM_1 and AMS factors. Colors indicate aromatic SOA (red) (red and dark red for the AMS low and high O/C aromatic SOA factors, respectively), alkane SOA (blue) (light blue and dark blue for the AMS low and high O/C alkane SOA factors, respectively), nighttime OA (green), PO SOA (black), and vegetative detritus (orange), and COA (purple) factors. (c) Normalized mass spectra of AMS factors.

and compositions (Figure 3.6a), indicating nearly the same factors were found for OM_1 and $OM_{2.5}$, which is consistent with the fact that 75% of $OM_{2.5}$ was in OM_1.

The first factor covaried in time with polycyclic aromatic hydrocarbon (PAH) oxidation products 2H-1-benzopyran-2-one, dibenzofuran, 1,8-naphthalic acid/anhydride, benzophenone, 4-hydroxy-9-fluorenone, and phthalic acid/anhydride [Kautzman et al., 2010; Lee and Lane, 2009, 2010; Webb et al., 2006] measured by TAG (Table 3.5) and phthalic acid ($r = 0.7$) measured by GC-MS. The factor composition, largely composed of nonacid carbonyl groups (59%), was consistent with oxidation products for aromatic hydrocarbons [Chan et al., 2009; Jaoui et al., 2008; Russell et al., 2011], including PAH and light aromatic compounds. Therefore, this factor was identified as an aromatic SOA factor,

representing SOA formed from aromatic hydrocarbons (PAHs and light aromatic compounds) that were likely emitted from gasoline- and diesel-powered vehicles [Schauer et al., 1999; 2002b]. This factor had the greatest contribution (31%) to Cluster 1 particles (Figure 3.4).

The time series of the second factor correlated most strongly to the time series of C_{11}-C_{14} ketones (undecanone, dodecanone, tridecanone, and tetradecanone) with r of 0.63 to 0.77 for the PM_1 factor and 0.58 of 0.90 for the $PM_{2.5}$ factor (Table 3.5 and 3.6). Note that the enhanced correlations for the $PM_{2.5}$ factor were likely caused by the longer duration of these daily samples, which averaged out any offsets between the time of formation in the gas and particle phases. The long-chain (C_{11}-C_{14}) ketones are suggested to be first-generation alkane oxidation products [Lim and Ziemann, 2005, 2009], indicating that this component likely formed from alkane oxidation processes. The factor spectra and functional group compositions were nearly identical to the fossil fuel combustion factors identified from the shipboard measurements near Houston and the ground-based measurements in Southern California, which were suggested to originate from alkane oxidation processes [Hawkins and Russell, 2010; Liu et al., 2011; Russell et al., 2009]. Thus this factor was denoted as alkane SOA factor.

The third factor from the PM_1 factor analysis correlated (r of 0.65) to pinonaldehyde measured by TAG and 3-Hydroxyglutaric acid (r of 0.5) measured by GC-MS, which are markers for biogenic SOA formed from oxidation of α-pinene [Hallquist et al., 1999; Claeys et al., 2007]. This factor, observed in high concentrations at night, was largely composed of alkane groups (79%) and had the largest mass fraction (8%) of organonitrate groups of all the factors; its composition was consistent with products from α-pinene and β-pinene oxidation by NO_3 radicals [Hallquist et al., 1999; Wangberg et al., 1997]. However, the factor showed a weaker correlation ($r \leq 0.50$) to PAH compounds, suggesting a contribution of primary anthropogenic sources to this factor. Thus, this factor was determined to be the nighttime biogenic SOA factor mixed with less oxygenated hydrocarbon-like anthropogenic emissions and denoted as nighttime OA. The $PM_{2.5}$ nighttime OA factor had similar composition to the PM_1 nighttime OA factor, being dominated

by alkane (57%) and organonitrate (17%) groups, but also contained a larger hydroxyl group mass and enhanced correlations to dust elements. Thus, the $PM_{2.5}$ nighttime OA factor likely included a small fraction of dust-related organic components.

The fourth factor of PM_1 correlated (r of 0.6) to the crude oil marker V (vanadium) [Khalaf et al., 1982]. Its IR spectrum was comparable to the "oil combustion/refining" factor spectrum identified from the shipboard measurements near Houston [Russell et al., 2009]. High mass fraction (40% to 65%) of hydroxyl groups indicates that this factor was likely secondarily formed in the atmosphere. The factor was identified as a petroleum operation SOA (PO SOA) factor, representing the oil extraction and refinery operations north and northwest of Bakersfield. The most commonly used method for oil extraction, steam injection, heats crude oil using high-temperature steams. The heated crude oil has reduced viscosity thereby it is easier to flow [Fatemi and Jamaloei, 2011]. The high-temperature steam comes from steam generators, which usually burns crude oil and likely emits V-rich pollutants that include NO_x, CO, and hydrocarbons [Myers, 1986]. The corresponding $PM_{2.5}$ factor spectrum was comparable to that of the PM_1 factor (Figure 3.6a), suggesting that they are the same factors. It is worth noting that V in $PM_{2.5}$ correlated well with dust elements, such as V correlating to Si with an r of 0.96 in $PM_{2.5}$ that is much greater than the correlation of V and Si ($r = 0.35$) in PM_1, indicating that V in $PM_{2.5}$ was largely from dust sources [Chow et al., 2003], resulting in a weakly negative correlation of the PO SOA factor and V in $PM_{2.5}$. The average concentration of the PO SOA factor peaked in the afternoon, which was consistent with the daytime northwesterly winds from the direction of the oil drilling and the associated petroleum operation activities located to the northwest of the sampling site.
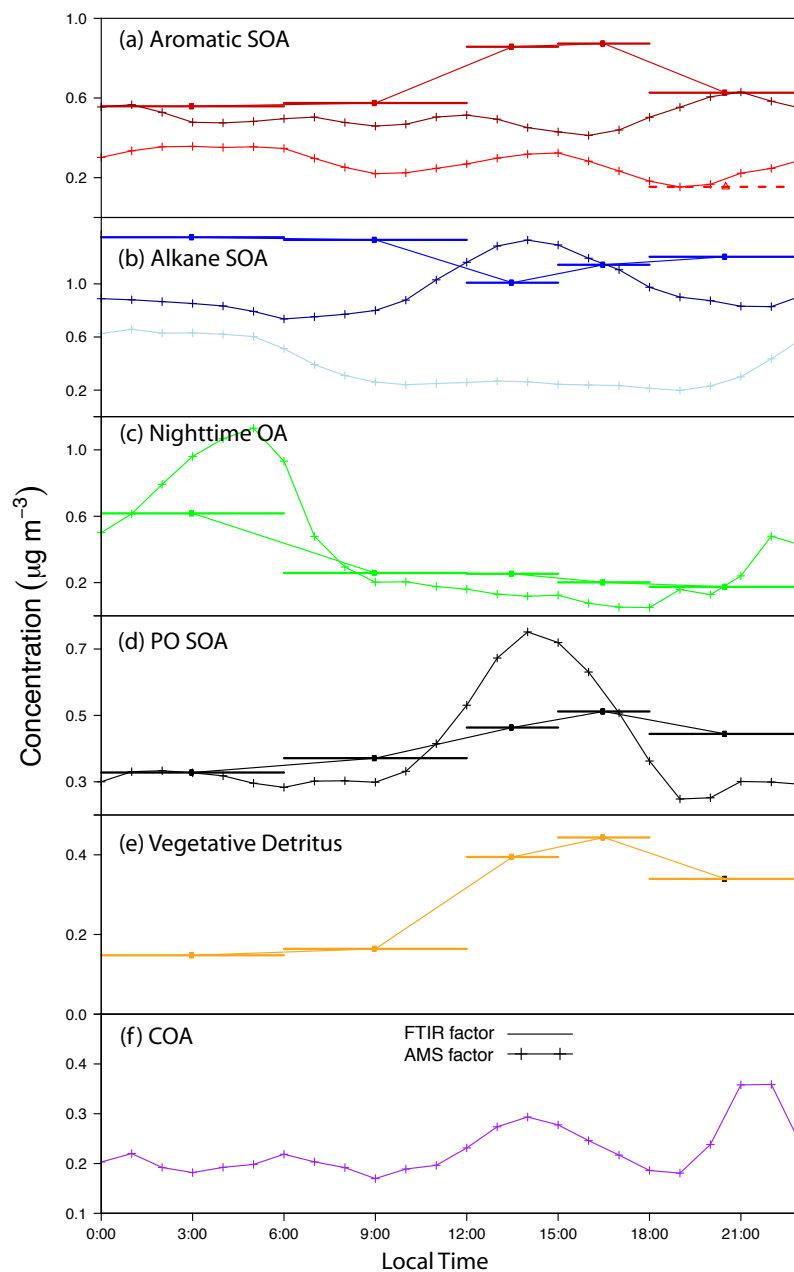
Figure 3.7: Diurnal cycles for (a) aromatic SOA_{FTIR} (red), low O/C aromatic SOA_{AMS} (red), and high O/C aromatic SOA_{AMS} (dark red), (b) alkane SOA_{FTIR} (blue), low O/C alkane SOA_{AMS} (light blue), and high O/C alkane SOA_{AMS} (dark blue), (c) nighttime OA_{FTIR} (green) and nighttime OA_{AMS} (green), (d) PO SOA_{FTIR} (black) and PO SOA_{AMS} (black), (e) vegetative detritus (orange), and (f) COA (purple) factors. In each panel, horizontal bars represent FTIR factors (PM_1 samples), with bar lengths indicating sampling duration; lines with markers represent AMS factors.

Table 3.2: Summary of O/C values for primary or HOA components from previous studies and O/C of SOA components in this study.

Source type	O/C[a]	References
Primary OA	< 0.1	This study
HOA (New York City)	0.06	Sun et al., 2011
HOA (Mexico City aircraft)	0.06	DeCarlo et al., 2010
Diesel exhaust	0.03	Aiken et al., 2008
	0.05	Nakao et al., 2011
Gasoline exhaust	0.04	Aiken et al., 2008
Cooking emission	0.08-0.13	He et al., 2010
COA	0.11	Huang et al., 2010
COA	0.05	This study
Nighttime OA	0.01	This study
COA	0.05	This study
Secondary OA	0.20–0.68	This study
Alkane SOA	0.27–0.63	
Aromatic SOA	0.36–0.68	This study
PO SOA	0.20	

[a] AMS-measured O/C excludes organonitrate and organosulfate contributions to O as the nitrate and sulfate components were not distinguishable from inorganic.

The fifth factor of the PM_1 and $PM_{2.5}$ solutions correlated to the dust elements Si, Al, Ca, and Mg, suggesting that the factor represented organic components associated with dust particles. Double peaks at 2850 cm^{-1} and 2920 cm^{-1}, along with a strong spectral absorption at 3500 cm^{-1}, indicated the existence of methylene and phenol groups, which likely originated from plant wax [Hawkins and Russell, 2010] and plant lignin compounds [Cass, 1998], respectively. The large fraction of hydroxyl groups (71% to 79%) in this factor was consistent with saccharide-type compounds in plant materials [Bianchi et al., 1993]. Association of the factor with dust and plant components suggests that this factor was likely from vegetative detritus that resuspended with dust particles. This factor was denoted as a vegetative detritus factor and appeared predominately in Cluster 4 particles (Figure 3.4).

3.3.1.2   Factors identified from AMS measurements

Six or seven factors were identified from the AMS measurements. The factors in the 6- and 7-factor solutions had similar factor time series and mass spectra (Figures 3.19 and 3.20). Compared to the 6-factor solution, an additional factor with high O/C (named as high O/C alkane SOA and discussed below) was identified in the 7-factor solution. We present both the 6- and 7-factor solutions to show the consistency and variability of the PMF factors. The factor m/z spectra, O/C, and H/C are shown in Figure 3.6c and Figure 3.19.

The first factor correlated strongly (r of 0.81 to 0.90) to particle-phase PAH marker compounds (Table 3.7 and 3.8), which are usually coemitted with light aromatic compounds in vehicular exhausts. This factor was characterized by a strong peak at m/z 44 and had an O/C of 0.36, which was higher than the typical O/C of HOA components ($\sim$0.10) observed in laboratory and field studies (Table 3.2) but in the O/C range of 0.20 to 0.60 for SV-OOA (semivolatile OOA) identified from a number of AMS measurements [Ng et al., 2010]. Thus, it suggests that this factor was oxidized but associated with a low oxidation state and, so, was termed low O/C aromatic SOA factor.

Compared to the low O/C aromatic SOA factor, the second factor more closely correlated to long-chain alkanes and alkane SOA components but showed a weaker correlation to PAH hydrocarbons (Table 3.7 and 3.8), suggesting that this factor likely originated from alkane-related sources. The H/C of this factor was 21% higher than the O/C of the low O/C aromatic SOA factor (Figure 3.6c). This result is consistent with the expectation of a higher H/C for alkane SOA than aromatic SOA: Since alkanes are more saturated than aromatics, alkane SOA is expected to be less oxygenated than aromatic SOA. As the factor O/C (0.27) was higher than expected for primary OM ($\sim$0.10) (Table 3.2), it was identified as a low O/C alkane SOA factor.

The third factor had the highest O/C (0.68-0.72) of all the factors, suggesting that this factor is also secondary but more oxidized than the first two factorspossibly because they formed in later generations [Jimenez et al., 2009]. The factor spectrum was nearly identical and resembled those of LV-OOA (low-

volatility OOA) [Ulbrich et al., 2009]. The time series of this factor correlated most strongly to PAH SOA marker compounds, suggesting that this factor likely represented the oxidation products of aromatic hydrocarbons, including light aromatics and PAH. This factor was identified as a high O/C aromatic SOA factor. The high O/C aromatic SOA factors in the 6- and 7-factor solutions had similar time series, with the former associated with greater mass concentration (Figure 3.19 and 3.20).

The fourth factor, the additional factor identified in the 7-factor solution, had similar mass spectra to the high O/C aromatic SOA factor. This factor correlated to both PAH SOA and alkane SOA markers. While the similarity of the factor spectra and correlations with source markers make it difficult to distinguish this factor and the high O/C aromatic SOA factor, their diurnal cycles were different (Figure 3.7a and 3.7b). The high O/C aromatic SOA factor peaked at noon and in the evening (2000 hr), while the fourth factor had a broad peak centered at 1500 hr. Distinct diurnal cycles suggested different formation pathways. The high O/C aromatic SOA factor and the fourth factor correlated weakly to long-chain alkane compounds (e.g., heptadecane and octadecane in Table 3.8), with the latter having stronger correlations (r of 0.25 to 0.27 for the high O/C aromatic SOA factor and r of 0.37 to 0.38 for the fourth factor). Furthermore, enhanced correlations to alkane compounds of 0.63 to 0.72 resulted from daily-averaged concentration of the fourth factor, but such a large enhancement was not observed under the same conditions for the high O/C aromatic SOA factor (r of 0.37 to 0.46). This suggests that the fourth factor was likely largely linked to alkane-related sources, although contribution of aromatic SOA to this factor cannot be entirely ruled out. Accordingly, the fourth factor was defined as a high O/C alkane SOA factor. The high O/C alkane SOA factor accounted for 71% of total alkane SOA, which includes high and low O/C alkane SOA components. This mass fraction is consistent with mechanism simulation that suggests more than 67% of alkane SOA was fourth and higher generation products after 10 hrs of reactions [Yee et al., 2012].

Concentrations of the fifth factor peaked at night (Figure 3.7c), having been associated with nighttime easterly and southeasterly winds. This pattern compares

to that of monoterpenes and their oxidation products (e.g., pinonaldehyde), which suggests contributions from biogenic sources to this factor. The very low O/C (<0.1) also indicates a contribution from primary OM. The mass spectrum was similar to spectrum of HOA (hydrocarbon-like organic aerosol) [Ulbrich et al., 2007; 2009], indicating unoxidized primary anthropogenic sources. As such, this factor was identified as nighttime OA.

The sixth factor had a stronger correlation to V than any other source markers. In addition, the factor's diurnal cycle matched the diurnal cycle of V, suggesting organic components from petroleum operations. The factor was characterized by m/z 43 (87% $C_2H_3O^+$ and 13% $C_3H_7^+$) with an O/C of 0.20, which is larger than 0.10 that is typical for HOA (Table 3.2). For this reason, this factor is considered secondary rather than primary and termed petroleum operation SOA (PO SOA).

The seventh factor was identified as a cooking organic aerosol (COA) factor for two reasons: The factor spectrum was similar to the previously identified COA factor mass spectra [Huang et al., 2010; Mohr et al., 2012] that were characterized by m/z 27, 41, 55, and 69 with Δm/z of 14, fragments specific for unsaturated fatty acids emitted from cooking activities [He et al., 2010]; and the factor correlated to the food cooking marker hexadecanoic acid (Table 3.7 and 3.8) [Allan et al., 2010; He et al., 2004]. Further, a low O/C (0.05) suggests that this factor was simply recondensed cooking oils from local sources that had undergone little or no oxidation in the atmosphere.

We have focused on the 7-factor solution in the following discussions since it may suggest differences in the oxidation products formed with time.

3.3.1.3   Comparison of FTIR (PM_1 and $PM_{2.5}$) and AMS factors

The FTIR PM_1 and $PM_{2.5}$ factors were similar in compositions but differed in mass. Overall, the reconstructed ratio of OM_1 (the sum of PM_1 factors) to $OM_{2.5}$ (the sum of $PM_{2.5}$ factors) was 0.85, 13% higher than the actual measured $OM_1/OM_{2.5}$ of 0.75. The greatest difference between PM_1 and $PM_{2.5}$ factors was observed in the vegetative detritus factor, the OM being 55% higher in
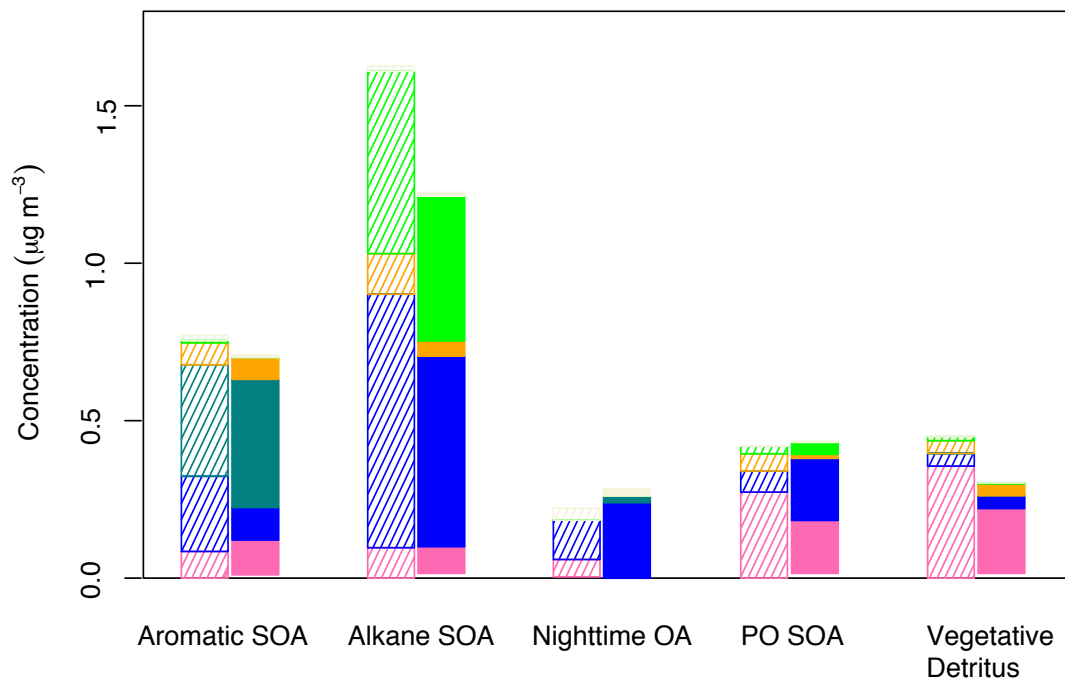
Figure 3.8: Mass concentration comparison of FTIR PM_1 and $PM_{2.5}$ factors. Striped and solid bars indicate PM_1 and $PM_{2.5}$ factors, respectively. Color assignments for functional groups are the same as in Figure 3.

$PM_{2.5}$. This difference was largely (92%) attributed to hydroxyl groups (Figure 3.8), which likely originated from plant materials and then mixed with dusts to result in a larger fraction with bigger particles. The aromatic SOA and alkane SOA factors were 12% and 33% higher, respectively, in $PM_{2.5}$, with the alkane groups accounting for the largest difference in each pair of factors. As aforementioned, the nighttime $OA_{FTIR2.5}$ likely had some dust fractions, indicating incomplete separation of this factor from $PM_{2.5}$ samples, so nighttime $OA_{FTIR2.5}$ was slightly smaller than nighttime OA_{FTIR}. The PO SOA_{FTIR} was higher in the alkane group mass and lower in the hydroxyl group mass compared to the PO $SOA_{FTIR2.5}$, resulting in comparable total OM between the two factors.

The factors identified from AMS measurements show consistencies and differences to the factors derived from FTIR measurements. The low O/C and high

O/C aromatic SOA_{AMS} factors, taken together, correlated to aromatic SOA_{FTIR} with an r of 0.73 (Figure 3.21). The sum of the low and high O/C aromatic SOA_{AMS} factors accounted for 25% of OM, consistent with the OM fraction (24%) of the aromatic SOA_{FTIR} factor (Figure 3.6b). Similarly, good correlation ($r = 0.74$) was observed for the sum of the low and high O/C alkane SOA_{AMS} factors and the alkane SOA_{FTIR} factor, each of which accounted for 41% to 42% of the OM. The difference between the FTIR and AMS high O/C factors can be seen from Figure 3.7: The diurnal cycle of the alkane SOA_{FTIR} is more similar to the low O/C alkane SOA_{AMS} than the total alkane SOA_{AMS}, and the diurnal cycle of the aromatic SOA_{FTIR} is more similar to the high O/C aromatic SOA_{AMS} than the total aromatic SOA_{AMS}. The difference in diurnal cycles may result from the scatter in their correlations as well as the uncertainties of the measurements and factorization. The PO SOA_{AMS} and PO SOA_{FTIR} (correlated with an r of 0.52) contributed 13% to 14% of OM. The campaign-average mass fractions of nighttime OA_{FTIR} and nighttime OA_{AMS} factors were 10% to 13%, with higher fractions of 21% to 24% during 0000–0600 hr. The difference between nighttime OA_{FTIR} and nighttime OA_{AMS} is that NOA_{FTIR} is likely a mixture of primary and secondary components and NOA_{AMS} is primaryincludes a substantial contribution of organonitrate functional groups (and a higher associated O/C from them) whereas the organonitrate mass was not distinguishable from the inorganic nitrate in the AMS. However, the AMS measurements were likely more sensitive to smaller particles that may have included a larger fraction of HOA that was not resolved by the FTIR PMF. These differences likely resulted in the relatively low correlation ($r = 0.52$) between NOA_{FTIR} and NOA_{AMS}. The vegetative detritus factor (10% OM) was identified only from FTIR measurements, likely because this component was mixed with dust in particles of 500 nm and larger, which have reduced transmission efficiency in the AMS aerodynamic lens and could not be detected effectively by the AMS. The COA_{AMS} (7% OM) was not found in the FTIR measurements. This difference between the AMS and FTIR factors may be due to COA components mainly existing as small particles (100–200 nm, as discussed in Section 4.3), where the small-particle collection efficiency of 1-μm Teflon filters drops off [Liu and Lee,

1976] and the small mass in this size range were insufficient for detection.

In summary, factors identified from PM_1 and $PM_{2.5}$ FTIR and AMS measurements showed good agreement in source type, mass fraction, and time series. The missing vegetative detritus factor for the AMS measurements and COA factor for the FTIR measurements contributed 10% of OM in PM_1, and both were within the expected uncertainties for each technique. The high O/C aromatic and alkane SOA factors were mathematically independent ($r < 0.7$) but their mass spectra were chemically similar (cosine similarity was 0.99) (cosine similarity is defined as cosine of the angle between two vectors [Stein and Scott, 1994], values ranging from 0 to 1, with higher values indicating higher similarity), thus source markers are needed to justify separation of these factors; in contrast, the FTIR aromatic and alkane SOA factors were mathematically independent ($r < 0.5$) and their IR spectra were chemically different (e.g., cosine similarity was 0.3), thus source markers are not needed to justify separation of the FTIR factors but provide a link to their precursors. The FTIR and AMS factors suggested that 80% to 90% of OM was secondary, even those measurements conducted near emission sources. Of these SOA components, aromatic and alkane SOA factors accounted for 65% of OM, indicating fossil fuel combustion that was likely from motor vehicles is the largest source at Bakersfield. This finding is consistent with previous source apportionment studies at Bakersfield [Hamilton et al., 2004; Kleeman et al., 1999; Schauer and Cass, 2000]. Also from these studies, wood combustion was identified as a significant source only in winter, likely because residential heating (the main source of wood burning) was not in use during the early summer period [Chow et al., 2006b]. However, the petroleum operation, categorized as having near-zero emissions in recent source inventory in southern SJV (Table 3.10), should be added given its contribution of 14% OM.

3.3.2 Identification of single-particle types

3.3.2.1 Single-particle NEXAFS spectra

Single-particle X-ray spectra (80 particles) were categorized into three major groups based on their spectroscopic similarities (Figure 3.9). To gain further
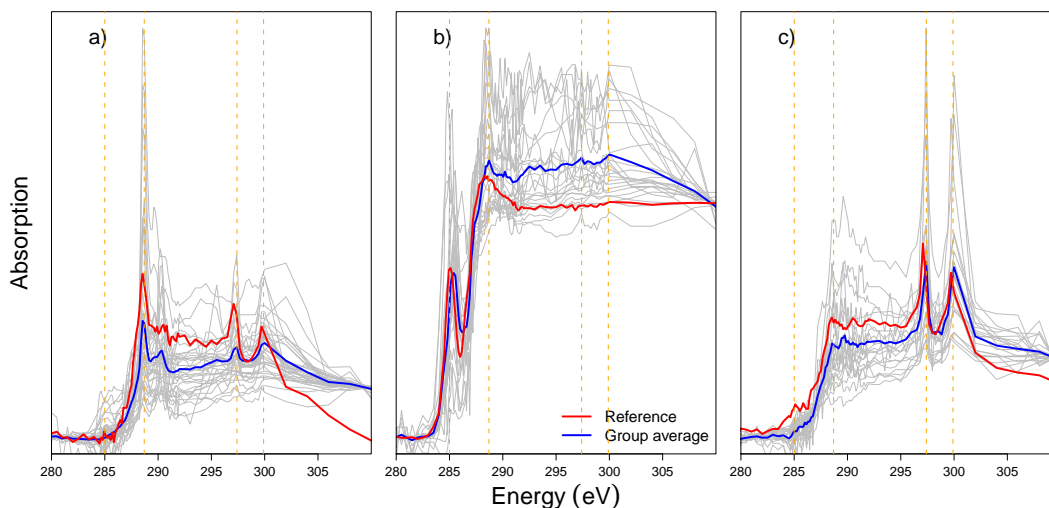
Figure 3.9: Normalized single-particle X-ray spectra for particle types: a) Group I (35 particles), b) Group II (24 particles), and c) Group III (21 particles). Other identifiers include individual particle spectra (gray) and group averages (blue). For comparison, note type "a", "h", and "k" particles (red) [as identified by Takahama et al. 2007], respectively, in panels a), b), and c). Vertical lines (orange) in each panel represent absorptions at energies 285.0, 288.7, 297.4, and 299.9 eV.

insight into their source types, each group was compared to single-particle X-ray spectra for each of the 14 types of particles identified by Takahama et al. [2007]: Group I particles showed strong carboxylic acid group absorption at 288.7 eV. Their particle spectra were comparable to type "a" particles, likely formed from atmospheric processing, which suggests the group's secondary origins. Group II spectra were characterized by strong absorption at 285.0 eV due to sp^2-bonding of soot or black carbon. Since these particles resembled Takahama's "strongly aromatic aerosols" (e.g., type "h" particles) (Figure 3.9b), defined as particles that have strong absorption at 285 eV due to sp^2 carbon bonding, diesel exhaust was the likely origin. Group III particles showed no significant peaks for organic functional groups. The lack of a C=C peak at 285.0 eV and a C-OH peak at ∼287.0 eV, which are characteristic for biomass-burning type particles, essentially excluded the possibility of Group III having a biomass burning source [Braun, 2005; Tivanski et al., 2007], although the C=C peak for such particles is relatively smaller

compared to that of diesel soot particles. Furthermore, high absorbance seen in the K region (at 297.4 and 299.9 eV) was consistent with dust sources, the likely origin of Group III's particles.

3.3.2.2 Single-particle mass spectra

Single-particle mass spectra for 147357 particles were clustered (detailed in Liu et al. [2012]) to reveal three single-particle clusters: Cluster I mass spectra were characterized by m/z 44 and were comparable to LV-OOA spectra in the AMS database [Ulbrich et al., 2009]. Cluster II particles had strong m/z 43 signals, and their spectra resembled those of SV-OOA components. Cluster III spectra were characterized by m/z 27, 29, 41, 55, 57, and 69, which were typical for hydrocarbon type aerosols (m/z 29, 57) or cooking organic aerosols (m/z 27, 41, 55, 69). This suggested that Cluster III particles likely originated from mixed local primary sources.

3.3.2.3 Single-particle types compared with bulk source types

The "secondary" (Group I), "diesel exhaust" (Group II), and "dust" (Group III) particle types resulting from single-particle X-ray spectra broadly matched the major source types identified from bulk particle functional group factor analysis. Secondary particles accounted for 44% of total measured particles, which was consistent with bulk particle analysis that suggested SOA was the major component of OM. Similarly, the "high m/z 44" (Cluster I), "high m/z 43" (Cluster II), and "mixed" (Cluster III) particle types derived from single-particle mass spectra analysis matched the major source types from the bulk particle mass spectra factor analysis. Taken together, the high m/z 44 and m/z 43 types accounted for 56% of identified particles, both by number and mass. Specifically, the group-average high m/z 44 single-particle spectrum correlated to the mass spectra for the high O/C alkane and aromatic SOA components with an r of 0.96 and 0.92, respectively. High spectral correlations were also observed for the high m/z 43 type particles that correlated to the low O/C alkane SOA with $r = 0.96$ and the mixed-type particles that correlated to COA, PO SOA, and nighttime OA with $r = 0.86$, 0.76,

and 0.70, respectively. Agreement of single and bulk particle types speaks to the ubiquity of SOA in fine OM at Bakersfield.

3.4 Discussion

The SOA components, which were derived from factor analysis, differed in mass, chemical composition, and diurnal cycle (summarized in Table 3.3), suggesting they were produced via distinct oxidation processes and likely favored by specific meteorological conditions. In this section, we compare the SOA components and discuss the underlying processes that likely led to their formation. Special attention is given to alkane SOA, aromatic SOA, and nighttime OA; the first two prevailed during daytime, and the last was a significant constituent at night. In addition, we discuss size distributions of SOA components, which confirm the source identification and indicate the likely formation process.

3.4.1 Contrasting formation of alkane and aromatic secondary organic aerosol components

The diurnal cycle for high O/C alkane SOA_{AMS} was consistent over the course of the study, with concentrations peaking in the afternoon for 74% of the 45-day campaign (Figure 3.10a). The average diurnal cycle resembled that of the odd oxygen (O_3 + NO_2), and the factor mass fraction correlated to odd oxygen with an r of 0.70 (higher temperature associated with larger odd oxygen mixing ratios and greater factor mass fractions) (Figure 3.10b), suggesting O_3 either played an important role in its formation or was coproduced with alkane SOA from similar precursors on similar time scales. Good correlation of alkane SOA to odd oxygen were also found by recent model simulations even without a role for O_3 in the oxidation of alkanes [Pye and Pouliot, 2012]. The alkane SOA_{FTIR} factor mole composition of 0.11/0.04/0.00/0.86 among carboxylic acid/hydroxyl/nonacid carbonyl/alkane groups compared well to C_{12} alkane oxidation products, with mole fractions of 0.12/0.13/0.02/0.73 for the carboxylic acid/hydroxyl/nonacid carbonyl/alkane groups [Russell et al., 2011]. This composition was inferred from a

Table 3.3: Summary of concentration, OM fraction (in parentheses), oxidant, peak time, O/C, organic functional group (OFG) composition, size range, and source of FTIR and the AMS factors. The colors in the pie charts represent alkane (blue), hydroxyl (hot pink), carboxylic acid (green), nonacid carbonyl (teal), and organonitrate (beige) functional groups.

	FTIR		AMS								
Factor	Concentration in PM$_1$ (μg m^{-3})	Concentration in PM$_{2.5}$ (μg m^{-3})	Factor	Concentration in PM$_1$ (μg m^{-3})	Oxidant	Peak Time	O/C	OFG	Size (nm)	Source	Primary or secondary
Aromatic SOA	0.61 (24%)	0.77 (23%)	Low O/C aromatic SOA	0.35 (9%)	OH	0–6; 12–18	0.36		250–900	Fossil fuel combustion	Secondary
			High O/C aromatic SOA	0.64 (16%)	OH	18–23	0.68		200–500	Fossil fuel combustion	Secondary
Alkane SOA	1.21 (41%)	1.43 (43%)	Low O/C alkane SOA	0.48 (12%)	OH	22–6	0.27		200–500	Fossil fuel combustion	Secondary
			High O/C alkane SOA	1.19 (30%)	O$_3$	10–17	0.63		200–500	Fossil fuel combustion	Secondary
Nighttime OA	0.30 (10%)	0.25 (8%)	Nighttime OA	0.50 (13%)	NO$_3$	0–6	0.01		400–700	Fossil fuel combustion/ biogenic emissions	Primary and secondary
PO SOA	0.42 (14%)	0.42 (13%)	PO SOA	0.49 (13%)	OH and/or O$_3$	10–17	0.20		100–200	Petroleum operations	Secondary
Vegetative detritus	0.29 (10%)	0.45 (14%)	-	-	-	12–18	1.09		-	Resuspended dusts and plant materials	Primary
-	-	-	COA	0.29 (7%)	-	12–18 20–23	0.05		100–200	Cooking activities	Primary

two-step oxidation pathway: 1) gas-phase alkane oxidation by OH radicals to form particle-phase dihydrofuran; and 2) evaporation of dihydrofuran followed by O_3 oxidation, forming carboxylic acid and alkane group dominated products [Russell et al., 2011]. The products from each step likely represented first and higher generation SOA components, respectively [Lim and Ziemann, 2005, 2009]. Therefore, that the high O/C alkane SOA_{AMS} factor correlated with odd oxygen indicated second or higher generation products from alkane oxidation. Neither the low O/C alkane SOA_{AMS} factor nor the sum of the high and low O/C alkane SOA_{AMS} factors (correlating to the alkane SOA_{FTIR} factor, $r = 0.74$) correlated to odd oxygen, indicating that the low O/C alkane SOA_{AMS} factor may have been associated with the first step of oxidation which happened faster than O_3 formation or for which O_3 was not required.
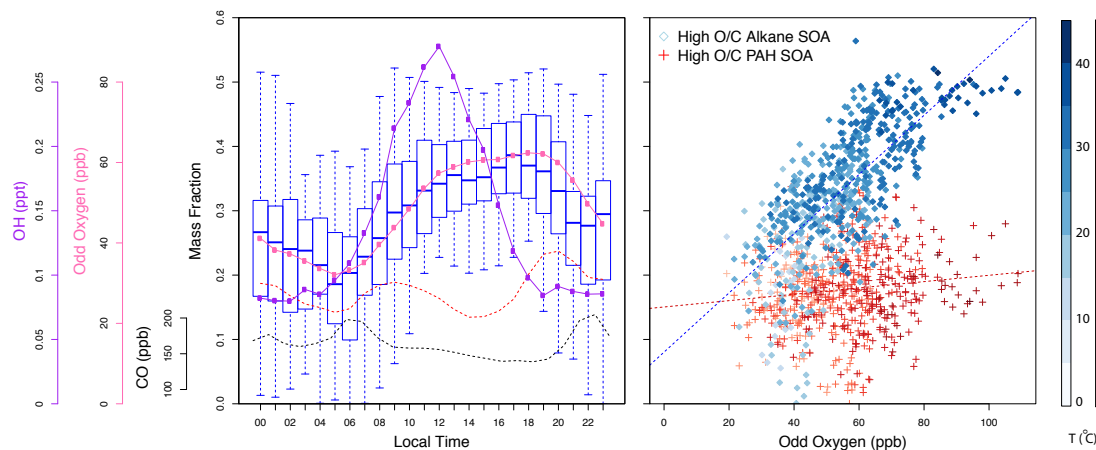
Figure 3.10: (a) Diurnal variations of mass fraction for the high O/C alkane SOA_{AMS} factor (blue boxes), mass fraction for the high O/C aromatic SOA_{AMS} factor (dashed red line), odd oxygen (pink), CO (black), and OH (purple). (OH radical was measured by William Brunes research group [Ahlm et al., 2012].) The horizontal bar in each box represents the median value. Upper and lower bounds of the boxes represent 25th and 75th percentiles, with whiskers extending to 5th and 95th percentiles. (b) Correlation of mass fraction of the high O/C alkane SOA_{AMS} (blue) and high O/C aromatic SOA_{AMS} (red) factors to odd oxygen. Darker colors indicate higher temperatures as the vertical color bars show.

For the diurnal cycle of the high O/C aromatic SOA_{AMS} factor, no consis-

tent pattern was identified. Day-to-day variation likely resulted from the variety of the aromatic species emitted from vehicular emissions, including light aromatic hydrocarbons and polycyclic aromatic hydrocarbons (PAHs), the quantities of which are highly dependent on combusted fuels [Richter and Howard, 2000]. In contrast, alkane compounds were relatively simple in their structure and could readily be grouped into linear, branched, and cyclic alkane classes, with SOA products fairly similar among these classes [Lim and Ziemann, 2009]. The mass yield of aromatic compounds may vary significantly as was found in SOA yields from naphthalene, which ranged from 2% to 22% [Shakya and Griffin, 2010] and from 19% to 74% [Chan et al., 2009] under comparable experimental conditions (i.e., OH concentration, initial hydrocarbon concentration, and initial NO_x-mixing ratio). This indicated that yields of aromatic hydrocarbons were extremely sensitive to environmental conditions. In addition, SOA components from PAH oxidation have been shown to be sensitive to NO_x mixing ratios, with ring-opening compounds being major products under high NO_x conditions and ring-retaining compounds formed under low NO_x conditions [Kautzman et al., 2010].

The variety of the aromatic compounds, sensitivity of their yields to the environmental conditions, and dependence of their oxidation products on NO_x, likely contributed to the variability of the diurnal cycle for the high O/C aromatic SOA_{AMS} factor. This factor's mass fraction (or mass concentration) did not correlate to odd oxygen (Figure 3.10), suggesting that O_3 played a minor role (if any) in its formation. The aromatic SOA_{FTIR} factor, which likely represented the average composition of a variety of aromatic SOA components, was largely composed of nonacid carbonyl groups (59%), which was consistent with the OH radical oxidation products for aromatic precursors, a majority of which contain ketone groups [Esteve et al., 2003; Lee and Lane, 2009; Lee and Lane, 2010; Wang et al., 2007; Webb et al., 2006]. The similarity of the aromatic SOA_{FTIR} factor to OH oxidation products for aromatic hydrocarbons suggests that OH was the main oxidant that oxidized primary aromatic compounds to their SOA products. This observation is consistent with previous kinetic studies that showed that aromatic hydrocarbons primarily react with OH radicals in the atmosphere [Kwok et al., 1994].

The functional group composition of alkane and aromatic SOA_{FTIR} factors are significantly different from the biogenic SOA factors identified in previous studies. For example, the biogenic SOA factor identified from Whistler, a remote forested site, has mole fractions of 0.44/0.25/0.16/0.10 for alkane, hydroxyl, nonacid, and carboxylic groups [Russell et al., 2011], i.e., the Whistler biogenic factor has a smaller alkane group fraction and a larger hydroxyl group fraction than the alkane SOA_{FTIR} factor. The biogenic SOA factor also has a smaller fraction of nonacid carbonyl groups than the aromatic SOA_{FTIR} factor.

3.4.2 Nighttime formation of biogenic secondary organic aerosols

While high O/C alkane and aromatic SOA_{AMS} components peaked during the day, high concentrations (20% to 52% OM) of the nighttime OA factors were observed at night (Figure 3.11a). The nighttime OA_{FTIR} factor, although influenced by primary anthropogenic sources, had significant signatures of biogenic SOA. The factor composition of alkane (57% to 79% OM), organonitrate (8% to 17% OM), and nonacid carbonyl groups (0% to 8% OM) was chemically similar to α-pinene and β-pinene SOA produced by NO_3 radical oxidation. These SOA components typically comprise 63% to 68% alkane groups, 8% to 26% organonitrate groups, and 2% to 24% nonacid carbonyl groups [Hallquist et al., 1999; Wangberg et al., 1997]. Therefore, the SOA fraction of the nighttime OA_{FTIR} factor likely formed via NO_3 radical oxidation. Supporting this argument is the correlation ($r = 0.5$) of nighttime OA_{FTIR} with nitrated organosulfates (e.g., $C_{10}H_{16}NO_7S^-$, $C_9H_{14}NO_8S^-$, and $C_{10}H_{16}NO_{10}S^-$ ions measured by UPLC/ESI-HR-Q-TOFMS), the most abundant organosulfate compound class (observed at the Bakersfield site) that is likely produced from NO_3 radical oxidation of α-pinene and limonene-like monoterpenes (e.g., myrcene) under dark conditions [Surratt et al., 2008].

As described in Section 3.1, easterly downslope winds prevailed at night, which likely carried biogenic VOCs to the sampling site. Biogenic VOCs (e.g., terpenes) typically contain one or more carbon-carbon double bonds, highly chemically active and readily oxidized typically by O_3 and NO_3 radicals under nighttime
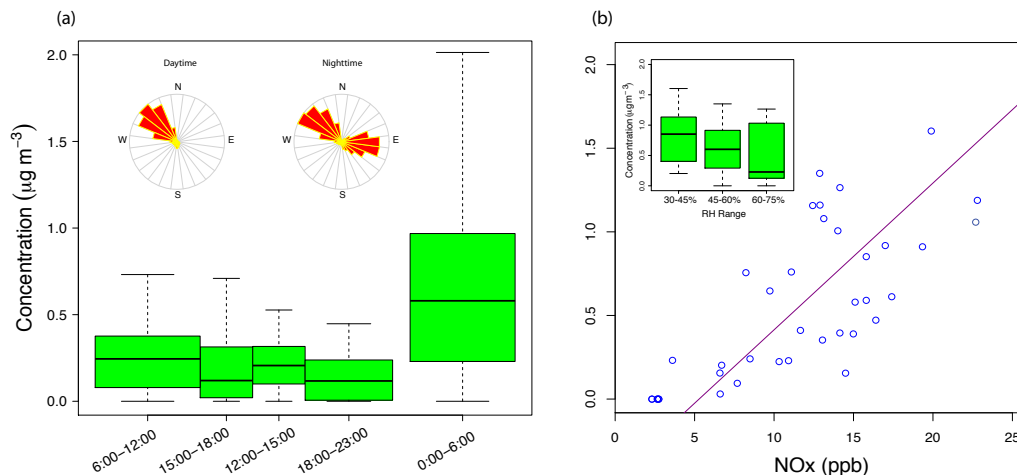
Figure 3.11: (a) Diurnal cycle of nighttime OA_{FTIR} with inner charts showing frequency of daytime and nighttime wind directions. (b) Correlation of nighttime OA_{FTIR} with NO_x for nighttime samples. The inner box plot shows dependence of factor concentration on RH, which included at least 10 points (45 points total) per bin. For each box in (a) and (b), upper and lower bounds represent 25th and 75th percentiles, and whiskers extend to 5th and 95th percentiles.

conditions. While some background O_3 was still detected at night ($\sim$10 ppb), no correlation was observed between the nighttime OA_{FTIR} factor and the O_3 concentration, indicating O_3 may not play a major role in formation of nighttime OA_{FTIR}. However, background O_3 could react with NO_2 to generate NO_3 radicals and could also convert NO to NO_2 to prevent loss of NO_3 radicals by reacting with NO. The nighttime OA_{FTIR} factor correlated to nighttime NO_x (Figure 3.11b), which is the precursor of NO_3 radicals, confirming that nighttime OA_{FTIR} was likely formed by NO_3 radical oxidation. Rollins et al. [2012] estimated that 1/3 of OM increase at night was accounted for by organonitrate group-containing molecules, which is consistent with the nighttime formation mechanism of the nighttime OA_{FTIR} factor. Moreover, the nighttime OA_{FTIR} factor accounted for 50% to 80% of the observed organonitrate group mass, which is consistent with an expected higher organonitate group yield from NO_3 oxidation reactions than that from OH radical and O_3 oxidation processes. Additionally, lower concentrations of nighttime OA_{FTIR} were associated with high RH (Figure 3.11b), which is consistent with the

loss of NO_3 radicals under high RH conditions (shifting the reaction $NO_3 + NO_2$ = N_2O_5 to the right through N_2O_5 uptake under high RH). Although alkane and aromatic hydrocarbons coexisted with biogenic VOCs at night, their oxidation rate constants for NO_3 radicals were typically less than 10^{-16} and 10^{-15} cm^3 molecule^{-1} s^{-1}, respectively [Atkinson and Arey, 2003]. These rate constants were 10^3 to 10^6 times smaller than rate constants of the biogenic hydrocarbons (oxidation by NO_3 radicals), which typically ranged from 10^{-10} to 10^{-12} cm^3 molecule^{-1} s^{-1} [Atkinson and Arey, 2003]. Therefore, NO_3 radicals mainly reacted with biogenic VOCs, forming biogenic SOA components with organonitrate functional groups in the nighttime atmosphere.

Compared to the biogenic SOA factors identified at Whistler (British Columbia, at 1020 m above sea level) [Schwartz et al., 2010], the nighttime OA_{FTIR} factor had significantly larger contribution of organonitrate groups. This difference likely arises from distinct oxidation conditions: O_3 or OH radical oxidation under low NO_x (1.5 ppb) at Whistler and NO_3 radical oxidation under high NO_x (15 ppb at night) at Bakersfield.

3.4.3 Insights of SOA formation from factor size distribution

Time series of the OM factors were correlated to time series of OM particle size sections (OM_{30-100}, $OM_{100-200}$, $OM_{200-300}$, $OM_{300-400}$, $OM_{400-500}$, $OM_{500-600}$, $OM_{600-700}$, $OM_{700-800}$, $OM_{800-900}$, $OM_{900-1000}$) derived from the AMS TOF mode measurements, resulting in a set of correlation coefficients for each factor. The square of the correlation coefficient (r^2) between an OM section and a factor represents the fraction of variability of an OM section that could be explained by variability of the factor [Rodgers and Nicewander, 1988]. The mean and variability (standard deviation) for the OM sections were comparable (Table 3.4), suggesting that most of the OM concentration was controlled by OM variability. Similarly, the factor concentration was controlled by variability in the factor concentration. Therefore, high r^2 between an OM section and a factor suggests that the mass of the OM section was likely accounted for by the factor, i.e., a majority of the

factor mass likely distributed in the same size range as the OM section. For this reason, the r^2 distribution (versus size) for each factor represents the factor mass size distribution to a great extent. Factor mass size distribution estimated from this approach can be validated by size distribution estimated from a marker-based method (e.g., size distribution of m/z 44 represents size distribution of SOA), which has proven to be approximately accurate [Ulbrich et al., 2012].
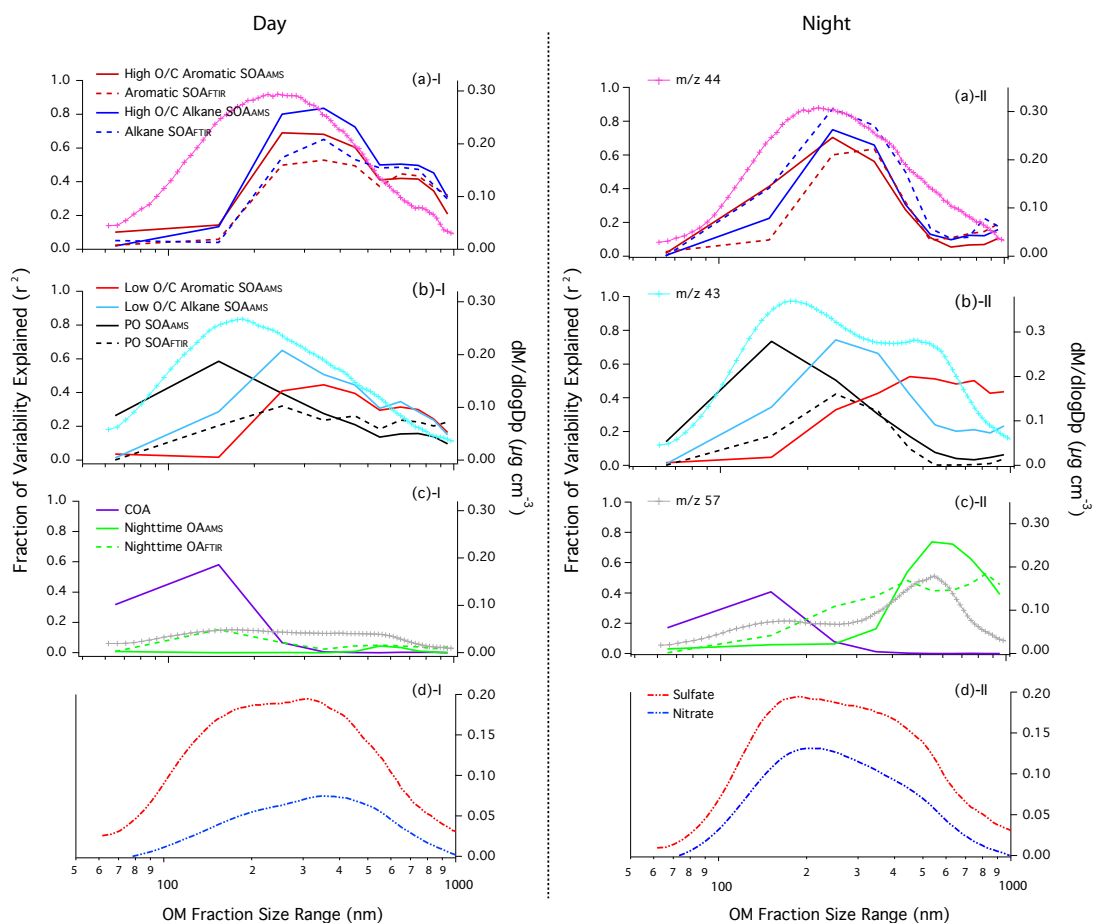
Figure 3.12: Size distributions of r^2 (fraction of variability explained) for FTIR and AMS factors (left axes) and mass size distributions of (a) m/z 44, (b) m/z 57, (c) m/z 43, and (d) sulfate and nitrate (right axes) for daytime (I) and nighttime (II) measurements. Legends for the factors and AMS-measured components are displayed on the left and right sides of the graphs, respectively.

Variability of OM in 200- to 500-nm-sized particles was accounted for by

the high O/C alkane and aromatic SOA factors (Figure 3.12a), suggesting that the high O/C factors peaked in 200- to 500-nm size range. Mass of fragment CO_2^+ (m/z 44), largely accounted for by high O/C alkane SOA (55%) and high O/C aromatic SOA (30%) factors, peaked in the 150- to 500-nm size range, which agreed well with r^2 distributions for the two high O/C factors. These peak size ranges are comparable to those for the OOA factor identified from Mexico City measurements using 3-D factorization analysis [Ulbrich et al., 2012]. Oxidized components enriched in 200- to 500-nm-sized particles typically form by condensation of gas-phase secondary organic species, because these particles provide most of the surface area that mass transfer mainly occurs in this size range [Seinfeld and Pandis, 2006]. In addition, oxidized components in 200- to 500-nm-sized particles are often associated with high O_3 mixing ratios [Alfarra et al., 2004; Liu et al., 2008; Zhang et al., 2005], suggesting that the high O/C factors were produced during photochemical processes. Note that r^2 size distributions of the high O/C factors shifted 50 nm (daytime) and 20 nm (nighttime) towards larger sized particles compared to the m/z 44 size distribution, a difference likely caused by variation of non-m/z 44 fragments in the high O/C factors that underwent different atmospheric processes compared to the processes experienced by fragment m/z 44. Larger daytime shifts reflect more complex processes, which could also explain the shoulder at 600- to 900-nm of daytime r^2 distributions. Low O/C alkane and aromatic SOA factors had similar r^2 size distributions compared to those for the high O/C factors, except the low O/C alkane SOA was broadly distributed (250 to 900 nm) (Figure 3.12b). This likely resulted from the low O/C alkane SOA's temperature-driven condensation at night [Lanz et al., 2007; Ng et al., 2010], as daily temperatures fluctuated widely (10–20°C). r^2 of another low O/C factor, PO SOA, peaked in the 100- to 200-nm size range. Fragment m/z 43 (72% $C_2H_3O^+$ and 28% $C_3H_7^+$) was representative of low O/C factors. Daytime size distribution of m/z 43 peaked in the 100- to 600-nm size range, as was consistent with size distributions of low O/C alkane SOA, low O/C aromatic SOA, and PO SOA factors. A distinct mode of m/z 43 at 400- to 700-nm occurred at night, likely a contribution of $C_3H_7^+$ from primary emissions.

Table 3.4: Mean concentration, variability, and fraction of variability explained by the AMS factors for the OM sections.

		OM_{30-100}	$OM_{100-200}$	$OM_{200-300}$	$OM_{300-400}$	$OM_{400-500}$	$OM_{500-600}$	$OM_{600-700}$	$OM_{700-800}$	$OM_{800-900}$	$OM_{900-1000}$
Mean concentration ($\mu g\ m^{-3}$)		0.12	0.55	0.30	0.20	0.11	0.07	0.04	0.03	0.01	0.01
Variability (standard deviation) ($\mu g\ m^{-3}$)		0.08	0.32	0.22	0.17	0.09	0.06	0.04	0.03	0.02	0.01
Ratio of variability to mean		0.69	0.58	0.71	0.83	0.83	0.83	0.95	1.05	1.20	1.50
Fraction of variability explained (r^2)	Low O/C aromatic SOA	0.03	0.04	0.36	0.44	0.49	0.45	0.43	0.45	0.38	0.35
	High O/C aromatic SOA	0.02	0.28	0.69	0.61	0.35	0.15	0.10	0.12	0.13	0.14
	Low O/C alkane SOA	0.01	0.26	0.60	0.53	0.44	0.30	0.27	0.27	0.24	0.25
	High O/C alkane SOA	0.01	0.16	0.67	0.64	0.31	0.12	0.10	0.13	0.14	0.15
	Nighttime OA	0.00	0.04	0.05	0.12	0.45	0.67	0.66	0.56	0.44	0.31
	PO SOA	0.25	0.53	0.33	0.20	0.08	0.02	0.01	0.02	0.03	0.03
	COA	0.21	0.48	0.07	0.01	0.00	0.00	0.00	0.00	0.00	0.00

The size distribution of r^2 of the nighttime OA factor peaked in the 400- to 700-nm size range at night (Figure 3.12c). This size range largely overlapped the larger mode in nighttime size distribution of m/z 57, which was expected because 60% of m/z 57 mass fragment was attributed to the nighttime OA factor. The 400- to 700-nm mode was not present in the size distribution of SOA components (such as fragment m/z 44, sulfate, and nitrate, Figure 3.12), suggesting that nighttime $OM_{400-700}$ was likely associated with primary emissions. A likely primary source was vehicular emission. Although fresh exhaust particles are typically smaller than 100 nm, a mode at 550 nm was observed from chase studies using AMS [Canagaratna et al., 2004]. In addition, Kleeman et al. [2009] attributed a significant mass of particles (560–1000 nm) to diesel fuel and gasoline combustion sources at the same site. Another source of particles in this mode could be vegetative detritus, which likely existed as large particles (Section 3.1). SOA produced at night (e.g., biogenic SOA) could condense on large primary particles to form internal mixtures. Therefore, the nighttime OA factor, which included a mixture of primary and secondary signatures, likely represented a mixture of primary hydrocarbons and condensed secondary biogenic SOA components formed by NO_3 oxidation.

The size distribution of r^2 for the COA factor peaked in 100- to 200-nm, a size range consistent with primarily emitted particles from meat charbroiling and frying activities [Hildmann et al., 1991; Wallace et al., 2004; Kleeman et al., 2009; Allan et al., 2010; Zhang et al., 2007], which agreed with the low O/C (0.04) for this factor.

3.5   Conclusions

Summertime measurements suggested that organic mass comprised the major component of fine aerosol particles at Bakersfield in the San Joaquin Valley. On average, OM in PM_1 and $PM_{2.5}$ was 2.42 and 3.23 μg m^{-3}, respectively. PMF analysis was applied to the FTIR and AMS measurements, resulting in very high agreement between the two sets of independently-derived factors, both of which suggested that SOA components accounted for 80% to 90% of fine particle OM.

The high O/C AMS factors were chemically similar, so that external source marker were needed to link them to specific sources; whereas the FTIR factors had distinct infrared spectra that could be used as references for future studies when source marker measurements are not available. Among the PMF-derived components, vehicular emission oxidation products, including the alkane and aromatic SOA factors, constituted 65% OM, whereas nighttime organic aerosols (the nighttime OA factor), a mixture of POA and SOA that likely originated from biogenic emissions, accounted for a relatively small fraction on average (10% OM), although it was higher at night (20% OM).

Potential formation mechanisms of the SOA components were discussed. Anthropogenic SOA components mainly formed during daytime. The alkane SOA consisted of alkane and carboxylic acid groups, consistent with the composition expected for oxidation products of C_{12}-C_{25} alkanes. Furthermore, organic mass fraction of alkane SOA covaried and correlated with odd oxygen, providing evidence for the ozone-driven formation of alkane SOA, a mechanism derived from laboratory studies. In contrast, aromatic SOA did not correlate with ozone. This component was largely composed of nonacid carbonyl groups, which is consistent with oxidation products formed from OH radical-driven reactions for aromatic hydrocarbons and, therefore, indicates formation by this process. The nighttime organic aerosol component accounted for 50% to 80% of organonitrate group mass during the project; the secondary fraction of nighttime OA likely formed from oxidation of biogenic precursors (e.g., terpenes) by nitrate radicals during nighttime hours.

Not only did anthropogenic and biogenic SOA components differ in composition, they also differed in size: namely, oxidized alkane and aromatic SOA components was largely distributed in 200- to 500-nm-sized particles, suggesting that they were formed from condensation of gas-phase oxidation products, while biogenic SOA was in 400- to 700-nm-sized particles at night, likely due to condensation of biogenic SOA on large primary particles.

We also identified aerosols likely emitted from local petroleum operations and cooking activities, which were likely in particles smaller than 200 nm. Though

these sources were negligibly small in the emission inventory for the Bakersfield site, they accounted for 13% and 7% of the PM_1 organic mass, respectively.

Overall, this work demonstrates that OOA components identified from factor analysis can be linked to SOA formed by different oxidants and precursors mainly from gasoline and diesel fuel combustion emissions with minor contributions from petroleum operation and biogenic sources. In addition, these SOA components were enriched at particular sizes. We conclude that SOA accounts for a major fraction of summertime OM, even in areas close to urban sources. This result provides a benefit to the SJV community because it identifies the need for regulating vehicular emissions as the largest source of PM_1 in summertime.

3.6 Appendix

PMF was applied to FTIR and AMS measurements to identify sources that contributed to OM. Solutions were grouped by number of factors, rotational values, and seed values. Mathematical criteria were used to evaluate PMF model fitting and facilitate solution selection. Detailed factor extraction procedures are presented as follows.

3.6.1 Appendix A: Factor extraction of FTIR PM_1 and $PM_{2.5}$ samples

PMF was applied to PM_1 (228 samples) and $PM_{2.5}$ (46 samples) mass-weighted FTIR spectra, respectively. Data matrices were composed of infrared absorptions, and scaling factor matrices were calculated from baselining errors using an automated algorithm described in Russell et al. [2009]. Robust mode was used (i.e., outliers were downweighted during fitting processes). "FPEAKs" (rotational values) of ± 1, ± 0.8, ± 0.6, ± 0.4, ± 0.2, and 0 were tested, resulting in nearly identical factors. Minimum $Q/Q_{expected}$, a mathematical diagnostic for PMF fitting (Paatero et al., 2002), corresponded to FPEAK of 0 in PM_1 and $PM_{2.5}$ factor analysis results (Figure 3.13). Therefore, factors with FPEAK of 0 were selected to represent solutions. To investigate consistency of the solutions, seed values of 0

to 100 (varied by 10) were tested. For each of the PM_1 and $PM_{2.5}$ measurements, factor spectra and strengths derived using different seed values correlated with r of 0.99 or better, demonstrating robustness of the factors.
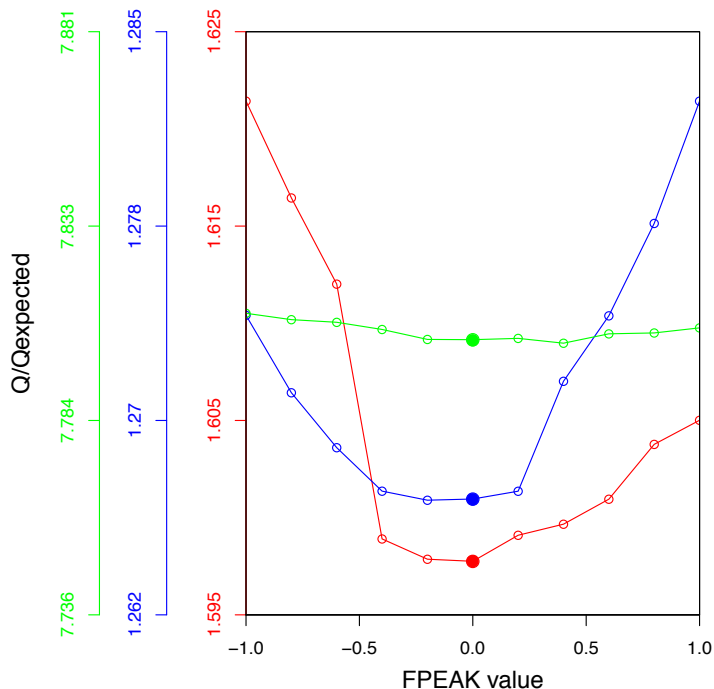
Figure 3.13: Dependence of $Q/Q_{expected}$ on FPEAK values for FTIR PM_1 (blue), FTIR $PM_{2.5}$ (green), and AMS (red) PMF analyses.

When exploring 2- to 8-factor solutions, $Q/Q_{expected}$ decreased with increasing factor numbers (Figure 3.14), indicating that the measured spectra were a better fit with more factors. However, too many factors may result in "factor spitting" [Ulbrich et al., 2009], and the "correct" number of factors should be evaluated on the basis of the physical meaning of the solutions. Therefore, solutions with $Q/Q_{expected}$ close to 1 (theoretical value of ideal solution) are not necessarily the best solutions. The 5-factor solution was chosen for PM_1 factor analysis because one or more factors ($\geq$ 12% OM) with specific source signatures were not identified from the 2-, 3-, and 4-factor solutions, and small ($\leq$ 7% OM) factors (i.e., unidentified factors) that did not correlate to any source markers were generated

when 6 or more factors were applied. For $PM_{2.5}$ factor analysis, a unique factor with 15% (mass fraction) organonitrate groups was not identified in solutions with less than 6 factors, and factors with unrealistic infrared spectra were found in solutions with more than 6 factors. Therefore, the 6-factor solution was selected for $PM_{2.5}$ measurements. In this solution, 2 factors had similar chemical compositions and correlated in time with an r of 0.60, indicating they were likely split from one source [Ulbrich et al., 2009]. The 2 correlated factors were combined into 1 factor (mass of the combined factor equals sum of factor masses used in combination), resulting in 5 linearly-independent factors, which explained the same degree of OM variability as the 6 factors prior to factor recombination.
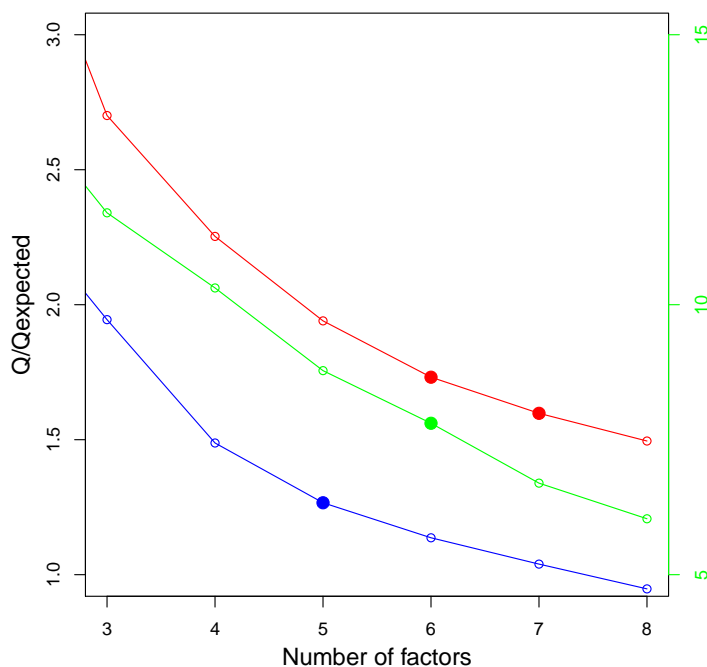
Figure 3.14: Dependence of $Q/Q_{expected}$ on number of factors for FTIR PM_1 (blue), FTIR $PM_{2.5}$ (green; right axis), and AMS (red) PMF analyses. Solid circles indicate selected solutions.

The normalized sum of residuals (sum of infrared absorptions for each sample) fluctuated around 0, with amplitude less than 7% for the PM_1 and $PM_{2.5}$

solutions (Figures 3.15a and 3.15b). No correlation was observed for the normalized sum of residuals and OM. Scaled residuals showed no evidence of characteristic functional group absorptions (Figures 3.16a and 3.16b). Random patterns of the normalized sum of residuals and scaled residuals suggested that residuals represented fitting noises and input matrices were well fit.
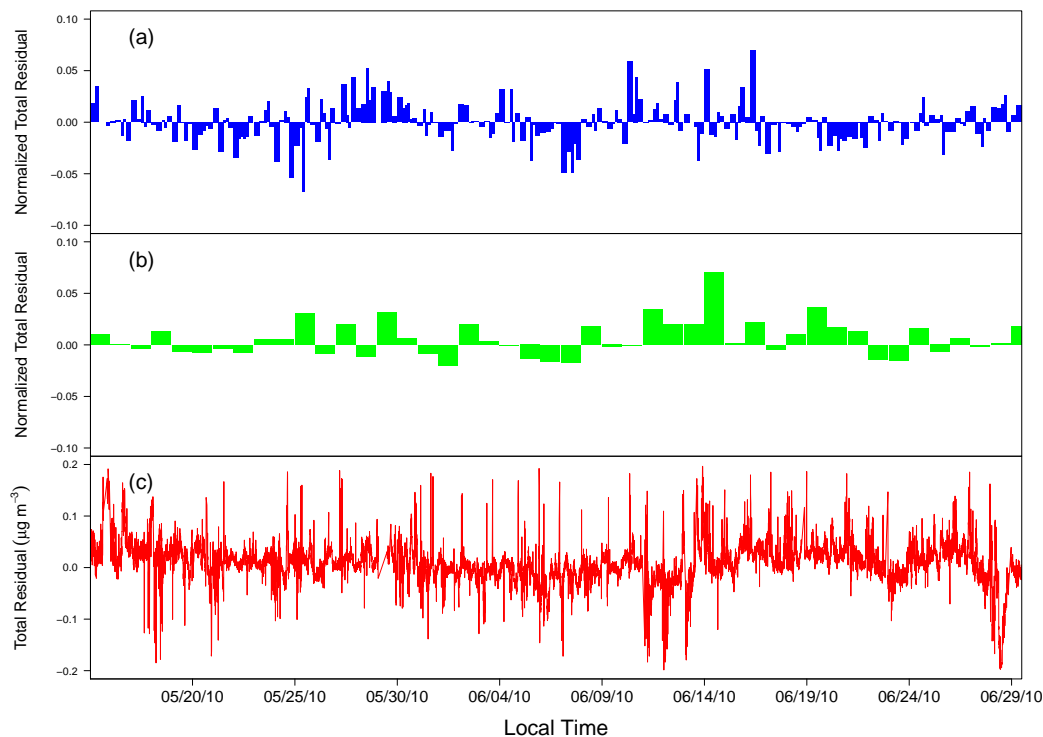
Figure 3.15: Time series for (a) normalized (by total infrared absorptions) sum of total residuals of FTIR PM_1 5-factor solution, (b) normalized sum of total residuals of FTIR $PM_{2.5}$ 6-factor solution, and (c) sum of total residuals of the AMS 6- or 7-factor solution.

3.6.2 Appendix B: Factor extraction of AMS measurements

PMF was applied to high-resolution mass spectra (V mode) measured by the HR-ToF-AMS. Data and error matrices were prepared using standard AMS data processing procedures (PIKA version 1.09) with Igor Pro 6 (Wavemetrics,

Table 3.5: Correlations of FTIR factors in PM_1 to source markers. Pearson's correlation coefficients (r) are shown in this study.

	PAH					PAH SOA						Alkane		Alkane SOA				Biogenic SOA	Petroleum operation	Dust				Cooking
	Methylanthraceene	Methylphenanthracene-1	Methylphenanthracene	Naphthalene-2-phenyl	1,2-Benzanthracene	2H-1-benzopyran-2-one	Dibenzofuran	1,8-Naphthalic acid/Naphthalic anhydride	Benzophenone	4-hydroxy-9-fluorenone	Phthalic acid/Phthalic anhydride	Heptadecane	Octadecane	Undecanone	Dodecanone	Tridecanone	Tetradecanone	Pinonaldehyde	V	Si	Ca	Al	Mg	Hexadecanoic acid[a]
Aromatic SOA	0.49	0.54	0.54	0.47	0.17	0.75	0.73	0.69	0.67	0.67	0.62	0.21	0.16	0.65	0.39	0.60	0.56	0.24	0.15	0.28	0.16	0.25	0.12	-
Alkane SOA	0.56	0.50	0.50	0.54	0.13	0.72	0.35	0.63	0.43	0.58	0.58	0.38	0.46	0.71	0.65	0.63	0.77	0.28	-0.01	0.19	0.22	0.15	0.06	-
Nighttime OA	0.50	0.47	0.47	0.40	0.37	-0.16	-0.17	0.04	-0.31	-0.20	0.01	0.50	0.53	0.20	-0.10	0.47	-0.07	0.65	-0.06	-0.01	0.07	-0.01	-0.03	-
PO SOA	0.11	0.11	0.05	0.12	-0.07	0.36	0.37	-0.09	0.39	0.21	0.28	-0.04	-0.10	0.42	0.03	0.32	0.26	0.12	0.60	0.02	-0.06	-0.01	-0.06	-
Vegetative detritus	-0.01	-0.07	-0.07	-0.03	0.15	-0.22	-0.05	-0.03	-0.07	-0.05	-0.08	-0.09	-0.14	0.42	0.18	0.13	0.04	-0.08	0.04	0.82	0.74	0.90	0.94	-

[a]Correlations are not reported for the cooking marker since less than 10 data points remained after averaging-to-filter sampling times.

Table 3.6: Correlations of FTIR factors in PM$_{2.5}$ to source markers.

	PAH					PAH SOA						Alkane		Alkane SOA				Biogenic SOA	Petroleum operation	Dust				Cooking
	Methylanthracene	Methylphenanthrene-1	Methylphenanthrene	Naphthalene-2-phenyl	1,2-Benzanthracene	2H-1-benzopyran-2-one	Dibenzofuran	1,8-Naphthalic acid/Naphthalic anhydride	Benzophenone	4-hydroxy-9-fluorenone	Phthalic acid/Phthalic anhydride	Heptadecane	Octadecane	Undecanone	Dodecanone	Tridecanone	Tetradecanone	Pinonaldehyde	V	Si	Ca	Al	Mg	Hexadecanoic acid[a]
Aromatic SOA	0.59	0.67	0.67	0.56	0.18	0.73	0.61	0.68	0.63	0.67	0.66	0.45	0.47	0.75	0.79	0.76	0.81	0.57	0.04	-0.03	-0.34	-0.04	-0.13	-
Alkane SOA	0.66	0.74	0.74	0.65	0.49	0.67	0.53	0.68	0.58	0.56	0.47	0.49	0.53	0.90	0.65	0.85	0.58	0.53	-0.52	-0.52	-0.03	-0.53	-0.56	-
Nighttime OA	0.45	0.41	0.41	0.26	0.59	-0.18	0.06	0.24	-0.09	-0.04	0.16	0.02	-0.05	0.29	-0.16	0.07	0.07	0.04	0.67	0.74	0.47	0.73	0.78	-
PO SOA	-0.20	-0.14	-0.14	0.00	0.07	-0.10	-0.19	-0.25	-0.09	0.04	-0.44	0.01	0.01	-0.19	-0.14	0.07	-0.32	-0.04	-0.31	-0.26	-0.10	-0.25	-0.25	-
Vegetative detritus	-0.30	-0.33	-0.33	-0.34	-0.24	-0.27	-0.29	-0.34	-0.30	-0.25	-0.12	-0.24	-0.24	0.03	-0.50	-0.35	-0.34	-0.18	0.78	0.81	0.41	0.82	0.77	-

[a]Correlations are not reported for the cooking marker since less than 10 data points remained after averaging-to-filter sampling times.

Table 3.7: Correlations of AMS factors to source markers for the 6-factor solution.

	PAH					PAH SOA						Alkane		Alkane SOA				Biogenic SOA	Petroleum operation	Dust				Cooking
	Methylanthracene	1-Methylphenanthrene	Methylphenanthrene	Naphthalene-2-phenyl	1, 2-Benzanthracene	2H-1-benzopyran-2-one	Dibenzofuran	1,8-Naphthalic acid/Naphthalic anhydride	Benzophenone	4-hydroxy-9-fluorenone	Phthalic acid/Phthalic anhydride	Heptadecane	Octadecane	Undecanone	Dodecanone	Tridecanone	Tetradecanone	Pinonaldehyde	V	Si	Ca	Al	Mg	Hexadecanoic acid
Low O/C aromatic SOA	0.71	0.60	0.60	0.60	0.55	0.43	0.25	0.40	0.22	0.40	0.36	0.42	0.42	0.36	0.40	0.54	0.52	0.25	0.29	0.22	0.27	0.17	0	0.46
Low O/C alkane SOA	0.75	0.81	0.81	0.76	0.60	0.34	0.12	0.71	0.03	0.37	0.23	0.69	0.68	0.61	0.73	0.82	0.70	0.67	-0.20	0.13	0.17	0.10	-0.32	0.23
High O/C aromatic SOA	0.58	0.62	0.59	0.55	0.56	0.76	0.62	0.75	0.72	0.65	0.62	0.34	0.33	0.46	0.40	0.62	0.59	0.30	0.15	0.43	0.38	0.39	0.17	0.48
Nighttime OA	0.32	0.25	0.26	0.31	0.36	-0.06	-0.18	0.04	-0.26	-0.13	-0.07	0.21	0.22	-0.01	0.50	0.29	0.27	0.00	-0.30	-0.11	0	-0.12	-0.24	0.17
PO SOA	-0.02	0	0.03	0.09	-0.22	0.50	0.27	0.01	0.35	0.39	0.34	0.09	0.15	0.28	0.22	0.13	0.09	0.28	0.39	0.10	0.13	0.10	0	0.14
COA	-0.08	-0.07	-0.14	-0.06	0.04	0.09	-0.14	-0.03	-0.13	0.16	-0.08	-0.04	0.01	-0.25	0.44	0.42	0.40	-0.13	0	-0.16	-0.15	-0.17	-0.39	0.81

Table 3.8: Correlations of AMS Group I factors to source markers for the 7-factor solution.

	PAH					PAH SOA						Alkane		Alkane SOA				Biogenic SOA	Petroleum operation	Dust				Cooking
	Methylanthracene	Methylphenanthracene-1	Methylphenanthracene	Naphthalene-2-phenyl	1, 2-Benzanthracene	2H-1-benzopyran-2-one	Dibenzofuran	1,8-Naphthalic acid/Naphthalic anhydride	Benzophenone	4-hydroxy-9-fluorenone	Phthalic acid/Phthalic anhydride	Heptadecane	Octadecane	Undecanone	Dodecanone	Tridecanone	Tetradecanone	Pinonaldehyde	V	Si	Ca	Al	Mg	Hexadecanoic acid
Low O/C aromatic SOA	0.90	0.84	0.84	0.82	0.81	0.43	0.32	0.69	0.26	0.39	0.38	0.56	0.60	0.58	0.49	0.66	0.62	0.35	0.00	0.35	0.38	0.31	0.22	0.43
Low O/C alkane SOA	0.72	0.78	0.78	0.73	0.57	0.29	0.07	0.67	-0.02	0.32	0.17	0.66	0.66	0.59	0.73	0.81	0.68	0.69	-0.09	0.08	0.12	0.08	-0.05	0.25
High O/C aromatic SOA	0.42	0.46	0.42	0.45	0.38	0.64	0.37	0.65	0.44	0.62	0.49	0.25	0.27	0.28	0.52	0.71	0.66	0.15	-0.03	0.32	0.29	0.29	0.14	0.62
High O/C alkane SOA	0.55	0.61	0.60	0.56	0.43	0.78	0.61	0.68	0.70	0.66	0.60	0.37	0.38	0.52	0.38	0.54	0.50	0.44	0.02	0.38	0.36	0.34	0.22	0.27
Nighttime OA	0.32	0.25	0.26	0.31	0.36	-0.07	-0.18	0.04	-0.27	-0.13	-0.07	0.21	0.22	0.00	0.49	0.29	0.27	0.00	-0.17	-0.10	0.00	-0.11	-0.10	0.15
PO SOA	-0.12	-0.12	-0.10	-0.04	-0.32	0.38	0.17	-0.13	0.24	0.31	0.28	0.01	0.08	0.21	0.22	0.10	0.07	0.16	0.40	0.07	0.10	0.03	0.01	0.19
COA	-0.19	-0.22	-0.21	-0.13	-0.09	0.07	-0.13	-0.27	-0.11	0.05	-0.14	-0.10	-0.03	-0.25	0.33	0.14	0.15	-0.13	-0.03	-0.18	-0.17	-0.18	-0.16	0.68

Table 3.9: Correlations of AMS Group II factors to source markers for the 7-factor solution.

	PAH					PAH SOA						Alkane		Alkane SOA				Biogenic SOA	Petroleum operation	Dust				Cooking
	Methylanthracene	Methylphenanthracene-1	Methylphenanthracene	Naphthalene-2-phenyl	1, 2-Benzanthracene	2H-1-benzopyran-2-one	Dibenzofuran	1,8-Naphthalic acid/Naphthalic anhydride	Benzophenone	4-hydroxy-9-fluorenone	Phthalic acid/Phthalic anhydride	Heptadecane	Octadecane	Undecanone	Dodecanone	Tridecanone	Tetradecanone	Pinonaldehyde	V	Si	Ca	Al	Mg	Hexadecanoic acid
F_1	0.26	0.33	0.34	0.37	0.08	0.59	0.30	0.33	0.36	0.50	0.33	0.28	0.33	0.41	0.40	0.41	0.33	0.44	0.25	0.12	0.15	0.13	-0.02	0.36
F_2	0.78	0.82	0.83	0.77	0.61	0.31	0.12	0.72	0.03	0.34	0.24	0.70	0.69	0.66	0.67	0.82	0.69	0.67	-0.20	0.16	0.21	0.11	-0.29	-0.09
F_3	0.57	0.59	0.56	0.52	0.58	0.74	0.64	0.73	0.75	0.63	0.63	0.31	0.29	0.42	0.35	0.57	0.56	0.24	0.18	0.45	0.40	0.40	0.19	0.47
F_4	0.01	0.07	0.00	0.06	0.06	0.24	-0.05	0.18	-0.02	0.31	0.09	0.04	0.10	-0.15	0.50	0.57	0.52	-0.04	-0.13	-0.01	-0.01	-0.02	-0.32	0.79
F_5	0.45	0.33	0.28	0.34	0.49	0.16	0.01	0.08	-0.03	0.10	0.02	0.25	0.26	-0.15	0.42	0.37	0.39	-0.04	0.05	-0.02	0.02	-0.05	-0.12	0.69
F_6	0.31	0.24	0.25	0.30	0.35	-0.07	-0.18	0.03	-0.27	-0.13	-0.07	0.20	0.22	-0.01	0.49	0.29	0.27	0.00	-0.3	-0.12	0.00	-0.13	-0.24	0.17
F_7	0.11	0.08	0.11	0.14	-0.14	0.49	0.30	0.05	0.36	0.42	0.43	0.15	0.19	0.32	0.20	0.19	0.15	0.26	0.44	0.14	0.18	0.13	0.03	0.02

Inc.). To appropriately weigh the data points, variables (time series of m/z) with S/N smaller than 0.2 were omitted from the analysis. Weak points (S/N between 0.2 and 2) and CO_2^+-related ions (m/z 16, 17, 18, 28, and 44) were downweighted by a factor of two [Paatero and Hopke, 2003; Ulbrich et al., 2009]. Robust mode was used in the fitting procedure. FPEAKs of ±1, ±0.8, ±0.6, ±0.4, ±0.2, and 0 were investigated, and no rotational effects were identified. Factors with an FPEAK of 0 corresponded to the minimum $Q/Q_{expected}$ (Figure 3.13), so they were selected to represent the solutions. Seeds of 0 to 100 (varied by 10) were tested, resulting in two groups of solutions: Group I was composed of solutions with seeds 10, 20, 30, 50, 70, 80, and 100, and Group II comprised solutions with seeds 0, 40, 60, 90. Within each group, the factors had nearly identical mass spectra and strengths (with $r \geq 0.94$ and $r \geq 0.99$ for Group I and Group II factors, respectively). Comparing Group I with Group II, factors had similar factor mass spectra ($r \geq 0.90$) but different factor strengths, resulting in different factor time series. The factors in Group I were more linearly independent and correlated better to the source markers than Group II factors. For example, F_1 and F_7 in the 7-factor solution in Group II correlated with an r of 0.82, and F_1 and F_7 did not significantly correlate to any group of source markers (Table 3.9). Therefore, the Group I factors were preferred in the PMF solutions.

Solutions with 2 to 8 factors were investigated to determine the optimal number of factors. For solutions with 5 or fewer factors, one or more physically meaningful factors with significant masses ($> 15\%$ OM) were missing; when 8 factors were applied, small ($< 6\%$ OM) and highly correlated (r of 0.80) factors were generated, indicating that some factors split into smaller factors that correlated in time, which could not be identified. Consistent factors were identified in the 6- and 7-factor solutions, with the 7-factor solution having an additional factor with high O/C (see Section 3.3.1.2 for detailed description). We present both the 6- and 7-factor solutions to show the consistency and variability of the solutions. The summed residual of this solution fluctuated around 0, with an absolute amplitude smaller than 0.2 μg m^{-3} (Figure 3.15c)—much smaller than OM variability of 2.2 μg m^{-3}. The pattern of scaled residuals resembled random noise (Figure 3.16c),
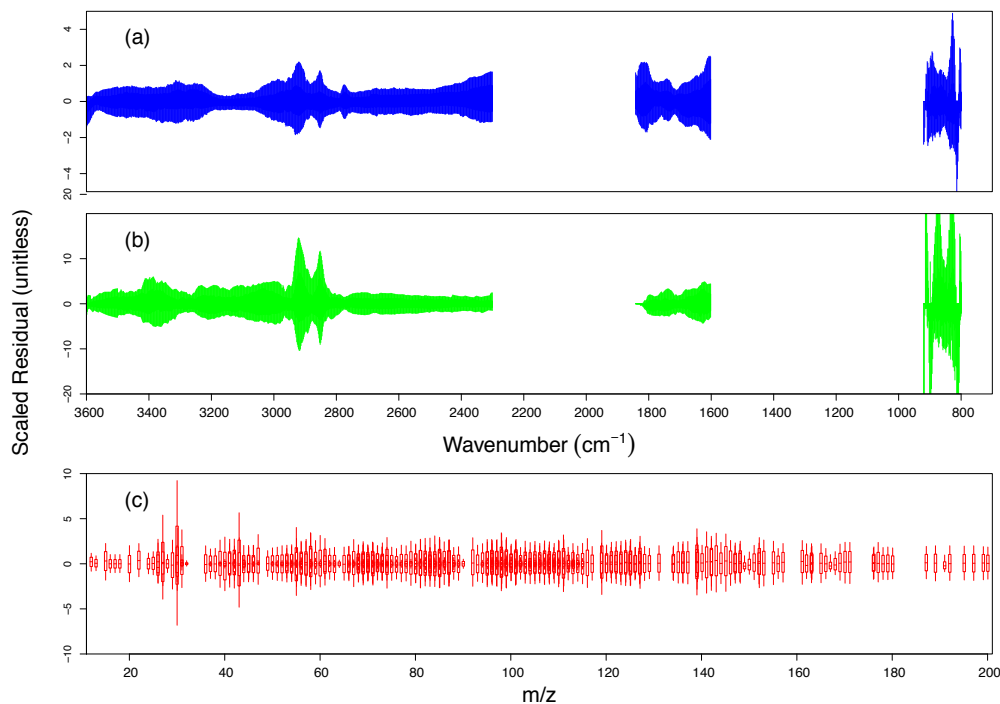
Figure 3.16: Box plots of scaled residuals for (a) FTIR PM$_1$ 5-factor solution, (b) FTIR PM$_{2.5}$ 6-factor solution, and (c) AMS 6- or 7-factor solution. Upper and lower bounds of the boxes represent 25th and 75th percentiles, and whiskers extend to 5th and 95th percentiles.

indicating the measurement was well fit by the factors.

3.7 Acknowledgments

Table 3.10: Source inventory of $PM_{2.5}$ for Kern County in the San Joaquin Valley in 2008 (downloaded from http://www.arb.ca.gov/ei/emissiondata.htm) (shown as percentage of $PM_{2.5}$) and sources identified in this study (shown as percentage of $OM_{2.5}$).

Source type		Inventory (%)	This study (%)
Mobile motor sources		31 (80)[a]	65
Petroleum production and refining		0 (1)	14
	Dust	16 (14)	10
	Cooking	2 (4)	7
Miscellaneous	Residential fuel combustion	7	ND[b]
processes	Farming operations	9	ND
	Construction and demolition	1	ND
	Managed burning and disposal	6	ND
Fuel (mainly natural gas) combustion		14	ND
Industrial processes		13	ND
Solvent evaporation		0	ND
Waste disposal		0	ND
Cleaning and surface coatings		0	ND

[a]The numbers in the parentheses represent percentage out of the four sources that are commonly identified in the source inventory and from this study.

[b]ND represents sources that were not detected from this study.
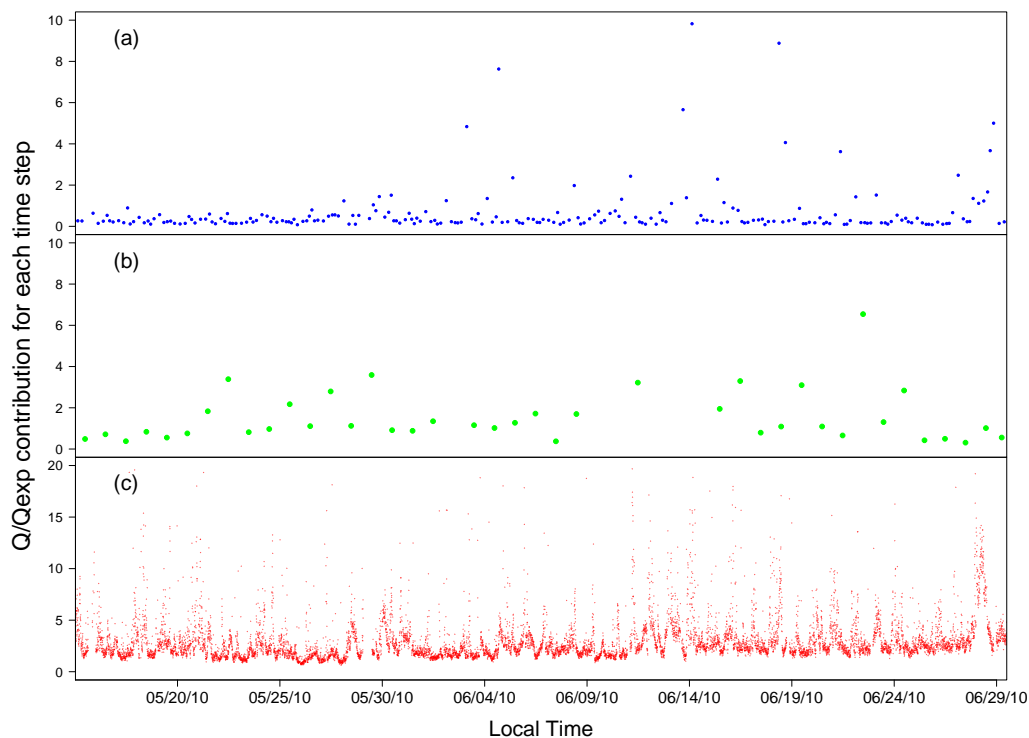
Figure 3.17: Time series of Q/Q_{exp} for (a) the 5-factor solution of FTIR PM_1, (b) the 6-factor solution of FTIR $PM_{2.5}$, and (c) the 6- or 7-factor solution of the AMS measurements.

staff for their generous help during the measurements. The statements and conclusions in this paper are those of the researchers (contractor) and not necessarily those of CARB. The mention of commercial products, their source, or their use in connection with material reported herein is not to be construed as actual or implied endorsement of such products.

Chapter 3, in full, has been submitted for publication to Journal of Geophysical Research-Atmospheres 2012. Liu, S., Ahlm, L., Day, D. A., Russell, L. M., Zhao, Y., Gentner, D. R., Weber, R. J., Goldstein, A. H., Jaoui, M., Offenberg, J. H., Kleindienst, T. E., Rubitschun, C., Surratt, J. D, Sheesley, R. J., and Scheller, S. (2012), Secondary organic aerosol formation from fossil fuel sources contribute majority of summertime organic mass at Bakersfield. The dissertation author was the primary investigator and author of this paper.
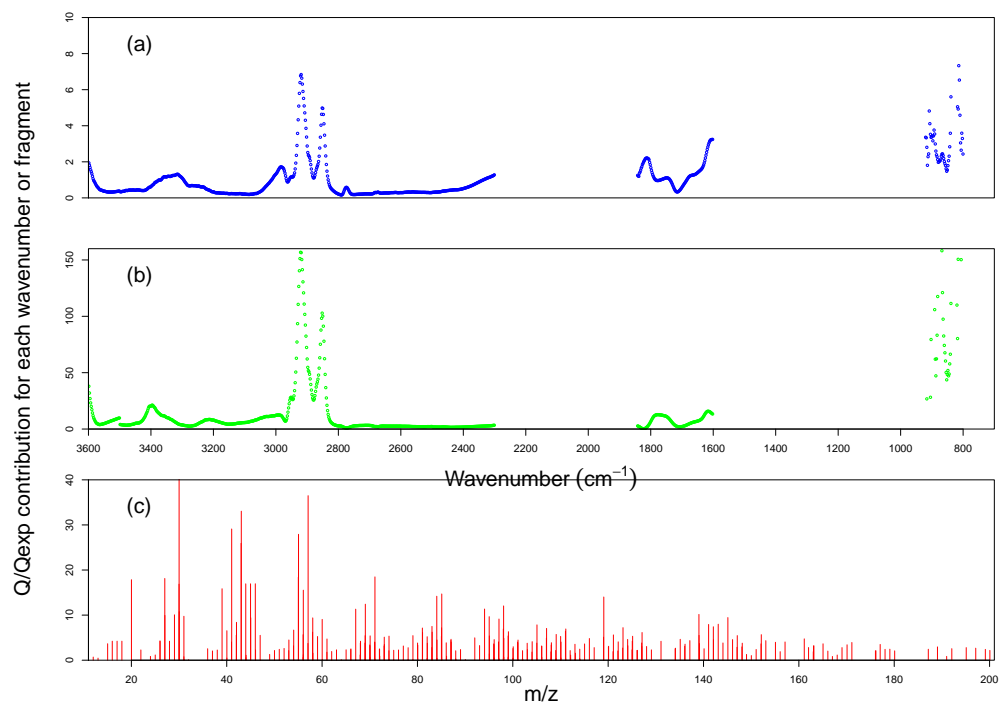
Figure 3.18: Q/Q_{exp} contribution to each wavenumber for (a) the 5-factor solution of FTIR PM_1 and (b) the 6-factor solution of FTIR $PM_{2.5}$. (c) Q/Q_{exp} contribution to each fragment for the 6- or 7-factor solution of the AMS measurements.
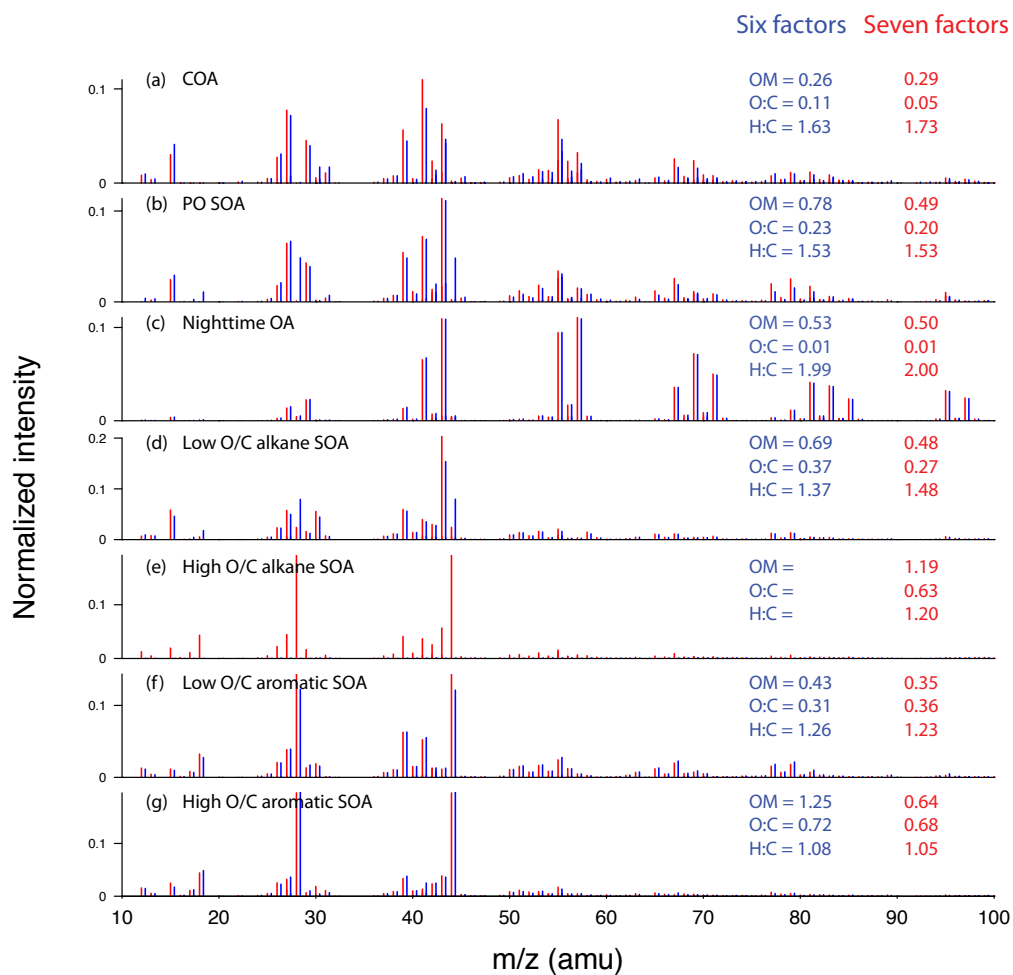
Figure 3.19: Factor mass spectra for the 6-factor (blue) and 7-factor (red) solution.
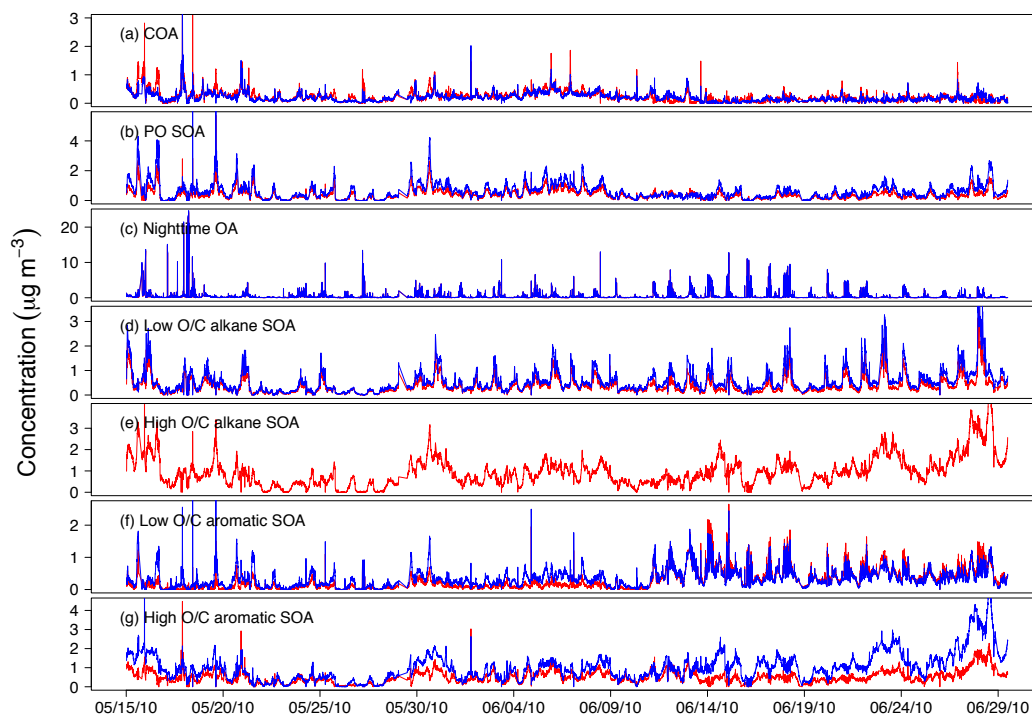
Figure 3.20: Factor time series for the 6-factor (blue) and 7-factor solutions.
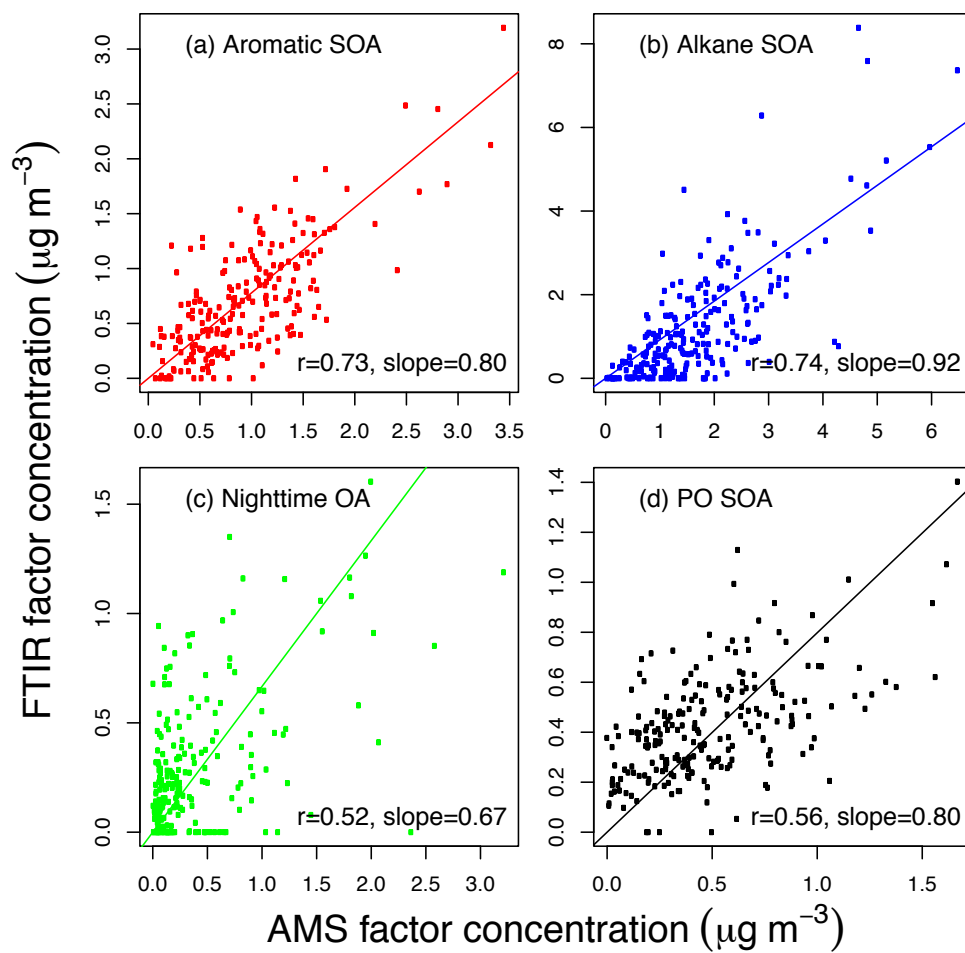
Figure 3.21: Correlation of the FTIR and AMS factors.

References

[1] Ahlm, L., et al. (2012), Formation and growth of ultrafine particles from secondary sources in Bakersfield, California, J. Geophys. Res., 117, D00V08, doi: 10.1029/2011JD017144.

[2] Aiken, A. C., et al. (2008), O/C and OM/OC ratios of primary, secondary, and ambient organic aerosols with high-resolution time-of-flight aerosol mass spectrometry, Environ. Sci. Technol., 42(12), 4478-4485.

[3] Alfarra, M. R., et al. (2004): Characterization of urban and rural organic particulate in the lower fraser valley using two aerodyne aerosol mass spectrometers, Atmos. Environ., 38(34), 5745-5758.

[4] Allan, J. D., P. I. Williams, W. T. Morgan, C. L. Martin, M. J. Flynn, J. Lee, E. Nemitz, G. J. Phillips, M. W. Gallagher, and H. Coe (2010), Contributions from transport, solid fuel burning and cooking to primary organic aerosols in two UK cities, Atmos. Chem. Phys., 10(2), 647-668.

[5] Atkinson, R. and J. Arey (2003), Atmospheric degradation of volatile organic compounds, Chem. Rev., 103(12), 4605-4638.

[6] Bianchi, G., A. Gamba, R. Limiroli, N. Pozzi, R. Elster, F. Salamini, and D. Bartels (1993), The unusual sugur composition in leaves of the resurrection plant myrothamnus-flabellifolia, Physiologia Plantarum, 87(2), 223-226.

[7] Braun, A. (2005), Carbon speciation in airborne particulate matter with C (1s) NEXAFS spectroscopy, J. Environ. Monit., 7(11), 1059-1065.

[8] Canagaratna, M. R., et al. (2004), Chase studies of particulate emissions from in-use New York City vehicles, Aerosol Sci. Technol., 38(6), 555-573.

[9] Canagaratna, M. R., et al. (2007), Chemical and microphysical characterization of ambient aerosols with the aerodyne aerosol mass spectrometer, Mass Spectrometry Reviews, 26(2), 185-222.

[10] Cass, G. R.: Organic molecular tracers for particulate air pollution sources, Trac-Trends in Analytical Chemistry, 17(6), 356-366, 1998.

[11] Chan, A. W. H., K. E. Kautzman, P. S. Chhabra, J. D. Surratt, M. N. Chan, J. D. Crounse, A. Kuerten, P. O. Wennberg, R. C. Flagan, and J. H. Seinfeld (2009), Secondary organic aerosol formation from photooxidation of naphthalene and alkylnaphthalenes: implications for oxidation of intermediate volatility organic compounds (IVOCs), Atmos. Chem. Phys., 9(9), 3049-3060.

[12] Chow, J. C., J. G. Watson, Z. Q. Lu, D. H. Lowenthal, C. A. Frazier, P. A. Solomon, R. H. Thuillier, and K. Magliano (1996), Descriptive analysis of PM2.5 and PM10 at regionally representative locations during SJVAQS/AUSPEX, Atmos. Environ., 30(12), 2079-2112.

[13] Chow, J. C., J. G. Watson, L. L. Ashbaugh, and K. L. Magliano (2003), Similarities and differences in PM10 chemical source profiles for geological dust from the San Joaquin Valley, California, Atmos. Environ., 37(9-10), 1317-1340.

[14] Chow, J. C., J. G. Watson, D. H. Lowenthal, L. W. A. Chen, and K. L. Magliano (2006a), Particulate carbon measurements in California's San Joaquin Valley, Chemosphere, 62(3), 337-348.

[15] Chow, J. C., L. W. A. Chen, J. G. Watson, D. H. Lowenthal, K. A. Magliano, K. Turkiewicz, and D. E. Lehrman (2006b), PM2.5 chemical composition and spatiotemporal variability during the California Regional PM10/PM2.5 Air Quality Study (CRPAQS), J. Geophys. Res., 111(D10), doi: 10.1029/2005JD006457.

[16] Claeys, M., et al. (2007), Hydroxydicarboxylic acids: Markers for secondary organic aerosol from the photooxidation of alpha-pinene, Environ. Sci. Technol., 41(5), 1628-1634.

[17] Cross, E. S., J. G. Slowik, P. Davidovits, J. D. Allan, D. R. Worsnop, J. T. Jayne, D. K. Lewis, M. Canagaratna, and T. B. Onasch (2007), Laboratory and ambient particle density determinations using light scattering in conjunction with aerosol mass spectrometry, Aerosol Sci. Technol., 41(4), 343-359.

[18] Day, D. A., S. Liu, L. M. Russell, and P. J. Ziemann (2010), Organonitrate group concentrations in submicron particles with high nitrate and organic fractions in coastal southern California, Atmos. Environ., 44(16), 1970-1979.

[19] DeCarlo, P. F., et al. (2010), Investigation of the sources and processing of organic aerosol over the Central Mexican Plateau from aircraft measurements during MILAGRO, Atmos. Chem. Phys., 10(12), 5257-5280.

[20] Esteve, W., H. Budzinski, and E. Villenave (2003), Heterogeneous reactivity of OH radicals with phenanthrene, Polycyclic Aromatic Compounds, 23(5), 441-456.

[21] Fatemi, S. M., and B. Y. Jamaloei (2011), Preliminary considerations on the application of toe-to-heel steam flooding (THSF): Injection well-producer well configurations, Chemical Engineering Research & Design, 89(11A), 2365-2379.

[22] Gray, H. A., G. R. Cass, J. J. Huntzicker, E. K. Heyerdahl, and J. A. Rau (1986), Characteristics of atmospheric organic and elemental carbon particle concentrations in Los Angeles, Environ. Sci. Technol., 20(6), 580-589.

[23] Gilardoni, S., S. Liu, S. Takahama, L. M. Russell, J. D. Allan, R. Steinbrecher, J. L. Jimenez, P. F. De Carlo, E. J. Dunlea, and D. Baumgardner (2009), Characterization of organic ambient aerosol during MIRAGE 2006 on three platforms, Atmos. Chem. Phys., 9(15), 5417-5432.

[24] Goldstein, A. H. and I. E. Galbally (2007), Known and unexplored organic constituents in the earth's atmosphere, Environ. Sci. Technol., 41(5), 1514-1521.

[25] Goldstein, A. H., C. D. Koven, C. L. Heald, and I. Y. Fung (2009), Biogenic carbon and anthropogenic pollutants combine to form a cooling haze over the southeastern United States, Proc. Natl. Acad. Sci., 106(22), 8835-8840.

[26] Grosjean, D. (1984), Particulate carbon in Los Angeles air, Science of the Total Environment, 32(2), 133-145.

[27] Hallquist, M., I. Wangberg, E. Ljungstrom, I. Barnes, and K. H. Becker (1999), Aerosol and product yields from NO3 radical-initiated oxidation of selected monoterpenes, Environ. Sci. Technol., 33(4), 553-559.

[28] Hamilton, J. F., P. J. Webb, A. C. Lewis, J. R. Hopkins, S. Smith, and P. Davy (2004), Partially oxidised organic components in urban aerosol using GCXGC-TOF/MS, Atmos. Chem. Phys., 4, 1279-1290.

[29] Han, J. S., K. J. Moon, S. J. Lee, Y. J. Kim, S. Y. Ryu, S. S. Cliff, and S. M. Yi (2006), Size-resolved source apportionment of ambient particles by positive matrix factorization at Gosan background site in East Asia, Atmos. Chem. Phys., 6, 211-223.

[30] Hatakeyama, S., T. Tanonaka, J. H. Weng, H. Bandow, H. Takagi, and H. Akimoto (1985), Ozone-cyclohexene reaction in air: quantitative analysis of particulate products and the reaction mechanism, Environ. Sci. Technol, 19(10), 935-942.

[31] Hatakeyama, S., M. Ohno, J. H. Weng, H. Takagi, and H. Akimoto (1987), Mechanism for the formation of gaseous and particulate products from ozone-cycloalkene reactions in air, Environ. Sci. Technol., 21(1), 52-57.

[32] Hawkins, L. N. and L. M. Russell (2010), Oxidation of ketone groups in transported biomass burning aerosol from the 2008 Northern California Lightning Series fires, Atmos. Environ., 44(34), 4142-4154.

[33] He, L. Y., M. Hu, X. F. Huang, B. D. Yu, Y. H. Zhang, and D. Q. Liu (2004), Measurement of emissions of fine particulate organic matter from Chinese cooking, Atmos. Environ., 38(38), 6557-6564.

[34] He, L. Y., Y. Lin, X. F. Huang, S. Guo, L. Xue, Q. Su, M. Hu, S. J. Luan, and Y. H. Zhang (2010), Characterization of high-resolution aerosol mass spectra of primary organic aerosol emissions from Chinese cooking and biomass burning, Atmos. Chem. Phys., 10(23), 11535-11543.

[35] Heald, C. L., J. H. Kroll, J. L. Jimenez, K. S. Docherty, P. F. DeCarlo, A. C. Aiken, Q. Chen, S. T. Martin, D. K. Farmer, and P. Artaxo (2010), A simplified description of the evolution of organic aerosol composition in the atmosphere, Geophys. Res. Lett., 37, L08803, doi: 10.1029/2010GL042737.

[36] Heintzenberg, J., D. C. Covert, and R. Van Dingenen (2000), Size distribution and chemical composition of marine aerosols: a compilation and review, Tellus Series B-Chemical and Physical Meteorology, 52(4), 1104-1122.

[37] Hildemann, L. M., G. R. Markowski, M. C. Jones, and G. R. Cass (1991), Submicrometer aerosol mass distributions of emissions from boilers, fireplaces, automobiles, diesel trucks, and meat cooking operations, Aerosol Sci. Technol., 14(1), 138-152.

[38] Hoppel, W. A., J. W. Fitzgerald, G. M. Frick, R. E. Larson, and E. J. Mack (1990), Aerosol size distributions and optical properties found in the marine boundary layer over the Atlantic Ocean, J. Geophys. Res., 95(D4), 3659-3686.

[39] Jaoui, M., T. E. Kleindienst, M. Lewandowski, and E. O. Edney (2004), Identification and quantification of aerosol polar oxygenated compounds bearing carboxylic or hydroxyl groups. 1. Method development, Analytical Chemistry, 76(16), 4765-4778.

[40] Jaoui, M., E. O. Edney, T. E. Kleindienst, M. Lewandowski, J. H. Offenberg, J. D. Surratt, and J. H. Seinfeld (2008), Formation of secondary organic aerosol from irradiated alpha-pinene/toluene/NOx mixtures and the effect of isoprene and sulfur dioxide, J. Geophys. Res., 113(D9), D09303, doi: 10.1029/2007JD009426.

[41] Jayne, J. T., D. C. Leard, X. F. Zhang, P. Davidovits, K. A. Smith, C. E. Kolb, and D. R. Worsnop (2000), Development of an aerosol mass spectrometer for size and composition analysis of submicron particles, Aerosol Sci. Technol., 33(1-2), 49-70.

[42] Jimenez, J. L., et al. (2009), Evolution of Organic Aerosols in the Atmosphere, Science, 326(5959), 1525-1529.

[43] Karanasiou, A. A., P. A. Siskos, and K. Eleftheriadis (2009), Assessment of source apportionment by Positive Matrix Factorization analysis on fine and coarse urban aerosol size fractions, Atmos. Environ., 43(21), 3385-3395.

[44] Kautzman, K. E., J. D. Surratt, M. N. Chan, A. W. H. Chan, S. P. Hersey, P. S. Chhabra, N. F. Dalleska, P. O. Wennberg, R. C. Flagan, and J. H. Seinfeld (2010), Chemical Composition of Gas- and Aerosol-Phase Products from the Photooxidation of Naphthalene, Journal of Physical Chemistry A, 114(2), 913-934.

[45] Kawamura, K., M. Narukawa, S.-M. Li, and L. A. Barrie (2007), Size distributions of dicarboxylic acids and inorganic ions in atmospheric aerosols collected during polar sunrise in the Canadian high Arctic, J. Geophys. Res., 112(D10), D10307, doi: 10.1029/2006JD008244.

[46] Khalaf, F., P. Literathy, and V. Anderlini (1982), Vanadium as a tracer of oil pollution in the sediments of Kuwait, Hydrobiologia, 91, 147-154.

[47] Kirchstetter, T. W., B. C. Singer, R. A. Harley, G. R. Kendall, and J. M. Hesson (1999), Impact of California reformulated gasoline on motor vehicle emissions. 2. Volatile organic compound speciation and reactivity, Environmental Science & Technology, 33(2), 329-336.

[48] Kittelson, D. B. (1998), Engines and nanoparticles: A review, Journal of Aerosol Science, 29(5-6), 575-588.

[49] Kleeman, M. J., Riddle, S. G., Robert, M. A., Jakober, C. A., Fine, P. M., Hays, M. D., Schauer, J. J. and Hannigan, M. P.: Source apportionment of fine (PM1.8) and ultrafine (PM0.1) airborne particulate matter during a severe winter pollution episode, Environ. Sci. Technol., 43(2), 272-279, 2009.

[50] Kleeman, M. J., L. S. Hughes, J. O. Allen, and G. R. Cass (1999), Source contributions to the size and composition distribution of atmospheric particles: Southern California in September 1996, Environ. Sci. Technol., 33(23), 4331-4341.

[51] Kleindienst, T. E., M. Jaoui, M. Lewandowski, J. H. Offenberg, and K. S. Docherty (2012), The formation of SOA and chemical tracer compounds from the photooxidation of naphthalene and its methyl analogs in the presence and absence of nitrogen oxides, Atmos. Chem. Phys. Discuss., 12, 12163-12201.

[52] Kleindienst, T. E., M. Jaoui, M. Lewandowski, J. H. Offenberg, C. W. Lewis, P. V. Bhave, and E. O. Edney (2007), Estimates of the contributions of biogenic

and anthropogenic hydrocarbons to secondary organic aerosol at a southeastern US location, Atmos. Environ., 41(37), 8288-8300.

[53] Kwok, E. S. C., W. P. Harger, J. Arey, and R. Atkinson (1994), Reactions of gas-phase phenanthrene under simulated atmospheric conditions, Environ. Sci. Technol, 28(3), 521-527.

[54] Lanz, V. A., Alfarra, M. R., Baltensperger, U., Buchmann, B., Hueglin, C. and Prevot, A. S. H.: Source apportionment of submicron organic aerosols at an urban site by factor analytical modelling of aerosol mass spectra, Atmos. Chem. Phys., 7(6), 1503-1522, 2007.

[55] Lee, J. and D. A. Lane (2009), Unique products from the reaction of naphthalene with the hydroxyl radical, Atmos. Environ., 43(32), 4886-4893.

[56] Lee, J. and D. A. Lane (2010), Formation of oxidized products from the reaction of gaseous phenanthrene with the OH radical in a reaction chamber, Atmos. Environ., 44(20), 2469-2477.

[57] Lim, Y. B., and P. J. Ziemann (2009), Chemistry of Secondary Organic Aerosol Formation from OH Radical-Initiated Reactions of Linear, Branched, and Cyclic Alkanes in the Presence of NOx, Aerosol Sci. Technol., 43(6), 604-619.

[58] Lim, Y. B., and P. J. Ziemann (2005), Products and mechanism of secondary organic aerosol formation from reactions of n-alkanes with OH radicals in the presence of NOx, Environ. Sci. Technol., 39(23), 9229-9236.

[59] Liu, B. Y. H. and K. W. Lee (1976), Efficiency of membrane and nuclepore filters for submicrometer aerosols, Environ. Sci. Technol., 10(4), 345-350.

[60] Liu, S., Hu, M., Slanina, S., He, L.-Y., Niu, Y.-W., Bruegemann, E., Gnauk, T. and Herrmann, H.: Size distribution and source analysis of ionic compositions of aerosols in polluted periods at xinken in pearl river delta (PRD) of china, Atmos. Environ., 42(25), 6284-6295, 2008.

[61] Liu, S., S. Takahama, L. M. Russell, S. Gilardoni, and D. Baumgardner (2009), Oxygenated organic functional groups and their sources in single and submicron organic particles in MILAGRO 2006 campaign, Atmos. Chem. Phys., 9(18), 6849-6863.

[62] Liu, S., D. A. Day, J. E. Shields, and L. M. Russell (2011), Ozone-driven daytime formation of secondary organic aerosol containing carboxylic acid groups and alkane groups, Atmos. Chem. Phys., 11(16), 8321-8341.

[63] Liu, S., L. M. Russell, D. T. Sueper, and T. B. Onasch (2012), Organic particle types by single-particle measurements using a time-of-flight aerosol mass spectrometer coupled with a light scattering module, Atmos. Meas. Tech. Discuss, 5, 3047-3077.

[64] Mader, B. T., R. C. Flagan, and J. H. Seinfeld (2001), Sampling atmospheric carbonaceous aerosols using a particle trap impactor/denuder sampler, Environ. Sci. Technol., 35(24), 4857-4867.

[65] Maria, S. F., L. M. Russell, B. J. Turpin, and R. J. Porcja (2002), FTIR measurements of functional groups and organic mass in aerosol samples over the Caribbean, Atmos. Environ., 36(33), 5185-5196.

[66] Maria, S. F., L. M. Russell, M. K. Gilles, and S. C. B. Myneni (2004), Organic aerosol growth mechanisms and their climate-forcing implications, Science, 306(5703), 1921-1924.

[67] Myers, C. O. (1986), Kern River cogeneration project, IEEE ElectroTechnol. Rev., 2, 113-114.

[68] Nakao, S., M. Shrivastava, N. Anh, H. Jung, and D. Cocker, III (2011), Interpretation of Secondary Organic Aerosol Formation from Diesel Exhaust Photooxidation in an Environmental Chamber, Aerosol Sci. Technol., 45(8).

[69] Ng, N. L., et al. (2010), Organic aerosol components observed in Northern Hemispheric datasets from Aerosol Mass Spectrometry, Atmos. Chem. Phys., 10(10), 4625-4641.

[70] Ng, N. L., M. R. Canagaratna, J. L. Jimenez, P. S. Chhabra, J. H. Seinfeld, and D. R. Worsnop (2011), Changes in organic aerosol composition with aging inferred from aerosol mass spectra, Atmos. Chem. Phys., 11(13), 6465-6474.

[71] Offenberg, J. H., M. Lewandowski, M. Jaoui, and T. E. Kleindienst (2011), Contributions of Biogenic and Anthropogenic Hydrocarbons to Secondary Organic Aerosol during 2006 in Research Triangle Park, NC, Aerosol and Air Quality Research, 11(2), 99-U15.

[72] Paatero, P. and U. Tapper (1994), Positive matrix factorization A nonnegative factor model with optimal utilization of error-estimates of data values, Environmetrics, 5(2), 111-126.

[73] Paatero, P. and P. K. Hopke (2003), Discarding or downweighting high-noise variables in factor analytic models, Analytica Chimica Acta, 490(1-2), 277-289.

[74] Pye, H. O. T., and G. A. Pouliot (2012), Modeling the Role of Alkanes, Polycyclic Aromatic Hydrocarbons, and Their Oligomers in Secondary Organic Aerosol Formation, Environ. Sci. Technol., doi: 10.1021/es300409w.

[75] Richard, A., Gianini, M. F. D., Mohr, C., Furger, M., Bukowiecki, N., Minguillon, M. C., Lienemann, P., Flechsig, U., Appel, K., DeCarlo, P. F., Heringa, M. F., Chirico, R., Baltensperger, U., Prevot, A. S. H.. (2011), Source apportionment of size and time resolved trace elements and organic aerosols from an urban courtyard site in Switzerland, Atmos. Chem. Phys, 11(17), 8945-8963.

[76] Richter, H. and J. B. Howard (2000), Formation of polycyclic aromatic hydrocarbons and their growth to soot - a review of chemical reaction pathways, Progress in Energy and Combustion Science, 26(4-6), 565-608.

[77] Rodgers, J. L. and W. A. Nicewander (1998), Thirteen ways to look at the correlation-coefficient, American Statistician, 42(1), 59-66.

[78] Russell, L. M., S. F. Maria, and S. C. B. Myneni (2002), Mapping organic coatings on atmospheric particles, Geophys. Res. Lett., 29 (16), doi: 10.1029/2002GL014874.

[79] Russell, L. M. (2003): Aerosol organic-mass-to-organic-carbon ratio measurements, Environ. Sci. Technol., 37(13), 2982-2987.

[80] Russell, L. M., S. Takahama, S. Liu, L. N. Hawkins, D. S. Covert, P. K. Quinn, and T. S. Bates (2009), Oxygenated fraction and mass of organic aerosol from direct emission and atmospheric processing measured on the R/V Ronald Brown during TEXAQS/GoMACCS 2006, J. Geophys. Res, 114, D00F05, doi: 10.1029/2008JD011275.

[81] Russell, L. M., R. Bahadur, and P. J. Ziemann (2011), Identifying organic aerosol sources by comparing functional group composition in chamber and atmospheric particles, Proc. Natl. Acad. Sci., 108(9), 3516-3521.

[82] Schade, G. W. and P. J. Crutzen (1995), Emission of Aliphatic-amines from animal husbandry and their reactions-potential source of N2O and HCN, Journal of Atmospheric Chemistry, 22 (3), 319-346.

[83] Schauer, J. J., Rogge, W. F., Hildemann, L. M., Mazurek, M. A., Cass, G. R. and Simoneit, B. R. T.: Source apportionment of airborne particulate matter using organic compounds as tracers, Atmos. Environ., 30(22), 3837-3855, 1996.

[84] Schauer, J. J., M. J. Kleeman, G. R. Cass, and B. R. T. Simoneit (1999), Measurement of emissions from air pollution sources. 2. C-1 through C-30 organic compounds from medium duty diesel trucks, Environ. Sci. Technol., 33(10), 1578-1587.

[85] Schauer, J. J., and G. R. Cass (2000), Source apportionment of wintertime gas-phase and particle-phase air pollutants using organic compounds as tracers, Environ. Sci. Technol., 34(9), 1821-1832.

[86] Schauer, J. J., M. P. Fraser, G. R. Cass, and B. R. T. Simoneit (2002a), Source reconciliation of atmospheric gas-phase and particle-phase pollutants during a severe photochemical smog episode, Environ. Sci. Technol., 36(17), 3806-3814.

[87] Schauer, J. J., M. J. Kleeman, G. R. Cass, and B. R. T. Simoneit (2002b), Measurement of emissions from air pollution sources. 5. C-1-C-32 organic compounds from gasoline-powered motor vehicles, Environ. Sci. Technol., 36(6), 1169-1180.

[88] Schwartz, R. E., et al. (2010), Biogenic oxidized organic functional groups in aerosol particles from a mountain forest site and their similarities to laboratory chamber products, Atmos. Chem. Phys., 10(11), 5075-5088.

[89] Sheesley, R. J., J. J. Schauer and D. Kenski (2004), Trends in secondary organic aerosol at a remote site in Michigan's Upper Peninsula, Environ. Sci. Technol., 38, 6491-6500.

[90] Seinfeld, J. H. and S. N. Pandis (2006): Atmospheric chemistry and physics-from air pollution to climate change, John Wiley & Sons New Jersey.

[91] Shakya, K. M. and R. J. Griffin (2010), Secondary Organic Aerosol from Photooxidation of Polycyclic Aromatic Hydrocarbons, Environ. Sci. Technol., 44(21), 8134-8139.

[92] Sorooshian, A., S. N. Murphy, S. Hersey, H. Gates, L. T. Padro, A. Nenes, F. J. Brechtel, H. Jonsson, R. C. Flagan, and J. H. Seinfeld (2008), Comprehensive airborne characterization of aerosol from a major bovine source, Atmos. Chem. Phys., 8(17), 5489-5520.

[93] Srivastava, A., S. Gupta, and V. K. Jain (2008), Source apportionment of total suspended particulate matter in coarse and fine size ranges over Delhi, Aerosol and Air Quality Research, 8(2), 188-200.

[94] Stein, S. E. and D. R. Scott (1994), Optimization and testing of mass-spectral library search algorithms for compound identification, Journal of the American Society for Mass Spectrometry, 5(9), 859-866.

[95] Sun, Y. L., Zhang, Q., Schwab, J. J., Demerjian, K. L., Chen, W. N., Bae, M. S., Hung, H. M., Hogrefe, O., Frank, B., Rattigan, O. V. and Lin, Y. C. (2011), Characterization of the sources and processes of organic and inorganic aerosols in new york city with a high-resolution time-of-flight aerosol mass apectrometer, Atmos. Chem. Phys., 11(4), 1581-1602.

[96] Surratt, J. D., et al. (2008), Organosulfate formation in biogenic secondary organic aerosol, Journal of Physical Chemistry A, 112(36), 8345-8378.

[97] Takahama, S., S. Liu, and L. M. Russell (2010), Coatings and clusters of carboxylic acids in carbon-containing atmospheric particles from spectromicroscopy and their implications for cloud-nucleating and optical properties, J. Geophys. Res., 115, D01202, doi: 10.1029/2009JD012622.

[98] Takahama, S., S. Gilardoni, L. M. Russell, and A. L. D. Kilcoyne (2007), Classification of multiple types of organic carbon composition in atmospheric particles by scanning transmission X-ray microscopy analysis, Atmos. Environ, 41(40), 9435-9451.

[99] Tanner, R. L. and B. Zielinska (1994), Determination of the biogenic emission rates of species contributing to VOC in the San Joaquin Valley of California, Atmos. Environ, 28(6), 1113-1120.

[100] Tegen, I., and A. A. Lacis (1996), Modeling of particle size distribution and its influence on the radiative properties of mineral dust aerosol, J. Geophys. Res., 101(D14), 19237-19244.

[101] Tivanski, A. V., R. J. Hopkins, T. Tyliszczak, and M. K. Gilles (2007), Oxygenated interface on biomass burn tar balls determined by single particle scanning transmission X-ray microscopy, Journal of Physical Chemistry A, 111(25), 5448-5458.

[102] Turpin, B. J., J. J. Huntzicker, S. M. Larson, and G. R. Cass (1991), Los Angeles summer midday particulate carbon-primary and secondary aerosol, Environ. Sci. Technol., 25(10), 1788-1793.

[103] Turpin, B. J., P. Saxena, and E. Andrews (2000), Measuring and simulating particulate organics in the atmosphere: Problems and prospects, Atmos. Environ., 34(18), 2983-3013. Ulbrich, I. M., M. Lechner, and J. L. Jimenez (2007), AMS Spectral Database, http://cires.colorado.edu/jimenez-group/AMSsd.

[104] Ulbrich, I. M., M. R. Canagaratna, Q. Zhang, D. R. Worsnop, and J. L. Jimenez (2009), Interpretation of organic components from Positive Matrix Factorization of aerosol mass spectrometric data, Atmos. Chem. Phys., 9(9), 2891-2918.

[105] Ulbrich, I. M., M. R. Canagaratna, M. J. Cubison, Q. Zhang, N. L. Ng, A. C. Aiken, and J. L. Jimenez: Three-dimensional factorization of size-resolved organic aerosol mass spectra from mexico city, Atmos. Meas. Tech., 5, 195-224, 2012.

[106] Usher, C. R., A. E. Michel, and V. H. Grassian (2003), Reactions on mineral dust, Chem. Rev., 103(12), 4883-4939.

[107] Wallace, L. A., S. J. Emmerich, and C. Howard-Reed (2004), Source strengths of ultrafine and fine particles due to cooking with a gas stove, Environ. Sci. Technol., 38(8), 2304-2311.

[108] Wang, L., R. Atkinson, and J. Arey (2007), Dicarbonyl products of the OH radical-initiated reactions of naphthalene and the C-1- and C-2-alkylnaphthalenes, Environ. Sci. Technol., 41(8), 2803-2810.

[109] Wangberg, I., I. Barnes, and K. H. Becker (1997), Product and mechanistic study of the reaction of NO3 radicals with alpha-pinene, Environ. Sci. Technol., 31(7), 2130-2135.

[110] Ward, J. H. (1963), Hierarchical grouping to optimize an objective function, J. Am. Stat. Assoc., 58(301), 236244, doi:10.2307/2282967.

[111] Webb, P. J., J. F. Hamilton, A. C. Lewis, and K. Wirtz (2006), Formation of oxygenated-polycyclic aromatic compounds in aerosol from the photo-oxidation of o-tolualdehyde, Polycyclic Aromatic Compounds, 26(4), 237-252.

[112] Whitby, K. T., B. Y. H. Liu, and Husar R. B. (1972), Aerosol size distribution of Los Angeles smog, Journal of Colloid and Interface Science, 39(1), 177-204.

[113] Williams, B. J., A. H. Goldstein, N. M. Kreisberg, and S. V. Hering (2006), An in-situ instrument for speciated organic composition of atmospheric aerosols: Thermal Desorption Aerosol GC/MS-FID (TAG), Aerosol Science and Technology, 40(8), 627-638.

[114] Worton, D. R., Goldstein, A. H., Farmer, D. K., Docherty, K. S., Jimenez, J. L., Gilman, J. B., Kuster, W. C., de Gouw, J., Williams, B. J., Kreisberg, N. M., Hering, S. V., Bench, G., McKay, M., Kristensen, K., Glasius, M., Surratt, J. D. and Seinfeld, J. H. (2011), Origins and composition of fine atmospheric carbonaceous aerosol in the Sierra Nevada Mountains, California, Atmos. Chem. Phys., 11(19), 10219-10241.

[115] Yee, L. D., J. S. Craven, C. L. Loza, K. A. Schilling, N. L. Ng, M. R. Canagaratna, P. J. Ziemann, R. C. Flagan, and J. H. Seinfeld (2012), Secondary Organic Aerosol Formation from Low-NOx Photooxidation of Dodecane: Evolution of Multi-Generation Gas-Phase Chemistry and Aerosol Composition, Journal of Physical Chemistry A, doi: 10.1021/jp211531h.

[116] Zhang, Q., Canagaratna, M. R., Jayne, J. T., Worsnop, D. R. and Jimenez, J. L. (2005), Time- and size-resolved chemical composition of submicron particles in Pittsburgh: Implications for aerosol sources and processes, J. Geophys. Res., 110 (D7), D07S09, doi:10.1029/2004JD004649.

[117] Zhang, Q., et al. (2007), Ubiquity and dominance of oxygenated species in organic aerosols in anthropogenically-influenced Northern Hemisphere midlatitudes, Geophys. Res. Lett., 34(13), L13801, doi:10.1029/2007GL029979.

[118] Zhang, H., J. D. Surratt, Y. H. Lin, J. Bapat, and R. M. Kamens (2011), Effect of relative humidity on SOA formation from isoprene/NO photooxidation: enhancement of 2-methylglyceric acid and its corresponding oligoesters under dry conditions, Atmos. Chem. Phys., 11(13), 6411-6424.

[119] Zheng, M., G. R. Cass, J. J. Schauer, and E. S. Edgerton (2002), Source apportionment of PM2.5 in the southeastern United States using solvent-extractable organic compounds as tracers, Environ. Sci. Technol., 36(11), 2361-2371.

[120] Zhong, S. Y., C. D. Whiteman, and X. D. Bian (2004), Diurnal evolution of three-dimensional wind and temperature structure in California's Central Valley, Journal of Applied Meteorology, 43(11), 1679-1699.

Chapter 4

Organic particle types by single-particle measurements using a time-of-flight aerosol mass spectrometer coupled with a light scattering module

Abstract. Chemical and physical properties of individual ambient aerosol particles can vary greatly, so measuring the chemical composition at the single-particle level is essential for understanding atmospheric sources and transformations. Here we describe 46 days of single-particle measurements of atmospheric particles using a time-of-flight aerosol mass spectrometer coupled with a light scattering module (LS-ToF-AMS). The light scattering module optically detects particles larger than180 nm vacuum aerodynamic diameter (130 nm geometric diameter) before they arrive at the chemical mass spectrometer and then triggers

the saving of single-particle mass spectra. 271641 particles were detected and sampled during 237 hours of sampling in single-particle mode. By comparing timing of the predicted chemical ion signals from the light scattering measurement with the measured chemical ion signals by the mass spectrometer for each particle, particle types were classified and their number fractions determined as follows: prompt vaporization (49%), delayed vaporization (7%), and null (44%). LS-ToF-AMS provided the first direct measurement of the size-resolved collection efficiency of ambient particles, with an approximate 50% number-based CE for particles above detection limit. Prompt and delayed vaporization particles (147357 particles) were clustered based on similarity of organic mass spectra (using K-means algorithm) to result in three major clusters: highly oxidized particles (dominated by m/z 44), relatively less oxidized particles (dominated by m/z 43), and particles associated with fresh urban emissions. Each of the three organic clusters had limited chemical properties of other clusters, suggesting that all of the sampled organic particle types were internally mixed to some degree; however, the internal mixing was never uniform and distinct particle types existed throughout the study. Furthermore, the single-particle mass spectra and time series of these clusters agreed well with mass-based components identified (using factor analysis) from simultaneous ensemble-averaged measurements, supporting the connection between ensemble-based factors and atmospheric particle sources and processes. Measurements in this study illustrate that LS-ToF-AMS provides unique information about organic particle types by number as well as mass.

4.1   Introduction

Rapid measurements are needed to accurately quantify atmospheric particle sources and compositions and to study their transformations. The Aerosol Mass Spectrometer (AMS) is one fast-developing and widely used technique used for monitoring size and composition of submicron particles in real time (Jayne et al., 2000). Quantified species include nonrefractory organic mass (OM), sulfate, nitrate, ammonium, and chloride. Recent developments enable separation of ions that are slightly different in mass and overlap in unit-mass spectrum by replacing the quadrupole mass spectrometer (in Q-AMS) with a compact time-of-flight mass spectrometer (C-ToF-AMS), as described in Drewnick et al. (2005), and a high resolution time-of-flight mass spectrometer (HR-ToF-AMS), described in DeCarlo et al. (2006). The ToF-AMS collects signals from the composition of ensembles of particles in each chopper cycle. In the brute force single particle (BFSP) mode of the ToF-AMS operation, mass spectrum extractions within a chopper cycle are saved, enabling acquisition of single-particle mass spectra. However, the BFSP mode is typically turned off during field measurements to conserve data storage and processing time. The only published analysis utilizing this mode came from field measurements made by Drewnick et al. (2005), whereby single-particle mass spectra were acquired several times, each for a few minutes. These single-particle spectra were used to investigate internal and external mixing properties of submicron particles. Cross et al. (2007; 2009) advanced the AMS by coupling a light scattering module (LS-ToF-AMS) in which particles are optically detected by a laser before they reach the vaporizer. In LS-ToF-AMS, single-particle mass spectra are recorded during the operation of the light scattering single particle (LSSP) mode. The LSSP mode is similar to the BFSP mode, except that particle light scattering signals trigger the saving of single-particle mass spectra, which considerably enhances the data transfer and saving efficiency compared to the BFSP mode operation, during which mass spectra in each chopper cycle are saved individually regardless of the existence of particles. The LS-ToF-AMS was successfully deployed during the MILAGRO (Megacity Initiative: Local and Global Research Observations) 2006 field campaign for a 75-h sampling period (Cross et al., 2009),

demonstrating its unique ability to provide insights into the atmospheric transformations of ambient particles.

Compared to other single-particle measurement techniques (Table 1), the LS-ToF-AMS has the advantage of providing simultaneously quantified single- and ensemble-particle mass spectra, although the single-particle detection limit of the LS-ToF-AMS is higher than most of the online single-particle mass spectrometers (using laser ablation) and refractory components are not measured by LS-ToF-MS. Single-particle measurement statistics of LS-ToF-AMS are comparable to other online single-particle mass spectrometers and much greater than offline electron microscopy techniques, although the latter provide additional information about particle morphology and elemental composition.

This study expands the previous work of Cross et al. (2007; 2009) to identify three chemically-distinguishable classes of particles with a 46-day field measurement using the LS-ToF-AMS at a polluted urban site. We used the modified standard light scattering and single-particle mass spectra processing algorithm Sparrow and describe single-particle post-processing procedures. To interpret the organic composition of the individual particles, we grouped single-particle mass spectra to reduce the large dataset into a few clusters, each with distinct characteristics.

4.2 Measurements

The LS-ToF-AMS (Aerodyne, Billerica, MA) was deployed from 15 May to 29 June 2010 at Bakersfield during the CalNex (California Research at the Nexus of Air Quality and Climate Change) field campaign. The instrument combines the well-characterized HR-ToF-AMS and a light scattering module specifically developed for ToF-AMS applications. The ToF-AMS has been widely used in laboratory and field studies and is described in detail previously (DeCarlo et al., 2006; Drewnick et al., 2005; Jayne et al., 2000). The use of the LS-ToF-AMS for single-particle detection was first reported by Cross et al. (2009) with a compact ToF-AMS system. The work reported here is the first time the LS module has been used to acquire single-particle data with a high resolution ToF system

Table 4.1: Comparison of single-particle measurement techniques and their detection limits.

	Technique	Measured components	Size DL (nm)		Size resolution	Method for DL determination	Reference
			d_{va}	d_g			
Laser ablation	LAMMA		-	500	-	Not specified	Wieser et al., 1980
	ATOFMS		200	-	25-40[a] nm	Smallest laboratory-calibrated particles	Noble and Prather 1996; Gard et al., 1997
	UF-ATOFMS		100	-	-	Smallest particles that have non-zero detection efficiency	Su et al., 2004
	PALMS	Refractory and nonrefractory components, including organics, salts, metals, and dusts in single particles	-	200	-	Not specified	Murphy and Thomson, 1995; Thomoson et al., 2000
	RSMS-III		50	-	5-20[b] nm	Smallest particles that have non-zero detection efficiency	Lake et al., 2003; Johnston and Wexler, 1995; Phares et al., 2002
	SPLAT-II		50	-	-	Smallest particles that have non-zero detection efficiency	Zelenyuk et al., 2009
Electron microscopy	SEM-EDX or ESEM	Single-particle elemental compositions and morphology	-	100	-	Smallest particles tested in the laboratory	Laskin et al., 2001
	STXM	Organic functional groups, potassium, carbonate in single particles	-	100	-	Smallest particles analyzed	Takahama et al., 2007
Thermal volatilization	LS-Q-AMS		-	180	5-10[c]	Smallest particles that have non-zero detection efficiency	Cross et al., 2007
	LS-ToF-AMS	Nonrefractory organics, sulfate, nitrate, ammonium, chloride of single and ensemble particles	180	130	5-10[c]	Smallest particles that produce significant optical signals (S/N $\geq$ 5) (optical detection limit)	This study
	LS-ToF-AMS		430	307	5-10[c]	Size at which 50% of particle number are detected (compared to DMA)	This study

[a] Calculated as the standard deviation of the size-calibration curve fitting.

[b] Inferred from reported size distributions.

[c] Calculated as d/Δd at FWHM (full width at half maximum).

(HR-ToF-AMS). Adding the light scattering module does not influence ToF-AMS performance but rather physically identifies all particles (both nonrefractory and refractory) that reach the vaporizer and are larger than its detection limit, thereby providing substantially more information about single particles. During the entire campaign, the LS-ToF-AMS was operated in the MS mode (measures ensemble average chemical composition), PToF mode (particle time-of-flight, provides size-resolved chemical composition for ensemble average), and LSSP mode (acquires single-particle mass spectrum) for 120, 120 and 80 seconds of approximately every 5 minutes.

Briefly, the LS-ToF-AMS has five major components: aerosol sampling inlet, particle time-of-flight chamber, light scattering module for single-particle detection, particle vaporization and ionization chamber, and in this case, a high resolution time-of-flight mass spectrometer. Aerosols sampled through a 100-μm critical orifice are focused by an aerodynamic lens system, forming a narrow (~ 1 mm diameter) and highly collimated particle beam. Focused particles are transmitted under high vacuum ($\sim 10^{-5}$ Pa) through a laser beam for optical detection to the vaporization and ionization chamber, where they impact a heated surface (~ 600 °C). The nonrefractory fractions of the particles are flash vaporized and ionized by electron impact. Orthogonally extracted ions are subsequently analyzed by a time-of-flight mass spectrometer, which generates a complete mass spectrum at each extraction. A rotating chopper placed at the front of the particle-sizing chamber chops the particle beam and sets the starting time of particle flight. By measuring particle flight time between the mechanical chopper and the thermal vaporizer, particle vacuum aerodynamic diameter (d_{va}) can be determined from a calibration curve, which relates particle velocity (calculated using the known distance between the chopper and the vaporizer and the measured flight time) to particle size. The calibration curve was derived using polystyrene spheres (PSL of diameter 200 nm, 350 nm, 500 nm, and 600 nm) and ammonium nitrate particles that were size-selected by a differential mobility analyzer (DMA). Comparison of nominal PSL size and mobility-selected size showed good agreement. In this study, geometric diameter (d_g) is calculated using d_{va} and particle density ($d_g = d_{va}/\rho$),

assuming spherical particles. The density (1.4 g cm^{-3}) was derived by comparing AMS-measured mass size distribution with SMPS (scanning mobility particle sizer)-measured volume size distributions detailed in Ahlm et al. (2012).

The laser used for optical detection was a 405 nm continuous wave 50 mW laser (CrystaLaser, LC BCL-050-405). In order to maximize the overlap of the laser and the particle beams, the laser beam was not focused (Cross et al., 2007). Light scattered by sampled particles are collected using an ellipsoidal mirror and detected with a photomultiplier tube. The current system differs from the LS-ToF-AMS used by Cross et al. (2009) in the mechanism used for detecting single particles and saving the optical and chemical information for each detected particle. The key technical improvements include (1) adding the detected light scattering signal to the chopper frequency signal for unambiguous correlation in time, where the chopper frequency is the fundamental clock for the PToF and LSSP mode ToF-AMS data acquisition, and (2) using an external comparator circuit to test for the presence of a single particle in the scattered light signal, using a user set threshold level. This test is performed without transferring data to the computer for software evaluation, a process that takes longer time than an individual chopper cycle. The comparator circuit triggers the saving of the mass spectral data. Once triggered, the DAQ reports individual mass spectra for the entire chopper period in which the LS event occurred (mass spectra obtained as a function of particle time-of-flight). This approach dramatically reduces the overhead associated with any data transfer for events where there are no particles and eliminates the need to transfer the data from the DAQ board to the computer for software detection of particles. The light scattering particle counter, which is part of the comparator circuit, counts all of the threshold crossers observed by the external comparator circuit in the LSSP, PToF, and MS modes. This includes LS pulses for which single-particle mass spectral data were not recorded due to the transfer and saving times. This counter provides a measure of the particle number concentration for all optically detected particles and allows for the accurate evaluation of the true duty cycle obtained by the LSSP mode and direct comparisons with independent aerosol instruments that measure particle number concentrations. In addition, the

GZIP compression algorithm is applied to the single-particle files, thereby reducing the data transfer time and enhancing the sampling efficiency of the LS-ToF-AMS.

The LSSP mode records full mass spectra as a function of time during each chopper cycle. In the current configuration, there are 319 mass spectra obtained per chopper cycle. Each mass spectrum is baseline corrected to account for background signal at each m/z, using the average of two user selected "DC" regions at the start and end of the chopper cycle. Single-particle spectra are obtained by adding together a subset ($\sim$5 spectra) of the total number of baseline corrected mass spectra collected during a single chopper cycle.

The chopper used during this study had a 0.02 duty cycle and operated at 125 to 160 Hz frequency (set to 143 Hz) during the measurement. With this frequency, there is typically $\sim$1 particle or less per chopper cycle on average (DeCarlo et al., 2006), allowing correlated measurements of single-particle light scattering and chemical compositions. Potential particle coincidence events were investigated by examining the light scattering profile (i.e., light scattering intensity as a function particle time-of-flight) for each LS event. Particle coincidence is identified as multiple crossing of thresholds, which are defined as 5 times the standard deviation of the baseline of the light scattering profile. Using this criterion, the number of particle coincidence events was 0.3% of the total particle events, suggesting that particle coincidence events are negligible. Particles in the coincidence events were excluded in the analysis.

The limiting issues with the LSSP mode include the typically low duty cycles of the chopper and the overhead associated with transferring and saving the mass spectral data for single particles (Kimmel et al., 2011). During the transferring and saving of mass spectral data for a single chopper cycle, data from the following 6 chopper cycles were not recorded. The resulting duty cycle due to data storage processes ranged from $\sim$0.14 (i.e., 1/7 chopper cycles) to 1.0, depending upon the sampled particle number concentration, with an average of $\sim$0.62 for this study. An additional duty cycle of 0.45 was present during this study due to an unusual noise spike (characterized by near-zero light scattering signals and were filtered out in single-particle analysis) in the LS channel that

triggered saves. Taken together, the LSSP mode data rates obtained during this study represent a single-particle detection efficiency improvement of greater than a factor of 5 from the Cross et al. (2009) study.

4.3   Results and discussion

We began by classifying single particles into vaporization types based on timing of optically and chemically detected signals. We then clustered individual particles' organic mass spectra with significant signals into groups, each of which is associated with distinct chemical signatures. Finally, we compared these single-particle groups with components extracted from ensemble measurements.

4.3.1   Classification of single particles into vaporization types

Light scattering and single-particle measurements were processed using an updated version of the standard AMS light scattering data processing software Sparrow 1.04A (written by D. Sueper, Aerodyne Research Inc. and University of Colorado-Boulder; downloadable at `http://cires.colorado.edu/jimenez-group/ToFAMSResources/ToFSoftware/index.html#Analysis4`), which classifies the particles by their vaporization types and generates the physical (particle size in d_{va}, light scattering intensity) and chemical (unit-mass spectrum and mass of organics, sulfate, nitrate, and ammonium) data of single particles. A total of 271641 particles were measured during the 46-day campaign. Figure 1a shows the time-integrated light scattering signals plotted versus d_{va} and d_g for all of the saved particles. The optical detection limit, defined as the size at which particles produce detectable optical signals (S/N $\geq$ 5), was 180 nm d_{va} (130 nm d_g). The optical detection efficiency, defined as the ratio of optically detected particle number concentrations to SMPS-measured number concentrations (Fig. 2a), dropped below 100% at 550 nm d_{va} (393 nm d_g) and below 50% at 430 nm d_{va} (307 nm d_g). In comparison, the size that corresponds to 50% optical detection efficiency, derived from LS-coupled Q-AMS system in the laboratory by Cross et al. (2007),

was 240 nm d_g—22% lower than 307 nm d_g, suggesting that the alignment of LS-ToF-AMS used in this study was less optimized than that of the Cross et al. laboratory study. A group of particles with relatively high organic mass fractions ($\sim$1) are distinct from the majority of the particles (Fig. 1a). This subset of particles are dominated by hydrocarbon-like organic aerosol (HOA) signals, have lower d_{va}'s and higher integrated scattering signals compared to the rest of the particles. As these particles are classified in Cluster III that may consist of substantial primary OM (Fig. 1b and Section 3.2), these particles may contain black carbon or other primary refractory components that modified the shape, density, or the combined real refractive index of the particles. A similar externally mixed, HOA-dominated particle type was observed in Mexico City and reported in Cross et al. (2009). However, more work needs to be done to fully characterize these particle types.

Total saved particles were scaled by overall duty cycle to derive average particle number size distribution for this study. The overall duty cycle accounted for the 0.02 chopper duty cycle, data transfer and saving duty cycle (ranged from 0.2-1.0 with an average of 0.62), and noise spike duty cycle (0.45). Figure 2a represents the first direct in situ measure of the particle number-based sampling efficiency of an AMS and comparison with simultaneous SMPS number-based measurements. The light scattering signals indicate that particle sampling efficiency for particle sizes greater than 550 nm d_{va} (393 nm d_g) is similar to the laboratory measurements for the aerodynamic inlet lens system, with decreasing transmission efficiency at larger particle sizes (Liu et al., 2007). Figure 2b shows the comparison of campaign-average ion signals measured by the LSSP and PToF modes of the LS-ToF-AMS operation. Particles with time-of-flight greater than 0.0035 s, corresponding to 600 nm d_{va}, showed good agreement between the LSSP mode and PToF mode measurements, consistent with the agreement of number concentrations for particles larger than 550 nm d_{va} (Fig. 2a). Cross et al. (2009) demonstrated that the LSSP mode and PToF mode measured ion signals agreed for particles larger than $\sim$350 nm d_{va}, indicating that the LS system in that work was more optimized.
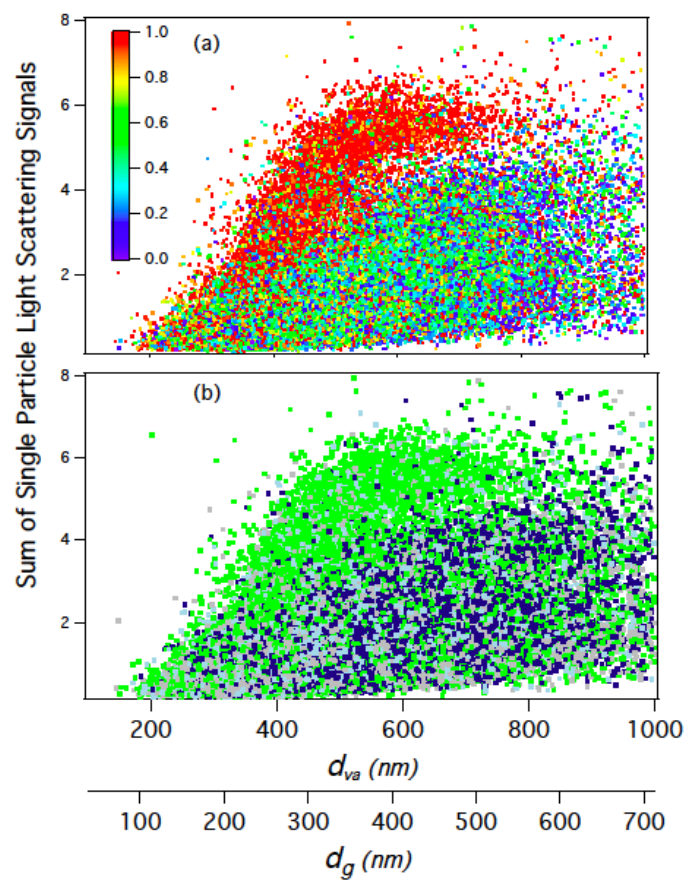
Figure 4.1: Sum of light scattering signals of prompt and delayed particles as a function of d_{va} (d_g). In **(a)**, each particle is colored by its organic mass fraction with colors shown in the color bar. In **(b)**, particles are colored by particle clusters derived cluster analysis in Sect. 3.2. Colors indicate Cluster I (dark blue), Cluster II (light blue), Cluster III (green), and unknown (grey).
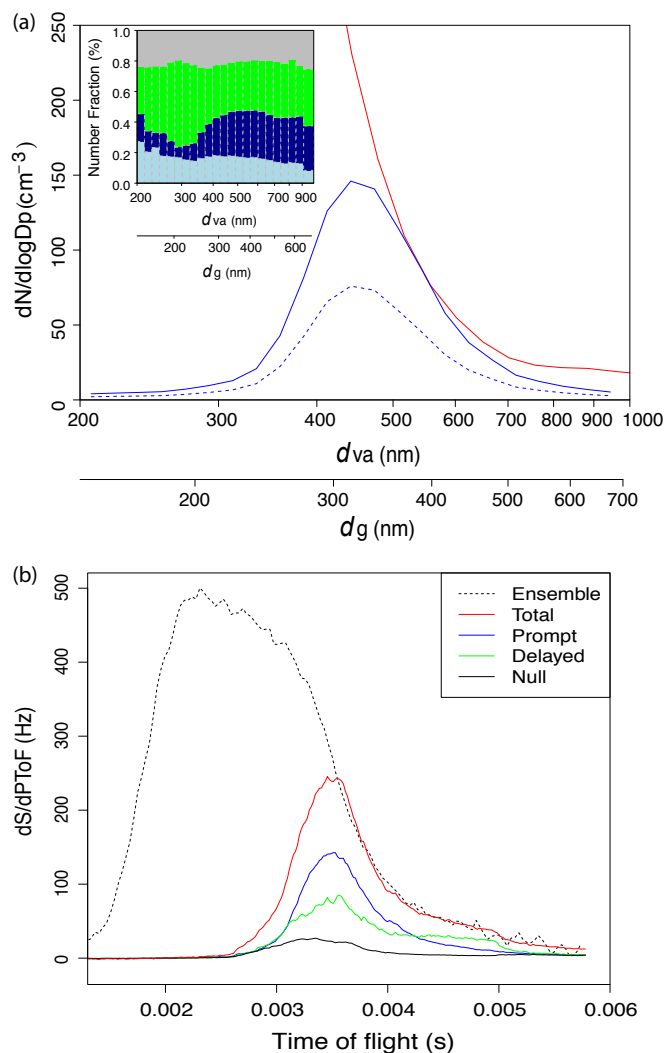
Figure 4.2: (a) Particle number size distributions measured by SMPS (red) and LS-ToF-AMS (solid blue). A density of 1.4 g cm^{-3} was used to convert SMPS mobility diameter to d_{va} (Ahlm et al., 2012). Dashed blue line represents number size distribution for sum of prompt and delayed particles. The inset shows number fractions for Cluster I (dark blue), Cluster II (light blue), Cluster III (green), and unknown (grey) particles. Particle size is binned logarithmically. For each size bin, logarithmic ratio of upper size to lower size is 0.03. (b) Comparison of campaign-average mass distribution as a function of particle time-of-flight of ensemble (dotted black line; PToF mode) and single-particle measurements (LSSP mode). The total (red) represents the sum of the prompt (blue), delayed (green), and null (black) particle signals measured by the LSSP mode.

Low detection efficiency for small particles likely resulted from (i) widening of particle beam beyond the region of overlap of the particle and laser beams or low detection efficiency for small particles passing through the edges of the laser beam and (ii) size detection limit of small particles by the laser. Comparison of LS-ToF-AMS- and SMPS-measured total particle number concentration showed similar time series, i.e., total number concentration of 560- to 1000-nm d_{va} (400- to 715-nm d_g) particles agreed reasonably well (Fig. S1)–the linear fit has a slope of 0.89 (the SMPS-measured concentration was 11% higher) and an intercept of 6.25, and the number concentrations correlated with an R of 0.7, while the total concentration of 200- to 560-nm d_{va} (140- to 400-nm d_g) particles measured by LS-ToF-AMS was much lower.

In order to determine the timing of the measured chemical signals, a mass intensity profile (i.e., mass intensity quantified by the ToF-MS mass spectrometer as a function of particle time-of-flight) is needed for each particle. The profile is the sum of profiles for all detected ion fragments (including organic and inorganic fragments) for each particle. Since the acquisition rate is faster than the particle vaporization time, several mass spectra are obtained during the ($\sim$100 μs) particle vaporization event. These individual spectra are co-added to accumulate the total measured ion intensity for the single particle. However, adding fragments with low intensities can significantly lower the contrast between real and background signals. Additionally, background-related fragments m/z 18 (H_2O^+), 28 (N_2^+), 32 (O_2^+), and 39 (K^+) can greatly mask real signals. Therefore, only the profiles of nonbackground high-intensity fragments were summed to construct a mass intensity profile for each particle.

Ensemble average concentrations (from the MS mode measurement) were used to estimate ion fragment abundance of single particles. Ten high-intensity ion fragments were selected for this campaign, including m/z 15, 27, 30, 41, 43, 44, 46, 48, 55, 57, and 64. This list combined organic- and inorganic- (nitrate, sulfate, and ammonium) dominated fragments. Additionally, selected organic fragments were characteristics of specific particle types; for example, m/z 44 is a tracer for oxygenated organic aerosols (OOA), and m/z 57 typically represents HOA (Zhang

et al., 2005).

Timing of the optical signals (T_{LS}) and chemical signals (T_{MS}) was retrieved by locating the maximum light scattering intensity and mass intensity from the light scattering (i.e., light scattering intensity as a function of particle time-of-flight) and mass intensity profiles, respectively. T_{LS} and T_{MS}, respectively, represent the particle flight time from the midpoint of chopper opening to the laser and to the mass spectrometer (including the vaporization and ion transit time from the vaporizer to the time-of-flight mass spectrometer). Using the particle velocity (calculated from T_{LS} and the chopper-to-laser distance) and the chopper-to-vaporizer distance, the timing of particle chemical signals can be predicted (T_{MS-P}). By comparing timing of the predicted particle chemical signals (T_{MS-P}) with the timing of the measured chemical signals (T_{MS}), the vaporization and ion flight time (T_{MS-ION}) can be estimated by the y-axis offset of the T_{MS-P} versus T_{MS} (scatter) plot. Using T_{MS} and the sum of $T_{MS-P}+T_{MS-ION}$, each single particle was classified as one of three discrete particle types: (1) "prompt," for which the deviation of $T_{MS}/(T_{MS-P}+T_{MS-ION})$ from 1 was less than 20% (i.e., particles optically and chemically detected at the expected time offset); (2) "delayed," for which the deviation of $T_{MS}/(T_{MS-P}+T_{MS-ION})$ from 1 was greater than 20% (i.e., T_{MS} significantly lagged $T_{MS-P}+T_{MS-ION}$); and (3) "null," for which optical signals were detected, but no significant chemical signals were observed. The criterion of insignificant chemical signals is a minimum sum of chemical signals for the mass intensity profile of 6 ions. Using this criterion, the null particles had typically 2-4 ions (Fig. S2) that are comparable to the number of ions generated in the nonparticle events (chopper cycles that have no particles).

Particle statistics associated with the three vaporization types (Table 2) show that prompt and null particles dominated, accounting for 46% and 48%, respectively, of the saved particles, while delayed particles accounted for a 6% fraction. The null particle fraction was comparable to that of the 51% fraction identified from the Mexico City measurement (Cross et al., 2009), suggesting that the AMS vaporization-ionization may typically miss about 50% of sampled particles (for particle diameters larger than 180 nm d_{va} or 130 nm d_g), based on
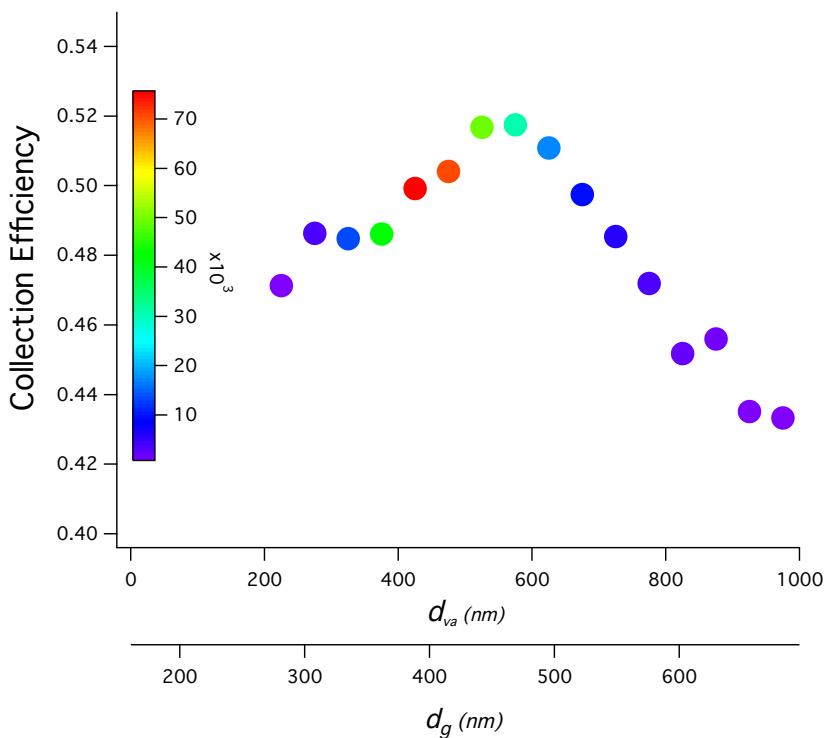
Figure 4.3: Collection efficiency versus particle size. Point colors indicate number of particles measured in the corresponding size, with color scale shown by the vertical bar.

particle number. The mass-based collection efficiency (CE) of the AMS is dependent on particle composition and is higher for low-sulfate particles (Quinn et al., 2006; Matthew et al., 2008; Middlebrook et al., 2012). While the prompt particle (46%) group points to a number-based CE of ~ 0.5 for particles larger than 180 nm d_{va} (130 nm d_g), smaller particles (<180 nm d_{va}), which accounted for 35% of submicron particle mass, may have had higher CE due to their low sulfate (15% of nonrefractory (NR)-PM$_1$) and high organic contents (75% of NR-PM$_1$) (Ahlm et al., 2012). Therefore, the number-based CE of 0.5 was lower compared to the average mass-based CE of 0.8, which was determined by scaling the AMS mass to the SMPS-derived mass for particles of all sizes smaller than 1000 nm (excluded masses of elemental carbon and dusts) (Ahlm et al., 2012). CE values ranged from 0.43 to 0.52 for particles larger than 180 nm d_{va}, with peak values associated

Table 4.2: Particle number and number fraction for the three vaporization types.

Particle vaporization type	Particle Number	Number fraction (%)
Prompt	130361	46
Delayed	16996	6
Null	124284	48

with 500-600 nm d_{va} particles (Fig. 3). Particles in 800- to 1000-nm d_{va} had the lowest CE values, likely due to enriched dust components in this size range (Silva et al., 2000) that were not vaporized by the AMS or because of the enhanced mass fraction of sulfate and decreased mass fraction of the organics (Fig. 1a).

4.3.2 Organic particle types identified from cluster analysis

Prompt and delayed particles that had significant mass spectrum signals were used for cluster analysis. The K-means clustering algorithm, applied to the 147357 single-particle organic mass spectra, divides spectra into K clusters such that the sum of squares of the distances between the spectra and their corresponding cluster centroid is minimized (Hartigan and Wong, 1979). Spectra were normalized before clustering so that the sum of intensities for each mass spectrum was 1. In order to identify organic particle types, only organic fragments were included in the cluster analysis. K values of 2 to 12 (varying by 1) were tested. For each run, 10 sets of random cluster centroids were iterated. Using $K \leq 6$ resulted in one dominating cluster (containing $\sim$75% of particles used for clustering) with an average spectrum characterized by mixed types of marker fragments (e.g., m/z 44 for OOA and m/z 57 for HOA), which indicated that particles in this cluster were not well separated; thus, $K \leq 6$ solutions were not preferred. However, three major clusters were consistently identified from the $K > 6$ clustering solutions, with each cluster associated to a distinct mass spectrum. Taken together, these particles accounted for $\sim$80% of the particles. Each of the remaining clusters typically contained less than 5% of the particles.

Cosine similarity is a useful tool for estimating mass spectrum similarity

(Stein and Scott, 1994) and was therefore used here as a metric to measure the within-cluster and cross-cluster similarity of single-particle spectra. In brief, cosine similarity is the cosine of the angle between two vectors (where each vector represents a mass spectrum) and is calculated using the following equation:

$$\cos\theta = \frac{\vec{A} \cdot \vec{B}}{\|\vec{A}\| \cdot \|\vec{B}\|} = \frac{\sum_i^n \vec{A}_i \times \vec{B}_i}{\sqrt{\sum_i^n (\vec{A}_i)^2} \times \sqrt{\sum_i^n (\vec{B}_i)^2}} \tag{4.1}$$

where $\|A\|$ and $\|B\|$, respectively, represent the magnitudes of vectors A and B, and A·B denotes the dot product of A and B. Cosine similarity ranges from 0 to 1, with higher values representing smaller angles and higher similarity. The cosine similarity between each single-particle spectrum and the three major cluster centroids (the average spectra) was calculated (Fig. 4). Spectra in Cluster I had significantly higher similarity (median value is > 0.8) to Cluster I centroid than Cluster II and III centroids (Fig. 4a). In other words, the within-cluster similarity was far higher than the cross-cluster similarity for Cluster I spectra. In addition, the variability of the within-cluster similarity was lower than that of the cross-cluster similarity, suggesting good separation of Cluster I spectra. Similar results were found for Cluster II spectra (Fig. 4b). Compared to Cluster I and Cluster II, the within-cluster similarity for Cluster III spectra had lower values (median value of 0.5) and greater variability (Fig. 4c). However, the within-cluster similarity was significantly higher than the cross-cluster similarity at 99% confidence level for Cluster III spectra. The cosine similarity analysis also suggests that each cluster may have limited chemical properties of other clusters, indicating that particles were likely internally mixed but dominated by one type so they can be grouped by the dominant signatures.

The effects of single-particle size and organic mass fraction on the derived single-particle clusters were examined. The number of organic ions detected for each single-particle is a function of the organic mass fraction (for a given threshold of 6 ions described in Section 3.1) and particle size (larger particles produce more ions). Sulfate and nitrate, the major inorganic ions, were found to be independent of organic cluster types (Fig. 5), i.e., sulfate and nitrate, respectively, accounted for 16% and 4% of single-particle mass for each cluster (on average). To test the effects
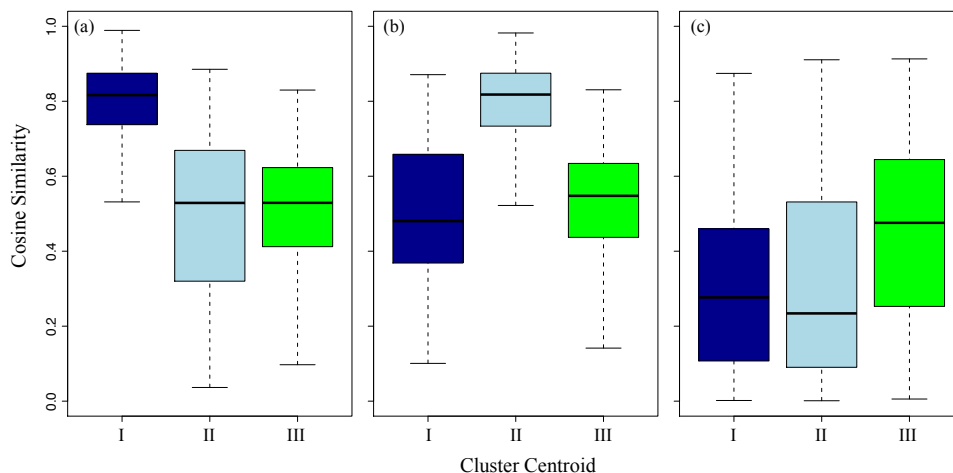
Figure 4.4: Spectrum similarity to Cluster I centroid (dark blue), Cluster II centroid (light blue), and Cluster III centroid (green) for **(a)** Cluster I spectra, **(b)** Cluster II spectra, and **(c)** Cluster III spectra. The horizontal bar in each box represents the median value. Each box's upper and lower bounds represent the 25th and the 75th percentiles, respectively, with the whiskers extending 1.5 interquartile ranges.

of organic mass fractions on the derived clusters, a K-means algorithm was applied to four subsets of the total 147357 particles, which were composed of particles with organic mass fractions greater than 10%, 20%, 30%, and 40% of the total particle mass, respectively. Three major clusters were identified in each case. The cluster centroids were identical to the centroids of Clusters I to III, and the relative cluster sizes (number of particles in the cluster) were comparable to the relative sizes of Clusters I to III, indicating that the same single-particle clusters were identified. The effects of particle size on clustering results were tested by applying a K-means analysis to three subsets of the total particles, which were composed of particles larger than 300 nm, 400 nm, and 500 nm d_{va}, respectively. The same clusters (as Clusters I to III) were identified. That the inorganic-to-organic mass ratio and particle size did not affect the results of cluster analysis indicated that the single-particle organic mass ions were sufficient for cluster analysis and the identified clusters were robust.

Examples of single-particle spectra for the three major clusters are shown in Fig. 5a. (The cluster centroids and time series of the minor clusters are shown in
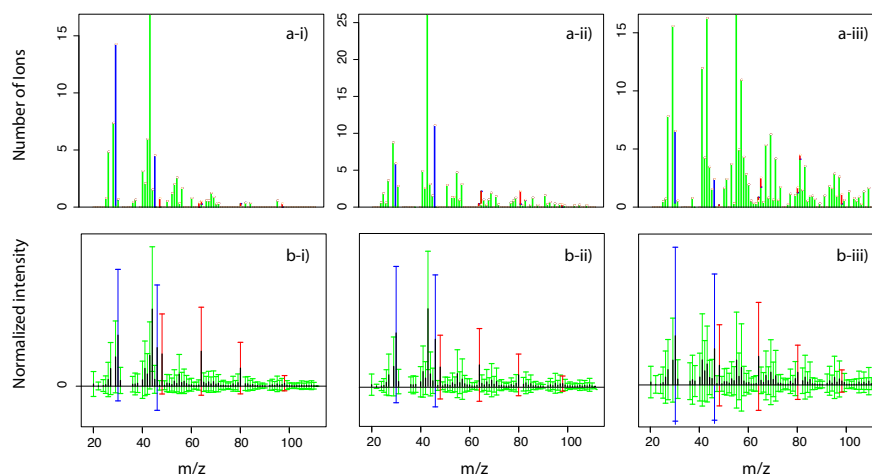
Figure 4.5: **(a)** Example single-particle spectra for (i) Cluster I, (ii) Cluster II, and (iii) Cluster III. The particles in (i), (ii), and (iii) were collected on 16 May ($d_{\text{va}} = 507\,\text{nm}$, $d_{\text{g}} = 362\,\text{nm}$), 31 May ($d_{\text{va}} = 402\,\text{nm}$, $d_{\text{g}} = 287\,\text{nm}$), and 16 May ($d_{\text{va}} = 492\,\text{nm}$, $d_{\text{g}} = 351\,\text{nm}$), respectively. **(b)** Variability of normalized single-particle spectra for each cluster for this study (15 May to 29 June 2010). In each panel, the black sticks show the average spectrum for the cluster, and the whiskers represent standard deviations (variability) at each m/z. Colors indicate organic (green), nitrate (blue), and sulfate (red) fragments.

Fig. S3 and S4, respectively, in the supplemental information.) While the single-particle spectra exhibit large variability (Fig. 5b), the centroids for the three particle types (Fig. 6a) show that the Cluster I spectrum was characterized by a dominant peak at m/z 44, comparable to that of LV-OOA (low-volatility OOA) components extracted from the positive matrix factorization (PMF) analysis in a number of field measurements (Ulbrich et al., 2009). This indicates that particles in this cluster were highly oxidized and associated with high O/C, which is consistent with the correlation of the number fraction of Cluster I particles with odd oxygen (Fig. 7a). It is suggested that Cluster II particles, which had strong m/z 43 signals and mass spectra resembling those of SV-OOA (semi-volatile OOA) components identified by Lanz et al. (2007), Ng et al. (2010), and Ulbrich et al. (2009), were relatively less oxidized SOA and, so, were likely associated with lower O/C than Cluster I particles. The number fraction of Cluster II particles increased at night and showed the opposite diurnal cycle to temperature (Fig. 7b), which is consistent

with the previous findings that the less processed component accumulated and condensed onto preexisting particles during nighttime hours (Lanz et al., 2007). However, the correlation of Cluster II particle number fraction with particle-phase nitrate, whose formation is strongly dependent on temperature, was not found, suggesting that there might be other factors that affected the formation of Cluster II particles. The average spectrum for Cluster III particles was characterized by m/z 27, 29, 41, 43, 55, 57, and 69, which are characteristic of both HOA and cooking organic aerosol (COA) components (He et al., 2010; Mohr et al., 2009; 2012). However, the HOA and COA components are not distinguishable due to the high similarity of their unit-mass spectra (Mohr et al., 2009; 2012), although both the HOA-influenced component (the nighttime OA factor) and the COA component were identified from the PMF analysis of the high-resolution ensemble mass spectra measured by the same LS-ToF-AMS during the CalNex campaign (Liu et al., submitted). The number fraction of Cluster III particles peaked at night, anti-correlating with temperature (Fig. 7c). Thus particles in Cluster III may be produced by a mixture of different sources, possibly including cooking oils and local unoxidized vehicular emissions at night.

Size distributions of particle types (Fig. 2a) show an increased number fraction of Cluster I type for particles larger than 300 nm d_{va} (215 nm d_g). In contrast, Cluster III type dominated particles smaller than 400 nm d_{va} (285 nm d_g). Compared to Cluster I and Cluster III particle types, Cluster II type was more evenly distributed across particle size. A likely explanation of size dependence of particle types is that oxidized particles (in Cluster I) formed by condensation of secondary vapors onto preexisting particles so that they grew bigger, whereas Cluster III particles were associated with fresh emissions in which particles were smaller.

4.3.3 Comparison of single-particle types with ensemble components

Cluster I, Cluster II, and Cluster III particle types broadly matched the OM components identified from ensemble factor analysis using PMF (Liu et al., sub-
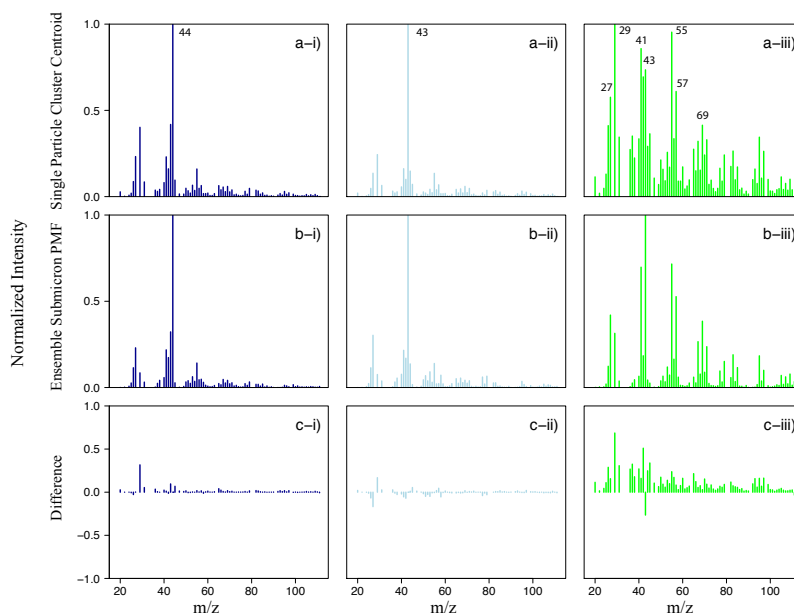
Figure 4.6: **(a)** Cluster centroid (group-average mass spectrum) for (i) Cluster I, (ii) Cluster II, and (iii) Cluster III particles. **(b)** Mass spectrum for (i) the high O/C alkane SOA factor, (ii) the low O/C alkane SOA factor, and (iii) mass-weighted average for the COA, PO SOA, and nighttime OA factors identified from the ensemble measurements using PMF analysis. **(c)** The difference between spectra in **(a)** and **(b)**.

mitted). Ensemble-based OM spectra were categorized into three groups according to their O/C values (calculated from the high resolution mass spectra using the method described by Aiken et al. (2007)): Group I consisted of high O/C alkane and aromatic SOA components (O/C = 0.63-0.68); Group II consisted of low O/C alkane and aromatic SOA components (O/C = 0.27-0.36); and Group III was likely a mixture of COA, petroleum operation (PO) SOA, and local traffic and biogenic nighttime OA components (O/C = 0.00-0.20). The mass fractions of m/z 44 (f_{44}; an indicator of O/C (Aiken et al., 2008)) for Cluster I (23.1%), Cluster II (4.1%), and Cluster III (2%) reasonably agreed with the f_{44} for the ensemble-based Group I (19.6%), Group II (2.4%), and Group III (0.5%), respectively. Specifically, the Cluster I centroid correlated to the mass spectra for high O/C alkane and aromatic SOA components with an R of 0.96 and 0.92, respectively (Fig. 6). The mass fraction of Cluster I particles had similar magnitude and time series to that
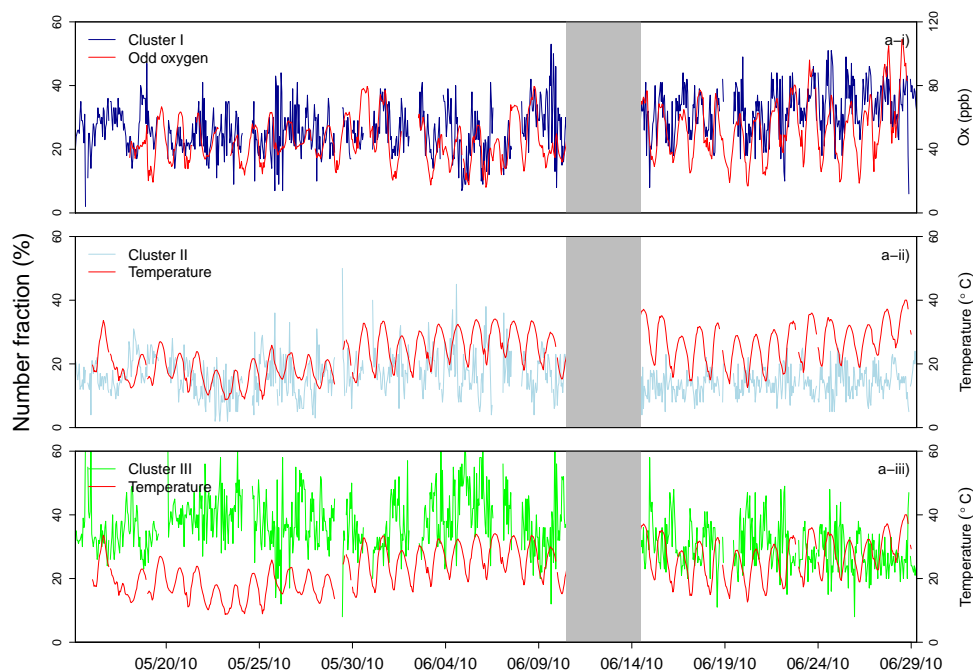
Figure 4.7: Time series of the number fraction for i) Cluster I (dark blue), ii) Cluster II (light blue), and Cluster III (green) particles. Time series of odd oxygen (O$_x$, shown in panel i) and temperature (panel ii and iii) are shown for comparison.

of the sum of high O/C alkane and aromatic SOA components (Fig. 8a; correlated in time with $R = 0.69$ shown in Table S1), supporting the consistency of Cluster I particles with high O/C components. The centroid for Cluster II particles correlated to that of the low O/C alkane SOA component with an R of 0.96. The Cluster III centroid correlated to the spectra for COA, PO SOA, and nighttime OA components with R values of 0.86, 0.76, and 0.70, respectively. Correlation of the Cluster III centroid to the mass-weighted average spectrum for COA, PO SOA and nighttime OA (Fig. 6b-iii) showed an R of 0.82. The mass fraction of Cluster III particles and the sum of ensemble-derived Group III components co-varied (Fig. 8c; $R = 0.63$ shown in Table S1), with low fractions during daytime and increased abundance at night. There were some deviations in magnitude and time series for single-particle clusters and ensemble-derived components, especially for Cluster II particles that only poorly correlated with the low O/C alkane SOA factor ($R = 0.22$). The differences were likely due to 1) measurement and analysis (cluster,

PMF, etc.) uncertainties, 2) internally mixed particles that were split between more than one cluster or assigned to one of the minor clusters (IV, V, VI, etc.), or 3) the low detection efficiency of single particles that were smaller than 550 nm d_{va} (Fig. 2a). However, the broad match of single-particle clusters and ensemble factors confirmed that the factors reflected organic components of different origins and atmospheric processes.
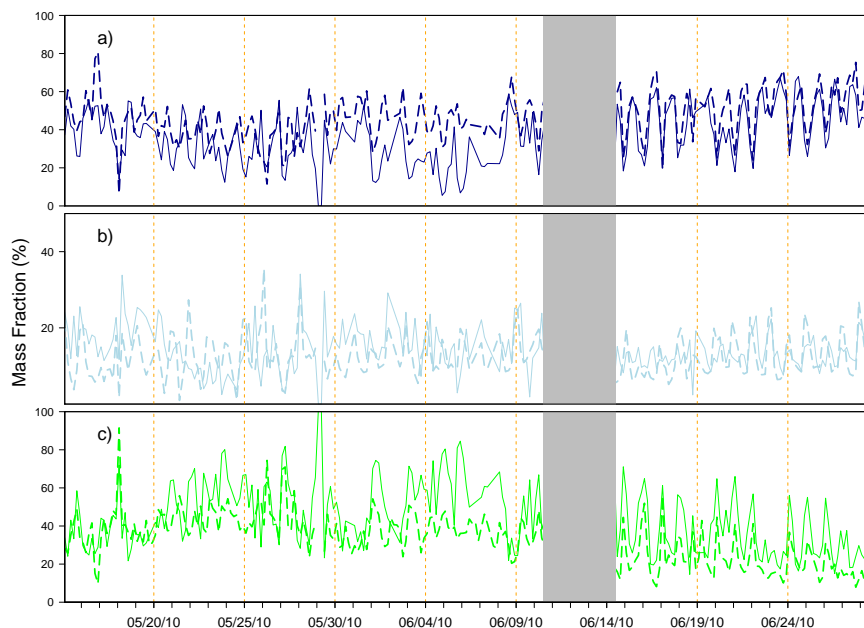
Figure 4.8: Solid lines show time series of the mass fraction for (a) Cluster I (dark blue), (b) Cluster II (light blue), and (c) Cluster III (green) particles. Dashed lines represent time series of the mass fraction for (a) the sum of high O/C alkane and aromatic SOA (dark blue), (b) the low O/C alkane SOA (light blue), and (c) the sum of COA, PO SOA, and nighttime OA factors (green) identified from ensemble measurements using PMF analysis (Liu et al., submitted). Measurements were averaged to 4-hour intervals.

4.4   Concluding remarks

The LS-ToF-AMS was valuable for separating single particles with different organic chemical compositions in a 46-day field campaign. 271641 single particles were optically detected and the chemical mass spectra saved and classified by

comparison of the optical and chemical information, with a 46% prompt fraction, a 48% null fraction, and a 6% delayed particle fraction. Thus, the LS-ToF-AMS provided a direct measure of the collection efficiency of ambient particles, resulting in an approximate 50% number-based CE for particles larger than180 nm d_{va} (130 nm d_g).

Single particles can be consistently represented by several particle types, each of which has distinct chemical compositions formed via different processes. A K-means clustering algorithm was applied to the organic mass spectra for all saved prompt and delayed single particles. We found that ~80% of single particles were dominated by chemical characteristics of one of the three clusters: Cluster I and II particles appeared to be formed from secondary organic components while Cluster III particles suggested a primary origin from fresh urban emissions. Additionally, Cluster I particles likely were more oxidized than particles in Cluster II due to the large contribution of m/z 44 in the Cluster I centroid. Mass spectra and time series of the three particle types broadly matched the organic factors identified from the ensemble-averaged measurements using the LS-ToF-AMS, providing evidence that the factors could represent organic components originating from different sources and processes.

Continual developments of LS-ToF-AMS, such as enhancing its ability to detect smaller particles and data transfer and saving efficiency, will result in more detailed information about the origin, transformation, and fate of atmospheric organic particles.

4.5   Appendix

4.5.1   Comparison of number concentration measured by LS-ToF-AMS and SMPS

Average particle detection rate (particles detected per second) for each saved LSSP mode file (run number) was scaled by the overall duty cycle (for the same file) to calculate total particle number concentration. Time series of
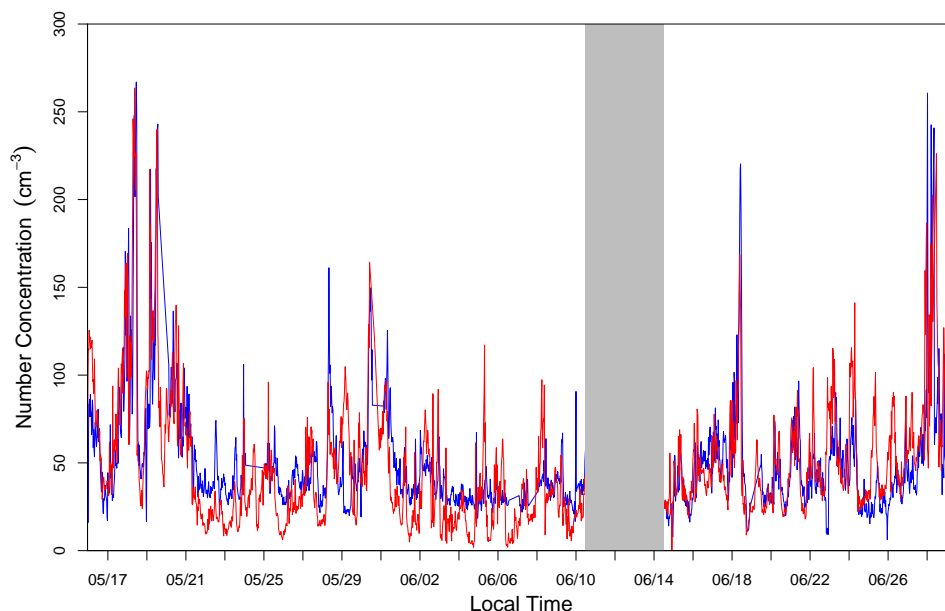
Figure 4.9: Time series of SMPS-measured (red) and LS-ToF-AMS-derived (blue) number concentration for particles in 400- to 1000-nm d_{va} (285- to 715-nm d_g) size range.

LS-ToF-AMS- and SMPS-measured number concentrations were averaged to 30-min intervals for comparison. Total number concentration for 560- to 1000-nm d_{va} (400- to 715-nm d_g) particles compared reasonably wellthe linear fit has a slope of 0.89 (the SMPS-measured concentration was 11% higher) and an intercept of 6.25, and the number concentrations correlated with an R of 0.7 (Fig. 4.9).

4.5.2 Comparison of ions generated by single particles of different vaporization types

The ions associated with the prompt and delayed, null, and non-particle events were compared using (a) the sum of non-background ions (i.e., m/z 15, 27, 30, 41, 43, 44, 46, 48, 55, 57, and 64) and (b) all the ions in the mass spectra. In both cases, prompt and delayed particles have significantly higher number of ions than in null- and non-particle events. For the non-particle and null-particle events,

there are typically 2-4 ions, which are below the 6-ion detection limit (Fig. 4.10).
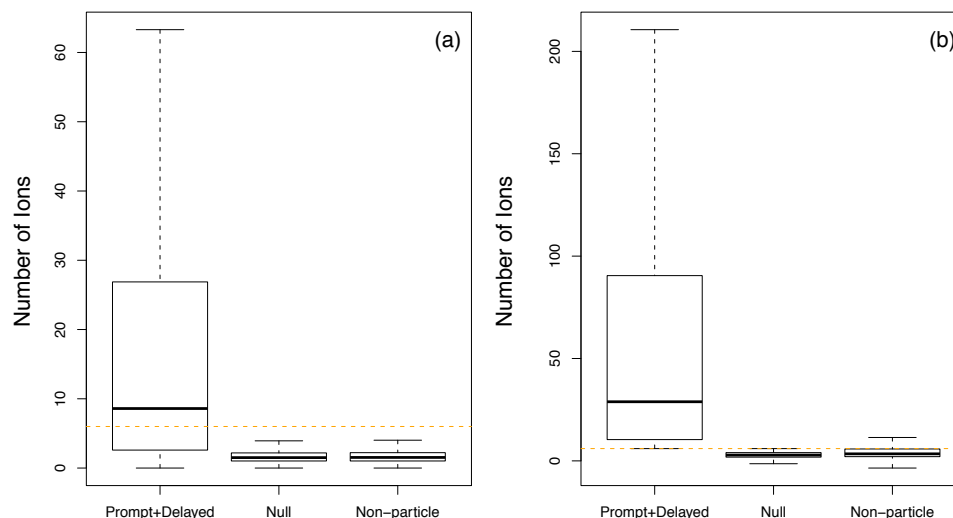
Figure 4.10: Comparison of number of ions associated with prompt and delayed, null, and non-particle events by using (a) the major ions including m/z 15, 27, 30, 41, 43, 44, 46, 48, 55, 57, and 64 and (b) using all ions (m/z 1 to m/z 111). Horizontal lines indicate the threshold of 6 ions.

4.5.3   The minor clusters

The single-particle spectra and time series of the minor clusters (the 9-cluster solution) are shown in Fig. 4.11 and 4.12, respectively.
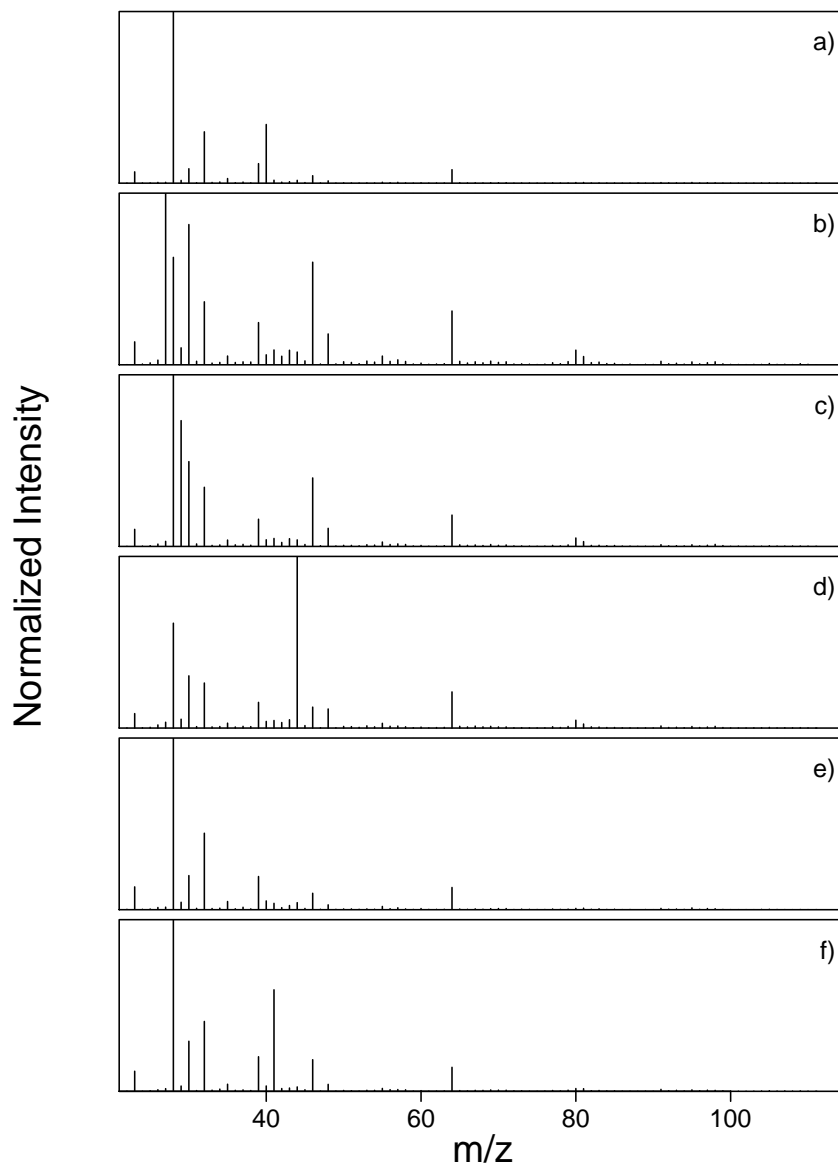
Figure 4.11: Cluster centroids of the minor clusters in the 9-cluster solution, with panels a) to f) showing the centroids for clusters IV to IX, respectively.
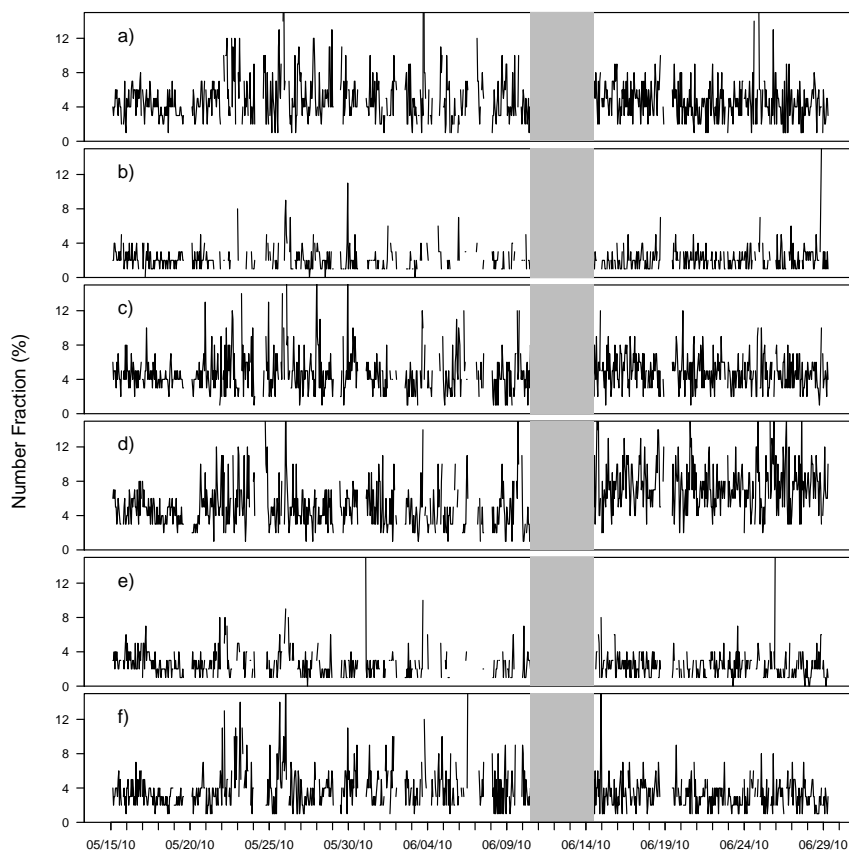
Figure 4.12: Time series of the number fraction for the minor clusters in the 9-cluster solution, with panels a) to f) representing clusters IV to IX, respectively.

4.5.4 Correlation of the single-particle clusters and the ensemble-derived PMF factors

Correlation of the single-particle clusters and the ensemble-derived PMF factors is shown in Table 4.3.

4.6 Acknowledgments

Table 4.3: Cross correlation of the mass fraction time series for the three single-particle clusters (Clusters I, II, and III) and the ensemble-derived factors. Persons correlation coefficients (R) are shown.

	High O/C alkane SOA + high O/C aromatic SOA	Low O/C alkane SOA	COA + PO SOA +Nighttime OA
Cluster I	0.69	-0.29	-0.62
Cluster II	0.02	0.22	-0.06
Cluster III	-0.67	0.18	0.63

with instrument operation, maintenance, and data collection. The authors are grateful to the CalNex-SJV research team, in particular Ron Cohen and Allen Goldstein who organized the campaign and Sally Pusede for coordination. John Karlik and the Kern County University of California Cooperative Extension staff hosted the field site, and their generous help is appreciated. The authors also thank John Jayne and Joel Kimmel for constructive comments. The statements and conclusions in this paper are those of the researchers (contractor) and not necessarily those of CARB. The mention of commercial products, their source, or their use in connection with material reported herein is not to be construed as actual or implied endorsement of such products.

Chapter 4, in full, is a reprint of the material as it appears in Atmospheric Measurement Techniques Discussion 2012 with slight modifications. Liu, S., Russell, L. M., Sueper, D. T., and Onasch, T. B. (2012), Organic particle types by single-particle measurements using a time-of-flight aerosol mass spectrometer coupled with a light scattering module, Atmospheric Measurement Techniques Discussion, 5, 3047-3077. The dissertation author was the primary investigator and author of this paper.

References

[1] Ahlm, L., Liu, S., Day, D. A., Russell, L. M., Weber, R., Gentner, D. R., Goldstein, A. H., DiGangi, J. P., Henry, S. B., Keutsch, F. N., VandenBoer, T. C., Markovic, M. Z., Murphy, J. G., Ren, X., and Scheller, S.: Formation and growth of ultrafine particles from secondary sources in bakersfield, california, J. Geophys. Res.-Atmos., 117, D00V08, doi:10.1029/2011JD017144, 2012.

[2] Aiken, A. C., DeCarlo, P. F., and Jimenez, J. L.: Elemental analysis of organic species with electron ionization high-resolution mass spectrometry, Anal. Chem., 79, 8350–8358, 2007.

[3] Aiken, A. C., Decarlo, P. F., Kroll, J. H., Worsnop, D. R., Huffman, J. A., Docherty, K. S., Ulbrich, I. M., Mohr, C., Kimmel, J. R., Sueper, D., Sun, Y., Zhang, Q., Trimborn, A., Northway, M., Ziemann, P. J., Canagaratna, M. R., Onasch, T. B., Alfarra, M. R., Prevot, A. S. H., Dommen, J., Duplissy, J., Metzger, A., Baltensperger, U., and Jimenez, J. L.: O/C and OM/OC ratios of primary, secondary, and ambient organic aerosols with high-resolution time-of-flight aerosol mass spectrometry, Environ. Sci. Technol., 42, 4478–4485, 2008.

[4] Allan, J. D., Bower, K. N., Coe, H., Boudries, H., Jayne, J. T., Canagaratna, M. R., Millet, D. B., Goldstein, A. H., Quinn, P. K., Weber, R. J., and Worsnop, D. R.: Submicron aerosol composition at trinidad head, california, during itct 2k2: Its relationship with gas phase volatile organic carbon and assessment of instrument performance, J. Geophys. Res.-Atmos., 109, D23S24, doi:10.1029/2003JD004208, 2004.

[5] Cross, E. S., Slowik, J. G., Davidovits, P., Allan, J. D., Worsnop, D. R., Jayne, J. T., Lewis, D. K., Canagaratna, M., and Onasch, T. B.: Laboratory and ambient particle density determinations using light scattering in conjunction with aerosol mass spectrometry, Aerosol Sci. Tech., 41, 343–359, 2007.

[6] Cross, E. S., Onasch, T. B., Canagaratna, M., Jayne, J. T., Kimmel, J., Yu, X.-Y., Alexander, M. L., Worsnop, D. R., and Davidovits, P.: Single particle characterization using a light scattering module coupled to a time-of-flight aerosol mass spectrometer, Atmos. Chem. Phys., 9, 7769–7793, doi:10.5194/acp-9-7769-2009, 2009.

[7] DeCarlo, P. F., Slowik, J. G., Worsnop, D. R., Davidovits, P., and Jimenez, J. L.: Particle morphology and density characterization by combined mobility and aerodynamic diameter measurements, Part 1: Theory, Aerosol Sci. Tech., 38, 1185–1205, 2004.

[8] DeCarlo, P. F., Kimmel, J. R., Trimborn, A., Northway, M. J., Jayne, J. T., Aiken, A. C., Gonin, M., Fuhrer, K., Horvath, T., Docherty, K. S., Worsnop, D. R., and Jimenez, J. L.: Field-deployable, high-resolution, time-of-flight aerosol mass spectrometer, Anal. Chem., 78, 8281–8289, 2006.

[9] Drewnick, F., Hings, S. S., DeCarlo, P., Jayne, J. T., Gonin, M., Fuhrer, K., Weimer, S., Jimenez, J. L., Demerjian, K. L., Borrmann, S., and Worsnop, D. R.: A new Time-of-Flight Aerosol Mass Spectrometer (ToF-AMS) – instrument description and first field deployment, Aerosol Sci. Tech., 39, 637–658, 2005.

[10] Gard, E., Mayer, J. E., Morrical, B. D., Dienes, T., Fergenson, D. P., and Prather, K. A.: Real-time analysis of individual atmospheric aerosol particles: design and performance of a portable atofms, Anal. Chem., 69, 4083–4091, 1997.

[11] Hartigan, J. A. and Wong, M. A.: A K-means clustering algorithm, Appl. Stat., 28, 100–108, doi:10.2307/2346830, 1979.

[12] He, L.-Y., Lin, Y., Huang, X.-F., Guo, S., Xue, L., Su, Q., Hu, M., Luan, S.-J., and Zhang, Y.-H.: Characterization of high-resolution aerosol mass spectra of primary organic aerosol emissions from Chinese cooking and biomass burning, Atmos. Chem. Phys., 10, 11535–11543, doi:10.5194/acp-10-11535-2010, 2010.

[13] Huang, X.-F., He, L.-Y., Hu, M., Canagaratna, M. R., Kroll, J. H., Ng, N. L., Zhang, Y.-H., Lin, Y., Xue, L., Sun, T.-L., Liu, X.-G., Shao, M., Jayne, J. T., and Worsnop, D. R.: Characterization of submicron aerosols at a rural site in Pearl River Delta of China using an Aerodyne High-Resolution Aerosol Mass Spectrometer, Atmos. Chem. Phys., 11, 1865–1877, doi:10.5194/acp-11-1865-2011, 2011.

[14] Jayne, J. T., Leard, D. C., Zhang, X. F., Davidovits, P., Smith, K. A., Kolb, C. E., and Worsnop, D. R.: Development of an aerosol mass spectrometer for size and composition analysis of submicron particles, Aerosol Sci. Tech., 33, 49–70, 2000.

[15] Johnston, M. V. and Wexler, A. S.: Ms of individual aerosol particles, Anal. Chem., 67, A721–A726, doi:10.1021/ac00119a002, 1995.

[16] Kimmel, J. R., Farmer, D. K., Cubison, M. J., Sueper, D., Tanner, C., Nemitz, E., Worsnop, D. R., Gonin, M., and Jimenez, J. L.: Real-time aerosol mass spectrometry with millisecond resolution, Int. J. Mass Spectrom., 303, 15–26, 2011.

[17] Lake, D. A., Tolocka, M. P., Johnston, M. V., and Wexler, A. S.: Mass spectrometry of individual particles between 50 and 750 nm in diameter at the baltimore supersite, Environ. Sci. Technol., 37, 3268–3274, 2003.

[18] Lanz, V. A., Alfarra, M. R., Baltensperger, U., Buchmann, B., Hueglin, C., and Prévôt, A. S. H.: Source apportionment of submicron organic aerosols at an urban site by factor analytical modelling of aerosol mass spectra, Atmos. Chem. Phys., 7, 1503–1522, 2007.

[19] Laskin, A. and Cowin, J. P.: Automated single particle sem/edx analysis of submicrometer particles down to 0.1 μm, Anal. Chem., 73, 1023–1029, 2001.

[20] Li, W. J., Zhou, S. Z., Wang, X. F., Xu, Z., Yuan, C., Yu, Y. C., Zhang, Q. Z., and Wang, W. X.: Integrated evaluation of aerosols from regional brown hazes over Northern China in winter: concentrations, sources, transformation, and mixing states, J. Geophys. Res.-Atmos., 116, D09301, doi:10.1029/2010JD015099, 2011.

[21] Liu, P. S. K., Deng, R., Smith, K. A., Williams, L. R., Jayne, J. T., Canagaratna, M. R., Moore, K., Onasch, T. B., Worsnop, D. R., and Deshler, T.: Transmission efficiency of an aerodynamic focusing lens system: Comparison of model calculations and laboratory measurements for the aerodyne aerosol mass spectrometer, Aerosol Sci. Tech., 41, 721–733, 2007.

[22] Liu, S., Ahlm, L., Day, D. A., Russell, L. M., Zhao, Y., Gentner, D. R., Weber, R. J., Goldstein, A. H., Jaoui, M., Offenberg, J. H., Kleindienst, T. E., Rubitschun, C., Surratt, J. D, Sheesley, R. J., and Scheller, S.: Secondary organic aerosol formation from fossil fuel sources contribute majority of summertime organic mass at Bakersfield, submitted, posted at `http://aerosol.ucsd.edu/publications.html`.

[23] Lohmann, U. and Feichter, J.: Global indirect aerosol effects: a review, Atmos. Chem. Phys., 5, 715–737, 2005.

[24] Matthew, B. M., Middlebrook, A. M., and Onasch, T. B.: Collection efficiencies in an aerodyne aerosol mass spectrometer as a function of particle phase for laboratory generated aerosols, Aerosol Sci. Tech., 42, 884–898, 2008.

[25] Middlebrook, A. M., Bahreini, R., Jimenez, J. L., and Canagaratna, M. R.: Evaluation of composition-dependent collection efficiencies for the aerodyne aerosol mass spectrometer using field data, Aerosol Sci. Tech., 46, 258–271, 2012.

[26] Mohr, C., P. F. DeCarlo, Heringa, M. F., Chirico, R., Slowik,J. G., Richter, R., Reche, C., Alastuey, A., Querol, X., Seco,R., Penuelas, J., Jimenez, J. L.,

Crippa, M., Zimmermann, R., Baltensperger, U., and Prevot, A. S. H.: Identification and quantification of organic aerosol from cooking and other sources in Barcelona using aerosol mass spectrometer data." Atmospheric Chemistry and Physics 12(4): 1649-1665, 2012.

[27] Mohr, C., Huffman, J. A., Cubison, M. J., Aiken, A. C., Docherty, K. S., Kimel, J. R., Ulbrich, I. M., Hannigan, M., and Jimenez, J. L.: Characterization of Primary Organic Aerosol Emissions from Meat Cooking, Trash Burning, and Motor Vehicles with High-Resolution Aerosol Mass Spectrometry and Comparison with Ambient and Chamber Observations." Environmental Science & Technology 43(7): 2443-2449, 2009.

[28] Murphy, D. M. and Thomson, D. S.: Laser ionization mass-spectroscopy of single aerosol-particles, Aerosol Sci. Tech., 22, 237–249, 1995.

[29] Ng, N. L., Canagaratna, M. R., Zhang, Q., Jimenez, J. L., Tian, J., Ulbrich, I. M., Kroll, J. H., Docherty, K. S., Chhabra, P. S., Bahreini, R., Murphy, S. M., Seinfeld, J. H., Hildebrandt, L., Donahue, N. M., DeCarlo, P. F., Lanz, V. A., Prévôt, A. S. H., Dinar, E., Rudich, Y., and Worsnop, D. R.: Organic aerosol components observed in Northern Hemispheric datasets from Aerosol Mass Spectrometry, Atmos. Chem. Phys., 10, 4625–4641, 2010.

[30] Noble, C. A. and Prather, K. A.: Real-time measurement of correlated size and composition profiles of individual atmospheric aerosol particles, Environ. Sci. Technol., 30, 2667–2680, 1996.

[31] Phares, D. J., Rhoads, K. P., and Wexler, A. S.: Performance of a single ultrafine particle mass spectrometer, Aerosol Sci. Tech., 36, 583–592, 2002.

[32] Pope, C. A., Burnett, R. T., Thurston, G. D., Thun, M. J., Calle, E. E., Krewski, D., and Godleski, J. J.: Cardiovascular mortality and long-term exposure to particulate air pollution – epidemiological evidence of general pathophysiological pathways of disease, Circulation, 109, 71–77, 2004.

[33] Quinn, P. K., Bates, T. S., Coffman, D., Onasch, T. B., Worsnop, D., Baynard, T., de Gouw, J. A., Goldan, P. D., Kuster, W. C., Williams, E., Roberts, J. M., Lerner, B., Stohl, A., Pettersson, A., and Lovejoy, E. R.: Impacts of sources and aging on submicrometer aerosol properties in the marine boundary layer across the gulf of maine, J. Geophys. Res.-Atmos., 111, D23S36, doi:10.1029/2006JD007582, 2006.

[34] Ramanathan, V., Crutzen, P. J., Lelieveld, J., Mitra, A. P., Althausen, D., Anderson, J., Andreae, M. O., Cantrell, W., Cass, G. R., Chung, C. E., Clarke, A. D., Coakley, J. A., Collins, W. D., Conant, W. C., Dulac, F., Heintzenberg, J., Heymsfield, A. J., Holben, B., Howell, S., Hudson, J., Jayaraman, A., Kiehl, J. T., Krishnamurti, T. N., Lubin, D., McFarquhar, G.,

Novakov, T., Ogren, J. A., Podgorny, I. A., Prather, K., Priestley, K., Prospero, J. M., Quinn, P. K., Rajeev, K., Rasch, P., Rupert, S., Sadourny, R., Satheesh, S. K., Shaw, G. E., Sheridan, P., and Valero, F. P. J.: Indian ocean experiment: An integrated analysis of the climate forcing and effects of the great indo-asian haze, J. Geophys. Res.-Atmos., 106, 28371–28398, 2001.

[35] Stein, S. E. and Scott, D. R.: Optimization and testing of mass-spectral library search algorithms for compound identification, J. Am. Soc. Mass Spectrom., 5, 859–866, 1994.

[36] Su, Y. X., Sipin, M. F., Furutani, H., and Prather, K. A.: Development and characterization of an aerosol time-of-flight mass spectrometer with increased detection efficiency, Anal. Chem., 76, 712–719, 2004.

[37] Sullivan, R. C., Guazzotti, S. A., Sodeman, D. A., and Prather, K. A.: Direct observations of the atmospheric processing of Asian mineral dust, Atmos. Chem. Phys., 7, 1213–1236, 2007.

[38] Takahama, S., Gilardoni, S., Russell, L. M., and Kilcoyne, A. L. D.: Classification of multiple types of organic carbon composition in atmospheric particles by scanning transmission X-ray microscopy analysis, Atmos. Environ., 41, 9435–9451, 2007.

[39] Thomson, D. S., Schein, M. E., and Murphy, D. M.: Particle analysis by laser mass spectrometry wb-57f instrument overview, Aerosol Sci. Tech., 33, 153–169, 2000.

[40] Ulbrich, I. M., Canagaratna, M. R., Zhang, Q., Worsnop, D. R., and Jimenez, J. L.: Interpretation of organic components from Positive Matrix Factorization of aerosol mass spectrometric data, Atmos. Chem. Phys., 9, 2891–2918, 2009.

[41] Wieser, P., Wurster, R., and Seiler, H.: Identification of airborne particles by laser-induced mass-spectroscopy, Atmos. Environ., 14, 485–494, 1980.

[42] Zelenyuk, A., Yang, J., Choi, E., and Imre, D.: Splat II: An aircraft compatible, ultra-sensitive, high precision instrument for in-situ characterization of the size and composition of fine and ultrafine particles, Aerosol Sci. Tech., 43, 411–424, 2009.

[43] Zhang, Q., Alfarra, M. R., Worsnop, D. R., Allan, J. D., Coe, H., Canagaratna, M. R., and Jimenez, J. L.: Deconvolution and quantification of hydrocarbon-like and oxygenated organic aerosols based on aerosol mass spectrometry, Environ. Sci. Technol., 39, 4938–4952, 2005.

Chapter 5

Hydrolysis of organonitrate functional groups in aerosol particles

Abstract. Organonitrate (ON) groups are thought to be important substituents in secondary organic aerosols. Model simulations and laboratory studies indicate a large fraction of ON groups in aerosol particles, but much lower quantities are observed in the atmosphere. Hydrolysis of ON groups in aerosol particles has been proposed recently to account for this discrepancy. To test this hypothesis, we simulated formation of ON molecules in a reaction chamber under a wide range of relative humidity (0% to 90%). The mass fraction of ON groups (5% to 20% for high-NO_x experiments) consistently decreased with increasing relative humidity, which was best explained by hydrolysis of ON groups at a rate of 4 day^{-1} (lifetime of 6 hours) for reactions under relative humidity greater than 20%. In addition, we found that secondary nitrogen-containing molecules absorb light, with greater absorption under dry and high-NO_x conditions. This work provides the first evidence for particle-phase hydrolysis of ON groups, a process that could substantially

reduce ON group concentration in atmospheric secondary organic aerosols.

5.1 Introduction

Atmospheric organonitrate (ON) molecules are produced by oxidation of volatile organic compounds (VOCs) in the presence of NO_x. Major oxidants in the atmosphere are OH radicals, ozone (O_3), and NO_3 radicals, and the VOCs responsible for secondary organic aerosol (SOA) formation are largely composed of aromatics, alkanes, and alkenes. The most important step during photochemical oxidation in which ON groups (ONO_2) form is the reaction of peroxy radicals (RO_2) with NO (Roberts 1990):

$$RO_2 + NO + M \rightarrow RONO_2 + M \tag{5.1}$$
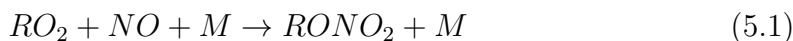
Laboratory studies suggest that reaction (1) is an important sink for peroxy radicals (Barket et al. 2004; Hallquist et al. 1999; Lockwood et al. 2010; Paulot et al. 2009), one of the most common intermediate products of VOC oxidation, indicating that ON groups are important products in SOA components. ON groups could also be produced in reactions of alkene molecules with NO_3 radicals at night (Roberts 1990; Wangberg et al. 1997). Yield of gas-phase ON molecules typically ranges from 5% to 20% in OH radical oxidation reactions (Atkinson and Arey 2003). Particle-phase ON molecule production has been observed in reaction chamber studies (Fry et al. 2009; Matsunaga and Ziemann 2009), with high molecular weight VOCs having higher ON molecular yields. A model study (Camredon et al. 2007) predicts that 18% of secondarily formed molecules in particle phase contain ON groups, suggesting that ON groups should account for a large fraction of organic mass (OM).

Despite these model predictions, direct measurements of particle-phase ON concentrations in both laboratory and ambient studies are scarce due to limitations of measuring techniques and ON concentrations often must be inferred. For example, Zaveri et al. (2010) inferred up to ~ 0.4 μg m^{-3} of particulate organonitrates (corresponding to$< 5\%$ of total particulate mass) in a nocturnal power plant plume based on particle acidity and gas-particle equilibrium analysis of Aerodyne quadrupole aerosol mass spectrometer (Q-AMS) measurements. While aerosol

mass spectroscopy is the most commonly employed technique for measuring the chemical composition of OM, it is not ideal for directly measuring ON concentrations (Farmer et al. 2010). Bruns et al. (2010) suggest that ON molecules can only be unambiguously identified by high-resolution time-offlight aerosol mass spectrometer (HR-ToF-AMS) when the ratio of ON groups to inorganic nitrate is larger than 3:20 to 3:5, which is 2 to 7 times higher than reported ratio of organic-to-inorganic nitrate measured in the atmosphere (Day et al. 2010). An alternative method of measuring the OM chemical composition is Fourier transform infrared (FTIR) spectroscopy (Maria et al. 2002). Measuring particle-phase ON groups using FTIR can be traced back to the 1990s (Allen et al. 1994), but quantification of ON group mass was not possible until recently (Day et al. 2010). Using the FTIR technique, ON groups were quantified as 3% of OM in fine particles in coastal Southern California (Day et al. 2010; Liu et al. 2011) and below detection limit in most other regions. The difference between observations and model predictions suggests a significant sink of ON exists that operates on timescales of several hours. One possibility proposed by Day et al. (2010) and Russell et al. (2011) is that ON groups hydrolyze under ambient conditions to give alcohols and nitric acid:

$$RONO_2 + H_2O \rightarrow ROH + HNO_3 \tag{5.2}$$
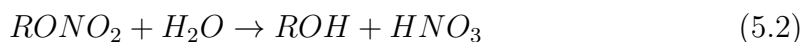
Hydrolysis of ON molecules has been studied in bulk solutions since the 1950s (Baker and Easty 1950). Nucleophilic substitution reactions of water and ON molecules to give alcohols and nitric acid (reaction (2)) has been suggested as the major reaction pathway (Boschan et al. 1955). Baker and Easty (1952) studied kinetics of neutral hydrolysis in bulk solution using methyl, ethyl, isopropyl, and tert-butyl nitrates at 60°C to 100°C. Their results suggest that hydrolysis rate of tert-butyl nitrate is 10^4 to 10^5 times faster than those of primary and secondary nitrates. Darer et al. (2011) and Hu et al. (2011) extended their work by conducting neutral hydrolysis experiments under atmospheric-relevant temperature ($\sim$25°C), confirming that tertiary ON molecules hydrolyze in minutes, while hydrolysis of primary and secondary ON molecules takes weeks. Despite the consistency of these

studies, all of which were conducted in bulk solutions, the conditions under which ON molecules hydrolyze in aerosol particles is still an open question and needs to be addressed to explain the gap between modeled and measured ON group concentrations.

In this study, we simulated formation of SOA that contains ON groups in a reaction chamber under controlled conditions. We used aromatic hydrocarbons, an important compound class that typically accounts for 20-30% of VOCs in urban areas (Lim and Ziemann 2005), as SOA precursors. 1,2,4-trimethylbennzene (TMB) was selected as the model precursor because of its abundance in aromatic hydrocarbons, e.g., 1,2,4-TMB accounted for 13% of measured aromatic hydrocarbons in Los Angeles in 1995 (Seinfeld and Pandis 2006). We focused on effects of RH and VOC-to-NO_x ratio, the two environmentally relevant variables, on formation and loss of ON groups. In order to put the results into a broader context, we investigate optical properties of nitrogen-containing SOA components. These measurements are built on complementary particle- and gas-phase measurements described below.

5.2   Experimental

5.2.1   Experimental procedures

Secondary organic aerosols were produced in a temperature-controlled (25°C), 10.6 m^3 Teflon reaction chamber at Pacific Northwest National Laboratory (Richland, WA). The chamber is surrounded by 104 UV blacklights (Q-labs, UV-340) with their output centered at 340 nm. A custom Teflon-coated stainless steel manifold is used to inject reactants and pure air into the chamber and to sample aerosol and gas-phase species. Teflon lines were used for the sampling of ozone and NO_x, stainless steel lines were used to sample aerosol particles, and a PEEK line was used to sample VOCs with the Proton Transfer Reaction Mass Spectrometer (PTR-MS). HONO was used as the NO_x and OH radical initiator and was generated by reaction of $NaNO_2$ (Sigma-Aldrich, $\geq$ 97%) with excess H_2SO_4 (Sigma-Aldrich, 99.999%) in a glass bulb at room temperature, and flushing the

bulb with 1.0 lpm of pure air. For low NO_x experiments, H_2O_2 was added to keep the OH radical concentrations generated in each experiment approximately equal. 1,2,4-Trimethylbezene (TMB) (Sigma-Aldrich, 98%), the VOC precursor, was introduced into the chamber by injecting the desired volume into a gently warmed glass bulb and flushing 1.0 lpm of pure air through the bulb for 20 minutes. After the injection, we allow 60 to 90 minutes for the HONO and TMB to become homogenously mixed in the chamber, as observed by the NO_x analyzer and PTR-MS. The reaction was initiated by turning on all 104 lights, which photolyzed the HONO and/or H_2O_2 to generate OH radicals that reacted with TMB. The pure air was generated with an AADCO pure air generator. For experiments with relative humidity (RH) greater than 0%, the chamber was conditioned with humid air, which was produced by mixing pure air (RH = 0%) with water vapor-saturated air (RH = 100%) generated from a heated water bubbler (18 $M\Omega$ cm). By adjusting flow rates of the dry and saturated air, desired chamber RH can be achieved. A HEPA filter was placed downstream of the water bubbler to eliminate particles. No seed aerosol was used in this study. The chamber was continuously flushed with pure air between all experiments.

Experimental conditions are summarized in Table 5.1. Two sets of experiments were conducted to study the effects of 1) RH and 2) NO_x on formation and loss of ON groups. The first set of experiments (March 12-28) were conducted under high-NO_x conditions (TMB:NO_x ~0.2) with RH being the only changing variable (varied from 0% to 90%). In the second set of experiments (April 2-7), SOA was produced with intermediate-NO_x (TMB:NO_x ~2) and low-NO_x (TMB:NO_x ~10) levels under dry (~0%) and intermediate RH (~50%).

5.2.2   Particle- and gas-phase measurements

A suite of particle- and gas-phase instruments was deployed around the chamber to measure chemical composition of SOA components. One filter (Teflo, Pall Inc., Ann Arbor, MI) sample was collected for each experiment to quantify organic functional group mass using a Brucker Tensor 37 FTIR (Brucker, Waltham, MA). The filter sample collection began ~1 hour after the lights were turned on,

Table 5.1: Experimental conditions including initial mixing ratios of TMB and NO_x, RH, mass fraction of organonitrate groups (F_{ON}), yield of OM (Y_{OM}), molar ratio of alkane and ON groups (R_{mole}) in SOA, and availability of PSAP measurements.

	Date	TMB_0 (ppb)	NO_{x0} (ppb)	$TMB:NO_x$	RH (%)	F_{ON} (%)	Y_{OM} (%)	R_{mole}	PSAP
	3/12/2011	454.8	1483.7	0.31	< 1.5	19.9	1.7	8.7	
Experiments	3/23/2011	291.8	1799.9	0.17	< 0.3	19.0	3.3	9.2	Yes
addressing RH	3/15/2011	370.1	1639.8	0.24	15.0-20.0	19.0	3.6	8.5	
effects	3/17/2011	366.8	2264.7	0.17	37.8-49.0	11.9	3.9	21.2	
	3/21/2011	380.6	1610.0	0.24	53.7-66.8	7.9	3.9	37.5	Yes
	3/28/2011	276.8	1854.8	0.17	85.2-86.5	4.8	4.5	73.1	
Experiments	4/2/2011	337.9	215.1	1.99	< 0.4	10.5	5.9	16.1	Yes
addressing NO_x	4/5/2011	310.2	250.0	1.42	37.3-51.0	8.2	5.3	29.9	Yes
effects	4/7/2011	206.2	30.2	10.78	0	5.3	3.5	41.7	Yes
	4/4/2011	237.6	30.3	12.45	46.1-60.0	2.2	2.8	139.7	

when SOA concentration reached its maximum and typically lasted 3 to 4 hours. The filter samples were measured immediately after sample collection with FTIR. Before each IR scan, the FTIR sample chamber (with sample in it) was purged with pure N_2 for 3 min to eliminate interference of CO_2 and (gas-phase and liquid) water. Organic functional groups, including alkane, hydroxyl, carboxylic acid, nonacid carbonyl, and ON groups, were quantified using algorithms described previously (Day et al. 2010; Gilardoni et al. 2009; Liu et al. 2011; Liu et al. 2009; Russell et al. 2009). The total FTIR-measured OM mass correlated well to the mass quantified by a scanning mobility particle sizer (SMPS, TSI 3080) (assuming a density of 1.4 g cm^{-3} for SOA particles) with an R of 0.90 and a slope of 1.05, well within the uncertainties of FTIR and SMPS.

In addition to the sample collected for FTIR analysis, one separate sample from each experiment was collected for X-ray analysis. This sample collection started ∼1 hour after the lights were on and lasted ∼30 min. Single-particle X-ray absorption spectra were acquired using scanning transmission X-ray microscopy (STXM) and near-edge X-ray absorption fine structure (NEXAFS) at the Advanced Light Source (Lawrence Berkeley National Laboratory, CA). Single-particle functional groups, including alkane, carboxylic acid, hydroxyl, ketone, and alkene groups were measured. Detailed analysis procedures are described in Takahama et al. (2010).

An Aerodyne HR-ToF-AMS (Billerica, MA) was used to measure SOA mass loadings with ∼10 minute time resolution. In this instrument, particles focused by a set of aerodynamic lenses impact on a heated surface (600°C). Nonrefractory components flash vaporize and are ionized and fragmented by electron impaction. The fragments are analyzed by a time-of-flight mass spectrometer (Tofwerk AG, Thun, Switzerland). In addition, particle size is measured by particle time-of-flight between a rotating chopper, which modulates the particle beam, and the vaporizer (Jayne et al. 2000), providing time-resolved size distribution measurements of particle fragments. A detailed description of HR-ToF-AMS is provided in DeCarlo et al. (2006).

Light absorption of SOA particles was continuously measured using a particle/soot absorption photometer (PSAP, Radiance Research, Seattle, WA). The absorption coefficient was quantified by measuring the change in transmittance across a filter on which SOA particles impacted. In this instrument, absorptions at three wavelengths were monitored, representing blue (467 nm), green (530 nm), and red (660 nm) light, respectively. The absorption coefficient retrieved from the PSAP measurements was corrected for flowrate, spot size, and light scattering interferences following the procedures described by Ogren (2010) and Bond et al. (1999). The light scattering coefficient was calculated from the SMPS-derived particle size distribution and an assumed refractive index of $1.45 + 0i$ (Kim et al. 2010) for the 30 min average around the peak absorption. The scattering calculations were performed using conventional Mie theory, which assumes the particles to be spherical. Note that the corrected absorption coefficient appeared slightly negative for experiments conducted on April 5 and April 7 when the raw (uncorrected) absorption coefficient of SOA was low, indicating that the light scattering coefficient might be slightly overestimated. However, we focus on the relative change in absorption coefficient to study the link of SOAs chemical composition and their light absorbing properties.

Additional measurements include 1) O_3 measured by an ultraviolet photometric O_3 analyzer (Thermo Electron Instruments, Model 49C), 2) NO and NO_x monitored by a NO-NO_2-NO_x Analyzer (Thermo Environmental Instruments,

42C), 3) 1,2,4-TMB mixing ratio recorded by a PTR-MS (Ionicon; Lindinger et al. 1998), and 4) RH and temperature were monitored by a Rotronic hygroclip (SC05) sensor.
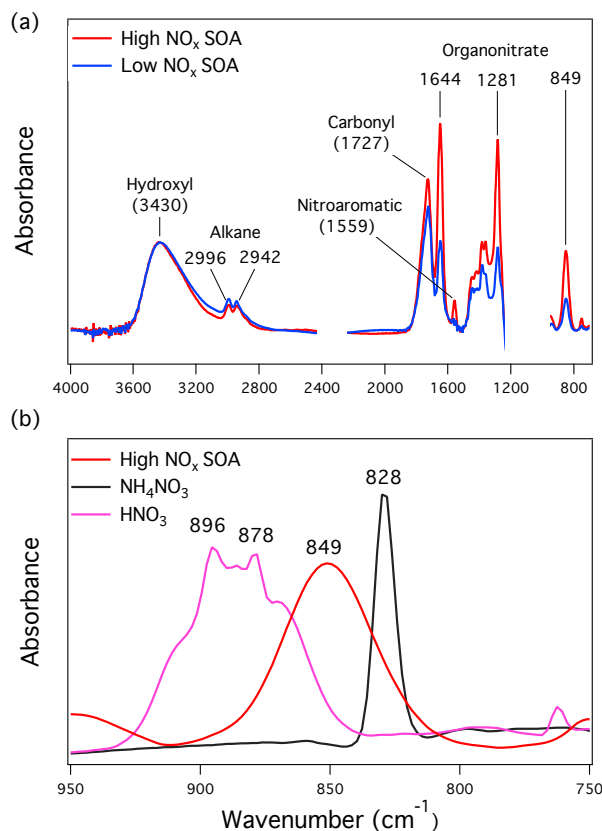
Figure 5.1: (a) Representative FTIR spectra for SOA produced under high-NO_x (March 23) and low-NO_x conditions (April 2). Absorptions near 1100 cm^{-1} and 2360 cm^{-1} are not shown due to interferences by Teflon substrates and CO_2, respectively. (b) Comparison of IR spectra in the 750 to 950 cm^{-1} region for high-NO_x SOA, ammonium nitrate, and condensed-phase nitric acid. Spectra are normalized in order to show differences.

5.2.3 Identification and quantification of organonitrate groups

ON groups were observed in all SOA samples, as indicated by peaks at 1644, 1281, and 849 cm^{-1} in the IR spectra (Fig. 5.1a) (Roberts 1990). To confirm that

there were no interferences from inorganic nitrates, most likely ammonium nitrate, an IR spectrum of ammonium nitrate was compared to the spectra of SOA samples (Fig. 5.1b). The ammonium nitrate sample was acquired by atomizing ammonium nitrate solution followed by particle collection on Teflon filter at sampling rate of $\sim$4 L min^{-1}, the same rate used for SOA sample collection. A sharp peak at 828 cm^{-1} was observed, consistent with documented peak locations for inorganic nitrate ions (Miller and Wilkins 1952). The distinct IR spectra of ON groups and inorganic nitrate exclude the existence of inorganic nitrate salts, which is expected since ammonia was not present in the reaction system. A sample of condensed-phase nitric acid was prepared by applying a droplet of nitric acid on Teflon filter. Vibration peaks between 860 and 900 cm^{-1} of nitric acid (Fig. 5.1b) were consistent with reported peak assignments (Maki and Wells 1992; McGraw et al. 1965; Sporleder and Ewing 2001). These peaks differ significantly from the 849 cm^{-1} peak of ON groups and were not observed in SOA samples, suggesting that nitric acid, a terminal sink of NO_x, was not in the particle phase or below detection limit of the FTIR analysis. Assuming all the NO_x in the chamber is converted to nitric acid, the maximum possible concentration of nitric acid in the chamber is 0.2 Pa (for 2000 ppb NO_x), which is well below its vapor pressure of 8000 Pa (Duisman and Stern, 1969), suggesting that nitric acid was too volatile to partition into the dry particle phase. Although Handley et al. (2007) observed that gas-phase nitric acid adsorbs and dissociates into proton and nitrate anion on dry, hydrophobic organic films at partial pressures below saturation pressure of nitric acid, which suggests uptake of nitric acid on dry organic particles, Handley et al. (2007) and Zhou et al. (2003) demonstrated effective photolysis loss of proton and nitrate anion (to the gas phase) under actinic radiation. Therefore, the adsorbed nitric acid on dry particles is unlikely to be significant in the photooxidation experiments. Assuming hygroscopic growth factors of 1.01, 1.02, 1.04, and 1.08, respectively, for reactions under 20%, 40%, 60%, and 85% RH (Baltensperger et al. 2005) and that all NO_x was converted to nitric acid, we find that a maximum of 0.4 μg m^{-3} (0.6% OM) of nitric acid (at 80% RH) could partition into the aqueous aerosol using Henrys law coefficient of 2.1x105 M atm^{-1} (Seinfeld and Pandis 2006). Finally,

the nitrate temporal profiles discussed below suggest that nitrates were formed on the same timescales as the TMB oxidation, while generation of nitric acid is delayed in time. By excluding interferences of inorganic nitrates (ammonium nitrate and nitric acid), the IR peak at 849 cm^{-1} was unambiguously assigned to ON group absorption. This peak was used to quantify ON group mass, using an absorptivity of 9.3 cm^{-1} μmol^{-1} derived by Day et al. (2010).
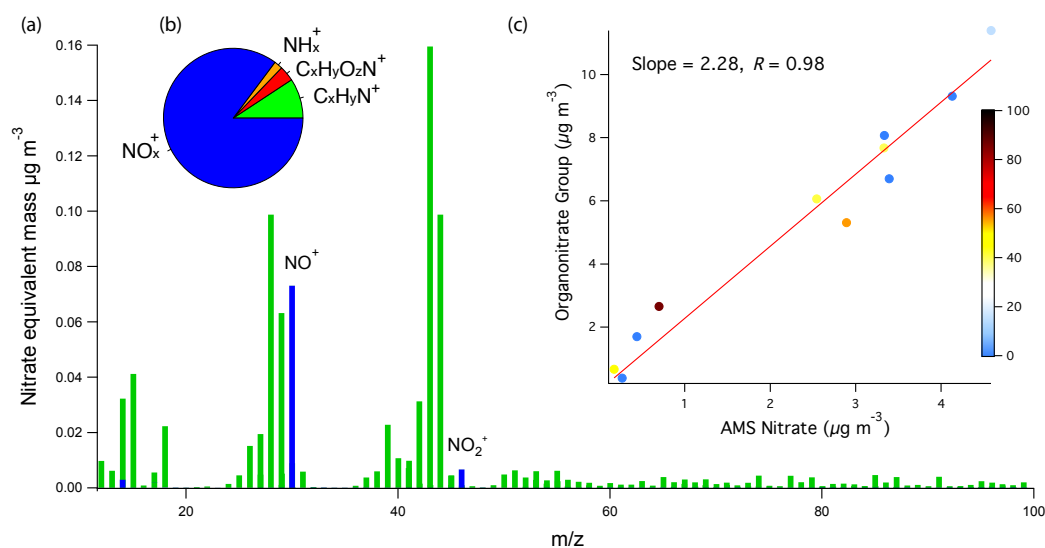
Figure 5.2: (a) Typical mass spectrum for SOA generated under high-NO$_x$ conditions (March 23). (b) Mass fraction of nitrogen-containing fragments (on March 23). (c) Comparison of FTIR-measured ON groups (ONO$_2$) and AMS-measured nitrate for all experiments. Colors indicate RH (%) as shown by the color bar.

In addition to FTIR, ON groups were measured by the HR-ToF-AMS. Since ammonium was not observed from the AMS measurements and nitric acid was excluded in the particle phase by the FTIR measurements, NO$^+$ and NO^{2+}, which typically accounted for more than 75% of nitrogen-containing fragments (Fig. 5.2b), most likely originated from ON group parents. The ratio of NO$^+$ to NO$_2^+$, 8.8$\pm$1.9 (Fig. 5.2a), was dramatically different from the ratio for NH$_4$NO$_3$ (2.4) and NaNO$_3$ (80) but consistent with the ratio for ON molecules (5-11) reported previously (Fry et al. 2009; Bruns et al. 2010). The FTIR-measured ON groups (with the formula of ONO$_2$) and AMS-measured nitrate (derived from NO$^+$
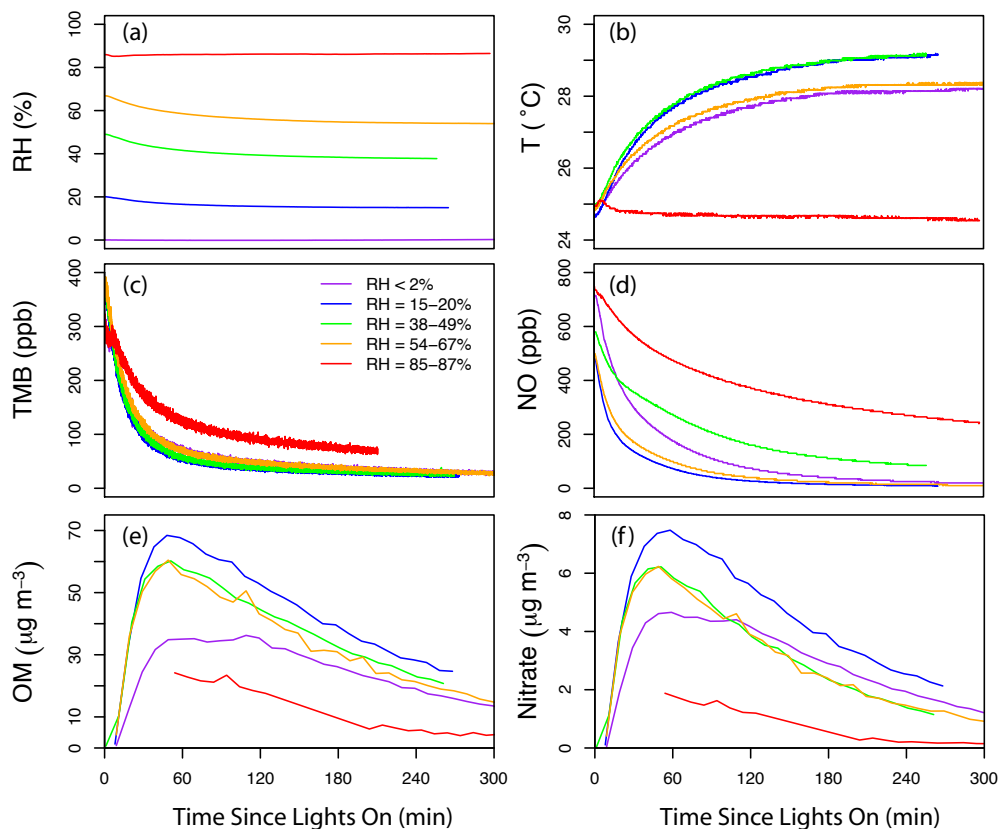
Figure 5.3: (a) Time-dependence of (a) RH, (b) temperature, (c) TMB, (d) NO, (e) AMS-measured OM, and (f) AMS-measured nitrate. The AMS measurements on March 28 (RH∼85%) were only available 1 hour after the lights were on due to improper experimental setup during the first hour.

and NO_2^+) correlated well ($R = 0.98$), with the former 2.28 times higher than the latter (Fig. 5.2c). Possible explanation for the large slope include: 1) ON groups are fragmented by electron impact ionization and do not have a uniform probability of carrying the positive charge necessary for detection (Bruns et al. 2010), or the related point 2) the true relative ionization efficiency of ON molecules is lower than the value of 1.1 used to calculate nitrate mass, or 3) ON groups dissociated (during ionization processes) to form other nitrogen-containing fragments (e.g., $C_xH_yO_zN^+$ in Fig. 5.2b) that were small (compared to NO^+ and NO_2^+) and caused the scatter in Fig. 5.2c.

5.3   Results and discussion

The time-dependence of AMS-measured OM and nitrate is shown in Fig. 5.3e and 5.3f, respectively. Concentrations of OM and nitrate are highly correlated ($R = 0.99$), suggesting that both participated in particle growth. Size distributions of OM and nitrate showed the same peak locations (Fig. 5.4), and their ratios were independent of particle size, suggesting that ON molecules were internally mixed with other SOA components, and processing of ON molecules (if any) occurred within the particles rather than on their surface. The concentration of nitrate increased rapidly at the beginning of the reaction and reached a maximum after ~1 hour. During the first 2 hours of reaction, TMB and NO decayed exponentially (Fig. 5.3c and 5.3d), suggesting that the majority of ON molecules were formed within 2 hours of the start of the reaction. Decay rates of TMB and NO for dry and humid experiments were similar (except for the lower decay rates observed on March 28 with RH of ~85%, for which the reason is not clear), which is consistent with the fact that water vapor has no effects on OH radical formation (Atkinson et al. 1992) at the wavelengths (centered at 340 nm) of light employed in this study. In addition, it has been shown that the reaction of RO_2 and NO (reaction (1)) is not affected by RH (Matsunaga and Ziemann, 2009). The evidence suggests that the effects of water vapor on gas-phase reactions, including formation of organonitrate groups, were likely negligible.

5.3.1   Organonitrate group mass fraction

The mass fraction of ON groups in high-NO_x experiments ranged from 4.8% to 19.9% (Table 5.1), with higher mass fraction observed under drier conditions (Fig. 5.5a). The mass fraction (4.8%) of ON groups under high-NO_x and high-RH conditions (March 28) matched the mass fraction (3.2±2.0%) measured at coastal Southern California (Day et al. 2010), a site that was significantly influenced by anthropogenic emissions (from the Los Angeles Basin) and associated with high RH. The yield of OM, quantified by FTIR and defined as the ratio of OM to the mass of reacted TMB (Odum et al. 1996), spanned from 1.7% to 5.9%—well
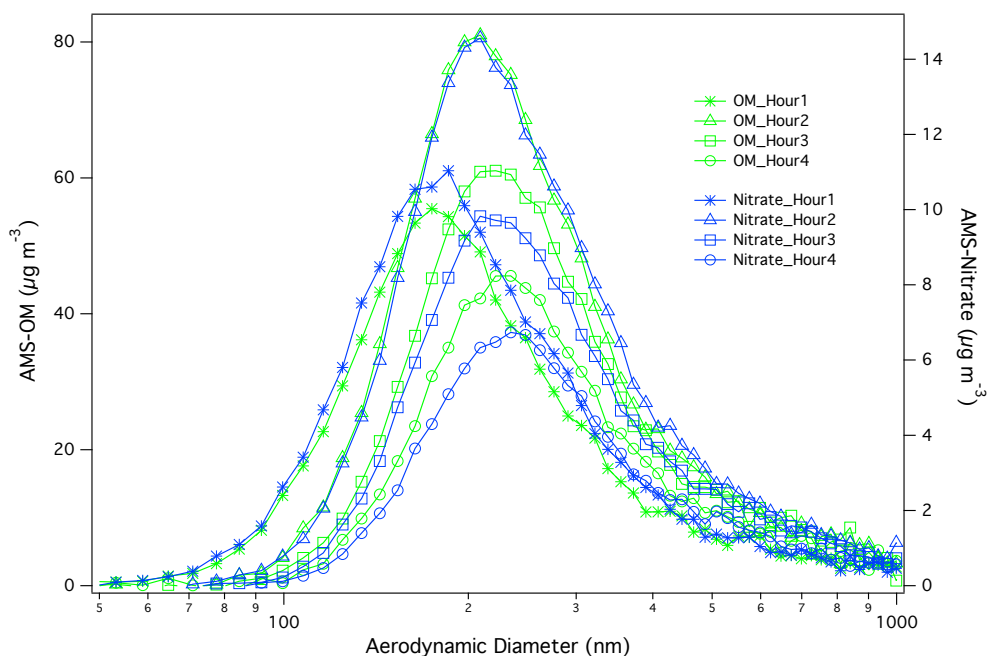
Figure 5.4: Example (March 15) time-dependence of size distributions of AMS-measured OM and nitrate.

agreed with reported SOA yield of TMB oxidation (Odum et al. 1996; Cocker et al. 2001; Wyche et al. 2009).

The mass fraction of ON groups decreased with decreasing logarithmic TMB-to-NO_x ratio. The decrease is likely due to the competitive chemistry of RO_2, which reacts with both HO_2 and NO. Under low NO_x conditions, reaction of RO_2 with HO_2 begins to compete with reaction with NO (Kroll and Seinfeld 2008), yielding smaller amount of ON groups.

5.3.2 Hydrolysis of organonitrate groups

The average ON group mass fraction consistently decreased with increasing RH (Fig. 5.5a), especially when RH was greater than 20%. In addition, the mass fraction of ON groups (represented by the AMS-derived nitrate-to-OM ratio) decreased over time (Fig. 5.6), with the decrease rate (slope) at RH > 20% twice as high as the decrease rate for RH < 20% conditions. Similar reduction of ON groups in humid conditions was reported in three reaction chamber studies. Baltensperger

et al. (2005) and Sax et al. (2005) studied oxidation (by OH radicals) product of 1,3,5-TMB under 50% to 60% RH using FTIR. Both studies showed that the abundance of ON groups decreased with time, but explanations were not given. Zhang et al. (2011) studied isoprene SOA formation under dry (15-40%) and humid (40-90%) conditions in the presence of high NO_x. The ON monomer (similar to 2-methylglyceric acid (2-MG) except one of the OH groups is replaced with a tertiary ON group) and its oligoester (retains the tertiary ON group) identified in the SOA components were significantly suppressed under humid conditions. While the decrease of the oligoester could be explained by constrained particle-phase esterification under humid conditions, the reduction of the ON monomer at high-RH level remains unresolved. Nguyen et al. (2011) explored RH effects on isoprene and OH radical reaction system under dry (RH < 2%) and humid (RH = 90%) conditions. In the humid experiments, relative abundance of nitrogen-containing compounds (measured by mass spectrometry and not assigned to specific compound classes) decreased by 40%. The explanation proposed by Nguyen et al. (2011) was that particle-phase water suppressed condensation-type reactions that generated water. The condensation-type processes may include 1) esterification of hydroxyl groups and nitric acid to form ON groups, and 2) oligomer formation from monomers containing ON groups—oligomers are more ionizable (than monomers) so they are more likely to be detected by the mass spectral technique used in Nguyen et al. (2011). Explanation 1) was excluded in this study, because particle-phase nitric acid—required for establishing equilibrium in esterification—was not observed, as discussed in the experimental section. Explanation 2) was not applicable in this work, since quantification of ON groups by FTIR does not require ionizing organic molecules. Finally, the temporal profiles (Fig. 5.3) show that SOA and ON production occurred simultaneously; if oligomerization reactions were a significant source of ON, we would expect that the nitrate signal would be delayed relative to the production of total OM.

The decrease of ON group mass fraction (as a function of RH), an indication of ON group loss, was supported by the increased decay rate of ON groups under humid conditions (RH > 20%). To quantify the decay rate, particle wall loss and
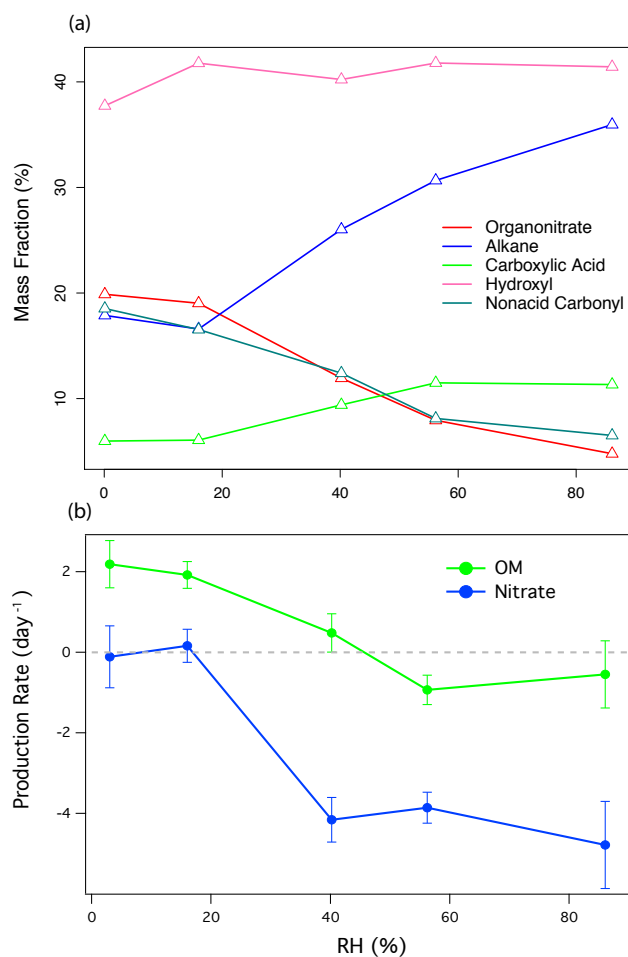
Figure 5.5: (a) RH dependence of organic functional group mass fraction for the high-NO$_x$ experiments (March 12-28). The mass fractions are derived from the FTIR measurements. (b) Production rate of AMS-measured OM and nitrate.

dilution of organonitrate group concentrations by condensation of nonnitrate SOA need to be taken into account. The wall loss rate was determined by fitting the decay curve of integrated particle number concentration (measured by the SMPS) to an exponential decay function (Paulsen et al. 2005):

$$\frac{dN(D_p, t)}{dt} = -kN(D_p, t) \tag{5.3}$$

where k and N represent the wall loss rate and integrated particle number concentration, respectively. The wall loss rates for AMS-measured OM and nitrate

were assumed to be the same because they were internally mixed (Fig. 5.4). The decay rates of OM and nitrate were derived using similar decay functions (by replacing number concentration with mass concentrations) as equation (3). Since the SMPS-derived mass (assuming constant density) and AMS-measured mass correlated with $R = 0.98$ or higher for each experiment, it is reasonable to use the SMPS-derived wall loss rate to account for the wall loss of OM and nitrate measured by the AMS. The difference of wall loss rate and decay rates of OM or nitrate, defined as production rate, represents production (positive values) or loss (negative values) of OM or nitrate. The production rate of OM and nitrate was calculated for each experiment and presented in Fig. 5.5b, showing that nitrate loss (at a rate of 4 day^{-1}) occurred when RH was greater than 20%, while the loss of OM (for RH > 20%) was negligible (near 0). Figure 5.5b and Fig. 5.6 suggest that the greater decrease rate of nitrate mass fraction under RH > 20% conditions resulted from loss of nitrate rather than production of OM. In contrast, the decrease of nitrate mass fraction over time at RH < 20% could be explained by OM production (Fig. 5.5b), which was likely the result of polymer formation, a reaction that is strongly affected by RH and highly unfavorable when RH is high (Jang et al. 2002; Jang et al. 2004).

Based on the following observations: 1) the only changing variable was RH (for the first set of experiments), 2) water vapor did not affect gas-phase chemistry, 3) condensedphase water increased with increasing RH (Seinfeld et al. 2001), and 4) the observed loss of ON group mass under humid conditions, particle-phase hydrolysis of ON groups via reaction (2) provides the most consistent explanation for the observations. According to Wyche et al. (2009), one likely product of 1,2,4-TMB and OH reaction system is molecule A, which contains a tertiary ON group and is sufficiently nonvolatile to partition into particle phase (Wyche et al. 2009; Johnson et al. 2004; Johnson et al. 2005).

Each molecule of A has 10 alkane groups and 1 ON group, consistent with the observed molar ratio of alkane to ON groups in SOA particles (Table 5.1) in dry conditions but much lower than the ratios for high-RH SOA. These observations suggest that product A likely hydrolyzed via reaction (2) under high-RH conditions
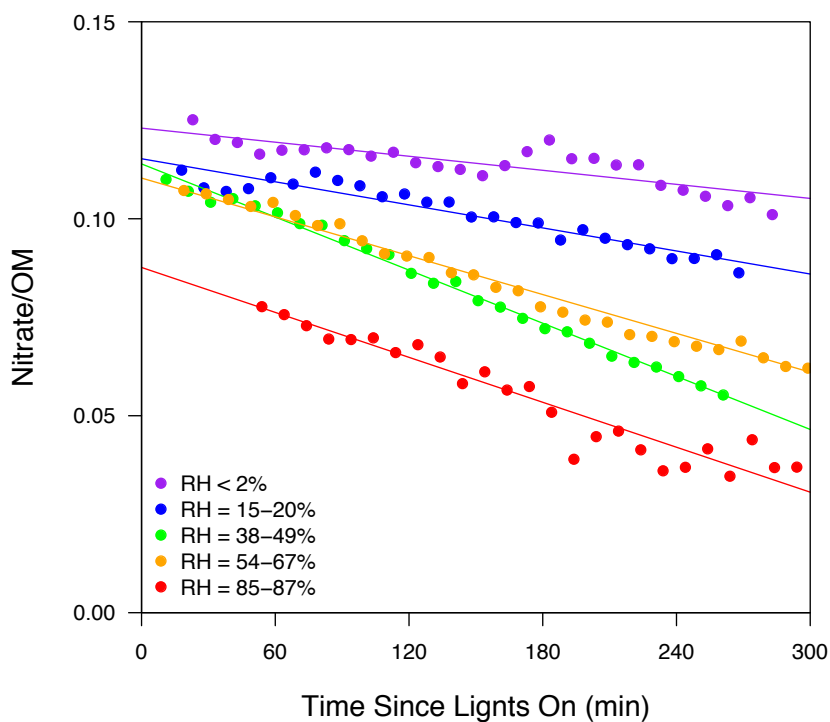
Figure 5.6: Time-dependence of nitrate-to-OM ratio (measured by the AMS). The lines represent linear fits of the measurements, with slopes of 7.1×10^{-5}, 1.0×10^{-4}, 2.2×10^{-4}, 1.7×10^{-4}, and 2.0×10^{-4} for RH < 2%, RH = 15-20%, RH = 38-49%, RH = 54-67%, and RH = 85-87% experiments, respectively.

where the amounts of condensedphase water was greatly enhanced. Assuming only tertiary ON molecules hydrolyze in aerosols based on the kinetic studies in bulk solutions (Hu et al. 2011), our measured particle-phase tertiary ON hydrolysis rate of 4 day^{-1} at RH greater than $\sim$20% is a factor of 200 times slower than the measured hydrolysis rate of tertiary ON molecules in dilute solutions (Hu et al., 2011). While the relative importance of tertiary ON groups versus primary or secondary ON groups in TMB oxidation products has not been reported, it is expected that the tertiary ON groups are produced in the alkyl group-substituted benzene carbons (e.g., product A). Since 1,2,4-TMB has three $–CH_3$ substituted

benzene carbons, we estimate that tertiary ON groups account for approximately 50% of the total ON groups in 1,2,4-TMB SOA, which is quantitatively consistent with the ∼50% decrease of ON group mass fraction after ∼5-hour reaction for the RH > 20% experiments (Figure 5.6). The slower particle-phase hydrolysis rate likely resulted from a combination of interrelated factors: limited availability of condensed-phase water and particle phase.

First, molecular diffusion coefficients for ON and water molecules in particles may be slower than in solutions, potentially reducing the hydrolysis rate. Recent studies suggest that laboratory and ambient SOA (both anthropogenic and biogenic) exist in an amorphous solid (glassy) state when RH < 30% (Saukko et al. 2012; Vaden et al. 2011; Virtanen et al. 2010). One likely consequence of this phase state is that molecular diffusion through the particle would be hindered. A moisture-induced phase transition of pure SOA from a solid state to a semi-solid or liquid state is suggested to occur at RH > 40% (Saukko et al. 2012; Shiraiwa et al. 2011). In the semisolid or liquid state, organic would diffuse to the organic interface much more rapidly (Vaden et al. 2011). The observed particle-phase ON group hydrolysis rate (Fig. 5.5b) is consistent with the phase transition of SOA from solid to semisolid/liquid particles: The hydrolysis rate was ∼ 0 and 4 day^{-1} (corresponding to a lifetime of 6 hours) for RH < 20% and RH > 40% experiments, respectively. The pronounced increase of hydrolysis rate at 40% RH also agrees with the hydrolysis loss rate of N_2O_5 on organic particles, which is dependent on water concentration when RH < 50% and appears to be independent of water when RH is greater than 50% (Thorton et al. 2003).

However, even after the SOA phase transition, two separate phases, an organic-rich phase and an aqueous phase, may form as the particle continues to hydrate. This phase separation has been observed for similar laboratory SOA samples and for ambient samples (You et al. 2012). The separation of the organic and aqueous phase would confine the interaction of water and ON molecules to the interface of the two phases, significantly lowering the rate of hydrolysis reactions.

Second, although particle-phase hydrolysis occurs at RH > 20%, water is likely the rate-limiting reagent in our experiments. In dilute solutions, the number

of water molecules consumed by hydrolysis is negligible compared to the total number of water molecules available; hydrolysis of ON molecule therefore follows a pseudo-first order rate law, where ON molecules are the rate-limit reagent (Hu et al. 2011). Such an approximation is not applicable to particle-phase hydrolysis because of the limited amount of water in the particles. Assuming hygroscopic growth factors of 1.01 (20% RH), 1.02 (40% RH), 1.04 (60% RH), and 1.08 (85% RH) (Baltensperger et al. 2005), the molar ratio of water to ON groups is 1, 2, 5, and 21 for reactions at 20%, 40%, 60%, and 85% RH, respectively. The comparable molar concentration of ON groups and water suggests that the hydrolysis reaction consumes significant fraction of condensed-phase water molecules and its rate is likely limited by both water and ON molecules. As a result, the establishment of hydrolysis equilibrium is expected to be slower than in dilute solutions.

The limited amount of particle-phase water may also limit dissolution of ON molecules, which likely slows down the hydrolysis process. In contrast, ON molecules will fully dissolve in dilute solutions, since the ON molecules are of intermediate solubility. For example, alkyl nitrates have Henrys law constants (H) of 1-4 M atm^{-1} (Roberts 1990), comparable to some aldehyde compounds, such as heptanal (H = 2.3 M atm^{-1}; Yaws and Yang 1992) and octanal (H = 2.1 M atm^{-1}; Zhou and Mopper 1990).

The hydrolysis mechanism could potentially explain the decrease of ON groups under high-RH conditions observed in previous chamber studies (Nguyen et al. 2011; Zhang et al. 2011). For example, the ON monomer identified in isoprene SOA by Zhang et al. (2011) could hydrolyze to form 2-MG, resulting in greater decrease of the monomer than the decrease of 2-MG under high-RH conditions, which is consistent with the reduction of ON monomer and 2-MG (compare to dry conditions) by factors of 2.9 and 1.8, respectively.

Similar to the ON groups, the mass fraction of nonacid carbonyl groups decreased as RH increased–likely resulted from hydration of nonacid carbonyl groups (ketones or aldehydes) to form acetals or hemiacetals, which could be catalyzed by secondary carboxylic acids (Jang et al. 2002; Kalberer et al. 2004) or by small, undetected amounts of adsorbed nitric acid. As a result of ON group hydrolysis

and carbonyl group hydration, the absolute mass of hydroxyl groups increased with increasing RH. However, the mass fraction of hydroxyl groups appeared independent of RH due to the enhancement of alkane and carboxylic acid group mass with increasing RH (Fig. 5.5a). The alkane and carboxylic groups correlated with R of 0.95 and 0.92 in ensemble particles (measured by FTIR) and single particles (measured by STXM-NEXAFS), respectively, suggesting that they likely formed in the same molecules and condensed simultaneously on the same particles.

(A)
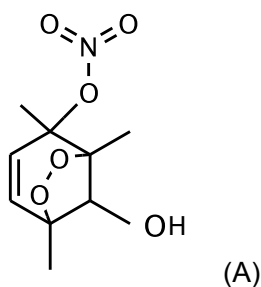
5.3.3 Light-absorbing properties of nitrogen-containing SOA

SOA formed under high-NO_x and low-NO_x conditions had different optical properties. The high-NO_x SOA appeared yellow by eye, while the low-NO_x SOA was white. The mass absorption coefficient (MAC) at 467 nm of the high-NO_x SOA was more than 3 times higher than that of the low-NO_x SOA for the dry and intermediate-RH experiments (Fig. 5.7), consistent with the observed yellow color of the high-NO_x SOA. Absorption of blue light by the high-NO_x SOA can be partially explained by the formation of nitroaromatic groups, which are naturally yellow (Booth 2007). Nitroaromatic groups form from the reaction of OH-TMB adduct (the aromatic radical produced from hydrogen abstraction of TMB by OH radicals) and NO_2 and are therefore more likely to form under high-NO_x conditions (Fig. 5.1a). Under high-NO_x conditions, the OH-TMB adduct may react with NO_2 or O_2, forming ON groups as well as nitroaromatic groups (Nishino et al. 2010; Nishino et al. 2008), which are low-volatility compounds and readily partition into
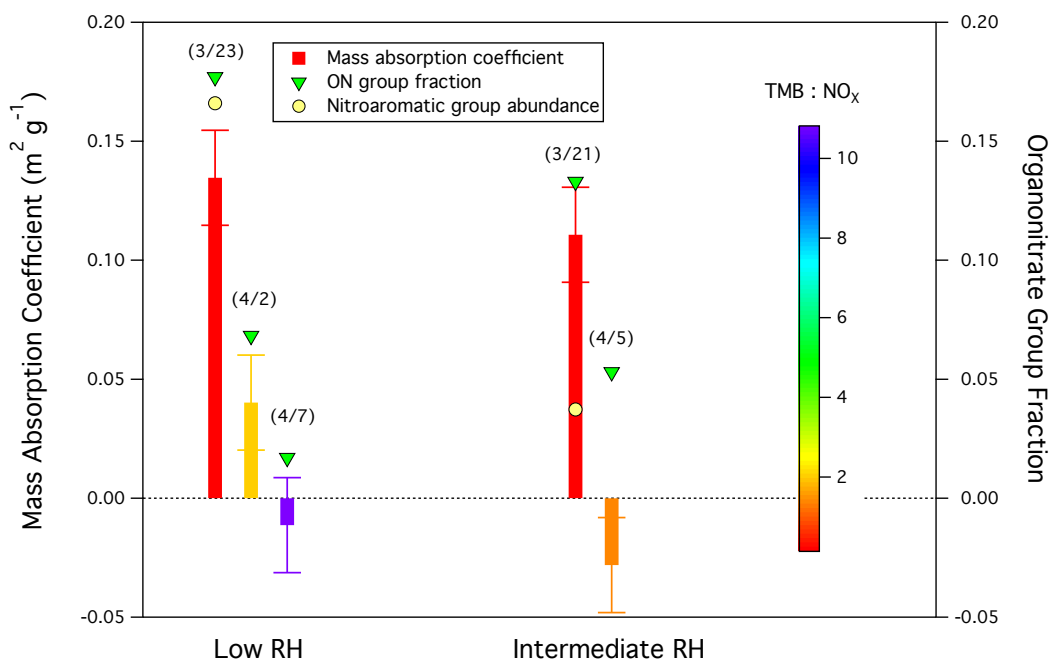
Figure 5.7: Mass absorption coefficient (MAC) (left axis), ON group mass fraction (right axis), and normalized (by OM) nitroaromatic group peak area (scale is not shown) for low-RH ($< 2\%$) and intermediate-RH ($\sim 50\%$) experiments (dates are shown in the parentheses), respectively. Colors for mass absorption coefficients represent TMB to NO_x ratios as indicated by the color bar. The ON group mass fraction was determined for the 30 min average around the peak absorption for each experiment using the scaled AMS nitrate mass fraction. The scaling factor was derived by linear regression (slope $= 0.60$; $r = 0.83$) of FTIR ON group mass fraction and AMS nitrate mass fraction.

particle phase. In contrast, OH-TMB adduct reacts predominately with O_2 when NO_x concentration is low—nitroaromatic groups do not form. Benzenenitroaromatic compounds are typically identified in highly-polluted, urban areas with high NO_x emissions, such as Los Angeles (Allen et al. 1994). The light-absorbing property of nitroaromatic groups is consistent with studies that suggest C-N bonds in SOA can absorb light (Galloway et al. 2009; Shapiro et al. 2009; Zhong and Jang 2011).

However, the difference of MAC for low-RH and intermediate-RH SOAs produced under low-NO_x conditions cannot be solely accounted for by nitroaromatic groups, because nitroaromatic groups were not observed in the FTIR spectra

when the TMB-to-NO$_x$ ratio was greater than 1. Under low-NO$_x$ conditions, the RH-induced differences in absorption were consistent with mass fractions of ON groups, i.e., higher MAC (absorption per SOA mass) corresponded to greater ON group mass fraction (ON group mass per SOA mass) (Fig. 5.7), suggesting that ON groups also play a role in absorbance of the 467 nm light. Further studies are needed to validate this connection.

5.4 Conclusions

In summary, this study demonstrates that ON groups may comprise up to 20% of the overall organic mass yield, but hydrolysis of ON groups in aerosol particles significantly reduces ON group mass fraction (2-4 times) under typical environmental conditions (RH $> 50\%$). We derive a hydrolysis rate of 4 day^{-1} (lifetime of 6 hours) from our measurements, which potentially explains the low ON group mass fraction measured in ambient air. Future work exploring the hydrolysis of ON molecules produced from precursor VOCs without alkyl-group substitutions (e.g., benzene, linear alkanes) would potentially clarify the atmospheric relevance of hydrolysis reactions. Such precursor compounds are not expected to form tertiary ON groups (i.e., only primary and secondary ON groups are produced), and therefore, based on studies in bulk solutions, hydrolysis of these ON molecules would not be expected to occur on atmospheric-relevant time scales. In light of these observations, model predictions should take hydrolysis into account, especially in coastal regions with high RH and high ON group production. In addition, nitrogen-containing SOA particles absorb visible light, suggesting that these compounds are potentially important for aerosols effects on the energy balance of the atmosphere.

5.5 Acknowledgments

operated for the U.S. Department of Energy by Battelle Memorial Institute under contract DE-AC06-76RLO 1830. The authors are grateful to the Lawrence Berkeley National Laboratory Advanced Light Source for providing facilities for the STXM analysis and beamline scientists David Kilcoyne and Tolek Tyliszczak for their generous help during sample analysis.

Chapter 5, in full, is a reprint of the material as it appears in Aerosol Science and Technology 2012. Liu, S., Shilling, J.E., Song, C., Hiranuma, N., Zaveri, A.Z., and Russell, L.M. (2012), Hydrolysis of organonitrate functional groups in aerosol particles, 46, 1359-1369. The dissertation author was the primary investigator and author of this paper.

References

[1] Allen, D. T., Palen, E. J., Haimov, M. I., Hering, S. V. and Young, J. R. (1994). Fourier Transform Infrared Spectroscopy of aerosol collected in a low pressure impactor (LPI/FTIR): Method development and field calibration. Aerosol Science and Technology 21:325-342.

[2] Atkinson, R. and Arey, J. (2003). Atmospheric degradation of volatile organic compounds. Chemical Reviews 103:4605-4638.

[3] Atkinson, R., Aschmann, S. M., Arey, J. and Shorees, B. (1992). Formation of radicals in the gas-phase reactions of O3 with a series of terpenes. Journal of Geophysical Research-Atmospheres 97:6065-6073.

[4] Baker, J. W. and Easty, D. M. (1950). Hydrolysis of organic nitrates. Nature 166:156-156.

[5] Baker, J. W. and Easty, D. M. (1952). Hydrolytic decomposition of esters of nitric acid. Part I. General experimental techniques. Alkaline hydrolysis and neutral solvolysis of methyl, ethyl, isopropyl, and tert-butyl nitrates in aqueous alcohol. Journal of the Chemical Society:1193-1207.

[6] Baltensperger, U., Kalberer, M., Dommen, J., Paulsen, D., Alfarra, M. R., Coe, H., Fisseha, R., Gascho, A., Gysel, M., Nyeki, S., Sax, M., Steinbacher, M., Prevot, A. S. H., Sjogren, S., Weingartner, E. and Zenobi, R. (2005). Secondary organic aerosols from anthropogenic and biogenic precursors. Faraday Discussions 130:265-278.

[7] Barket, D. J., Grossenbacher, J. W., Hurst, J. M., Shepson, P. B., Olszyna, K., Thornberry, T., Carroll, M. A., Roberts, J., Stroud, C., Bottenheim, J. and Biesenthal, T. (2004). A study of the NO_x dependence of isoprene oxidation. Journal of Geophysical Research-Atmospheres 109.

[8] Bond, T. C., Anderson, T. L. and Campbell, D. (1999). Calibration and intercomparison of filter-based measurements of visible light absorption by aerosols. Aerosol Science and Technology 30:582-600.

[9] Booth, G. (2007). Nitro Compounds, Aromatic, in Ullmann's Encyclopedia of Industrial Chemistry, John Wiley & Sons, New York.

[10] Boschan, R., Merrow, R. T. and Vandolah, R. W. (1955). The chemistry of nitrate esters. Chemical Reviews 55:485-510.

[11] Bruns, E. A., Perraud, V., Zelenyuk, A., Ezell, M. J., Johnson, S. N., Yu, Y., Imre, D., Finlayson-Pitts, B. J. and Alexander, M. L. (2010). Comparison of FTIR and Particle Mass Spectrometry for the Measurement of Particulate Organic Nitrates. Environmental Science & Technology 44:1056-1061.

[12] Camredon, M., Aumont, B., Lee-Taylor, J. and Madronich, S. (2007). The SOA/VOC/NO$_x$ system: an explicit model of secondary organic aerosol formation. Atmospheric Chemistry and Physics 7:5599-5610.

[13] Cocker, D. R., Mader, B. T., Kalberer, M., Flagan, R. C. and Seinfeld, J. H. (2001). The effect of water on gas-particle partitioning of secondary organic aerosol: II. m-xylene and 1,3,5-trimethylbenzene photooxidation systems. Atmospheric Environment 35:6073-6085.

[14] Darer, A. I., Cole-Filipiak, N. C., O'Connor, A. E. and Elrod, M. J. (2011). Formation and Stability of Atmospherically Relevant Isoprene-Derived Organosulfates and Organonitrates. Environmental Science & Technology 45:1895-1902.

[15] Day, D. A., Liu, S., Russell, L. M. and Ziemann, P. J. (2010). Organonitrate group concentrations in submicron particles with high nitrate and organic fractions in coastal southern California. Atmospheric Environment 44:1970-1979.

[16] DeCarlo, P. F., Kimmel, J. R., Trimborn, A., Northway, M. J., Jayne, J. T., Aiken, A. C., Gonin, M., Fuhrer, K., Horvath, T., Docherty, K. S., Worsnop, D. R. and Jimenez, J. L. (2006). Field-deployable, high-resolution, time-of-flight aerosol mass spectrometer. Analytical Chemistry 78:8281-8289.

[17] Farmer, D. K., Matsunaga, A., Docherty, K. S., Surratt, J. D., Seinfeld, J. H., Ziemann, P. J. and Jimenez, J. L. (2010). Response of an aerosol mass spectrometer to organonitrates and organosulfates and implications for atmospheric chemistry. Proceedings of the National Academy of Sciences of the United States of America 107:6670-6675.

[18] Fraser, M. P., Cass, G. R. and Simoneit, B. R. T. (1998). Gas-phase and particle-phase organic compounds emitted from motor vehicle traffic in a Los Angeles roadway tunnel. Environmental Science & Technology 32:2051-2060.

[19] Fry, J. L., Kiendler-Scharr, A., Rollins, A. W., Wooldridge, P. J., Brown, S. S., Fuchs, H., Dube, W., Mensah, A., dal Maso, M., Tillmann, R., Dorn, H. P., Brauers, T. and Cohen, R. C. (2009). Organic nitrate and secondary organic aerosol yield from NO(3) oxidation of beta-pinene evaluated using a gas-phase kinetics/aerosol partitioning model. Atmospheric Chemistry and Physics 9:1431-1449.

[20] Galloway, M. M., Chhabra, P. S., Chan, A. W. H., Surratt, J. D., Flagan, R. C., Seinfeld, J. H. and Keutsch, F. N. (2009). Glyoxal uptake on ammonium sulphate seed aerosol: reaction products and reversibility of uptake under dark and irradiated conditions. Atmospheric Chemistry and Physics 9:3331-3345.

[21] Gilardoni, S., Liu, S., Takahama, S., Russell, L. M., Allan, J. D., Steinbrecher, R., Jimenez, J. L., De Carlo, P. F., Dunlea, E. J. and Baumgardner, D. (2009). Characterization of organic ambient aerosol during MIRAGE 2006 on three platforms. Atmospheric Chemistry and Physics 9:5417-5432.

[22] Hallquist, M., Wangberg, I., Ljungstrom, E., Barnes, I. and Becker, K. H. (1999). Aerosol and product yields from NO3 radical-initiated oxidation of selected monoterpenes. Environmental Science & Technology 33:553-559.

[23] Handley, S. R., Clifford, D. and Donaldson, D. J. (2007). Photochemical loss of nitric acid on organic films: A possible recycling mechanism for NOx. Environmental Science & Technology 41:3898-3903.

[24] Hu, K. S., Darer, A. I. and Elrod, M. J. (2011). Thermodynamics and kinetics of the hydrolysis of atmospherically relevant organonitrates and organosulfates. Atmospheric Chemistry and Physics 11:8307-8320.

[25] Jang, M. S., Czoschke, N. M., Lee, S. and Kamens, R. M. (2002). Heterogeneous atmospheric aerosol production by acid-catalyzed particle-phase reactions. Science 298:814-817.

[26] Jang, M., Czoschke, N. M. and Northcross, A. L. (2004). Atmospheric organic aerosol production by heterogeneous acid-catalyzed reactions. Chemphyschem 5:1647-1661.

[27] Jayne, J. T., Leard, D. C., Zhang, X. F., Davidovits, P., Smith, K. A., Kolb, C. E. and Worsnop, D. R. (2000). Development of an aerosol mass spectrometer for size and composition analysis of submicron particles. Aerosol Science and Technology 33:49-70.

[28] Johnson, D., Jenkin, M. E., Wirtz, K. and Martin-Reviejo, M. (2004). Simulating the Formation of Secondary Organic Aerosol from the Photooxidation of Toluene. Environmental Chemistry 1:150-165.

[29] Johnson, K. S., Zuberi, B., Molina, L. T., Molina, M. J., Iedema, M. J., Cowin, J. P., Gaspar, D. J., Wang, C. and Laskin, A. (2005). Processing of soot in an urban environment: case study from the Mexico City Metropolitan Area. Atmospheric Chemistry and Physics 5:3033-3043.

[30] Kalberer, M., Paulsen, D., Sax, M., Steinbacher, M., Dommen, J., Prevot, A. S. H., Fisseha, R., Weingartner, E., Frankevich, V., Zenobi, R. and Baltensperger, U. (2004). Identification of polymers as major components of atmospheric organic aerosols. Science 303:1659-1662.

[31] Kim, H., Barkey, B. and Paulson, S. E. (2010). Real refractive indices of alpha- and beta-pinene and toluene secondary organic aerosols generated from ozonolysis and photo-oxidation. Journal of Geophysical Research-Atmospheres 115.

[32] Kroll, J. H. and Seinfeld, J. H. (2008). Chemistry of secondary organic aerosol: Formation and evolution of low-volatility organics in the atmosphere. Atmospheric Environment 42:3593-3624.

[33] Lindinger, W., Hansel, A. and Jordan, A. (1998). On-line monitoring of volatile organic compounds at pptv levels by means of proton-transfer-reaction mass spectrometry (PTR-MS) - Medical applications, food control and environmental research. International Journal of Mass Spectrometry 173:191-241.

[34] Lim, Y. B. and Ziemann, P. J. (2005). Products and mechanism of secondary organic aerosol formation from reactions of n-alkanes with OH radicals in the presence of NOx. Environmental Science & Technology 39:9229-9236.

[35] Liu, S., Day, D. A., Shields, J. E. and Russell, L. M. (2011). Ozone-driven daytime formation of secondary organic aerosol containing carboxylic acid groups and alkane groups. Atmospheric Chemistry and Physics 11:8321-8341.

[36] Liu, S., Takahama, S., Russell, L. M., Gilardoni, S. and Baumgardner, D. (2009). Oxygenated organic functional groups and their sources in single and submicron organic particles in MILAGRO 2006 campaign. Atmospheric Chemistry and Physics 9:6849-6863.

[37] Lockwood, A. L., Shepson, P. B., Fiddler, M. N. and Alaghmand, M. (2010). Isoprene nitrates: preparation, separation, identification, yields, and atmospheric chemistry. Atmospheric Chemistry and Physics 10:6169-6178.

[38] Maki, A. G. and Wells, J. S. (1992). MEASUREMENT AND ANALYSIS OF THE FERMI RESONANCE BETWEEN NU-5 AND 2-NU-9 OF NITRIC-ACID. Journal of Molecular Spectroscopy 152:69-79.

[39] Maria, S. F., Russell, L. M., Turpin, B. J. and Porcja, R. J. (2002). FTIR measurements of functional groups and organic mass in aerosol samples over the Caribbean. Atmospheric Environment 36:5185-5196.

[40] Matsunaga, A. and Ziemann, P. J. (2009). Yields of beta-Hydroxynitrates and Dihydroxynitrates in Aerosol Formed from OH Radical-Initiated Reactions

of Linear Alkenes in the Presence of NO(x). Journal of Physical Chemistry A 113:599-606.

[41] McGraw, G. E., Bernitt, D. L. and Hisatsun.Ic (1965). Vibrational spectra of isotopic nitric acids. Journal of Chemical Physics 42:237-244.

[42] Miller, F. A. and Wilkins, C. H. (1952). Infrared spectra and characteristic frequences of inorganic ions-thier use in quantitative analysis. Analytical Chemistry 24:1253-1294. Nguyen, T. B., Roach, P. J., Laskin, J., Laskin, A. and Nizkorodov, S. A. (2011). Effect of humidity on the composition of isoprene photooxidation secondary organic aerosol. Atmospheric Chemistry and Physics 11:6931-6944.

[43] Nishino, N., Arey, J. and Atkinson, R. (2010). Formation Yields of Glyoxal and Methylglyoxal from the Gas-Phase OH Radical-Initiated Reactions of Toluene, Xylenes, and Trimethylbenzenes as a Function of NO(2) Concentration. Journal of Physical Chemistry A 114:10140-10147.

[44] Nishino, N., Atkinson, R. and Arey, J. (2008). Formation of Nitro Products from the Gas-Phase OH Radical-Initiated Reactions of Toluene, Naphthalene, and Biphenyl: Effect of NO(2) Concentration. Environmental Science & Technology 42:9203-9209.

[45] Odum, J. R., Hoffmann, T., Bowman, F., Collins, D., Flagan, R. C. and Seinfeld, J. H. (1996). Gas/particle partitioning and secondary organic aerosol yields. Environmental Science & Technology 30:2580-2585.

[46] Ogren, J. A. (2010). Comment on oCalibration and Intercomparison of Filter-Based Measurements of Visible Light Absorption by Aerosolso. Aerosol Science and Technology 44:589-591.

[47] Paulot, F., Crounse, J. D., Kjaergaard, H. G., Kroll, J. H., Seinfeld, J. H. and Wennberg, P. O. (2009). Isoprene photooxidation: new insights into the production of acids and organic nitrates. Atmospheric Chemistry and Physics 9:1479-1501.

[48] Paulsen, D., Dommen, J., Kalberer, M., Prevot, A. S. H., Richter, R., Sax, M., Steinbacher, M., Weingartner, E. and Baltensperger, U. (2005). Secondary organic aerosol formation by irradiation of 1,3,5-trimethylbenzene-NO_x-H2O in a new reaction chamber for atmospheric chemistry and physics. Environmental Science & Technology 39:2668-2678.

[49] Roberts, J. M. (1990). The atmospheric chemistry of organic nitrates. Atmospheric Environment Part a-General Topics 24:243-287.

[50] Robinson, A. L., Donahue, N. M., Shrivastava, M. K., Weitkamp, E. A., Sage, A. M., Grieshop, A. P., Lane, T. E., Pierce, J. R. and Pandis, S. N. (2007). Rethinking organic aerosols: Semivolatile emissions and photochemical aging. Science 315:1259-1262.

[51] Russell, L. M., Bahadur, R. and Ziemann, P. J. (2011). Identifying organic aerosol sources by comparing functional group composition in chamber and atmospheric particles. Proceedings of the National Academy of Sciences of the United States of America 108:3516-3521.

[52] Russell, L. M., Takahama, S., Liu, S., Hawkins, L. N., Covert, D. S., Quinn, P. K. and Bates, T. S. (2009). Oxygenated fraction and mass of organic aerosol from direct emission and atmospheric processing measured on the R/V Ronald Brown during TEXAQS/GoMACCS 2006. Journal of Geophysical Research-Atmospheres 114.

[53] Saukko, E., Lambe, A. T., Massoli, P., Koop, T., Wright, J. P., Croasdale, D. R., Pedernera, D. A., Onasch, T. B., Laaksonen, A., Davidovits, P., Worsnop, D. R. and Virtanen, A. (2012). Humidity-dependent phase state of SOA particles from biogenic and anthropogenic precursors. Atmospheric Chemistry and Physics Discussions 12:4447-4476.

[54] Sax, M., Zenobi, R., Baltensperger, U. and Kalberer, M. (2005). Time resolved infrared spectroscopic analysis of aerosol formed by photo-oxidation of 1,3,5-trimethylbenzene and alpha-pinene. Aerosol Science and Technology 39:822-830.

[55] Seinfeld, J. H., Erdakos, G. B., Asher, W. E. and Pankow, J. F. (2001). Modeling the formation of secondary organic aerosol (SOA). 2. The predicted effects of relative humidity on aerosol formation in the alpha-pinene-, beta-pinene-, sabinene-, Delta(3)-Carene-, and cyclohexene-ozone systems. Environmental Science & Technology 35:1806-1817.

[56] Shapiro, E. L., Szprengiel, J., Sareen, N., Jen, C. N., Giordano, M. R. and McNeill, V. F. (2009). Light-absorbing secondary organic material formed by glyoxal in aqueous aerosol mimics. Atmospheric Chemistry and Physics 9:2289-2300.

[57] Shiraiwa, M., Ammann, M., Koop, T. and Poeschl, U. (2011). Gas uptake and chemical aging of semisolid organic aerosol particles. Proceedings of the National Academy of Sciences of the United States of America 108:11003-11008.

[58] Sporleder, D. and Ewing, G. E. (2001). Infrared spectroscopic investigation of the heterogeneous reaction of HNO3 and NaCl(100). Journal of Physical Chemistry A 105:1838-1846.

[59] Takahama, S., Liu, S. and Russell, L. M. (2010). Coatings and clusters of carboxylic acids in carbon-containing atmospheric particles from spectromicroscopy and their implications for cloud-nucleating and optical properties. J. Geophys. Res.-Atmos., 115, D01202, doi: 10.1029/2009JD012622.

[60] Thornton, J. A., Braban, C. F. and Abbatt, J. P. D. (2003). N2O5 hydrolysis on sub-micron organic aerosols: the effect of relative humidity, particle phase, and particle size. Physical Chemistry Chemical Physics 5:4593-4603.

[61] Vaden, T. D., Imre, D., Beranek, J., Shrivastava, M. and Zelenyuk, A. (2011). Evaporation kinetics and phase of laboratory and ambient secondary organic aerosol. Proceedings of the National Academy of Sciences of the United States of America 108:2190-2195.

[62] Virtanen, A., Joutsensaari, J., Koop, T., Kannosto, J., Yli-Pirila, P., Leskinen, J., Makela, J. M., Holopainen, J. K., Poeschl, U., Kulmala, M., Worsnop, D. R. and Laaksonen, A. (2010). An amorphous solid state of biogenic secondary organic aerosol particles. Nature 467:824-827.

[63] Wangberg, I., Barnes, I. and Becker, K. H. (1997). Product and mechanistic study of the reaction of NO3 radicals with alpha-pinene. Environmental Science & Technology 31:2130-2135.

[64] Wyche, K. P., Monks, P. S., Ellis, A. M., Cordell, R. L., Parker, A. E., Whyte, C., Metzger, A., Dommen, J., Duplissy, J., Prevot, A. S. H., Baltensperger, U., Rickard, A. R. and Wulfert, F. (2009). Gas phase precursors to anthropogenic secondary organic aerosol: detailed observations of 1,3,5-trimethylbenzene photooxidation. Atmospheric Chemistry and Physics 9:635-665.

[65] Yaws, C. L. and Yang, H.-C. (1992). Henrys law constant for compound in water, in Thermodynamic and Physical Property Data, C. L. Yaws, ed., Gulf Publishing Company, Houston.

[66] You, Y., Renbaum-Wolff, L., Carreras-Sospedra, M., Hanna, S. J., Hiranuma, N., Kamal, S., Smith, M. L., Zhang, X., Weber, R. J., Shilling, J. E., Dabdub, D., Martin, S. T. and Bertram, A. K. (2012). Images reveal that atmospheric particles can undergo liquid-liquid phase separations. Proceedings of the National Academy of Sciences of the United States of America, in press.

[67] Zaveri, R. A., Berkowitz, C. M., Brechtel, F. J., Gilles, M. K., Hubbe, J. M., Jayne, J. T., Kleinman, L. I., Laskin, A., Madronich, S., Onasch, T. B., Pekour, M. S., Springston, S. R., Thornton, J. A., Tivanski, A. V. and Worsnop, D. R. (2010). Nighttime chemical evolution of aerosol and trace gases in a power plant plume: Implications for secondary organic nitrate and organosulfate aerosol formation, NO3 radical chemistry, and N2O5 heterogeneous hydrolysis. Journal of Geophysical Research-Atmospheres 115.

[68] Zhang, H., Surratt, J. D., Lin, Y. H., Bapat, J. and Kamens, R. M. (2011). Effect of relative humidity on SOA formation from isoprene/NO photooxidation: enhancement of 2-methylglyceric acid and its corresponding oligoesters under dry conditions. Atmospheric Chemistry and Physics 11:6411-6424.

[69] Zhong, M. and Jang, M. (2011). Light absorption coefficient measurement of SOA using a UV-Visible spectrometer connected with an integrating sphere. Atmospheric Environment 45:4263-4271.

[70] Zhou, X. L., Gao, H. L., He, Y., Huang, G., Bertman, S. B., Civerolo, K. and Schwab, J. (2003). Nitric acid photolysis on surfaces in low-NOx environments: Significant atmospheric implications. Geophysical Research Letters 30:doi:10.1029/2003GL018620.

[71] Zhou, X. L. and Mopper, K. (1990). Apparent partition-coefficients of 15 carbonyl compounds between air and sea water and between air and fresh water-implications for air sea exchange. Environmental Science & Technology 24:1864-1869.

Conclusion

Field measurements at Mexico City and its surrounding areas, Scripps Pier (downwind the Los Angeles basin), and Bakersfield suggest that OM accounts for 40– 60% of submicron particle mass. The OM in all three of these sites is largely composed of alkane (35–65%), carboxylic acid (10–35%), and hydroxyl groups (12–22%), followed by smaller mass fractions of nonacid carbonyl (0–11%), amine (2–11%), ON (0–2%), and organosulfur groups (0–2%). Concentrations of these components change diurnally, typically with alkane and carboxylic acid groups peaking in the afternoon, suggesting that these groups likely formed in the same molecules via photooxidation reactions and condensed simultaneously. By applying the PMF analysis separately to the FTIR and AMS measurements, a variety of robust sources is identified, including fossil fuel combustion, biomass burning, petroleum operation, vegetative detritus, biogenic emission, and marine origin. Among these sources, fossil fuel combustion is the source that accounts for the largest fraction of OM in all three regions (60–90% OM). Organic aerosols formed from this source are often oxidized, making the OM largely (typically 60–90%) composed of SOA, which generally formed within 1–3 days based on the diurnal cycle analysis of the SOA components in the Scripps Pier study.

Evidence of the SOA components produced from fossil fuel combustions, specifically from alkane and aromatic hydrocarbons, has been shown in measurements taken from the Scripps Pier (Chapter 2) and Bakersfield (Chapters 3 and 4). The finding that alkane SOA correlates to O_3 supports the hypothesis (proposed by Russell et al., 2011) that O_3 plays a role in the formation of acid groups in this component. The aromatic SOA components are more consistent with OH radical-driven oxidation products. Further, the size dependence of the ratio of

OOA to PM suggests that OOA components are formed through surface-limited processes, most likely by condensation on particles of 200–500-nm vacuum aerodynamic diameter. When compared with the fossil fuel combustion emission, the biogenic source is minor in urban environments. The biogenic SOA component has only been identified in significant amount (10–20% of the OM) at Bakersfield, where it is likely to have been produced via NO_3 oxidation processes at night, when wind favors the transport of biogenic (monoterpene) precursors to the sampling site. The biogenic SOA component accounted for 50–80% of ON groups. Reaction chamber studies (Chapter 5) suggest that hydrolysis reactions occur when relative humidity is greater than 20% at a rate constant of 4 day^{-1} (lifetime of 6 hours). In summary, this work shows that SOA components produced in urban emissions contribute significantly to fine particle mass. These components have distinct chemical compositions, sources, formation mechanisms, and fates that are distinguishable using a combination of techniques. Vehicular emission, the major source of SOA in this work, is the largest source in Southern California and should be limited in emission regulations.

Future measurements could be designed to address the questions raised in this work. One issue that remains challenging is that of how the size distribution of SOA changes during atmospheric processing. Many atmospheric processes, such as new particle formation, condensational growth, evaporation, and deposition can change particle size. Therefore, evolution of SOA size distribution provides insights for identifying formation and transformation mechanisms of the SOA components. The size distribution question is raised from the CalNex study, where size distribution of the PMF factors was indirectly estimated by correlating time series of the factors to the size-resolved OM fractions measured by the AMS. This method is limited because it only gives the average factor size distribution for the entire campaign and, as a result, variation of the size of the SOA components with time remains unknown. This limitation speaks to the need for improved measurement of SOA's size distribution, which can be accomplished by collecting time- and size-resolved filter samples using micro-orifice uniform-deposition impactor for FTIR analysis. Applying PMF to the size-resolved infrared spectra would yield a set of

factors for each OM fraction. By comparing the common factors of all the size fractions, the size distribution of the factors can be derived, which could be combined with the functional group size distribution to investigate the formation and evolution of SOA. Size-resolved ambient particle samples are suggested to be collected in heavily polluted areas (e.g., the Los Angeles basin) to ensure enough mass for each mass fraction. Simultaneous sample collection in roadway tunnels close to the ambient sampling site has the added benefit of obtaining size distribution of POA that is directly emitted from primary sources. By quantitative measurement of the size distribution difference of POA and SOA and by evaluating the variation of this difference with time, the effects of atmospheric processing (aging) on urban emissions can be studied. The results of SOA size distribution can also be used to tighten constraints of model predictions of SOA's optical properties, which heavily rely on particle sizes and are critical for assessing the effects of SOA on the Earth's radiative balance and climate change.